

1 **The Sensitivity to Oscillation Parameters**
2 **from a Simultaneous Beam and**
3 **Atmospheric Neutrino Analysis that**
4 **combines the T2K and SK Experiments**



6 Daniel Robert Clement Barrow
7 Magdalen College
8 University of Oxford

9 A thesis submitted for the degree of
10 *Doctor of Philosophy*
11 Michaelmas 2022

Abstract

12

13 Lorem ipsum dolor sit amet, consectetur adipiscing elit. Pellentesque sit amet
14 nibh volutpat, scelerisque nibh a, vehicula neque. Integer placerat nulla massa,
15 et vestibulum velit dignissim id. Ut eget nisi elementum, consectetur nibh in,
16 condimentum velit. Quisque sodales dui ut tempus mattis. Duis malesuada arcu
17 at ligula egestas egestas. Phasellus interdum odio at sapien fringilla scelerisque.
18 Mauris sagittis eleifend sapien, sit amet laoreet felis mollis quis. Pellentesque
19 dui ante, finibus eget blandit sit amet, tincidunt eu neque. Vivamus rutrum
20 dapibus ligula, ut imperdiet lectus tincidunt ac. Pellentesque ac lorem sed
21 diam egestas lobortis.

22 Suspendisse leo purus, efficitur mattis urna a, maximus molestie nisl. Aenean
23 porta semper tortor a vestibulum. Suspendisse viverra facilisis lorem, non
24 pretium erat lacinia a. Vestibulum tempus, quam vitae placerat porta, magna
25 risus euismod purus, in viverra lorem dui at metus. Sed ac sollicitudin nunc.
26 In maximus ipsum nunc, placerat maximus tortor gravida varius. Suspendisse
27 pretium, lorem at porttitor rhoncus, nulla urna condimentum tortor, sed suscipit
28 nisi metus ac risus.

29 Aenean sit amet enim quis lorem tristique commodo vitae ut lorem. Duis
30 vel tincidunt lacus. Sed massa velit, lacinia sed posuere vitae, malesuada vel
31 ante. Praesent a rhoncus leo. Etiam sed rutrum enim. Pellentesque lobortis
32 elementum augue, at suscipit justo malesuada at. Lorem ipsum dolor sit amet,
33 consectetur adipiscing elit. Praesent rhoncus convallis ex. Etiam commodo nunc
34 ex, non consequat diam consectetur ut. Pellentesque vitae est nec enim interdum
35 dapibus. Donec dapibus purus ipsum, eget tincidunt ex gravida eget. Donec
36 luctus nisi eu fringilla mollis. Donec eget lobortis diam.

37 Suspendisse finibus placerat dolor. Etiam ornare elementum ex ut vehicula.
38 Donec accumsan mattis erat. Quisque cursus fringilla diam, eget placerat neque
39 bibendum eu. Ut faucibus dui vitae dolor porta, at elementum ipsum semper.
40 Sed ultrices dui non arcu pellentesque placerat. Etiam posuere malesuada turpis,
41 nec malesuada tellus malesuada.

42

Statement of Originality

43 Lorem ipsum dolor sit amet, consectetur adipiscing elit. Pellentesque sit amet
44 nibh volutpat, scelerisque nibh a, vehicula neque. Integer placerat nulla massa,
45 et vestibulum velit dignissim id. Ut eget nisi elementum, consectetur nibh in,
46 condimentum velit. Quisque sodales dui ut tempus mattis. Duis malesuada arcu
47 at ligula egestas egestas. Phasellus interdum odio at sapien fringilla scelerisque.
48 Mauris sagittis eleifend sapien, sit amet laoreet felis mollis quis. Pellentesque
49 dui ante, finibus eget blandit sit amet, tincidunt eu neque. Vivamus rutrum
50 dapibus ligula, ut imperdiet lectus tincidunt ac. Pellentesque ac lorem sed
51 diam egestas lobortis.

52 Suspendisse leo purus, efficitur mattis urna a, maximus molestie nisl. Aenean
53 porta semper tortor a vestibulum. Suspendisse viverra facilisis lorem, non
54 pretium erat lacinia a. Vestibulum tempus, quam vitae placerat porta, magna
55 risus euismod purus, in viverra lorem dui at metus. Sed ac sollicitudin nunc.
56 In maximus ipsum nunc, placerat maximus tortor gravida varius. Suspendisse
57 pretium, lorem at porttitor rhoncus, nulla urna condimentum tortor, sed suscipit
58 nisi metus ac risus.

Acknowledgements

60 Personal

61 This is where you thank your advisor, colleagues, and family and friends.

62 Lorem ipsum dolor sit amet, consectetur adipiscing elit. Vestibulum feugiat
63 et est at accumsan. Praesent sed elit mattis, congue mi sed, porta ipsum. In
64 non ullamcorper lacus. Quisque volutpat tempus ligula ac ultricies. Nam sed
65 erat feugiat, elementum dolor sed, elementum neque. Aliquam eu iaculis est,
66 a sollicitudin augue. Cras id lorem vel purus posuere tempor. Proin tincidunt,
67 sapien non dictum aliquam, ex odio ornare mauris, ultrices viverra nisi magna
68 in lacus. Fusce aliquet molestie massa, ut fringilla purus rutrum consectetur.
69 Nam non nunc tincidunt, rutrum dui sit amet, ornare nunc. Donec cursus
70 tortor vel odio molestie dignissim. Vivamus id mi erat. Duis porttitor diam
71 tempor rutrum porttitor. Lorem ipsum dolor sit amet, consectetur adipiscing
72 elit. Sed condimentum venenatis consectetur. Lorem ipsum dolor sit amet,
73 consectetur adipiscing elit.

74 Aenean sit amet lectus nec tellus viverra ultrices vitae commodo nunc. Mauris
75 at maximus arcu. Aliquam varius congue orci et ultrices. In non ipsum vel
76 est scelerisque efficitur in at augue. Nullam rhoncus orci velit. Duis ultricies
77 accumsan feugiat. Etiam consectetur ornare velit et eleifend.

78 Suspendisse sed enim lacinia, pharetra neque ac, ultricies urna. Phasellus sit
79 amet cursus purus. Quisque non odio libero. Etiam iaculis odio a ex volutpat, eget
80 pulvinar augue mollis. Mauris nibh lorem, mollis quis semper quis, consequat
81 nec metus. Etiam dolor mi, cursus a ipsum aliquam, eleifend venenatis ipsum.
82 Maecenas tempus, nibh eget scelerisque feugiat, leo nibh lobortis diam, id laoreet
83 purus dolor eu mauris. Pellentesque habitant morbi tristique senectus et netus
84 et malesuada fames ac turpis egestas. Nulla eget tortor eu arcu sagittis euismod
85 fermentum id neque. In sit amet justo ligula. Donec rutrum ex a aliquet egestas.

86 Institutional

87 If you want to separate out your thanks for funding and institutional support,
88 I don't think there's any rule against it. Of course, you could also just remove
89 the subsections and do one big traditional acknowledgement section.

90 Lorem ipsum dolor sit amet, consectetur adipiscing elit. Ut luctus tempor ex at
91 pretium. Sed varius, mauris at dapibus lobortis, elit purus tempor neque, facilisis
92 sollicitudin felis nunc a urna. Morbi mattis ante non augue blandit pulvinar.
93 Quisque nec euismod mauris. Nulla et tellus eu nibh auctor malesuada quis
94 imperdiet quam. Sed eget tincidunt velit. Cras molestie sem ipsum, at faucibus
95 quam mattis vel. Quisque vel placerat orci, id tempor urna. Vivamus mollis,
96 neque in aliquam consequat, dui sem volutpat lorem, sit amet tempor ipsum felis
97 eget ante. Integer lacinia nulla vitae felis vulputate, at tincidunt ligula maximus.
98 Aenean venenatis dolor ante, euismod ultrices nibh mollis ac. Ut malesuada
99 aliquam urna, ac interdum magna malesuada posuere.

Contents

¹⁰¹	1 Introduction	1
¹⁰²	2 Neutrino Oscillation Physics	2
¹⁰³	2.1 Discovery of Neutrinos	3
¹⁰⁴	2.2 Theory of Neutrino Oscillation	4
¹⁰⁵	2.3 Neutrino Oscillation Measurements	8
¹⁰⁶	2.4 Summary Of Oscillation Parameter Measurements	18
¹⁰⁷	2.5 Overview of Oscillation Effects	19
¹⁰⁸	3 T2K and SK Experiment Overview	27
¹⁰⁹	3.1 The Super-Kamiokande Experiment	27
¹¹⁰	3.2 The Tokai to Kamioka Experiment	38
¹¹¹	4 Bayesian Statistics and Markov Chain Monte Carlo Techniques	53
¹¹²	4.1 Bayesian Statistics	54
¹¹³	4.2 Monte Carlo Simulation	56
¹¹⁴	4.3 Understanding the MCMC Results	64
¹¹⁵	5 Simulation, Reconstruction, and Event Reduction	69
¹¹⁶	5.1 Simulation	69
¹¹⁷	5.2 Event Reconstruction at SK	75
¹¹⁸	5.3 Event Reduction at SK	86
¹¹⁹	6 Sample Selections and Systematics	91
¹²⁰	6.1 Atmospheric Samples	93
¹²¹	6.2 Near Detector Beam Samples	101
¹²²	6.3 Far Detector Beam Samples	103
¹²³	6.4 Systematic Uncertainties	109
¹²⁴	6.5 Likelihood Calculation	129
¹²⁵	7 Oscillation Probability Calculation	133
¹²⁶	7.1 Treatment of Fast Oscillations	134
¹²⁷	7.2 Calculation Engine	141
¹²⁸	7.3 Matter Density Profile	145
¹²⁹	7.4 Production Height Averaging	150

¹³⁰	8 Oscillation Analysis	153
¹³¹	8.1 Monte Carlo Prediction	154
¹³²	8.2 Likelihood Scans	155
¹³³	8.3 Sensitivity Studies	167
¹³⁴	8.4 Summary of Sensitivity Studies	219
¹³⁵	9 Conclusions and Outlook	221

1

Introduction

136

137

2

138

139

Neutrino Oscillation Physics

140 When first proposed, neutrinos were expected to be approximately massless
141 fermions that only interact through weak and gravitational forces. This meant
142 they were very difficult to detect as they can pass through significant amounts
143 of matter without interacting. Despite this, experimental neutrino physics has
144 developed many different detection techniques and observed neutrinos from
145 both natural and artificial sources. In direct tension with Standard Model physics,
146 neutrinos have been determined to oscillate between different lepton flavours,
147 requiring them to have mass.

148 The observation techniques which led to the discovery of the neutrino are doc-
149 umented in section 2.1. The theory underpinning neutrino oscillation is described
150 in section 2.2 and includes the approximations which can be made to simplify
151 the understanding of neutrino oscillation in the two-flavour approximation. Past,
152 current, and future neutrino experiments are detailed in section 2.3, including the
153 reactor, atmospheric, and long-baseline accelerator neutrino sources that have
154 been used to successfully constrain oscillation parameters. Finally, the current
155 state of oscillation parameter measurements are summarised in section 2.4.

156 2.1 Discovery of Neutrinos

157 At the start of the 20th century, the electrons emitted from the β -decay of the
158 nucleus were found to have a continuous energy spectrum [1, 2]. This observation
159 seemingly broke the energy conservation invoked within that period’s nuclear
160 models. In 1930, Pauli provided a solution to this problem in the form of a
161 new particle, the neutrino (originally termed “neutron”). It was theorized to
162 be an electrically neutral spin-1/2 fermion with a mass smaller than that of the
163 electron [3]. This neutrino was emitted with the electron in β -decay to alleviate
164 the apparent breaking of energy conservation. As a predecessor of today’s weak
165 interaction model, Fermi’s theory of β -decay developed the understanding by
166 coupling the four constituent particles: electron, proton, neutron, and neutrino,
167 into a quantitative model [4].

168 Whilst Pauli was not convinced of the ability to detect neutrinos, the first
169 observations of the particle were made in the mid-1950s when neutrinos from
170 a reactor were observed via the inverse β -decay (IBD) process, $\bar{\nu}_e + p \rightarrow n + e^+$
171 [5, 6]. The detector consisted of two parts: a neutrino interaction medium and
172 a liquid scintillator. The interaction medium was built from two water tanks,
173 loaded with cadmium chloride to allow for increased efficiency in the detection
174 of neutron capture. The positron emitted from IBD annihilates, $e^+ + e^- \rightarrow 2\gamma$,
175 generating a prompt signal and the neutron is captured on the cadmium via
176 $n + ^{108}Cd \rightarrow ^{109*}Cd \rightarrow ^{109}Cd + \gamma$, producing a delayed signal. An increase in
177 the coincidence rate was observed when the reactor was operating which was
178 interpreted as interactions from neutrinos generated in the reactor.

179 After the discovery of the ν_e , the question of how many flavours of neu-
180 trino exist was asked. In 1962, a measurement of the ν_μ was conducted at the
181 Brookhaven National Laboratory [7]. A proton beam was directed at a beryllium
182 target, generating pions which then decayed via $\pi^\pm \rightarrow \mu^\pm + (\nu_\mu, \bar{\nu}_\mu)$, and the
183 subsequent interactions of the ν_μ were observed. As the subsequent interaction
184 of the neutrino generated muons rather than electrons, it was determined that

the ν_μ was fundamentally different from ν_e . The final observation to be made was that of the ν_τ from the DONUT experiment [8]. Three neutrinos seem the obvious solution as it mirrors the known number of charged leptons (as they form weak isospin doublets) but there could be evidence of more. Several neutrino experiments have found anomalous results [9, 10] which could be attributed to “sterile” neutrinos. These hypothesised particles are not affected by gauge interactions in the Standard Model so their presence can only be inferred through the observation of non-standard oscillation modes. However, cosmological observations indicate the number of neutrino species $N_{eff} = 2.99 \pm 0.17$ [11], as measured from the cosmic microwave background power spectrum. LEP also measured the number of active neutrino flavours to be $N_\nu = 2.9840 \pm 0.0082$ [12] from measurements of the Z-decay width, but this does not strongly constrain the number of sterile neutrinos.

2.2 Theory of Neutrino Oscillation

A neutrino generated with lepton flavour α can change into a different lepton flavour β after propagating some distance. This phenomenon is called neutrino oscillation and requires that neutrinos must have a non-zero mass. This behaviour has been characterised by the Pontecorvo-Maki-Nakagawa-Sakata (PMNS) [13–15] mixing matrix which describes how the flavour and mass of neutrinos are associated. This is analogous to the Cabibbo-Kobayashi-Maskawa (CKM) [16] matrix measured in quark physics.

2.2.1 Three Flavour Oscillations

The PMNS parameterisation defines three flavour eigenstates, ν_e , ν_μ and ν_τ (indexed ν_α), which are eigenstates of the weak interaction and three mass eigenstates, ν_1 , ν_2 and ν_3 (indexed ν_i). Each mass eigenstate is the superposition

²¹⁰ of all three flavour states,

$$|\nu_i\rangle = \sum_{\alpha} U_{\alpha i} |\nu_{\alpha}\rangle. \quad (2.1)$$

²¹¹ Where U is the 3×3 PMNS matrix which is unitary and connects the mass
²¹² and flavour eigenstates.

²¹³ The weak interaction, when interacting via a W^{\pm} boson, couples to flavour
²¹⁴ eigenstates so neutrinos interact with leptons of the same flavour. The prop-
²¹⁵ agation of a neutrino flavour eigenstate, in a vacuum, can be re-written as a
²¹⁶ plane-wave solution to the time-dependent Schrödinger equation,

$$|\nu_{\alpha}(t)\rangle = \sum_i U_{\alpha i}^{*} |\nu_i\rangle e^{-i\phi_i}. \quad (2.2)$$

²¹⁷ The ϕ_i term can be expressed in terms of the energy, E_i , and magnitude of the
²¹⁸ three momenta, p_i , of the neutrino, $\phi_i = E_i t - p_i x$ (t and x being time and position
²¹⁹ coordinates). The probability of observing a neutrino of flavour eigenstate β from
²²⁰ one which originated as flavour α can be calculated as,

$$P(\nu_{\alpha} \rightarrow \nu_{\beta}) = |\langle \nu_{\beta} | \nu_{\alpha}(t) \rangle|^2 = \sum_{i,j} U_{\alpha i}^{*} U_{\beta i} U_{\alpha j} U_{\beta j}^{*} e^{-i(\phi_j - \phi_i)}. \quad (2.3)$$

²²¹ The term within the exponential can be represented as,

$$\phi_j - \phi_i = E_j t - E_i t - p_j x + p_i x. \quad (2.4)$$

²²² For a relativistic particle, $E_i \gg m_i$, a Taylor series expansion means,

$$p_i = \sqrt{E_i^2 - m_i^2} \approx E_i - \frac{m_i^2}{2E_i}. \quad (2.5)$$

²²³ Making the approximations that neutrinos are relativistic, the mass eigenstates
²²⁴ were created with the same energy and that $x = L$, where L is the distance
²²⁵ travelled by the neutrino, Equation 2.4 then becomes

$$\phi_j - \phi_i = \frac{\Delta m_{ij}^2 L}{2E}, \quad (2.6)$$

where $\Delta m_{ij}^2 = m_i^2 - m_j^2$. This, combined with further use of unitarity relations results in Equation 2.3 becoming

$$\begin{aligned} P(\nu_\alpha \rightarrow \nu_\beta) &= \delta_{\alpha\beta} - 4 \sum_{i>j} \Re \left(U_{\alpha i}^* U_{\beta i} U_{\alpha j} U_{\beta j}^* \right) \sin^2 \left(\frac{\Delta m_{ij}^2 L}{4E} \right) \\ &\quad + (-) 2 \sum_{i>j} \Im \left(U_{\alpha i}^* U_{\beta i} U_{\alpha j} U_{\beta j}^* \right) \sin \left(\frac{\Delta m_{ij}^2 L}{2E} \right). \end{aligned} \quad (2.7)$$

Where $\delta_{\alpha\beta}$ is the Kronecker delta function and the negative sign on the last term is included for the oscillation probability of antineutrinos. As an important point to note, the observation of oscillation probability requires a non-zero value of Δm_{ij}^2 , which in turn requires that neutrinos have differing masses.

Typically, the PMNS matrix is parameterised into three mixing angles, a charge parity (CP) violating phase δ_{CP} , and two Majorana phases $\alpha_{1,2}$,

$$U = \underbrace{\begin{pmatrix} 1 & 0 & 0 \\ 0 & c_{23} & s_{23} \\ 0 & -s_{23} & c_{23} \end{pmatrix}}_{\text{Atmospheric, Accelerator}} \underbrace{\begin{pmatrix} c_{13} & 0 & s_{13} e^{-i\delta_{CP}} \\ 0 & 1 & 0 \\ -s_{13} e^{-i\delta_{CP}} & 0 & c_{13} \end{pmatrix}}_{\text{Reactor, Accelerator}} \times \underbrace{\begin{pmatrix} c_{12} & s_{12} & 0 \\ -s_{12} & c_{12} & 0 \\ 0 & 0 & 1 \end{pmatrix}}_{\text{Reactor, Solar}} \underbrace{\begin{pmatrix} e^{i\alpha_1/2} & 0 & 0 \\ 0 & e^{i\alpha_2/2} & 0 \\ 0 & 0 & 1 \end{pmatrix}}_{\text{Majorana}}. \quad (2.8)$$

Where $s_{ij} = \sin(\theta_{ij})$ and $c_{ij} = \cos(\theta_{ij})$. The oscillation parameters are often grouped: (1,2) as “solar”, (2,3) as “atmospheric” and (1,3) as “reactor”. Many neutrino experiments aim to measure the PMNS parameters from a wide array of origins, as is the purpose of this thesis.

The Majorana phase, $\alpha_{1,2}$, included within the fourth matrix in Equation 2.8 is only included for completeness. For an oscillation analysis experiment, any terms containing this phase disappear due to taking the expectation value of the PMNS matrix. Measurements of these phases can be performed by experiments searching for neutrino-less double β -decay [17].

243 A two-flavour approximation can be obtained when one assumes the third
244 mass eigenstate is degenerate with another. This results in the two-flavour
245 approximation being reasonable for understanding the features of the oscillation.
246 In this two-flavour case, the mixing matrix becomes,

$$U_{2\text{ Flav.}} = \begin{pmatrix} \cos(\theta) & \sin(\theta) \\ -\sin(\theta) & \cos(\theta) \end{pmatrix}. \quad (2.9)$$

247 This culminates in the oscillation probability,

$$\begin{aligned} P(\nu_\alpha \rightarrow \nu_\alpha) &= 1 - \sin^2(2\theta) \sin^2\left(\frac{\Delta m^2 L}{4E}\right), \\ P(\nu_\alpha \rightarrow \nu_\beta) &= \sin^2(2\theta) \sin^2\left(\frac{\Delta m^2 L}{4E}\right). \end{aligned} \quad (2.10)$$

248 Where $\alpha \neq \beta$. For a fixed neutrino energy, the oscillation probability is
249 a sinusoidal function depending upon the distance over which the neutrino
250 propagates. The frequency and amplitude of oscillation are dependent upon
251 $\Delta m^2/4E$ and $\sin^2 2\theta$, respectively. The oscillation probabilities presented thus far
252 assume $c = 1$, where c is the speed of light in a vacuum. In more familiar units, the
253 maximum oscillation probability for a fixed value of θ is given at $L[\text{km}] / E[\text{GeV}] \sim$
254 $1.27/\Delta m^2$. It is this calculation that determines the best L/E value for a given
255 experiment to be designed around for measurements of a specific value of Δm^2 .

256 2.2.2 The MSW Effect

257 The theory of neutrino oscillation in a vacuum has been described in subsec-
258 tion 2.2.1. However, the beam neutrinos and atmospheric neutrinos originating
259 from below the horizon propagate through the matter in the Earth. The coherent
260 scattering of neutrinos from a material target modifies the Hamiltonian of the
261 system which results in a change in the oscillation probability. This modification
262 is termed the Mikheyev-Smirnov-Wolfenstein (MSW) effect [18–20]. This occurs
263 because charged current scattering ($\nu_e + e^- \rightarrow \nu_e + e^-$, propagated by a W boson)
264 only affects electron neutrinos whereas the neutral current scattering ($\nu_l + l^- \rightarrow$

265 $\nu_l + l^-$, propagated by a Z^0 boson) interacts through all neutrino flavours equally.

266 In the two-flavour approximation, the effective mixing parameter becomes

$$\sin^2(2\theta) \rightarrow \sin^2(2\theta_m) = \frac{\sin^2(2\theta)}{(A/\Delta m^2 - \cos(2\theta))^2 + \sin^2(2\theta)}, \quad (2.11)$$

267 where $A = 2\sqrt{2}G_F N_e E$, N_e is the electron density of the medium and G_F
268 is Fermi's constant. It is clear that there exists a value of $A = \Delta m^2 \cos(2\theta)$ for
269 $\Delta m^2 > 0$, which results in a divergent mixing parameter, colloquially called the
270 matter resonance. This resonance regenerates the electron neutrino component of
271 the neutrino flux [18–20]. The density at which the resonance occurs is given by

$$N_e = \frac{\Delta m^2 \cos(2\theta)}{2\sqrt{2}G_F E}. \quad (2.12)$$

272 At densities lower than this critical value, the oscillation probability will
273 be much closer to that of vacuum oscillation. For antineutrinos, $N_e \rightarrow -N_e$
274 [21]. The resonance occurring from the MSW effect depends on the sign of Δm^2 .
275 Therefore, any neutrino oscillation experiment which observes neutrinos and
276 antineutrinos which have propagated through matter can have some sensitivity
277 to the ordering of the neutrino mass eigenstates.

278 2.3 Neutrino Oscillation Measurements

279 As evidence of beyond Standard Model physics, the 2015 Nobel Prize in Physics
280 was awarded to the Super-Kamiokande (SK) [22] and Sudbury Neutrino Ob-
281 servatory (SNO) [23] collaborations for the first definitive observation of solar
282 and atmospheric neutrino oscillation [24]. Since then, the field has seen a wide
283 array of oscillation measurements from a variety of neutrino sources. As seen
284 in subsection 2.2.1, the neutrino oscillation probability is dependent on the ratio
285 of the propagation baseline, L , to the neutrino energy, E . It is this ratio that
286 determines the type of neutrino oscillation a particular experiment is sensitive to.

287 As illustrated in Figure 2.1, there are many neutrino sources that span a
288 wide range of energies. The least energetic neutrinos are from reactor and

²⁸⁹ terrestrial sources at $O(1)$ MeV whereas the most energetic neutrinos originate
²⁹⁰ from atmospheric and galactic neutrinos of $> O(1)$ TeV.

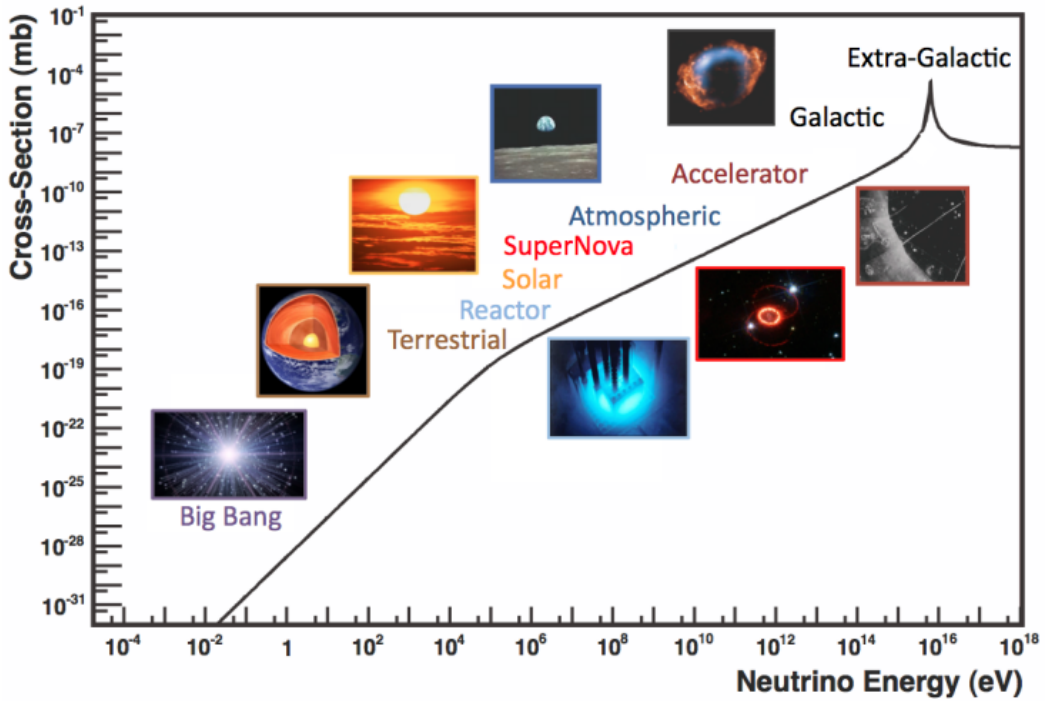


Figure 2.1: The electro-weak cross-section for $\bar{\nu}_e + e^- \rightarrow \bar{\nu}_e + e^-$ scattering on free electrons from various natural and man-made neutrino sources, as a function of neutrino energy. Taken from [25]

²⁹¹ 2.3.1 Solar Neutrinos

²⁹² Solar neutrinos are emitted from fusion reaction chains at the centre of the Sun.
²⁹³ The solar neutrino flux, given as a function of neutrino energy for different
²⁹⁴ fusion and decay chains, is illustrated in Figure 2.2. Whilst proton-proton fusion
²⁹⁵ generates the largest flux of neutrinos, the neutrinos are low energy and are
²⁹⁶ difficult to reconstruct due to the IBD interaction threshold of 1.8MeV [26].
²⁹⁷ Consequently, most experiments focus on the neutrinos from the decay of 8B
²⁹⁸ (via $^8B \rightarrow ^8Be^* + e^+ + \nu_e$), which are higher energy.

²⁹⁹ The first measurements of solar neutrinos observed a significant reduction in
³⁰⁰ the event rate compared to predictions from the Standard Solar Model [28, 29]. A
³⁰¹ proposed solution to this “solar neutrino problem” was $\nu_e \leftrightarrow \nu_\mu$ oscillations in a

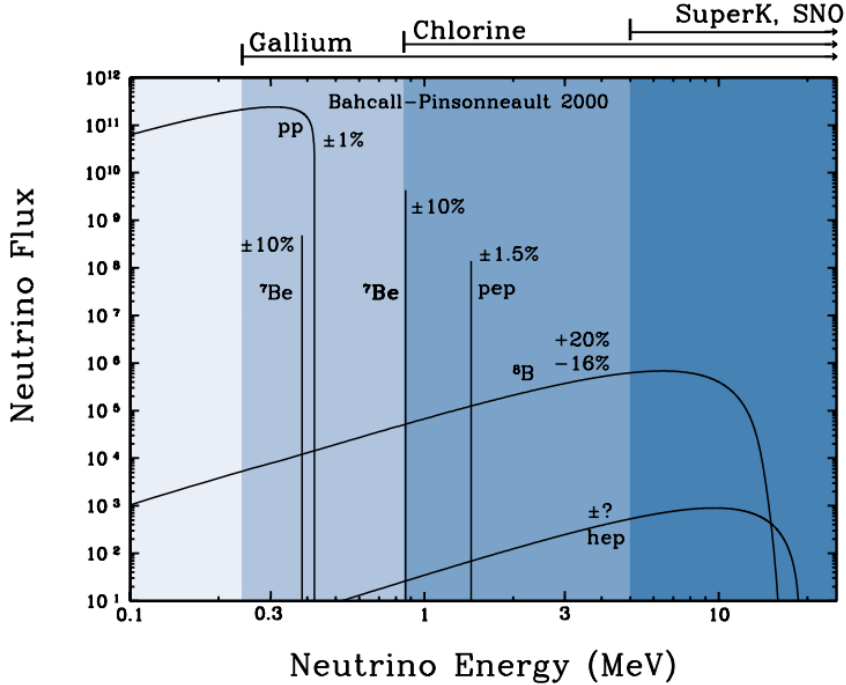


Figure 2.2: The solar neutrino flux as a function of neutrino energy for various fusion reactions and decay chains as predicted by the Standard Solar Model. Taken from [27].

302 precursory version of the PMNS model [30]. The Kamiokande [31], Gallex [32]
 303 and Sage [33] experiments confirmed the ~ 0.5 factor deficit of solar neutrinos.

304 The conclusive solution to this problem was determined by the SNO col-
 305 laboration [23]. Using a deuterium water target to observe 8B neutrinos, the
 306 event rate of charged current (CC), neutral current (NC), and elastic scattering
 307 (ES) interactions (Given in Equation 2.13) was simultaneously measured. CC
 308 events can only occur for electron neutrinos, whereas the NC channel is agnostic
 309 to neutrino flavour, and the ES reaction has a small excess sensitivity for the
 310 detection of electron neutrino interactions. This meant that there were direct
 311 measurements of the ν_e and ν_x neutrino flux. It was concluded that the CC and
 312 ES interaction rates were consistent with the deficit previously observed. Most
 313 importantly, the NC reaction rate was only consistent with the others under the

³¹⁴ hypothesis of flavour transformation.

$$\begin{aligned} \nu_e + d &\rightarrow p + p + e^- & (CC) \\ \nu_x + d &\rightarrow p + n + \nu_x & (NC) \\ \nu_x + e^- &\rightarrow \nu_x + e^- & (ES) \end{aligned} \quad (2.13)$$

³¹⁵ Since the SNO measurement, many experiments have since measured the
³¹⁶ neutrino flux of different interaction chains within the sun [34–36]. The most
³¹⁷ recent measurement was that of CNO-cycle neutrinos which were recently
³¹⁸ observed with 5σ significance by the Borexino collaboration [34].

³¹⁹ 2.3.2 Accelerator Neutrinos

³²⁰ The concept of using an artificial “neutrino beam” was first realised in 1962 [7].
³²¹ Since then, many experiments have adopted the same fundamental concepts.
³²² Typically, a proton beam is aimed at a target producing charged mesons that
³²³ decay to neutrinos. The mesons can be sign-selected by the use of magnetic
³²⁴ focusing horns to generate a neutrino or antineutrino beam. Pions are the primary
³²⁵ mesons that decay and depending on the orientation of the magnetic field, a
³²⁶ muon (anti-)neutrino beam is generated via $\pi^+ \rightarrow \mu^+ + \nu_\mu$ or $\pi^- \rightarrow \mu^- + \bar{\nu}_\mu$.
³²⁷ The decay of muons and kaons results in an irreducible intrinsic electron neutrino
³²⁸ background. In T2K, this background contamination is $O(< 1\%)$ [37]. There is
³²⁹ also an approximately $\sim 5\%$ “wrong-sign” neutrino background of $\bar{\nu}_\mu$ generated
³³⁰ via the same decays. As the beam is generated by proton interactions (rather
³³¹ than anti-proton interactions), the wrong-sign component in the antineutrino
³³² beam is larger when operating in neutrino mode.

³³³ Tuning the proton energy in the beam and using beam focusing techniques
³³⁴ allows the neutrino energy to be set to a value that maximises the disappear-
³³⁵ ance oscillation probability in the L/E term in Equation 2.10. This means that
³³⁶ accelerator experiments are typically more sensitive to the mixing parameters as
³³⁷ compared to a natural neutrino source. However, the disadvantage compared
³³⁸ to atmospheric neutrino experiments is the cost of building a facility to provide

339 high-energy neutrinos, with a high flux, which is required for longer baselines.
 340 Consequently, there is typically less sensitivity to matter effects and the ordering
 341 of the neutrino mass eigenstates.

342 A neutrino experiment measures

$$R(\vec{x}) = \Phi(E_\nu) \times \sigma(E_\nu) \times \epsilon(\vec{x}) \times P(\nu_\alpha \rightarrow \nu_\beta), \quad (2.14)$$

343 where $R(\vec{x})$ is the event rate of neutrinos at position \vec{x} , $\Phi(E_\nu)$ is the flux of
 344 neutrinos with energy E_ν , $\sigma(E_\nu)$ is the cross-section of the neutrino interaction and
 345 $\epsilon(\vec{x})$ is the efficiency and resolution of the detector. In order to leverage the most
 346 out of an accelerator neutrino experiment, the flux and cross-section systematics
 347 need to be constrained. This is typically done via the use of a “near detector”,
 348 situated at a baseline of $O(1)$ km. This detector observes the unoscillated neutrino
 349 flux and constrains the parameters used within the flux and cross-section model.

350 The first accelerator experiments to precisely measure oscillation parameters
 351 were MINOS [38] and K2K [39]. These experiments confirmed the ν_μ disappear-
 352 ance seen in atmospheric neutrino experiments by finding consistent parameter
 353 values for $\sin^2(\theta_{23})$ and Δm_{32}^2 . The current generation of accelerator neutrino
 354 experiments, T2K and NO ν A extended this field by observing $\bar{\nu}_\mu \rightarrow \bar{\nu}_e$ and lead
 355 the sensitivity to atmospheric mixing parameters as seen in Figure 2.6 [40]. The
 356 two experiments differ in their peak neutrino energy, baseline, and detection tech-
 357 nique. The NO ν A experiment is situated at a baseline of 810km from the NuMI
 358 beamline which delivers 2GeV neutrinos. The T2K neutrino beam is peaked
 359 around 0.6GeV and propagates 295km [41]. Additionally, the NO ν A experiment
 360 uses functionally identical detectors (near and far) whereas T2K uses a plastic
 361 scintillator technique at the near detector and a water Cherenkov far detector.
 362 The future generation experiments DUNE [42] and Hyper-Kamiokande [43]
 363 will succeed these experiments as the high-precision era of neutrino oscillation
 364 parameter measurements develops.

365 Several anomalous results have been observed in the LSND [9] and Mini-
 366 BooNE [10] detectors which were designed with purposefully short baselines.

367 Parts of the neutrino community attributed these results to oscillations induced
368 by a fourth “sterile” neutrino [44] but several searches in other experiments,
369 MicroBooNE [45] and KARMEN [46], found no hints of additional neutrino
370 species. The solution to the anomalous results is still being determined.

371 2.3.3 Atmospheric Neutrinos

372 The interactions of primary cosmic ray protons in the Earth’s upper atmosphere
373 generate showers of energetic hadrons. These are mostly pions and kaons that
374 decay to produce a natural source of neutrinos spanning energies of MeV to
375 TeV [47]. The main decay is via,

$$\begin{aligned} \pi^\pm &\rightarrow \mu^\pm + (\nu_\mu, \bar{\nu}_\mu), \\ \mu^\pm &\rightarrow e^\pm + (\nu_e, \bar{\nu}_e) + (\nu_\mu, \bar{\nu}_\mu), \end{aligned} \tag{2.15}$$

376 such that for a single pion decay, three neutrinos can be produced. The
377 atmospheric neutrino flux energy spectra as predicted by the Bartol [48], Honda
378 [49–51], and FLUKA [52] models are illustrated in Figure 2.3. The flux distribution
379 peaks at an energy of $O(10)$ GeV. The uncertainties associated with these models
380 are dominated by the hadronic production of kaon and pions as well as the
381 primary cosmic flux.

382 Unlike long-baseline experiments which have a fixed baseline, the distance
383 atmospheric neutrinos propagate is dependent upon the zenith angle at which
384 they interact. This is illustrated in Figure 2.4. Neutrinos that are generated
385 directly above the detector ($\cos(\theta) = 1.0$) have a baseline equivalent to the
386 height of the atmosphere, whereas neutrinos that interact directly below the
387 detector ($\cos(\theta) = -1.0$) have to travel a length equal to the diameter of the Earth.
388 This means atmospheric neutrinos have a baseline that varies from $O(20)$ km to
389 $O(6 \times 10^3)$ km. Any neutrino generated at or below the horizon will be subject
390 to MSW matter resonance as they propagate through the Earth.

391 Figure 2.5 highlights the neutrino flux as a function of the zenith angle for
392 different slices of neutrino energy. For medium to high-energy neutrinos (and to

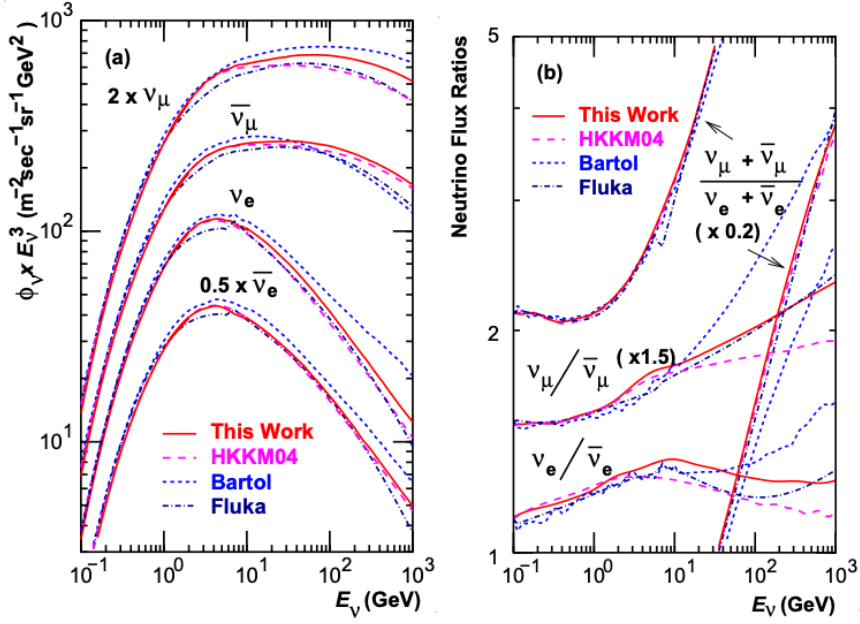


Figure 2.3: Left panel: The atmospheric neutrino flux for different neutrino flavours as a function of neutrino energy as predicted by the 2007 Honda model (“This work”) [49], the 2004 Honda model (“HKKM04”)[50], the Bartol model [48] and the FLUKA model [52]. Right panel: The ratio of the muon to electron neutrino flux as predicted by all the quoted models. Both figures taken from [49].

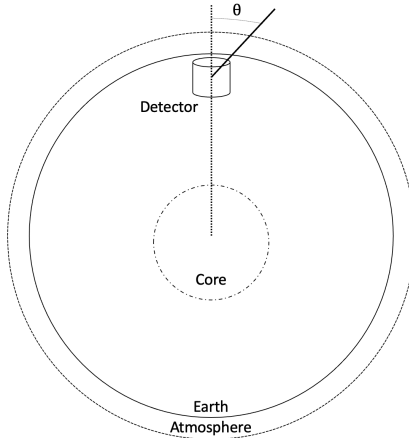


Figure 2.4: A diagram illustrating the definition of zenith angle as used in the Super Kamiokande experiment [53].

393 a lesser degree for low-energy neutrinos), the flux is approximately symmetric
 394 around $\cos(\theta) = 0$. To the accuracy of this approximation, the systematic
 395 uncertainties associated with atmospheric flux for comparing upward-going
 396 and down-going neutrino cancels. This allows the down-going events, which are

397 mostly insensitive to oscillation probabilities, to act as an unoscillated prediction
 398 (similar to a near detector in an accelerator neutrino experiment).

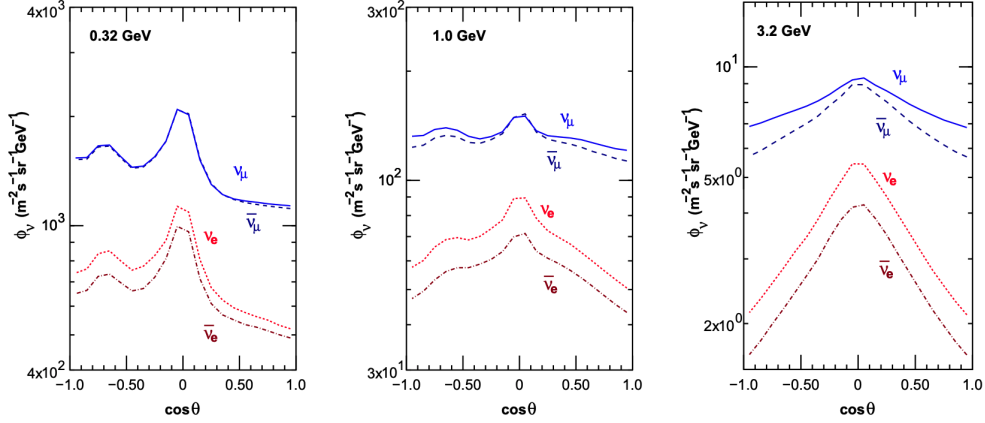


Figure 2.5: Prediction of ν_e , $\bar{\nu}_e$, ν_μ , $\bar{\nu}_\mu$ fluxes as a function of zenith angle as calculated by the HKKM model [51]. The left, middle and right panels represent three values of neutrino energy, 0.32GeV, 1.0GeV and 3.2GeV respectively. Predictions for other models including Bartol [48], Honda [49] and FLUKA [52] are given in [53].

399 Precursory hints of atmospheric neutrinos were observed in the mid-1960s
 400 searching for $\nu_\mu + X \rightarrow X^* + \mu^\pm$ [54]. This was succeeded by the IMB-3 [55]
 401 and Kamiokande [56] experiments which measured the double ratio of muon
 402 to electron neutrinos in data to Monte Carlo, $R(\nu_\mu/\nu_e) = (\mu/e)_{Data}/(\mu/e)_{MC}$.
 403 Both experiments were found to have a consistent deficit of muon neutrinos,
 404 with $R(\nu_\mu/\nu_e) = 0.67 \pm 0.17$ and $R(\nu_\mu/\nu_e) = 0.658 \pm 0.016 \pm 0.035$, respectively.
 405 Super-Kamiokande (SK) [53] extended this analysis by fitting oscillation pa-
 406 rameters in $P(\nu_\mu \rightarrow \nu_\tau)$ which found best fit parameters $\sin^2(2\theta) > 0.92$ and
 407 $1.5 \times 10^{-3} < \Delta m^2 < 3.4 \times 10^{-3}\text{eV}^2$.

408 Since then, atmospheric neutrino experiments have been making precision
 409 measurements of the $\sin^2(\theta_{23})$ and Δm^2_{32} oscillation parameters. Atmospheric
 410 neutrino oscillation is dominated by $P(\nu_\mu \rightarrow \nu_\tau)$, where SK observed a 4.6σ
 411 discovery of ν_τ appearance [57]. Figure 2.6 illustrates the current estimates on
 412 the atmospheric mixing parameters, from a wide range of atmospheric and
 413 accelerator neutrino observatories.

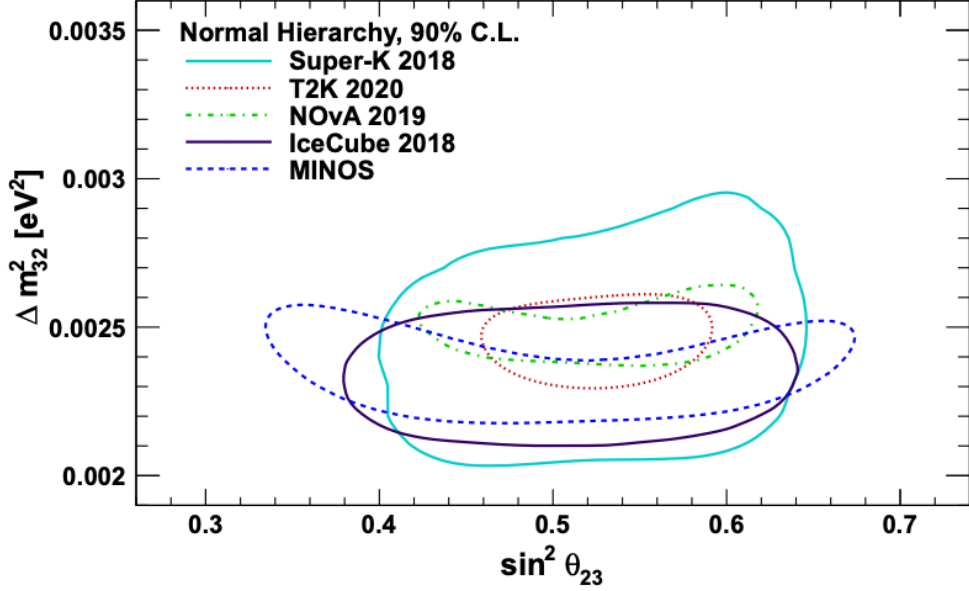


Figure 2.6: Constraints on the atmospheric oscillation parameters, $\sin^2(\theta_{23})$ and Δm_{32}^2 , from atmospheric and long-baseline experiments: SK [58], T2K [59], NOvA [60], IceCube [61] and MINOS [62]. Figure taken from [63].

2.3.4 Reactor Neutrinos

As illustrated in the first discovery of neutrinos (section 2.1), nuclear reactors are a very useful artificial source of electron antineutrinos. For reactors that use low-enriched uranium ^{235}U as fuel, the antineutrino flux is dominated by the β -decay fission of ^{235}U , ^{238}U , ^{239}Pu and ^{241}Pu [64] as illustrated in Figure 2.7.

Due to their low energy, reactor electron antineutrinos predominantly interact via the inverse β -decay (IBD) interaction. The typical signature contains two signals delayed by $O(200)\mu\text{s}$; firstly the prompt photons from positron annihilation, and secondly the photon emitted ($E_{tot}^\gamma = 2.2\text{MeV}$) from de-excitation after neutron capture on hydrogen. Searching for both signals improves the detector's ability to distinguish between background and signal events [65].

There are many short baseline experiments ($L \sim O(1)\text{km}$) that have measured the $\sin^2(\theta_{13})$ and Δm_{32}^2 oscillation parameters. Daya Bay [66], RENO [67] and Double Chooz [68] have all provided precise measurements, with the first discovery of a non-zero θ_{13} made by Daya Bay and RENO (and complemented by T2K [68]). The constraints on $\sin^2(\theta_{13})$ by the reactor experiments lead the field. They

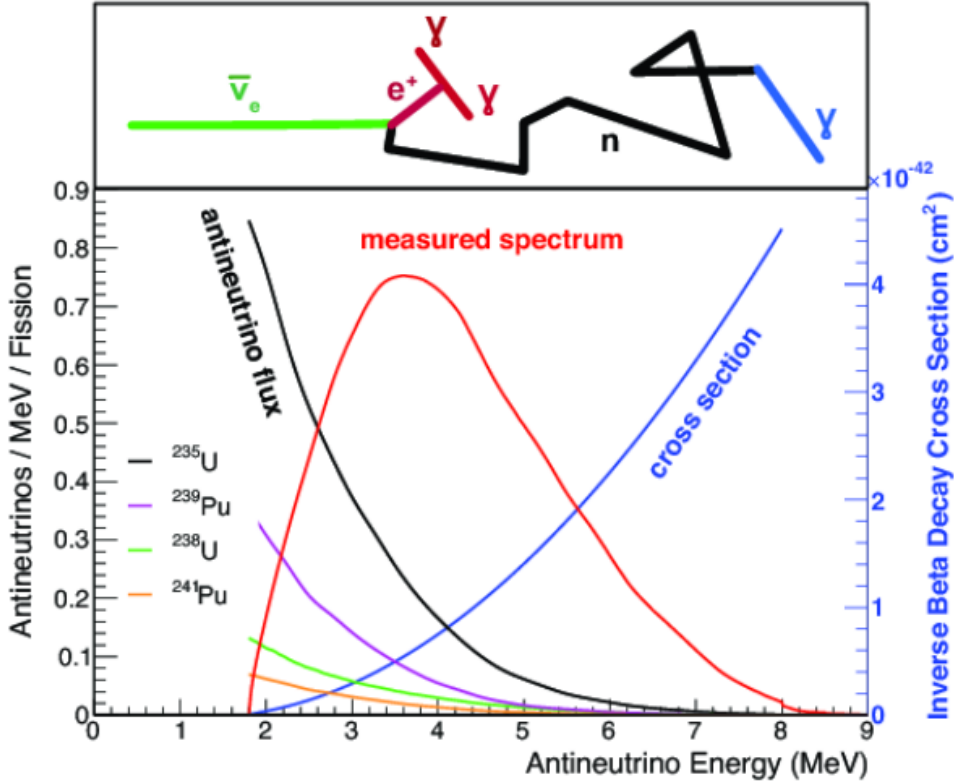


Figure 2.7: Reactor electron antineutrino fluxes for ^{235}U (Black), ^{238}U (Green), ^{239}Pu (Purple), and ^{241}Pu (Orange) isotopes. The inverse β -decay cross-section (Blue) and corresponding measurable neutrino spectrum (Red) are also given. Top panel: Schematic of Inverse β -decay interaction including the eventual capture of the emitted neutron. This capture emits a γ -ray which provides a second signal of the event. Taken from [63].

are often used as external inputs to accelerator neutrino experiments to improve their sensitivity to δ_{CP} and mass hierarchy determination. JUNO-TAO [69], a small collaboration within the larger JUNO experiment, is a next-generation reactor experiment that aims to precisely measure the isotopic antineutrino yields from the different fission chains.

Kamland [70] is the only experiment to have observed reactor neutrinos using a long baseline (flux weighted averaged baseline of $L \sim 180\text{km}$) which allows it to have sensitivity to Δm_{21}^2 . Combined with the SK solar neutrino experiment, the combined analysis puts the most stringent constraint on Δm_{21}^2 [71].

439 2.4 Summary Of Oscillation Parameter Measurements

440 Since the first evidence of neutrino oscillations, numerous measurements of the
 441 mixing parameters have been made. Many experiments use neutrinos as a tool
 442 for the discovery of new physics (diffuse supernova background, neutrinoless
 443 double beta decay and others) so the PMNS parameters are summarised in the
 444 Particle Data Group (PDG) review tables. The analysis presented in this thesis
 445 focuses on the 2020 T2K oscillation analysis presented in [72] which the 2020
 446 PDG constraints [73] were used. These constraints are outlined in Table 2.1.

Parameter	2020 Constraint
$\sin^2(\theta_{12})$	0.307 ± 0.013
Δm_{21}^2	$(7.53 \pm 0.18) \times 10^{-5} \text{ eV}^2$
$\sin^2(\theta_{13})$	$(2.18 \pm 0.07) \times 10^{-2}$
$\sin^2(\theta_{23})$ (I.H.)	0.547 ± 0.021
$\sin^2(\theta_{23})$ (N.H.)	0.545 ± 0.021
Δm_{32}^2 (I.H.)	$(-2.546^{+0.034}_{-0.040}) \times 10^{-3} \text{ eV}^2$
Δm_{32}^2 (N.H.)	$(2.453 \pm 0.034) \times 10^{-3} \text{ eV}^2$

Table 2.1: The 2020 Particle Data Group constraints of the oscillation parameters taken from [73]. The value of Δm_{32}^2 is given for both normal hierarchy (N.H.) and inverted hierarchy (I.H.) and $\sin^2(\theta_{23})$ is broken down by whether its value is below (Q1) or above (Q2) 0.5.

447 The $\sin^2(\theta_{13})$ measurement stems from the electron antineutrino disappearance,
 448 $P(\bar{\nu}_e \rightarrow \bar{\nu}_e)$, and is taken as the average best-fit from the combination of
 449 Daya Bay, Reno and Double Chooz. It is often used as a prior uncertainty within
 450 other neutrino oscillation experiments, typically termed the reactor constraint.
 451 The $\sin^2(\theta_{12})$ parameter is predominantly measured through electron neutrino
 452 disappearance, $P(\nu_e \rightarrow \nu_{\mu,\tau})$, in solar neutrino experiments. The long-baseline
 453 reactor neutrino experiment Kamland also has a sensitivity to this parameter and
 454 is used in a joint fit to solar data from SNO and SK, using the reactor constraint.
 455 Measurements of $\sin^2(\theta_{23})$ are made by long-baseline and atmospheric neutrino
 456 experiments. The PDG value is a joint fit of T2K, NO ν A, MINOS and IceCube
 457 DeepCore experiments. The latest T2K-only measurement, provided at Neu-
 458 trino2020 and is the basis of this thesis, is given as $\sin^2(\theta_{23}) = 0.546^{+0.024}_{-0.046}$ [72].

The PDG constraint on Δm_{21}^2 is provided by the KamLAND experiment using solar and geoneutrino data. This measurement utilised a $\sin^2(\theta_{13})$ constraint from accelerator (T2K, MINOS) and reactor neutrino (Daya Bay, RENO, Double Chooz) experiments. Accelerator measurements make some of the most stringent constraints on Δm_{32}^2 although atmospheric experiments have more sensitivity to the mass hierarchy determination. The PDG performs a joint fit of accelerator and atmospheric data, in both normal and inverted hierarchies separately. The latest T2K-only result is $\Delta m_{32}^2 = 2.49^{+0.058}_{-0.082} \times 10^{-3} \text{ eV}^2$ favouring normal hierarchy [72]. The value of δ_{CP} is largely undetermined. CP-conserving values of 0 and π were rejected with $\sim 2\sigma$ intervals, as published in Nature, although more recent analyses have reduced the credible intervals to 90%. Since the 2020 PDG publication, there has been a new measurement of $\sin^2(\theta_{13}) = (2.20 \pm 0.07) \times 10^{-2}$ [74], alongside updated Δm_{32}^2 and $\sin^2(\theta_{23})$ measurements.

Throughout this thesis, several sample spectra predictions and contours are presented, which require oscillation parameters to be assumed. Table 2.2 defines two sets of oscillation parameters, with “Asimov A” set being close to the preferred values from a previous T2K-only fit [75] and “Asimov B” being CP-conserving and further from maximal θ_{23} mixing.

Parameter	Asimov A	Asimov B
Δm_{12}^2	$7.53 \times 10^{-5} \text{ eV}^2$	
Δm_{32}^2	$2.509 \times 10^{-3} \text{ eV}^2$	
$\sin^2(\theta_{12})$	0.304	
$\sin^2(\theta_{13})$	0.0219	
$\sin^2(\theta_{23})$	0.528	0.45
δ_{CP}	-1.601	0.0

Table 2.2: Reference values of the neutrino oscillation parameters for two different oscillation parameter sets.

2.5 Overview of Oscillation Effects

The analysis presented within this thesis focuses on the determination of oscillation parameters from atmospheric and beam neutrinos. Whilst subject to the

480 same oscillation formalism, the way in which the two samples have sensitivity
 481 to the different oscillation parameters differs significantly.

482 Atmospheric neutrinos have a varying baseline, or “path length” L , such that
 483 the distance each neutrino travels before interacting is dependent upon the zenith
 484 angle, θ_Z . As primary cosmic rays can interact anywhere between the Earth’s
 485 surface and $\sim 50\text{km}$ above that, the height, h , in the atmosphere at which the
 486 neutrino was generated also affects the path length,

$$L = \sqrt{(R_E + h)^2 - R_E^2(1 - \cos^2(\theta_Z))} - R_E \cos(\theta_Z). \quad (2.16)$$

487 Where $R_E = 6,371\text{km}$ is the Earth’s radius. This assumes a spherically
 488 symmetric Earth model. Therefore, the oscillation probability is dependent upon
 489 two parameters, $\cos(\theta_Z)$ and E_ν .

490 The oscillation probability used within this analysis is based on [21]. The
 491 neutrino wavefunction in the vacuum Hamiltonian evolves in each layer of
 492 constant matter density via

$$i \frac{d\psi_j(t)}{dt} = \frac{m_j^2}{2E_\nu} \psi_j(t) - \sum_k \sqrt{2} G_F N_e U_{ej} U_{ke}^\dagger \psi_k(t), \quad (2.17)$$

493 where m_j^2 is the square of the j^{th} vacuum eigenstate mass, E_ν is the neutrino
 494 energy, G_F is Fermi’s constant, N_e is the electron number density and U is the
 495 PMNS matrix. The transformation $N_e \rightarrow -N_e$ and $\delta_{CP} \rightarrow -\delta_{CP}$ is applied for
 496 antineutrino propagation. Thus, a model of the Earth’s density is required for
 497 neutrino propagation. Following the official SK-only methodology [76], this
 498 analysis uses the Preliminary Reference Earth Model (PREM) [77] which provides
 499 piecewise cubic polynomials as a function of the Earth’s radius. This density
 500 profile is illustrated in Figure 2.8. As the propagator requires layers of constant
 501 density, the SK methodology approximates the PREM model by using four layers
 502 of constant density [76], detailed in Table 2.3.

503 The atmospheric neutrino oscillation probabilities can be presented as two di-
 504 mensional “oscillograms” as illustrated in Figure 2.9. The distinct discontinuities,
 505 as a function of $\cos(\theta_Z)$, are due to the discontinuous density in the PREM model.

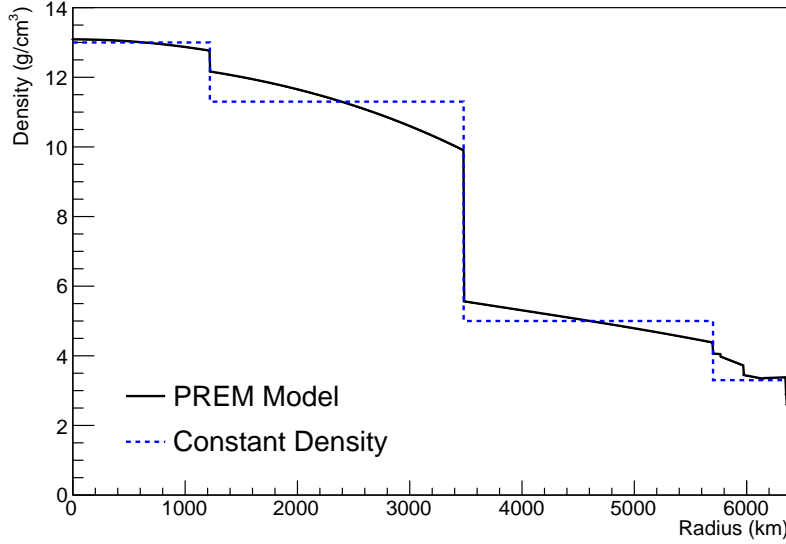


Figure 2.8: The density of the Earth given as a function of the radius, as given by the PREM model (Black), and the constant density four-layer approximation (Blue), as used in the official SK-only analysis.

Layer	Outer Radius [km]	Density [g/cm ³]	Chemical composition (Z/A)
Inner Core	1220	13	0.468 ± 0.029
Outer Core	3480	11.3	0.468 ± 0.029
Lower Mantle	5701	5.0	0.496
Transition Zone	6371	3.3	0.496

Table 2.3: Description of the four layers of the Earth invoked within the constant density approximation of the PREM model [77].

Atmospheric neutrinos have sensitivity to δ_{CP} through the overall event rate. Figure 2.10 illustrates the difference in oscillation probability between CP-conserving ($\delta_{CP} = 0.$) and a CP-violating ($\delta_{CP} = -1.601$) value taken from Asimov A oscillation parameter set (Table 2.2). The result is a complicated oscillation pattern in the appearance probability for sub-GeV upgoing neutrinos. The detector does not have sufficient resolution to resolve these individual patterns so the sensitivity to δ_{CP} for atmospheric neutrinos comes via the overall normalisation of these events.

The presence of matter means that the effect δ_{CP} has on the oscillation probability is not equal between neutrinos and antineutrinos. Furthermore, the interaction cross-section for neutrinos is larger than for antineutrinos so the two

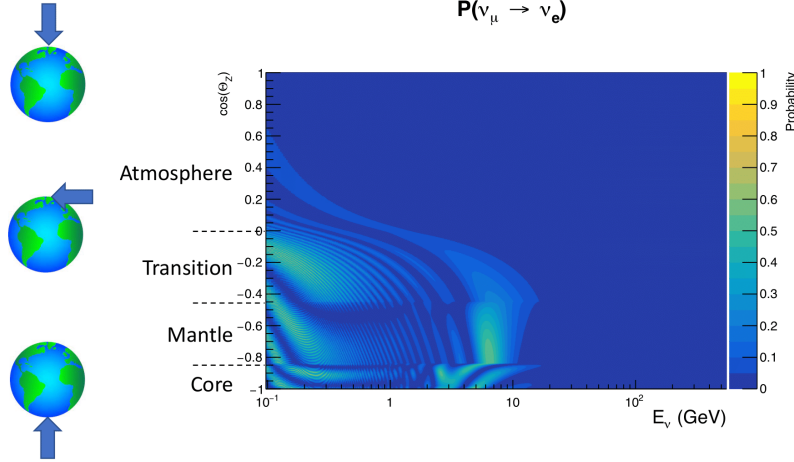


Figure 2.9: An “oscillogram” that depicts the $P(\nu_\mu \rightarrow \nu_e)$ oscillation probability as a function of neutrino energy and cosine of the zenith angle. The zenith angle is defined such that $\cos(\theta_Z) = 1.0$ represents neutrinos that travel from directly above the detector. The four-layer constant density PREM model approximation is used and Asimov A oscillation parameters are assumed (Table 2.2).

517 effects have to be disentangled. These effects are further convoluted by detector
 518 efficiencies as SK cannot distinguish neutrinos and antineutrinos well. All of
 519 these effects lead to a difference in the number of neutrinos detected compared
 520 to antineutrinos. This changes how the δ_{CP} normalisation term is observed,
 521 resulting in a very complex sensitivity to δ_{CP} .

522 The vacuum and matter oscillation probabilities for $P(\nu_e \rightarrow \nu_e)$ and $P(\bar{\nu}_e \rightarrow$
 523 $\bar{\nu}_e)$ are presented in Figure 2.11, where the PREM model has been assumed. The
 524 oscillation probability for both neutrinos and antineutrinos is affected in the
 525 presence of matter. However, the resonance effects around $O(5)\text{GeV}$ only occur
 526 for neutrinos in the normal mass hierarchy and antineutrinos in the inverse mass
 527 hierarchy. The exact position and amplitude of the resonance depend on $\sin^2(\theta_{23})$,
 528 further increasing the atmospheric neutrinos’ sensitivity to the parameter.

529 As the T2K beam flux is centered at the first oscillation maximum ($E_\nu =$
 530 0.6GeV) [41], the sensitivity to δ_{CP} is predominantly observed as a change in the
 531 event-rate of e-like samples in $\nu/\bar{\nu}$ modes. Figure 2.12 illustrates the $P(\nu_\mu \rightarrow \nu_e)$
 532 oscillation probability for a range of δ_{CP} values. A circular modulation of the

$$\mathbf{P}(\nu_\mu \rightarrow \nu_e; \delta_{CP} = -1.601) - \mathbf{P}(\nu_\mu \rightarrow \nu_e; \delta_{CP} = 0)$$

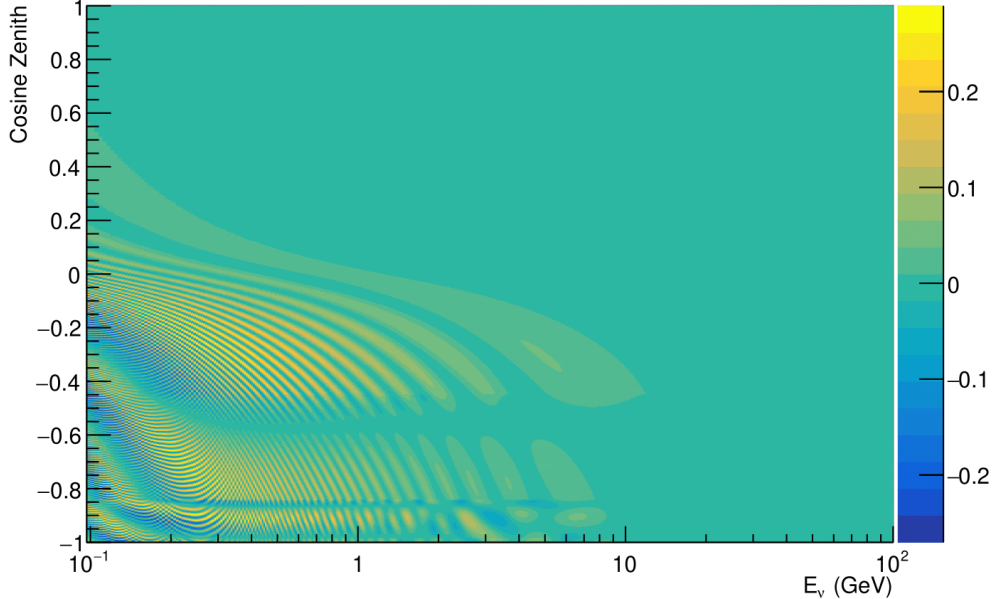


Figure 2.10: The effect of δ_{CP} for atmospheric neutrinos given in terms of the neutrino energy and zenith angle. This oscillogram compares the $P(\nu_\mu \rightarrow \nu_e)$ oscillation probability for a CP conserving ($\delta_{CP} = 0.0$) and a CP violating ($\delta_{CP} = -1.601$) value taken from the Asimov A parameter set. The other oscillation parameters assume the Asimov A oscillation parameter set given in Table 2.2.

533 first oscillation peak (in both magnitude and position) is observed when varying
 534 throughout the allowable values of δ_{CP} . The CP-conserving values of $\delta_{CP} = 0, \pi$
 535 have a lower(higher) oscillation maximum than the CP-violating values of $\delta_{CP} =$
 536 $-\pi/2$ ($\delta_{CP} = \pi/2$). A sub-dominant shift in the energy of the oscillation peak is
 537 also present, which aids in separating the two CP-conserving values of δ_{CP} .

538 T2K's sensitivity to $\sin^2(\theta_{23})$ and Δm_{32}^2 is observed as a shape-based variation
 539 of the muon-like samples, as illustrated in Figure 2.12. The value of Δm_{32}^2 laterally
 540 shifts the position of the oscillation dip (around $E_\nu \sim 0.6\text{GeV}$) in the $P(\nu_\mu \rightarrow \nu_\mu)$
 541 oscillation probability. A variation of $\sin^2(\theta_{23})$ is predominantly observed as
 542 a vertical shift of the oscillation dip with second-order horizontal shifts being
 543 due to matter effects. The beam neutrinos have limited sensitivity to matter
 544 effects due to the relatively shorter baseline as well as the Earth's mantle being
 545 a relatively low-density material (as compared to the Earth's core). For some

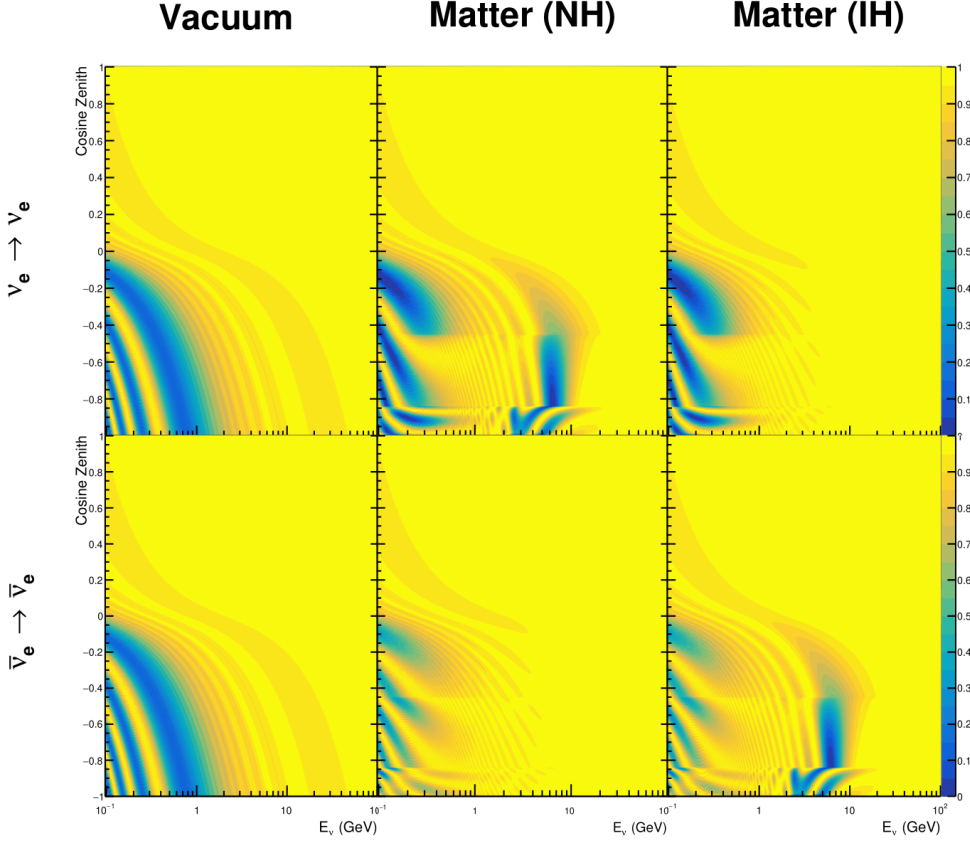


Figure 2.11: An illustration of the matter-induced effects on the oscillation probability, given as a function of neutrino energy and zenith angle. The top row of panels gives the $P(\nu_e \rightarrow \nu_e)$ oscillation probability and the bottom row illustrates the $P(\bar{\nu}_e \rightarrow \bar{\nu}_e)$ oscillation probability. The left column highlights the oscillation probability in a vacuum, whereas the middle and right column represents the oscillation probabilities when the four-layer fixed density PREM model is assumed. All oscillation probabilities assume the “Asimov A” set given in Table 2.2, but importantly, the right column sets an inverted mass hierarchy. The “matter resonance” effects at $E_\nu \sim 5\text{GeV}$ can be seen in the $P(\nu_e \rightarrow \nu_e)$ for normal mass hierarchy and $P(\bar{\nu}_e \rightarrow \bar{\nu}_e)$ for inverted hierarchy.

546 values of δ_{CP} , the degeneracy in the number of e-like events allows the mass
 547 hierarchy to be broken. This leads to a δ_{CP} -dependent mass hierarchy sensitivity
 548 which can be seen in Figure 2.13.

549 Whilst all oscillation channels should be included for completeness, the
 550 computational resources required to run a fit are limited and any reasonable
 551 approximations which reduce the number of oscillation probability calculations
 552 that need to be made should be applied. The $\nu_e \rightarrow \nu_{e,\mu,\tau}$ (and antineutrino

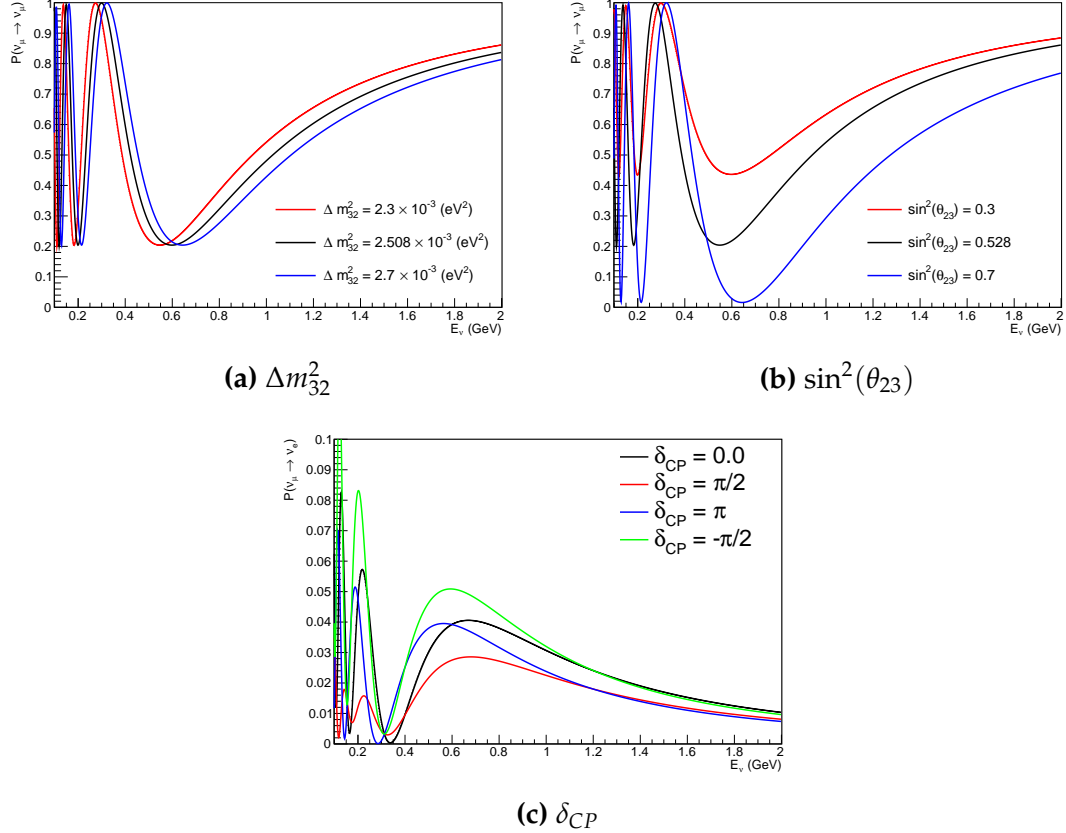


Figure 2.12: The oscillation probability for beam neutrino events given as a function of neutrino energy. All oscillation parameters assume the “Asimov A” set given in Table 2.2 unless otherwise stated. Each panel represents a change in one of the oscillation parameters whilst keeping the remaining parameters fixed.

equivalent) oscillations can be ignored for beam neutrinos as the $\nu_e/\bar{\nu}_e$ fluxes are approximately two orders of magnitude smaller than the corresponding $\nu_\mu/\bar{\nu}_\mu$ flux. Furthermore, as the peak neutrino energy of the beam is well below the threshold for charged current tau production ($E_\nu = 3.5\text{GeV}$ [57]), only a small proportion of the neutrinos produced in the beam have the required energy. For the few neutrinos that have sufficient energy, the oscillation probability is very small due to their energy being well above the oscillation maximum (small value of L/E). Whilst these approximations have been made for the beam neutrinos, the atmospheric flux of ν_e is of the same order of magnitude as the ν_μ flux and the energy distribution of atmospheric neutrinos extends well above the tau production threshold. These events can have non-negligible oscillation

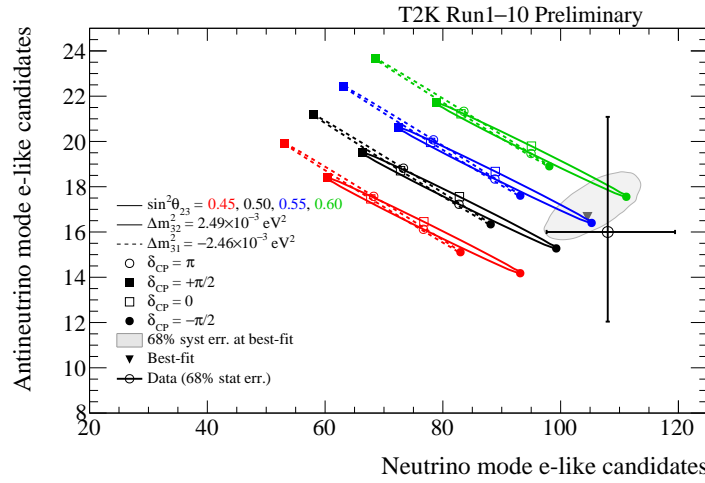


Figure 2.13: The number of electron-like events in the FHC and RHC operating mode of the beam, as a function of the oscillation probabilities. Both normal hierarchy (Solid) and inverse hierarchy (Dashed) values of Δm_{32}^2 are given.

⁵⁶⁴ probabilities due to the further distance they travel.

3

565

566

T2K and SK Experiment Overview

567 As the successor of the Kamiokande experiment, the Super-Kamiokande (SK)
568 collaboration has been leading atmospheric neutrino oscillation analyses for
569 over two decades. The detector has provided some of the strongest constraints
570 on proton decay and the first precise measurements of the Δm_{32}^2 and $\sin^2(\theta_{23})$
571 neutrino oscillation parameters. The history, detection technique, and operation
572 of the SK detector is described in section 3.1.

573 The Tokai-to-Kamioka (T2K) experiment was one of the first long-baseline
574 experiments to use both neutrino and antineutrino beams to precisely measure
575 charge parity violation within the neutrino sector. The T2K experiment observed
576 the first hints of a non-zero $\sin^2(\theta_{13})$ measurement and continues to lead the
577 field with the constraints it provides on $\sin^2(\theta_{13})$, $\sin^2(\theta_{23})$, Δm_{32}^2 and δ_{CP} . In
578 section 3.2, the techniques that T2K use to generate the neutrino beam and
579 constrain systematic parameter through near detector constraints are described.

580 3.1 The Super-Kamiokande Experiment

581 The SK experiment began taking data in 1996 [78] and has had many modifi-
582 cations throughout its operation. There have been seven defined periods of
583 data taking as noted in Table 3.1. Data taking began in SK-I which ran for five

584 years. Between the SK-I and SK-II periods, approximately 55% of the PMTs were
 585 damaged during maintenance [79]. Those that survived were equally distributed
 586 throughout the detector in the SK-II era, which resulted in a reduced 19% photo-
 587 coverage. From SK-III onwards, repairs to the detector meant the full suite of
 588 PMTs was operational recovering the 40% photo-coverage. Before the start of
 589 SK-IV, the data acquisition and electronic systems were upgraded. Between
 590 SK-IV and SK-V, a significant effort was placed into tank open maintenance and
 591 repair/replacement of defective PMTs in preparation for the Gadolinium upgrade;
 592 a task for which the author of this thesis was required. Consequently, the detector
 593 conditions were significantly changed from this point. SK-VI marked the start of
 594 the SK-Gd era, with the detector being doped with gadolinium at a concentration
 595 of 0.01% by concentration. SK-VII, which started during the writing of this thesis,
 596 has increased the gadolinium concentration to 0.03% for continued operation [80].

597 The oscillation analysis presented within this thesis focuses on the SK-IV
 598 period of running and the data taken within it. This follows from the recent
 599 SK analysis presented in [81]. Therefore, the information presented within this
 600 section focuses on that period.

Period	Start Date	End Date	Live-time (days)
I	April 1996	July 2001	1489.19
II	October 2002	October 2005	798.59
III	July 2006	September 2008	518.08
IV	September 2008	May 2018	3244.4
V	January 2019	July 2020	461.02
VI	July 2020	May 2022	583.3
VII	May 2022	Ongoing	N/A

Table 3.1: The various SK periods and their respective live-time. The SK-VI live-time is calculated until 1st April 2022. SK-VII started during the writing of this thesis.

601 3.1.1 The SK Detector

602 The basic structure of the Super-Kamiokande (SK) detector is a cylindrical tank
 603 with a diameter 39.3m and height 41.1m filled with ultrapure water [79]. A
 604 diagram of the significant components of the SK detector is given in Figure 3.1.

605 The SK detector is situated in the Kamioka mine in Gifu, Japan. The mine is under-
 606 ground with roughly 1km rock overburden (2.7km water equivalent overburden)
 607 [82]. At this depth, the rate of cosmic ray muons is significantly decreased to a
 608 value of $\sim 2\text{Hz}$ (net rate). The top of the tank is covered with stainless steel which
 609 is designed as a working platform for maintenance, calibration, and location for
 610 high voltage and data acquisition electronics.

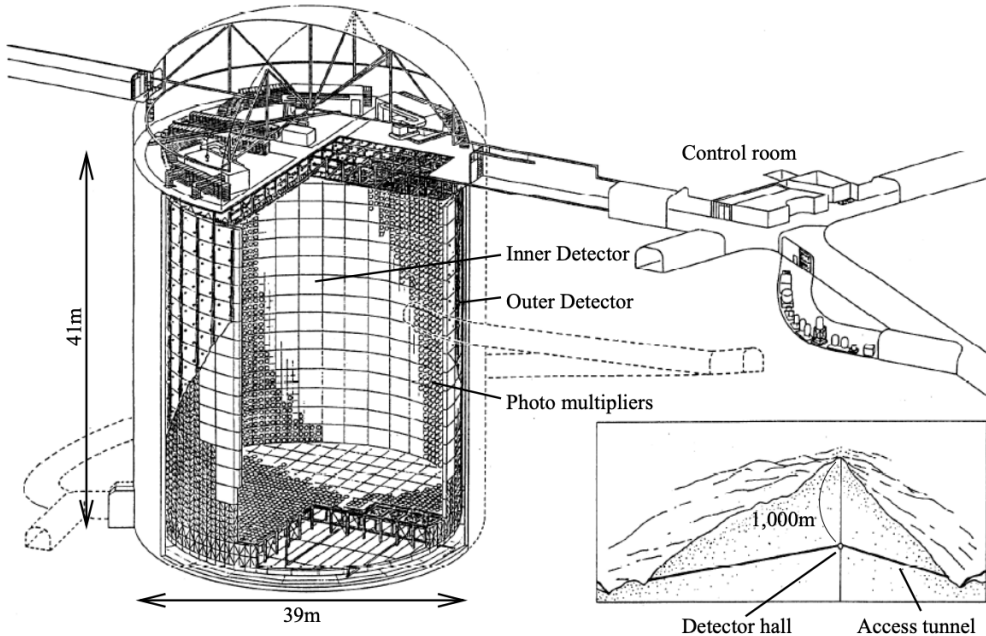


Figure 3.1: A schematic diagram of the Super-Kamiokande Detector. Taken from [83].

611 A smaller cylindrical structure (36.2m diameter, 33.8m height) is situated
 612 inside the tank, with an approximate 2m gap between this structure and the outer
 613 tank wall. The purpose of this structure is to support the photomultiplier tubes
 614 (PMTs). The volume inside and outside the support structure is referred to as the
 615 inner detector (ID) and outer detector (OD), respectively. In the SK-IV era, the
 616 ID and OD are instrumented by 11,129 50cm and 1,885 20cm PMTs respectively
 617 [79]. The ID contains a 32kton mass of water. Many analyses performed at SK
 618 use a “fiducial volume” defined by the volume of water inside the ID excluding
 619 some distance to the ID wall. This reduces the volume of the detector which is
 620 sensitive to neutrino events but reduces radioactive backgrounds and allows for

better reconstruction performance. The nominal fiducial volume is defined as the area contained inside 2m from the ID wall for a total of 22.5kton water [84].

The two regions of the detector (ID and OD) are optically separated with opaque black plastic hung from the support structure. The purpose of this is to determine whether an event entered or exited the ID. This allows cosmic ray muons and partially contained events to be tagged and separated from neutrino events entirely contained within the ID. This black plastic is also used to cover the area between the ID PMTs to reduce photon reflection from the ID walls. Opposite to this, the OD is lined with a reflective material to allow photons to reflect around inside the OD until collected by one of the PMTs. Furthermore, each OD PMT is optically coupled with $50 \times 50\text{cm}$ plates of wavelength shifting acrylic which increases the efficiency of light collection [82].

In the SK-IV data-taking period, the photocathode coverage of the detector, or the fraction of the ID wall instrumented with PMTs, is $\sim 40\%$ [82]. The PMTs have a quantum efficiency (the ratio of detected electrons to incident photons) of $\sim 21\%$ for photons with wavelengths of $360\text{nm} < \lambda < 390\text{nm}$ [85, 86]. The proportion of photoelectrons that produce a signal in the dynode of a PMT, termed the collection efficiency, is $> 70\%$ [82]. The PMTs used within SK are most sensitive to photons with wavelength $300\text{nm} \leq \lambda \leq 600\text{nm}$ [82]. One disadvantage of using PMTs as the detection media is that the Earth's geomagnetic field can modify its response. Therefore, a set of compensation coils is built around the inner surface of the detector to mitigate this effect [82].

The SK detector is filled with ultrapure water, which in a perfect world, contains no impurities. However, bacteria and organic compounds can significantly degrade the water quality. This decreases the attenuation length, which reduces the total number of photons that hit a PMT. To combat this, a sophisticated water treatment system has been developed [82, 87]. UV lights, mechanical filters, and membrane degasifiers are used to reduce the bacteria, suspended particulates, and radioactive materials from the water. The flow of water within the tank is also critical as it can remove stagnant bacterial growth or build-up of dust

651 on the surfaces within the tank. Gravity drifts impurities in the water towards
652 the bottom of the tank which, if left uncontrolled, can create asymmetric water
653 conditions between the top and bottom of the tank. Typically, the water entering
654 the tank is cooled below the ambient temperature of the tank to control convection
655 and inhibit bacteria growth. Furthermore, the rate of dark noise hits within PMTs
656 is sensitive to the PMT temperature [88]. Therefore controlling the temperature
657 gradients within the tank is beneficial for stable measurements.

658 SK-VI is the first phase of the SK experiment to use gadolinium dopants
659 within the ultrapure water [80]. As such, the SK water system had to be replaced
660 to avoid removing the gadolinium concentrate from the ultrapure water [65]. For
661 an inverse β -decay (IBD) interaction on a water target, the emitted neutron is
662 thermally captured on hydrogen. This process releases a 2.2MeV γ ray which is
663 difficult to detect as the resulting Compton scattered electrons are very close to the
664 Cherenkov threshold, limiting detection capability. Thermal capture of neutrons
665 on gadolinium generates γ rays with higher energy (8MeV [65]) meaning they
666 are more easily detected and reconstructed. SK-VI has 0.01% Gd loading (0.02%
667 gadolinium sulphate by mass) which causes \approx 50% of neutrons emitted by IBD
668 to be captured on gadolinium[89]. Whilst predominantly useful for low energy
669 analyses, Gd loading allows better $\nu/\bar{\nu}$ separation for atmospheric neutrino
670 event selections [90]. Efforts are currently in place to increase the gadolinium
671 concentrate to 0.03% for \approx 75% neutron capture efficiency on gadolinium [91].
672 The final stage of loading targets 0.1% concentrate for \approx 90% neutron capture
673 efficiency on gadolinium.

674 3.1.2 Calibration

675 The calibration of the SK detector is documented in [79] and summarised below.
676 The analysis presented within this thesis is dependent upon ‘high energy events’
677 (Charged particles with $O(> 100)$ MeV momenta). These are events that are
678 expected to generate a larger number of photons such that each PMT will
679 be hit with multiple photons. The reconstruction of these events depends

upon the charge deposited within each PMT and the timing response of each individual PMT. Therefore, the most relevant calibration techniques to this thesis are outlined.

Before installation, 420 PMTs were calibrated to have identical charge responses and then distributed throughout the tank in a cross-shape pattern (As illustrated by Figure 3.2). These are used as a standardised measure for the rest of the PMTs installed at similar geometric positions within SK to be calibrated against. To perform this calibration, a xenon lamp is located at the center of the SK tank which flashes uniform light at 1Hz. This allows for geometrical effects, water quality variation, and timing effects to be measured in situ throughout normal data-taking periods.

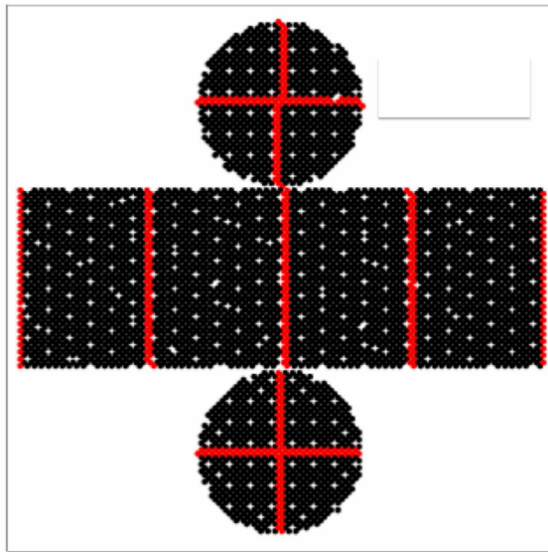


Figure 3.2: The location of “standard PMTs” (red) inside the SK detector. Taken from [79].

When specifically performing calibration of the detector (in out-of-data taking mode), the water in the tank was circulated to avoid top/bottom asymmetric water quality. Any non-uniformity within the tank significantly affects the PMT hit probability through scattering or absorption. This becomes a dominant effect for very low-intensity light sources that are designed such that only one photon is incident upon a given PMT.

697 The gain of a PMT is defined as the ratio of the total charge of the signal
 698 produced compared to the charge of photoelectrons emitted by the photocathodes
 699 within the PMT. To calibrate the signal of each PMT, the “relative” and “absolute”
 700 gain values are measured. The relative gain is the variation of gain among each
 701 of the PMTs whereas the absolute gain is the average gain of all PMTs.

702 The relative gain is calibrated as follows. A laser is used to generate two
 703 measurements: a high-intensity flash that illuminates every PMT with a sufficient
 704 number of photons, and a low-intensity flash in which only a small number
 705 of PMTs collect light. The first measurement creates an average charge, $Q_{obs}(i)$
 706 on PMT i , whereas the second measurement ensures that each hit PMT only
 707 generates a single photoelectron. For the low-intensity measurement, the number
 708 of times each PMT records a charge larger than 1/4 photoelectrons, $N_{obs}(i)$, is
 709 counted. The values measured can be expressed as

$$\begin{aligned} Q_{obs}(i) &\propto I_H \times f(i) \times \epsilon(i) \times G(i), \\ N_{obs}(i) &\propto I_L \times f(i) \times \epsilon(i). \end{aligned} \tag{3.1}$$

710 Where I_H and I_L is the intensity of the high and low flashes, $f(i)$ is the
 711 acceptance efficiency of the i^{th} PMT, $\epsilon(i)$ is the product of the quantum and
 712 collection efficiency of the i^{th} PMT and $G(i)$ is the gain of the i^{th} PMT. The relative
 713 gain for each PMT can be determined by taking the ratio of these quantities.

714 The absolute gain calibration is performed by observing fixed energy γ -rays
 715 of $E_\gamma \sim 9\text{MeV}$ emitted isotropically from neutron capture on a NiCf source
 716 situated at the center of the detector. This generates a photon yield of about 0.004
 717 photoelectrons/PMT/event, meaning that $> 99\%$ of PMT signals are generated
 718 from single photoelectrons. A charge distribution is generated by performing
 719 this calibration over all PMTs, and the average value of this distribution is taken
 720 to be the absolute gain value.

721 As mentioned in subsection 3.1.1, the average quantum and collection effi-
 722 ciency for the SK detector PMTs is $\sim 21\%$ and $> 70\%$ respectively. However,
 723 these values do differ between each PMT and need to be calibrated accordingly.

724 Consequently, the NiCf source is also used to calibrate the “quantum \times collection”
725 efficiency (denoted “QE”) value of each PMT. The NiCf low-intensity source is
726 used as the PMT hit probability is proportional to the QE ($N_{obs}(i) \propto \epsilon(i)$ in
727 Equation 3.1). A Monte Carlo prediction which includes photon absorption,
728 scattering, and reflection is made to estimate the number of photons incident on
729 each PMT and the ratio of the number of predicted to observed hits is calculated.
730 The difference is attributed to the QE efficiency of that PMT. This technique is
731 extended to calculate the relative QE efficiency by normalizing the average of
732 all PMTs which removes the dependence on the light intensity.

733 Due to differing cable lengths and readout electronics, the timing response
734 between a photon hitting the PMT and the signal being captured by the data
735 acquisition can be different between each PMT. Due to threshold triggers (De-
736 scribed in subsection 3.1.3), the time at which a pulse reaches a threshold is
737 dependent upon the size of the pulse. This is known as the ‘time-walk’ effect
738 and also needs to be accounted for in each PMT. To calibrate the timing response,
739 a pulse of light with width 0.2ns is emitted into the detector through a diffuser.
740 Two-dimensional distributions of time and pulse height (or charge) are made
741 for each PMT and are used to calibrate the timing response. This is performed
742 in-situ during data taking with the light source pulsing at 0.03Hz.

743 The top/bottom water quality asymmetry is measured using the NiCf calibra-
744 tion data and cross-referencing these results to the “standard PMTs”. The water
745 attenuation length is continuously measured by the rate of vertically-downgoing
746 cosmic-ray muons which enter via the top of the tank.

747 Dark noise is where a PMT registers a pulse that is consistent with a single
748 photoelectron emitted from photon detection despite the PMT being in complete
749 darkness. This is predominately caused by two processes. Firstly there is
750 intrinsic dark noise which is where photoelectrons gain enough thermal energy
751 to be emitted from the photocathode, and secondly, the radioactive decay of
752 contaminants inside the structure of the PMT. Typical dark noise rate for PMTs
753 used within SK are $O(3)\text{kHz}$ [82]. This is lower than the expected number of

754 photons generated for a ‘high energy event’ (As described in subsection 3.1.4)
755 but instability in this value can cause biases in reconstruction. Dark noise is
756 related to the gain of a PMT and is calibrated using hits inside a time window
757 recorded before an event trigger [92].

758 3.1.3 Data Acquisition and Triggering

759 As the analysis presented in this thesis will only use the SK-IV period of the
760 SK experiment so this subsection focuses on the relevant points of the data
761 acquisition and triggering systems to that SK period. The earlier data acquisition
762 and triggering systems are documented in [93, 94].

763 Before the SK-IV period started, the existing front-end electronics were re-
764 placed with “QTC-Based Electronics with Ethernet, QBEE” systems [95]. When
765 the QBEE observes a signal above a 1/4 photoelectron threshold, the charge-to-
766 time (QTC) converter generates a rectangular pulse. The start of the rectangular
767 pulse indicates the time at which the analog photoelectron signal was received
768 and the width of the pulse indicates the total charge integrated throughout the
769 signal. This is then digitized by time-to-digital converters and sent to the “front-
770 end” PCs. The digitized signal from every QBEE is then chronologically ordered
771 and sent to the “merger” PCs. It is the merger PCs that apply the software trigger.
772 Any triggered events are passed to the “organizer” PC. This sorts the data stream
773 of multiple merger PCs into chronologically ordered events, which are then saved
774 to disk. The schematic of data flow from PMTs to disk is illustrated in Figure 3.3.

775 The software trigger (described in [97]) operates by determining the number
776 of PMT hits within a 200ns sliding window, N_{200} . This window coincides with the
777 maximum time that a Cherenkov photon would take to traverse the length of the
778 SK tank [94]. For lower energy events that generate fewer photons, this technique
779 is useful for eliminating background processes like dark noise and radioactive
780 decay which would be expected to be separated in time. When the value of
781 N_{200} exceeds some pre-defined threshold, a software trigger is issued. There are
782 several trigger thresholds used within the SK-IV period which are detailed in

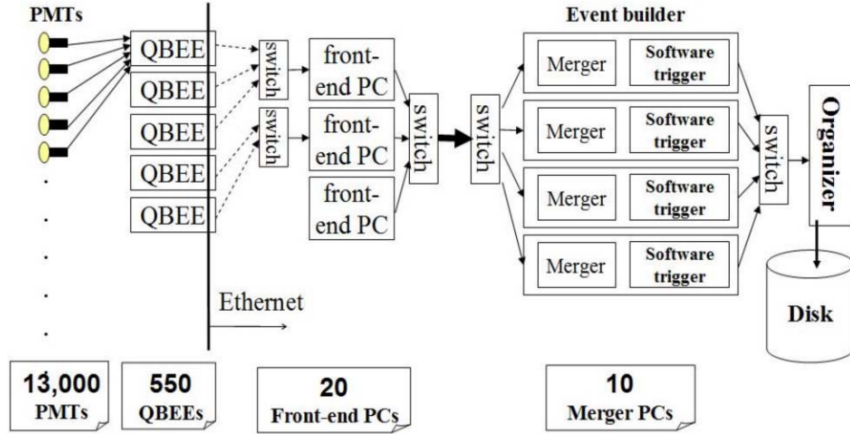


Figure 3.3: Schematic view of the data flow through the data acquisition and online system. Taken from [96].

783 Table 3.2. If one of these thresholds is met, the PMT hits within an extended time
 784 window are also read out and saved to disk. In the special case of an event that
 785 exceeds the SHE trigger but does not exceed the OD trigger, the AFT trigger looks
 786 for delayed coincidences of 2.2MeV gamma rays emitted from neutron capture in
 787 a $535\mu\text{s}$ window after the SHE trigger. A similar but more complex “Wideband
 788 Intelligent Trigger (WIT)” has been deployed and is described in [98].

Trigger	Acronym	Condition	Extended time window (μs)
Super Low Energy	SLE	>34/31 hits	1.3
Low Energy	LE	>47 hits	40
High Energy	HE	>50 hits	40
Super High Energy	SHE	>70/58 hits	40
Outer Detector	OD	>22 hits in OD	N/A

Table 3.2: The trigger thresholds and extended time windows saved around an event which were utilised throughout the SK-IV period. The exact thresholds can change and the values listed here represent the thresholds at the start and end of the SK-IV period.

3.1.4 Cherenkov Radiation

790 Cherenkov light is emitted from any highly energetic charged particle traveling
 791 with relativistic velocity, β , greater than the local speed of light in a medium [99].

792 Cherenkov light is formed at the surface of a cone with a characteristic pitch angle,

$$\cos(\theta) = \frac{1}{\beta n}. \quad (3.2)$$

793 Where n is the refractive index of the medium. Consequently, the Cherenkov
 794 momentum threshold, P_{thres} , is dependent upon the mass, m , of the charged
 795 particle moving through the medium,

$$P_{thres} = \frac{m}{\sqrt{n^2 - 1}}. \quad (3.3)$$

796 For water, where $n = 1.33$, the Cherenkov threshold momentum and energy
 797 for various particles are given in Table 3.3. In contrast, γ -rays are detected
 798 indirectly via the combination of photons generated by Compton scattering
 799 and pair production. The threshold for detection in the SK detector is typically
 800 higher than the threshold for photon production. This is due to the fact that the
 801 attenuation of photons in the water means that typically $\sim 75\%$ of Cherenkov
 802 photons reach the ID PMTs. Then the collection and quantum efficiencies
 803 described in subsection 3.1.1 result in the number of detected photons being
 804 lower than the number of photons which reach the PMTs.

Particle	Threshold Momentum (MeV)	Threshold Energy (MeV)
Electron	0.5828	0.7751
Muon	120.5	160.3
Pion	159.2	211.7
Proton	1070.0	1423.1

Table 3.3: The threshold momentum and total energy for a particle to generate Cherenkov light in ultrapure water, as calculated in Equation 3.2 in ultrapure water which has refractive index $n = 1.33$.

805 The Frank-Tamm equation [100] describes the relationship between the num-
 806 ber of Cherenkov photons generated per unit length, dN/dx , the wavelength of
 807 the photons generated, λ , and the relativistic velocity of the charged particle,

$$\frac{d^2N}{dxd\lambda} = 2\pi\alpha \left(1 - \frac{1}{n^2\beta^2}\right) \frac{1}{\lambda^2}. \quad (3.4)$$

808 where α is the fine structure constant. For a 100MeV momentum electron,
 809 approximately 330 photons will be produced per centimeter in the $300\text{nm} \leq \lambda \leq$
 810 700nm region which the ID PMTs are most sensitive to [82].

811 3.2 The Tokai to Kamioka Experiment

812 The Tokai to Kamioka (T2K) experiment is a long-baseline neutrino oscillation
 813 experiment located in Japan. Proposed in the early 2000s [83, 101] to replace
 814 K2K [102], T2K was designed to observe electron neutrino appearance whilst
 815 precisely measuring the oscillation parameters associated with muon neutrino
 816 disappearance [103]. The experiment consists of a neutrino beam generated
 817 at the Japan Proton Accelerator Research Complex (J-PARC), a suite of near
 818 detectors situated 280m from the beam target, and the Super Kamiokande far
 819 detector positioned at a 295km baseline. The cross-section view of the T2K
 820 experiment is drawn in Figure 3.4.

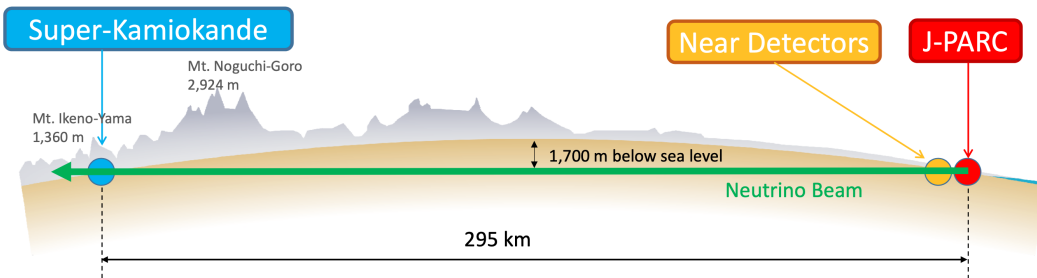


Figure 3.4: The cross-section view of the Tokai to Kamioka experiment illustrating the beam generation facility at J-PARC, the near detector situated at a baseline of 280m and the Super Kamiokande far detector situated 295km from the beam target.

821 The T2K collaboration makes world-leading measurements of the $\sin^2(\theta_{23})$,
 822 Δm_{32}^2 , and δ_{CP} oscillation parameters. Improvements in the precision and accu-
 823 racy of parameter estimates are still being made by including new data samples
 824 and developing the models which describe the neutrino interactions and detector
 825 responses [104]. Electron neutrino appearance was first observed at T2K in 2014
 826 [105] with 7.3σ significance.

827 The near detectors provide constraints on the beam flux and cross-section
 828 model parameters used within the oscillation analysis by observing the unoscil-
 829 lated neutrino beam. There are a host of detectors situated in the near detector hall
 830 (As illustrated in Figure 3.5): ND280 (subsection 3.2.3), INGRID (subsection 3.2.4),
 831 NINJA [106], WAGASCI [107], and Baby-MIND [108]. The latter three are not
 832 currently used within the oscillation analysis presented in this thesis.

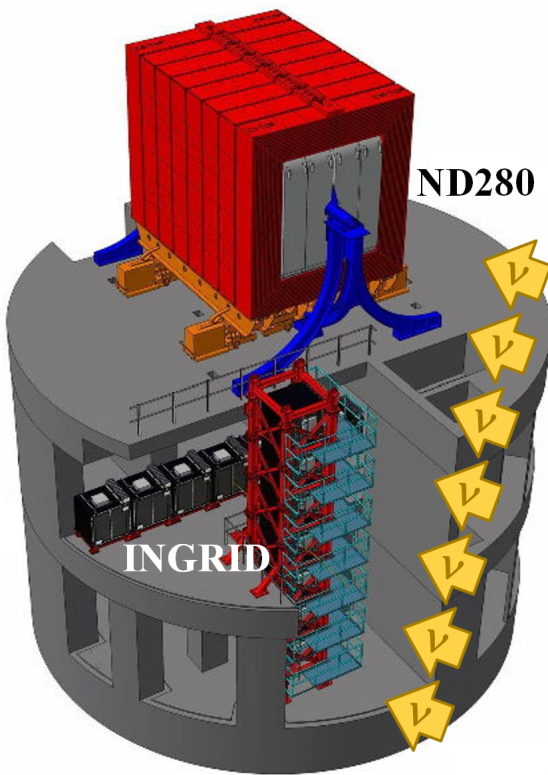


Figure 3.5: The near detector suite for the T2K experiment showing the ND280 and INGRID detectors. The distance between the detectors and the beam target is 280m.

833 Whilst this thesis presents the ND280 in terms of its purpose for the oscillation
 834 analysis, the detector can also make many cross-section measurements at neutrino
 835 energies of $O(1)$ GeV for the different targets within the detector [109, 110]. These
 836 measurements are of equal importance as they can lead the way in determining
 837 the model parameters used in the interaction models for the future high-precision
 838 era of neutrino physics.

3.2.1 Analysis Overview

There are two independent fitters, MaCh3 and BANFF, which perform the near detector fit. MaCh3 uses a bayesian Markov Chain Monte Carlo fitting technique, whereas BANFF uses a frequentist gradient descent technique. The output of each fitter is compared as a method of cross-checking the behaviour of the two fitters. This is done by comparing: the Monte Carlo predictions using various tunes, the likelihood that is calculated in each fitter and the post-fit constraint associated with every parameter used in the fit. Once validated, the output converted into a covariance matrix to describe the error and correlations between all the flux and cross-section parameters. This is then propagated to the far-detector oscillation analysis group.

The far detector group has three independent fitters: P-Theta, VALOR and MaCh3. The first two fitters use a hybrid frequentist fitting technique where the likelihood is minimised with respect to the parameters of interest and marginalised over all other parameters. These fitters use the covariance provided by the near detector fitters as a basis for implementing the near detector constraints. The MaCh3 fitter uses a simultaneous fit of all near and far detector samples. This removes any Gaussian assumptions when making the covariance matrix from the near detector results. The results for all three fitters are compares using a technique similar to the validation of the near detector fitters.

There are three particular tunes of the T2K flux and low energy cross section model typically considered. Firstly, the “generated” tune which is the set of dial values with which the Monte Carlo was generated. Secondly, the set of dial values which are taken from external data measurements and used as inputs. These are the “pre-fit” dial values. The reason these two sets of dial values are different is that the external data measurements are continually updated but it is very computationally intensive to regenerate a Monte Carlo prediction after each update. The final tune is the “post-fit”, “post-ND fit” or “post-BANFF” dial values. These are the values taken from the constraints provided by the near detector.

3.2.2 The Neutrino Beam

The neutrino beam used within the T2K experiment is described in [37, 41] and summarised below. The accelerator facility at J-PARC is composed of two sections; the primary and secondary beamlines. Figure 3.6 illustrates a schematic of the beamline, focusing mostly on the components of the secondary beamline. The primary beamline has three accelerators that progressively accelerate protons; a linear accelerator, a rapid-cycling synchrotron, and the main-ring (MR) synchrotron. Once fully accelerated by the MR, the protons have a kinetic energy of 30GeV. Eight bunches of these protons, separated by 500ns, are extracted per “spill” from the MR and directed towards a graphite target (a rod of length 91.4cm and diameter 2.6cm). Spills are extracted at 0.5Hz with $\sim 3 \times 10^{14}$ protons contained per spill.

The secondary beamline consists of three main components: the target station, the decay volume, and the beam dump. The target station is comprised of the target, beam monitors, and three magnetic focusing horns. The proton beam interacts with the graphite target to form a secondary beam of mostly pions and kaons. The secondary beam travels through a 96m long decay volume, generating neutrinos through the following decays [37],

$$\begin{array}{ll}
\pi^+ \rightarrow \mu^+ + \nu_\mu & \pi^- \rightarrow \mu^- + \bar{\nu}_\mu \\
K^+ \rightarrow \mu^+ + \nu_\mu & K^- \rightarrow \mu^- + \bar{\nu}_\mu \\
\rightarrow \pi^0 + e^+ + \nu_e & \rightarrow \pi^0 + e^- + \bar{\nu}_e \\
\rightarrow \pi^0 + \mu^+ + \nu_\mu & \rightarrow \pi^0 + \mu^- + \bar{\nu}_\mu \\
K_L^0 \rightarrow \pi^- + e^+ + \nu_e & K_L^0 \rightarrow \pi^+ + e^- + \bar{\nu}_e \\
\rightarrow \pi^- + \mu^+ + \nu_\mu & \rightarrow \pi^+ + \mu^- + \bar{\nu}_\mu \\
\mu^+ \rightarrow e^+ + \bar{\nu}_\mu + \nu_e & \mu^- \rightarrow e^- + \nu_\mu + \bar{\nu}_e.
\end{array}$$

The electrically charged component of the secondary beam is focused towards the far detector by the three magnetic horns. These horns direct charged particles of a particular polarity towards SK whilst defocusing the oppositely charged particles. This allows a mostly neutrino or mostly antineutrino beam to be used within the experiment, denoted as “forward horn current (FHC)” or “reverse horn current (RHC)” respectively.

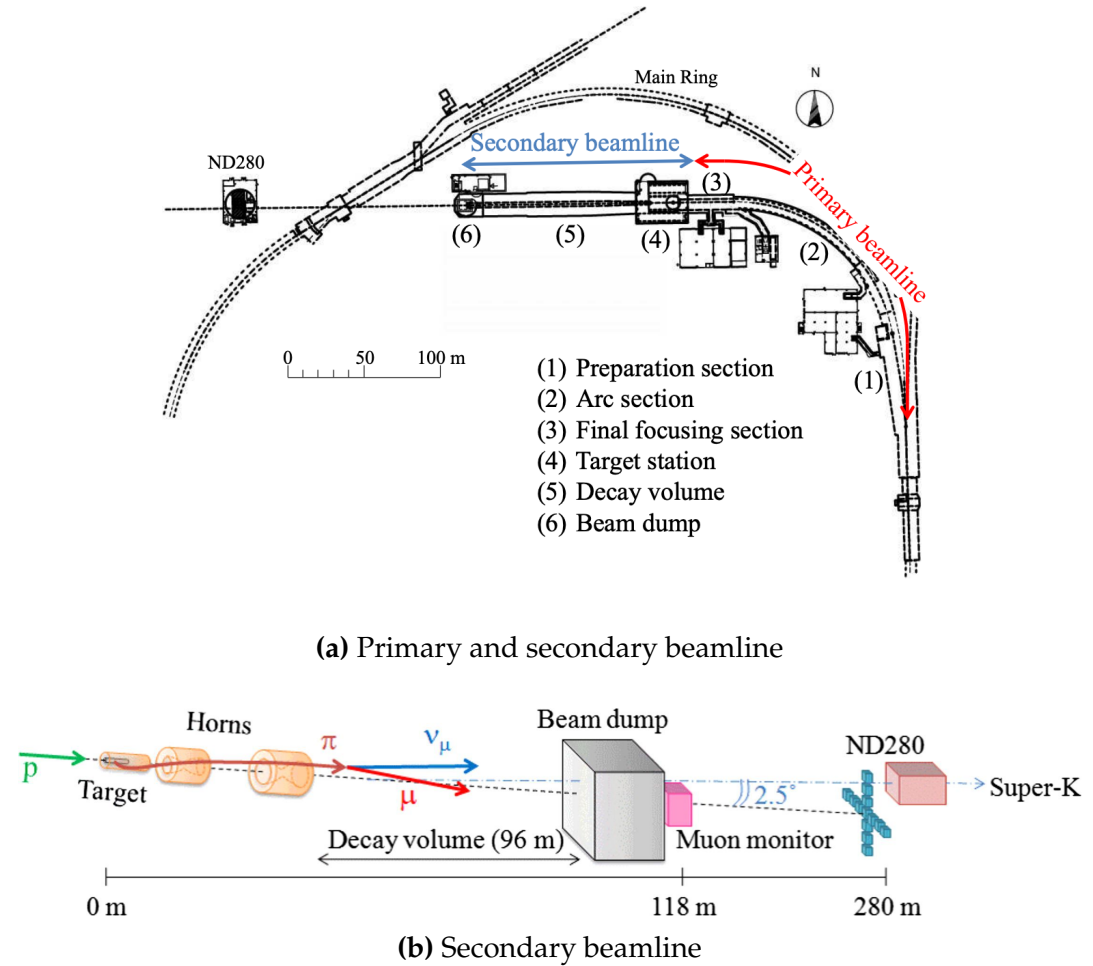


Figure 3.6: Top panel: Bird's eye view of the most relevant part of primary and secondary beamline used within the T2K experiment. The primary beamline is the main-ring proton synchrotron, kicker magnet, and graphite target. The secondary beamline consists of the three focusing horns, decay volume, and beam dump. Figure taken from [41]. Bottom panel: The side-view of the secondary beamline including the focusing horns, beam dump and neutrino detectors. Figure taken from [111].

894 Figure 3.7 illustrates the different contributions to the FHC and RHC neutrino
 895 flux. The low energy flux is dominated by the decay of pions whereas kaon
 896 decay becomes the dominant source of neutrinos for $E_\nu > 3\text{GeV}$. The “wrong-
 897 sign” component, which is the $\bar{\nu}_\mu$ background in a ν_μ beam, and the intrinsic
 898 irreducible ν_e background, are predominantly due to muon decay for $E_\nu <$
 899 2GeV . As the antineutrino production cross-section is smaller than the neutrino
 900 cross-section, the wrong-sign component is more dominant in the RHC beam
 901 as compared to that in the FHC beam.

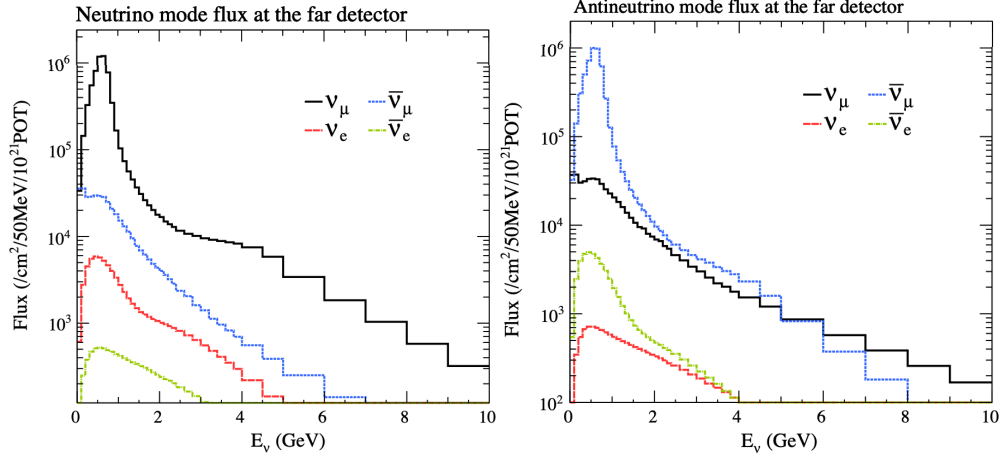


Figure 3.7: The Monte Carlo prediction of the energy spectrum for each flavour of neutrino (ν_e , $\bar{\nu}_e$, ν_μ and $\bar{\nu}_\mu$) in the neutrino dominated beam FHC mode (Left) and antineutrino dominated beam RHC mode (Right) expected at SK. Taken from [112].

902 The beam dump, situated at the end of the decay volume, stops all charged
 903 particles other than highly energetic muons ($p_\mu > 5\text{GeV}$). The MuMon detector
 904 monitors the penetrating muons to determine the beam direction and inten-
 905 sity which is used to constrain some of the beam flux systematics within the
 906 analysis [111, 113].

907 The T2K experiment uses an off-axis beam to narrow the neutrino energy
 908 distribution. This was the first implementation of this technique in a long-
 909 baseline neutrino oscillation experiment after its original proposal [114]. Pion
 910 decay, $\pi \rightarrow \mu + \nu_\mu$, is a two-body decay. Consequently, the neutrino energy,
 911 E_ν , can be determined based on the pion energy, E_π , and the angle at which
 912 the neutrino is emitted, θ ,

$$E_\nu = \frac{m_\pi^2 - m_\mu^2}{2(E_\pi - p_\pi \cos(\theta))}, \quad (3.5)$$

913 where m_π and m_μ are the mass of the pion and muon respectively. For a fixed
 914 energy pion, the neutrino energy distribution is dependent upon the angle at
 915 which the neutrinos are observed from the initial pion beam direction. For the
 916 295km baseline at T2K, $E_\nu = 0.6\text{GeV}$ maximises the electron neutrino appearance
 917 probability, $P(\nu_\mu \rightarrow \nu_e)$, whilst minimising the muon disappearance probability,

918 $P(\nu_\mu \rightarrow \nu_\mu)$. Figure 3.8 illustrates the neutrino energy distribution for a range of
 919 off-axis angles, as well as the oscillation probabilities most relevant to T2K.

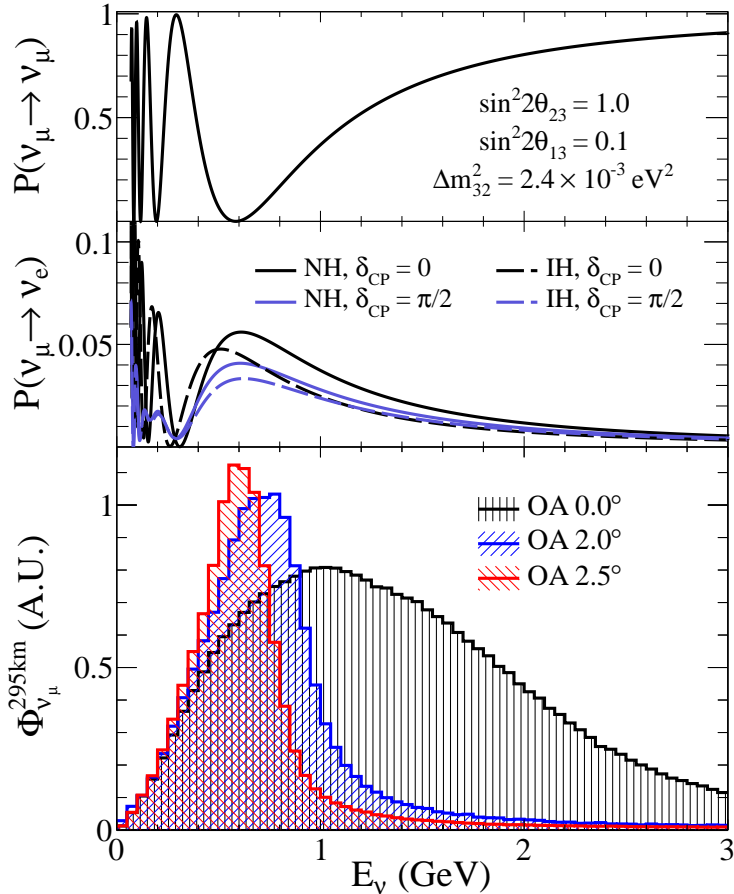


Figure 3.8: Top panel: T2K muon neutrino disappearance probability as a function of neutrino energy. Middle panel: T2K electron neutrino appearance probability as a function of neutrino energy. Bottom panel: The neutrino flux distribution for three different off-axis angles (Arbitrary units) as a function of neutrino energy.

920 3.2.3 The Near Detector at 280m

921 Whilst all the near detectors are situated in the same “pit” located at 280m from
 922 the beamline, the “ND280” detector is the off-axis detector which is situated at
 923 the same off-axis angle as the Super-Kamiokande far detector. It has two primary
 924 functions; firstly it measures the neutrino flux and secondly, it counts the event
 925 rates of different types of neutrino interactions. Both of these constrain the flux
 926 and cross-section systematics invoked within the model for a more accurate
 927 prediction of the expected event rate at the far detector.

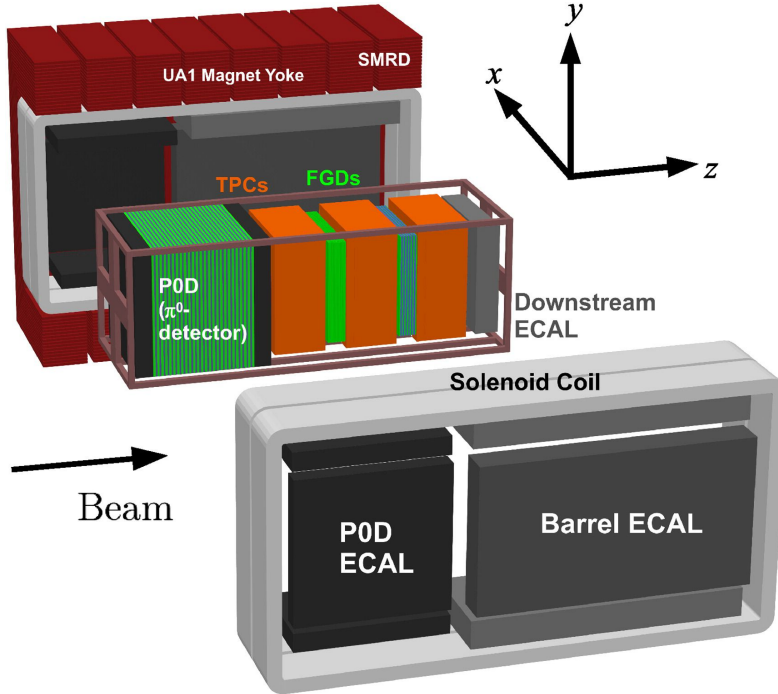


Figure 3.9: The components of the ND280 detector. The neutrino beam travels from left to right. Taken from [41].

As illustrated in Figure 3.9, the ND280 detector consists of several sub-detectors. The most important part of the detector for this analysis is the tracker region. This is comprised of two-time projection chambers (TPCs) sandwiched between three fine grain detectors (FGDs). The FGDs contain both hydrocarbon plastics and water targets for neutrino interactions and provide track reconstruction near the interaction vertex. The emitted charged particles can then propagate into the TPCs which provide particle identification and momentum reconstruction. The FGDs and TPCs are further described in subsubsection 3.2.3.1 and subsubsection 3.2.3.2 respectively. The electromagnetic calorimeter (ECAL) encapsulates the tracker region alongside the π^0 detector (P0D). The ECAL measures the deposited energy from photons emitted from interactions within the FGD. The P0D constrains the cross-section of neutral current interactions which generate neutral pions, which is one of the largest backgrounds in the electron neutrino appearance oscillation channel. The P0D and ECAL detectors are detailed in subsubsection 3.2.3.3 and subsubsection 3.2.3.4 respectively. The entire detector is located within a large yoke magnet which produces a 0.2T magnetic field.

944 field. This design of the magnet also includes a scintillating detector called the
945 side muon range detector (SMRD), which is used to track high-angle muons as
946 well as acting as a cosmic veto. The SMRD is described in subsubsection 3.2.3.5.

947 **3.2.3.1 Fine Grained Detectors**

948 The T2K tracker region is comprised of two fine-grained detectors (FGD) and
949 three Time Projection Chambers (TPC). A detailed description of the FGD design,
950 construction, and assembly is found in [115] and summarised below. The FGDS
951 are the primary target for neutrino interactions with a mass of 1.1 tonnes per FGD.
952 Alongside this, the FGDS are designed to be able to track short-range particles
953 which do not exit the FGD. Typically, short-range particles are low momentum
954 and are observed as tracks that deposit a large amount of energy per unit length.
955 This means the FGD needs good granularity to resolve these particles. The
956 FGDS have the best timing resolution ($\sim 3\text{ns}$) of any of the sub-detectors of the
957 ND280 detector. As such, the FGDS are used for time of flight measurements
958 to distinguish forward-going positively charged particles from backward-going
959 negatively charged particles. Finally, any tracks which pass through multiple
960 sub-detectors are required to be track matched to the FGD.

961 Both FGDS are made from square scintillator planes of side length 186cm and
962 width 2.02cm. Each plane consists of two layers of 192 scintillator bars in an
963 X or Y orientation. A wavelength-shifting fiber is threaded through the center
964 of each bar and is read out by a multi-pixel photon counter (MPPC). FGD1 is
965 the most upstream of the two FGDS and contains 15 planes of carbon plastic
966 scintillator which is a common target in external neutrino scattering data. As
967 the far detector is a pure water target, 7 of the 15 scintillator planes in FGD2
968 have been replaced with a hybrid water-scintillator target. Due to the complexity
969 of the nucleus, nuclear effects can not be extrapolated between different nuclei.
970 Therefore having the ability to take data on one target which is the same as
971 external data and another target which is the same as the far detector target is
972 beneficial for reliable model parameter estimates.

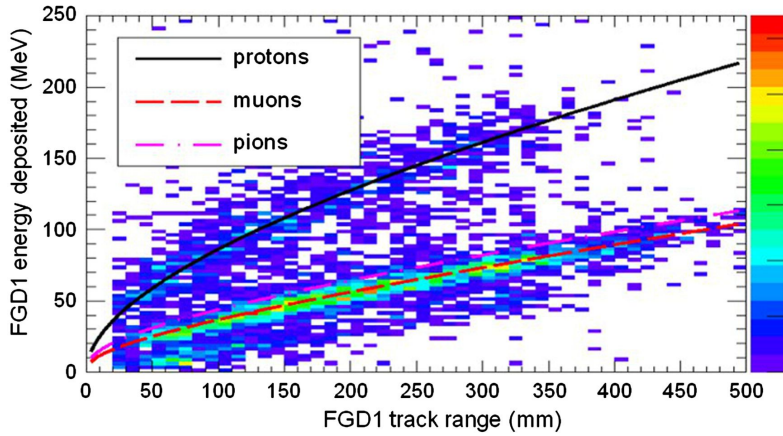


Figure 3.10: Comparison of data to Monte Carlo prediction of integrated deposited energy as a function of track length for particles that stopped in FGD1. Taken from [115].

973 The integrated deposited energy is used for particle identification. The FGD
 974 can distinguish protons from other charged particles by comparing the integrated
 975 deposited energy from data to Monte Carlo prediction as seen in Figure 3.10.

976 3.2.3.2 Time Projection Chambers

977 The majority of particle identification and momentum measurements within
 978 ND280 are provided by three Time Projection Chambers (TPCs) [116]. The
 979 TPCs are located on either side of the FGDs. They are located inside of the
 980 magnetic field meaning the momentum of a charged particle can be determined
 981 from the bending of the track.

982 Each TPC module consists of two gas-tight boxes, as shown in Figure 3.11,
 983 which are made of non-magnetic material. The outer box is filled with CO₂ which
 984 acts as an electrical insulator between the inner box and the ground. The inner box
 985 forms the field cage which produces a uniform electric drift field of $\sim 275\text{V/cm}$
 986 and is filled with an argon gas mixture. Charged particles moving through this
 987 gas mixture ionize the gas and the ionised charge is drifted towards micromegas
 988 detectors which measure the ionization charge. The time and position information
 989 in the readout allows a three-dimensional image of the neutrino interaction.

990 The particle identification of tracks that pass through the TPCs is performed
 991 using dE/dx measurements. Figure 3.12 illustrates the data to Monte Carlo

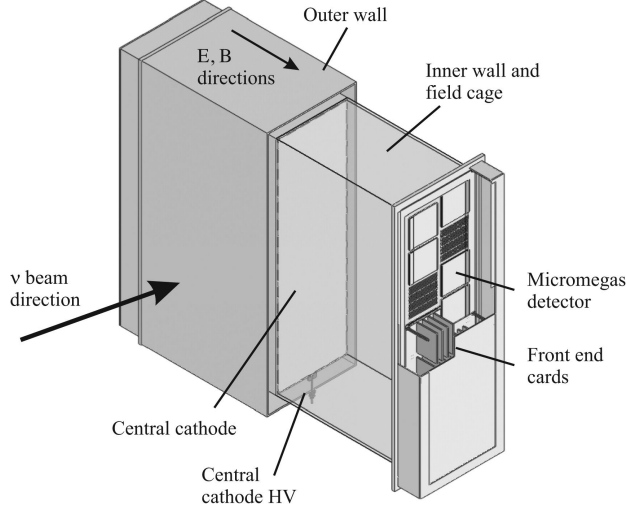


Figure 3.11: Schematic design of a Time Projection Chamber detector. Taken from [116].

992 distributions of the energy lost by a charged particle passing through the TPC as
 993 a function of the reconstructed particle momentum. The resolution is $7.8 \pm 0.2\%$
 994 meaning that electrons and muons can be distinguished. This allows reliable
 995 measurements of the intrinsic ν_e component of the beam.

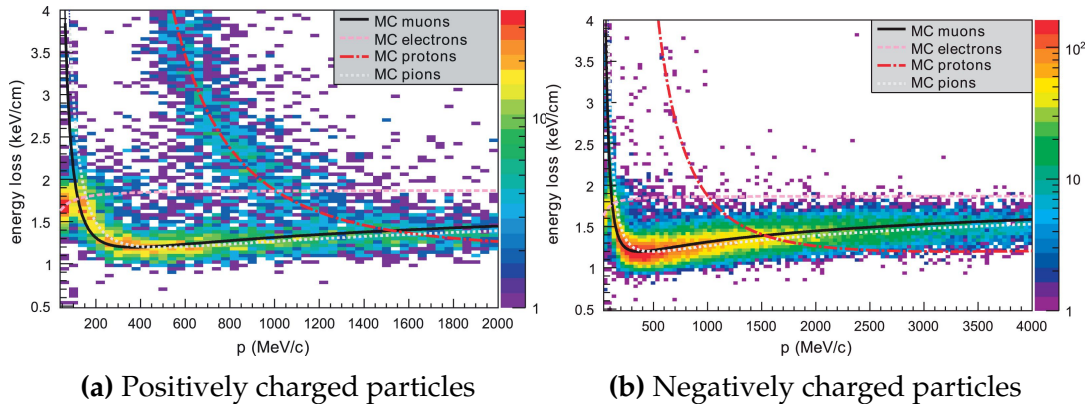


Figure 3.12: The distribution of energy loss as a function of reconstructed momentum for charged particles passing through the TPC, comparing data to Monte Carlo prediction. Taken from [116].

996 **3.2.3.3 π^0 Detector**

997 If one of the γ -rays from a $\pi^0 \rightarrow 2\gamma$ decay is missed at the far detector, the
 998 reconstruction will determine that event to be a charge current ν_e -like event.
 999 This is one of the main backgrounds hindering the electron neutrino appearance

1000 searches. The π^0 detector (P0D) measures the cross-section of the neutral current
 1001 induced neutral pion production on a water target to constrain this background.

1002 The P0D is a cube of approximately 2.5m length consisting of layers of scin-
 1003 tillating bars, brass and lead sheets, and water bags as illustrated in Figure 3.13.
 1004 Two electromagnetic calorimeters are positioned at the most upstream and most
 1005 downstream position in the sub-detector and the water target is situated in
 1006 between them. The scintillator layers are built from two triangular bars orientated
 1007 in opposite directions to form a rectangular layer. Each triangular scintillator bar
 1008 is threaded with optical fiber which is read out by MPPCs. The high-Z brass and
 1009 lead regions produce electron showers from the photons emitted in π^0 decay.

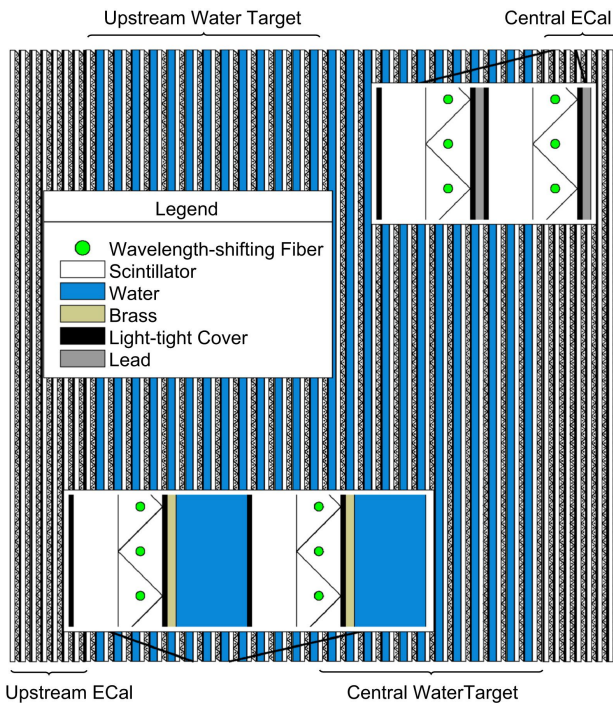


Figure 3.13: A schematic of the P0D side-view. Taken from [117].

1010 The sub-detector can generate measurements of NC1 π^0 cross-sections on a
 1011 water target by measuring the event rate both with and without the water target,
 1012 with the cross-section on a water target being determined as the difference. The to-
 1013 tal active mass is 16.1 tonnes when filled with water and 13.3 tonnes when empty.

3.2.3.4 Electromagnetic Calorimeter

The electromagnetic calorimeter [118] (ECal) encapsulates the P0D and tracking sub-detectors. Its primary purpose is to aid π^0 reconstruction from any interaction in the tracker. To do this, it measures the energy and direction of photon showers from $\pi^0 \rightarrow 2\gamma$ decay. It can also distinguish pion and muon tracks depending on the shape of the photon shower deposited.

The ECal is comprised of three sections; the P0D ECal which surrounds the P0D, the barrel ECal which encompasses the tracking region, and the downstream ECal which is situated downstream of the tracker region. The barrel and downstream ECals are tracking calorimeters that focus on electromagnetic showers from high-angle particles emitted from the tracking sub-detectors. Particularly in the TPC, high-angle tracks (those which travel perpendicularly to the beam-axis) can travel along a single scintillator bar resulting in very few hits. The width of the barrel and downstream ECal corresponds to ~ 11 electron radiation lengths to ensure a significant amount of the π^0 energy is contained. As the P0D has its own calorimetry which reconstructs showers, the P0D ECal determines the energy which escapes the P0D.

Each ECal is constructed of multiple layers of scintillating bars sandwiched between lead sheets. The scintillating bars are threaded with optical fiber and read out by MPPCs. Each sequential layer of the scintillator is orientated perpendicular to the previous which allows a three-dimensional event reconstruction. The target mass of the P0D ECal, barrel ECal, and downstream ECal are 1.50, 4.80, and 6.62 tonnes respectively.

3.2.3.5 Side Muon Range Detector

As illustrated in Figure 3.9, the ECal, FGDs, P0D, and TPCs are enclosed within the UA1 magnet. Reconditioned after use in the UA1 [119] and NOMAD [120] experiments, this magnet provides a uniform horizontal magnetic field of 0.2T with an uncertainty of 2×10^{-4} T.

1042 Built into the UA1 magnet, the side muon range detector (SMRD)[121] monitors
1043 high-energy muons which leave the tracking region and permeate through
1044 the ECal. It additionally acts as a cosmic muon veto and trigger.

1045 **3.2.4 The Interactive Neutrino GRID**

1046 The Interactive Neutrino GRID (INGRID) detector is situated within the same
1047 “pit” as the other near detectors. It is aligned with the beam in the “on-axis”
1048 position and measures the beam direction, spread, and intensity. The detector
1049 was originally designed with 16 identical modules [41] (two modules have since
1050 been decommissioned) and a “proton” module. The design of the detector is 14
1051 modules oriented in a cross with length and height 10m × 10m, as illustrated
1052 in Figure 3.14.

1053 Each module is composed of iron sheets interlaced with eleven tracking
1054 scintillator planes for a total target mass of 7.1 tonnes per module. The scintillator
1055 design is an X-Y pattern of 24 bars in both orientations, where each bar contains
1056 wave-length shifting fibers which are connected to multi-pixel photon counters
1057 (MPPCs). Each module is encapsulated inside veto planes to aid the rejection
1058 of charged particles entering the module.

1059 The proton module is different from the other modules in that it consists
1060 of entirely scintillator planes with no iron target. The scintillator bars are also
1061 smaller than those used in the other modules to increase the granularity of
1062 the detector and improve tracking capabilities. The module sits in the center
1063 of the beamline and is designed to give precise measurements of quasi-elastic
1064 charged current interactions to evaluate the performance of the Monte Carlo
1065 simulation of the beamline.

1066 The INGRID detector can measure the beam direction to an uncertainty of
1067 0.4mrad and the beam centre within a resolution of 10cm [41]. The beam direction
1068 in both the vertical and horizontal directions is discussed in [122] and it is found
1069 to be in good agreement with the MUMON monitor described in subsection 3.2.2.

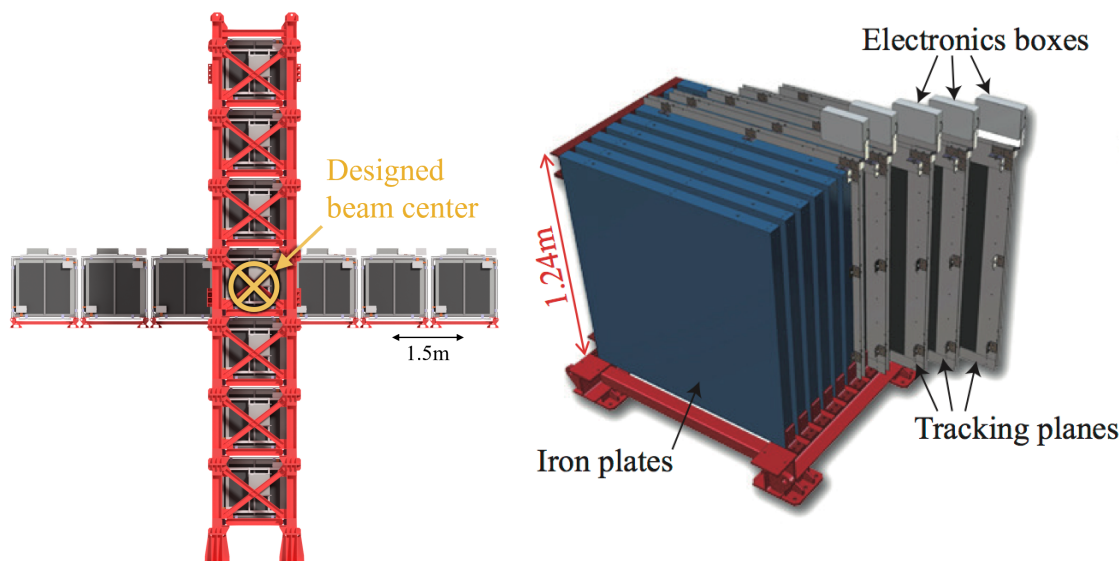


Figure 3.14: Left panel: The Interactive Neutrino GRID on-axis Detector. 14 modules are arranged in a cross-shape configuration, with the center modules being directly aligned with the on-axis beam. Right panel: The layout of a single module of the INGRID detector. Both figures are recreated from [41].

4

1070

1071

1072

Bayesian Statistics and Markov Chain Monte Carlo Techniques

1073 This thesis presents a Bayesian oscillation analysis. To extract the oscillation
1074 parameters, a Markov Chain Monte Carlo (MCMC) method is used. This chapter
1075 explains the theory of how parameter estimates can be determined using this
1076 technique and condenses the material found in the literature [123–126].

1077 The oscillation parameter determination presented here is built upon a si-
1078 multaneous fit to neutrino beam data in the near detector, beam data at SK, and
1079 atmospheric data at SK. In total, there are four oscillation parameters of interest
1080 ($\sin^2(\theta_{23})$, $\sin^2(\theta_{13})$, Δm_{32}^2 , and δ_{CP}), two oscillation parameters to which this
1081 study will not be sensitive ($\sin^2(\theta_{12})$, Δm_{21}^2) and many nuisance parameters that
1082 control the systematic uncertainty models.

1083 This analysis uses a Monte Carlo technique to generate a multi-dimensional
1084 probability distribution across all of the model parameters used in the fit. To
1085 determine an estimate for each parameter, this multi-dimensional object is in-
1086 tegrated over all other parameters. This process is called Marginalisation and
1087 is described in subsection 4.3.1. Monte Carlo techniques approximate the prob-
1088 ability distribution of each parameter within the limit of generating infinite
1089 samples. As ever, generating a large number of samples is time and resource-

1090 dependent. Therefore, an MCMC technique is utilised within this analysis to
1091 reduce the required number of steps to sufficiently sample the parameter space.
1092 This technique is described in further detail in subsection 4.2.1.

1093 The Bayesian analysis techniques used within this thesis are built within the
1094 MaCh3 framework [127]. This uses a custom MCMC library package exclusively
1095 supported and developed by the MaCh3 collaborators (which includes the author
1096 of this thesis).

1097 4.1 Bayesian Statistics

1098 Bayesian inference treats observable data, D , and model parameters, $\vec{\theta}$, on equal
1099 footing such that a probability model of both data and parameters is required.
1100 This is the joint probability distribution $P(D, \vec{\theta})$ and can be described by the
1101 prior distribution for model parameters $P(\vec{\theta})$ and the likelihood of the data given
1102 the model parameters $P(D|\vec{\theta})$,

$$P(D, \vec{\theta}) = P(D|\vec{\theta})P(\vec{\theta}). \quad (4.1)$$

1103 The prior distribution, $P(\vec{\theta})$, describes all previous knowledge about the
1104 parameters within the model. For example, if the risk of developing health
1105 problems is known to increase with age, the prior distribution would describe the
1106 increase. For the purpose of this analysis, the prior distribution is typically
1107 the best-fit values taken from external data measurements with a Gaussian
1108 uncertainty. The prior distribution can also contain correlations between model
1109 parameters. In an analysis using Monte Carlo techniques, the likelihood of
1110 measuring some data assuming some set of model parameters is calculated
1111 by comparing the Monte Carlo prediction generated at that particular set of
1112 model parameters to the data.

1113 It is parameter estimation that is important for this analysis and as such, Bayes'
1114 theorem [128] is applied to calculate the probability for each parameter to have a

1115 certain value given the observed data, $P(\vec{\theta}|D)$, which is known as the posterior
1116 distribution (often termed the posterior). This can be expressed as

$$P(\vec{\theta}|D) = \frac{P(D|\vec{\theta})P(\vec{\theta})}{\int P(D|\vec{\theta})P(\vec{\theta})d\vec{\theta}}. \quad (4.2)$$

1117 The denominator in Equation 4.2 is the integral of the joint probability distri-
1118 bution over all values of all parameters used within the fit. For brevity, the
1119 posterior distribution is

$$P(\vec{\theta}|D) \propto P(D|\vec{\theta})P(\vec{\theta}). \quad (4.3)$$

1120 For the purposes of this analysis, it is acceptable to neglect the normalisation
1121 term and focus on this proportional relationship.

1122 4.1.1 Application of Prior Knowledge

1123 The posterior distribution is proportional to the prior uncertainty applied to
1124 each parameter, as illustrated by Equation 4.3. This means that it is possible
1125 to change the prior after the posterior distribution has been determined. The
1126 prior uncertainty of a particular parameter can be ‘divided’ out of the posterior
1127 distribution and the resulting distribution can be reweighted using the new
1128 prior uncertainty that is to be applied. The methodology and implementation
1129 of changing the prior follows that described in [129].

1130 An example implementation that is useful for this analysis is the application
1131 of the “reactor constraint”. As discussed in section 2.4, an external constraint
1132 on $\sin^2(\theta_{13})$ is determined from measurements taken from reactor experiments.
1133 However, the sensitivities from just using the T2K and SK samples is equally
1134 as important. Without this technique, two fits would have to be run, doubling
1135 the required resources. Therefore, the key benefit for this analysis is the fact that
1136 only a single ‘fit’ has to be performed and can be used to build the two posterior
1137 distributions of the with and without reactor constraint applied.

1138 4.2 Monte Carlo Simulation

1139 Monte Carlo techniques are used to numerically solve a complex problem that
1140 does not necessarily have an analytical solution. These techniques rely on
1141 building a large ensemble of samples from an unknown distribution and then
1142 using the ensemble to approximate the properties of the distribution.

1143 An example that uses Monte Carlo techniques is to calculate the area under-
1144 neath a curve. For example, take the problem of calculating the area under a
1145 straight line with gradient $M = 0.4$ and intercept $C = 1.0$. Analytically, one can
1146 calculate the area under the line is equal to 30 units for $0 \leq x \leq 10$. Using Monte
1147 Carlo techniques, one can calculate the area under this line by throwing many
1148 random values for the x and y components of each sample and then calculating
1149 whether that point falls below the line. The area can then be calculated by the
1150 ratio of points below the line to the total number of samples thrown multiplied by
1151 the total area in which samples were scattered. The study is shown in Figure 4.1
1152 highlights this technique and finds the area under the curve to be 29.9 compared
1153 to an analytical solution of 30.0. The deviation of the numerical to analytical
1154 solution can be attributed to the number of samples used in the study. The
1155 accuracy of the approximation in which the properties of the Monte Carlo samples
1156 replicate those of the desired distribution is dependent on the number of samples
1157 used. Replicating this study with a differing number of Monte Carlo samples
1158 used in each study (As shown in Figure 4.2) highlights how the Monte Carlo
1159 techniques are only accurate within the limit of a high number of samples.

1160 Whilst the above example has an analytical solution, these techniques are just
1161 as applicable to complex solutions. Clearly, any numerical solution is only as
1162 useful as its efficiency. As discussed, the accuracy of the Monte Carlo technique is
1163 dependent upon the number of samples generated to approximate the properties
1164 of the distribution. Furthermore, if the positions at which the samples are
1165 evaluated are not ‘cleverly’ picked, the efficiency of the Monte Carlo technique
1166 significantly drops. Given the example in Figure 4.1, if the region in which the

1167 samples are scattered significantly extends passed the region of interest, many
1168 calculations will be calculated but do not add to the ability of the Monte Carlo
1169 technique to achieve the correct result. For instance, any sample evaluated at
1170 a $y \geq 5$ could be removed without affecting the final result. This does bring in
1171 an aspect of the ‘chicken and egg’ problem in that to achieve efficient sampling,
1172 one needs to know the distribution beforehand.

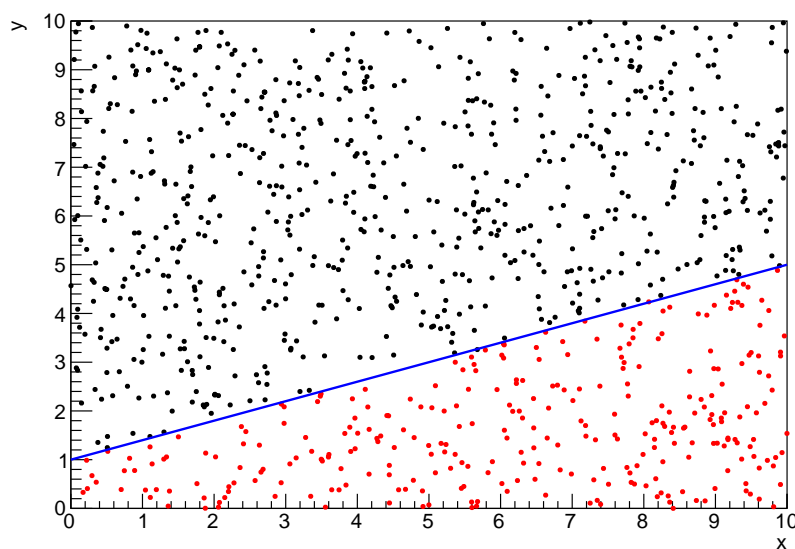


Figure 4.1: Example of using Monte Carlo techniques to find the area under the blue line. The gradient and intercept of the line are 0.4 and 1.0 respectively. The area found to be under the curve using one thousand samples is 29.9 units.

1173 4.2.1 Markov Chain Monte Carlo

1174 This analysis utilises a multi-dimensional probability distribution, with some
1175 dimensions being significantly more constrained than others. These constraints
1176 can be from prior knowledge of parameter distributions from external data or
1177 un-physical regions in which parameters can not exist. To maximise the efficiency
1178 of building the posterior distribution, a Markov Chain Monte Carlo (MCMC)
1179 technique is used. This employs a Markov chain to select the points at which
1180 to sample the posterior distribution. It performs a semi-random stochastic walk
1181 through the allowable parameter space. This builds a posterior distribution

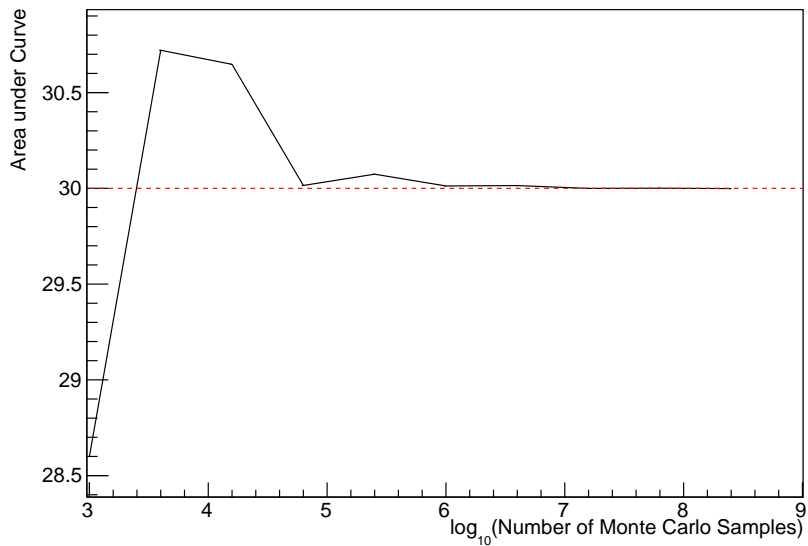


Figure 4.2: The area under a line of gradient 0.4 and intercept 1.0 for the range $0 \leq x \leq 10$ as calculated using Monte Carlo techniques as a function of the number of samples used in each repetition. The analytical solution to the area is 30 units as given by the red line.

1182 which has the property that the density of sampled points is proportional to the
 1183 probability density of that parameter. This means that the samples produced by
 1184 this technique are not statistically independent but they will cover the space
 1185 of the distribution.

1186 A Markov chain functions by selecting the position of step \vec{x}_{i+1} based on the
 1187 position of \vec{x}_i . The space in which the Markov chain selects samples is dependent
 1188 upon the total number of parameters utilised within the fit, where a discrete point
 1189 in this space is described by the N-dimensional space \vec{x} . In a perfectly operating
 1190 Markov chain, the position of the next step depends solely on the previous step
 1191 and not on the further history of the chain (\vec{x}_0, \vec{x}_1 , etc.). However, in solving
 1192 the multi-dimensionality of the fit used within this analysis, each step becomes
 1193 correlated with several of the steps preceding itself. Providing the MCMC chain is
 1194 well optimised, it will begin to converge towards a unique stationary distribution.
 1195 The period between the chain's initial starting point and the convergence to the
 1196 unique stationary distribution is colloquially known as the burn-in period. Once
 1197 the chain reaches the stationary distribution, all points sampled after that point

1198 will look like samples from that distribution.

1199 Further details of the theories underpinning MCMC techniques are discussed
1200 in [124] but can be summarised by the requirement that the chain satisfies the
1201 three ‘regularity conditions’:

- 1202 • Irreducibility: From every position in the parameter space \vec{x} , there must
1203 exist a non-zero probability for every other position in the parameter space
1204 to be reached.
- 1205 • Recurrence: Once the chain arrives at the stationary distribution, every step
1206 following from that position must be samples from the same stationary
1207 distribution.
- 1208 • Aperiodicity: The chain must not repeat the same sequence of steps at any
1209 point throughout the sampling period.

1210 The output of the chain after burn-in (i.e. the sampled points after the chain
1211 has reached the stationary distribution) can be used to approximate the posterior
1212 distribution and model parameters $\vec{\theta}$. To achieve the requirement that the unique
1213 stationary distribution found by the chain be the posterior distribution, one
1214 can use the Metropolis-Hastings algorithm. This guides the stochastic process
1215 depending on the likelihood of the current proposed step compared to that
1216 of the previous step.

1217 4.2.2 Metropolis-Hastings Algorithm

1218 As a requirement for MCMCs, the Markov chain implemented in this technique
1219 must have a unique stationary distribution that is equivalent to the posterior
1220 distribution. To ensure this requirement and that the regularity conditions are
1221 met, this analysis utilises the Metropolis-Hastings (MH) algorithm [130, 131].
1222 For the i^{th} step in the chain, the MH algorithm determines the position in the
1223 parameter space to which the chain moves to based on the current step, \vec{x}_i , and
1224 the proposed step, \vec{y}_{i+1} . The proposed step is randomly selected from some

1225 proposal function $f(\vec{x}_{i+1}|\vec{x}_i)$, which depends solely on the current step (ie. not
1226 the further history of the chain). The next step in the chain \vec{x}_{i+1} can be either the
1227 current step or the proposed step determined by whether the proposed step is
1228 accepted or rejected. To decide if the proposed step is selected, the acceptance
1229 probability, $\alpha(\vec{x}_i, \vec{y}_i)$, is calculated as

$$\alpha(\vec{x}_i, \vec{y}_{i+1}) = \min\left(1, \frac{P(\vec{y}_{i+1}|D)f(\vec{x}_i|\vec{y}_{i+1})}{P(\vec{x}_i|D)f(\vec{y}_{i+1}|\vec{x}_i)}\right). \quad (4.4)$$

1230 Where $P(\vec{y}_{i+1}|D)$ is the posterior distribution as introduced in section 4.1. To
1231 simplify this calculation, the proposal function is required to be symmetric such
1232 that $f(\vec{x}_i|\vec{y}_{i+1}) = f(\vec{y}_{i+1}|\vec{x}_i)$. In practice, a multi-variate Gaussian distribution
1233 centered on \vec{x}_i is used to throw parameter proposals. This reduces Equation 4.4 to

$$\alpha(\vec{x}_i, \vec{y}_{i+1}) = \min\left(1, \frac{P(\vec{y}_{i+1}|D)}{P(\vec{x}_i|D)}\right). \quad (4.5)$$

1234 After calculating this quantity, a random number, β , is generated uniformly
1235 between 0 and 1. If $\beta \leq \alpha(\vec{x}_i, \vec{y}_{i+1})$, the proposed step is accepted. Otherwise,
1236 the chain sets the next step equal to the current step. This procedure is repeated
1237 for subsequent steps. This can be interpreted as if the posterior probability
1238 of the proposed step is greater than that of the current step, ($P(\vec{y}_{i+1}|D) \geq$
1239 $P(\vec{x}_i|D)$), the proposed step will always be accepted. If the opposite is true,
1240 ($P(\vec{y}_{i+1}|D) \leq P(\vec{x}_i|D)$), the proposed step will be accepted with probability
1241 $P(\vec{x}_i|D)/P(\vec{y}_{i+1}|D)$. This ensures that the Markov chain does not get trapped
1242 in any local minima in the potentially non-Gaussian posterior distribution. The
1243 outcome of this technique is that the density of steps taken in a discrete region
1244 is directly proportional to the probability density in that region.

1245 4.2.3 MCMC Optimisation

1246 As discussed in subsection 4.2.2, the proposal function invoked within the MH
1247 algorithm can take any form and the chain will still converge to the stationary
1248 distribution. At each set of proposed parameter values, a prediction of the same
1249 spectra has to be generated which requires significant computational resources.

1250 Therefore, the number of steps taken before the unique stationary distribution
1251 is found should be minimised as only steps after convergence add information
1252 to the oscillation analysis. Furthermore, the chain should entirely cover the
1253 allowable parameter space to ensure that all values have been considered. Tuning
1254 the distance that the proposal function jumps between steps on a parameter-by-
1255 parameter basis can both minimise the length of the burn-in period and ensure
1256 that the correlation between step \vec{x}_i and \vec{x}_j is sufficiently small.

1257 The effect of changing the width of the proposal function is highlighted in
1258 Figure 4.3. Three scenarios, each with the same underlying stationary distribution
1259 (A Gaussian of width 1.0 and mean 0.), are presented. The only difference between
1260 the three scenarios is the width of the proposal function, colloquially known as
1261 the ‘step size σ ’. Each scenario starts at an initial parameter value of 10.0 which
1262 would be considered an extreme variation. For the case where $\sigma = 0.1$, it is
1263 clear to see that the chain takes a long time to reach the expected region of the
1264 parameter. This indicates that this chain would have a large burn-in period and
1265 does not converge to the stationary distribution until step ~ 500 . Furthermore,
1266 whilst the chain does move towards the expected region, each step is significantly
1267 correlated with the previous. Considering the case where $\sigma = 5.0$, the chain
1268 approaches the expected parameter region almost instantly meaning that the
1269 burn-in period is not significant. However, there are clearly large regions of steps
1270 where the chain does not move. This is likely due to the chain proposing steps
1271 in the tails of the distribution which have a low probability of being accepted.
1272 Consequently, this chain would take a significant number of steps to fully span
1273 the allowable parameter region. For the final scenario, where $\sigma = 0.5$, you can
1274 see a relatively small burn-in period of approximately 100 steps. Once the chain
1275 reaches the stationary distribution, it moves throughout the expected region of
1276 parameter values many times, sufficiently sampling the full parameter region.
1277 This example is a single parameter varying across a continuous distribution and
1278 does not fully reflect the difficulties in the many-hundred multi-variate parameter

1279 distribution used within this analysis. However, it does give a conceptual idea of
1280 the importance of selecting the proposal function and associated step size.

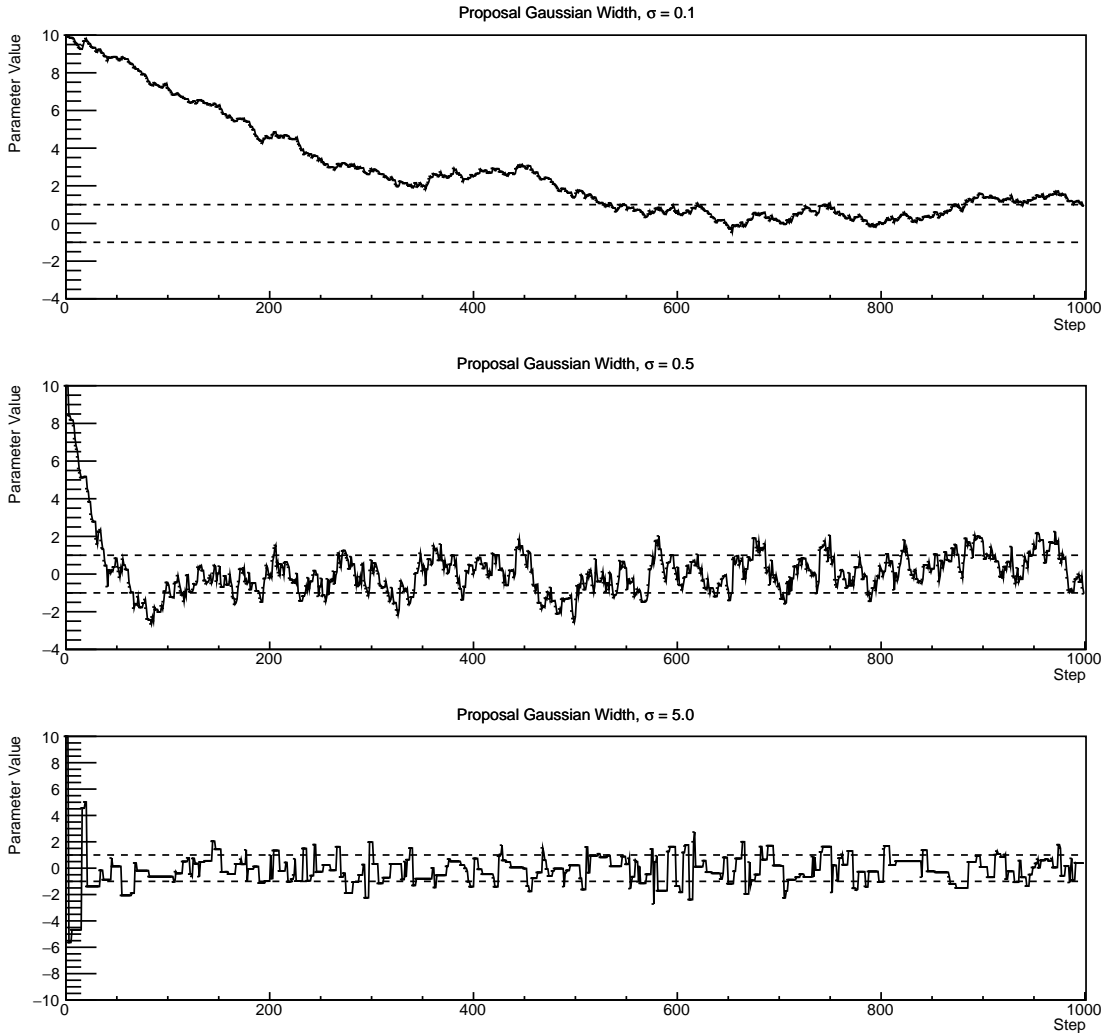


Figure 4.3: Three MCMC chains, each with a stationary distribution equal to a Gaussian centered at 0 and width 1 (As indicated by the black dotted lines). All of the chains use a Gaussian proposal function but have different widths (or ‘step size σ ’). The top panel has $\sigma = 0.1$, middle panel has $\sigma = 0.5$ and the bottom panel has $\sigma = 5.0$.

1281 As discussed, step size tuning directly correlates to the average step accep-
1282 tance rate. If the step size is too small, many steps will be accepted but the
1283 chain moves slowly. If the opposite is true, many steps will be rejected as the
1284 chain proposes steps in the tails of the distribution. Discussion in [132] suggests
1285 that the ‘ideal’ acceptance rate of a high dimension MCMC chain should be

₁₂₈₆ approximately $\sim 25\%$. An “ideal” step size [132] of

$$\sigma = \frac{2.4}{N_p}, \quad (4.6)$$

₁₂₈₇ where N_p is the number of parameters included in the MCMC fit. However,
₁₂₈₈ the complex correlations between systematics mean that some parameters have
₁₂₈₉ to be hand-tuned and many efforts have been taken to select a set of parameter-
₁₂₉₀ by-parameter step sizes to approximately reach the ideal acceptance rate.

₁₂₉₁ Figure 4.4 highlights the likelihood as calculated by the fit in subsection 8.3.4
₁₂₉₂ as a function of the number of steps in each chain. In practice, many independent
₁₂₉₃ MCMC chains are run simultaneously to parallelise the task of performing the
₁₂₉₄ fit. This figure overlays the distribution found in each chain. As seen, the
₁₂₉₅ likelihood decreases from its initial value and converges towards a stationary
₁₂₉₆ distribution after $\sim 1 \times 10^5$ steps.

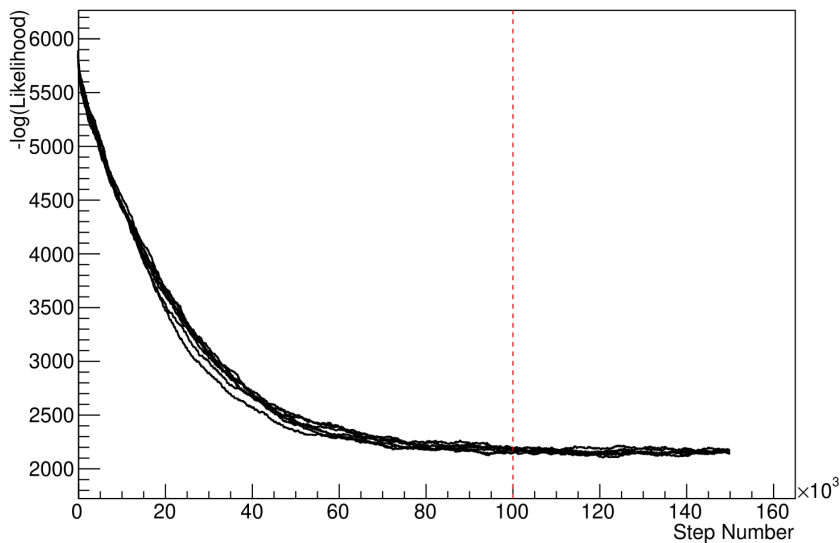


Figure 4.4: The log-likelihood from the fit detailed in subsection 8.3.4 as a function of the number of steps accumulated in each fit. Many independent MCMC chains were run in parallel and overlaid on this plot. The red line indicates the 1×10^5 step burn-in period after which the log-likelihood becomes stable.

₁₂₉₇ Multiple configurations of this analysis have been performed throughout this
₁₂₉₈ thesis where different samples or systematics have been used. For all of these con-
₁₂₉₉ figurations, it was found that a burnin period of 1×10^5 was sufficient in all cases.

1300 4.3 Understanding the MCMC Results

1301 The previous sections have described how to generate the posterior probability
1302 distribution using Bayesian MCMC techniques. However, this analysis focuses
1303 on oscillation parameter determination. The posterior distribution output from
1304 the chain is a high-dimension object, with as many dimensions as there are
1305 parameters included in the oscillation analysis. However, this multi-dimensional
1306 object is difficult to conceptualize so parameter estimations are often presented
1307 in one or two-dimensional projections of this probability distribution. To do
1308 this, marginalisation techniques are invoked.

1309 4.3.1 Marginalisation

1310 The output of the MCMC chain is a highly dimensional probability distribution
1311 which is very difficult to interpret. From the standpoint of an oscillation analysis
1312 experiment, the one or two-dimensional ‘projections’ of the oscillation parameters
1313 of interest are most relevant. Despite this, the best fit values and uncertainties on
1314 the oscillation parameters of interest should correctly encapsulate the correlations
1315 to the other systematic uncertainties (colloquially called ‘nuisance’ parameters).
1316 For this joint beam and atmospheric analysis, the oscillation parameters of
1317 interest are $\sin^2(\theta_{23})$, $\sin^2(\theta_{13})$, Δm_{32}^2 , and δ_{CP} . All other parameters (includ-
1318 ing the oscillation parameters this fit is insensitive to) are deemed nuisance
1319 parameters. To generate these projections, the posterior distribution is integrated
1320 over all nuisance parameters. This is called marginalisation. This technique
1321 also explains why it is acceptable to neglect the normalisation constant of the
1322 posterior distribution, which was discussed in section 4.1.

1323 A simple example of the marginalisation technique is to imagine the scenario
1324 where two coins are flipped. To determine the probability that the first coin
1325 returned a ‘head’, the exact result of the second coin flip is disregarded and
1326 simply integrated over. For the parameters of interest, $\vec{\theta}_i$, the marginalised

1327 posterior is calculated by integrating over the nuisance parameters, $\vec{\theta}_n$. In this
1328 case, Equation 4.2 becomes

$$P(\vec{\theta}_i|D) = \frac{\int P(D|\vec{\theta}_i, \vec{\theta}_n)P(\vec{\theta}_i, \vec{\theta}_n)d\vec{\theta}_n}{\int P(D|\vec{\theta})P(\vec{\theta})d\vec{\theta}}. \quad (4.7)$$

1329 Where $P(\vec{\theta}_i, \vec{\theta}_n)$ encodes the prior knowledge about the uncertainty and
1330 correlations between the parameters of interest and the nuisance parameters.
1331 In practice, this is simply taking the one or two-dimensional projection of the
1332 multi-dimensional probability distribution.

1333 While in principle an easy solution to a complex problem, correlations be-
1334 tween the interesting and nuisance parameters can bias the marginalised results.
1335 A similar effect is found when the parameters being marginalised over have
1336 non-Gaussian probability distributions. For example, Figure 4.5 highlights the
1337 marginalisation bias in the probability distribution found for a parameter when
1338 requiring a correlated parameter to have a positive parameter value. Due to
1339 the complex nature of the oscillation parameter fit presented in this thesis, there
1340 are correlations occurring between the oscillation parameters of interest and the
1341 other nuisance parameters included in the fit.

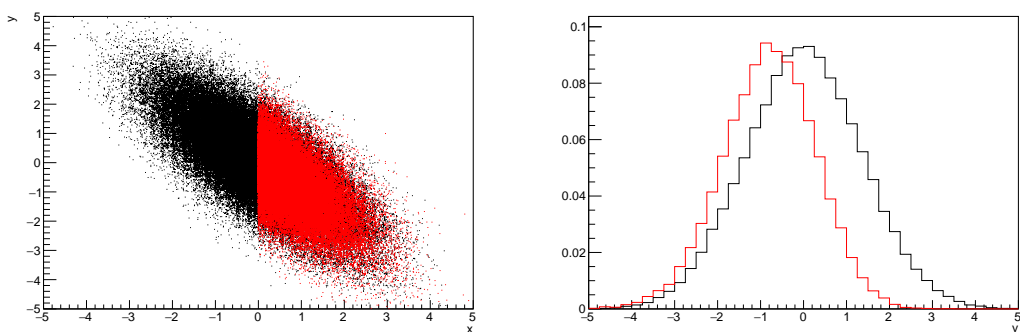


Figure 4.5: Left: The two-dimensional probability distribution for two correlated parameters x and y . The red distribution shows the two-dimensional probability distribution when $0 \leq x \leq 5$. Right: The marginalised probability distribution for the y parameter found when requiring the x to be bound between $-5 \leq x \leq 5$ and $0 \leq x \leq 5$ for the black and red distribution, respectively.

¹³⁴² **4.3.2 Parameter Estimation and Credible Intervals**

¹³⁴³ The purpose of this analysis is to determine the best fit values for the oscillation
¹³⁴⁴ parameters that the beam and atmospheric samples are sensitive to: $\sin^2(\theta_{23})$,
¹³⁴⁵ $\sin^2(\theta_{13})$, Δm_{32}^2 , and δ_{CP} . The posterior probability density, taken from the output
¹³⁴⁶ MCMC chain, is binned in these parameters. The parameter best-fit point is then
¹³⁴⁷ taken to be the value that has the highest posterior probability. This is performed
¹³⁴⁸ in both one and two-dimensional projections.

¹³⁴⁹ However, the single best-fit point in a given parameter is not of much use on its
¹³⁵⁰ own. The uncertainty on the best-fit point must also be presented using credible
¹³⁵¹ intervals. The definition of the 1σ credible interval is that there is 68% belief
¹³⁵² that the parameter is within those bounds. For a more generalised definition,
¹³⁵³ the credible interval is the region, R , of the posterior distribution that contains
¹³⁵⁴ a specific fraction of the total probability, such that

$$\int_R P(\theta|D)d\theta = \alpha. \quad (4.8)$$

¹³⁵⁵ Where θ is the parameter being evaluated. This technique then calculates
¹³⁵⁶ the $\alpha \times 100\%$ credible interval.

¹³⁵⁷ In practice, this analysis uses the highest posterior density (HPD) credible in-
¹³⁵⁸ tervals which are calculated through the following method. First, the probability
¹³⁵⁹ distribution is area-normalised such that it has an integrated area equal to 1.0.
¹³⁶⁰ The bins of probability are then summed from the highest to lowest until the sum
¹³⁶¹ exceeds the 1σ level (0.68 in this example). This process is repeated for a range of
¹³⁶² credible intervals, notably the 1σ , 2σ and 3σ along with other levels where the
¹³⁶³ critical values for each level can be found in [73]. This process can be repeated
¹³⁶⁴ for the two-dimensional probability distributions by creating two-dimensional
¹³⁶⁵ contours of credible intervals rather than a one-dimensional result.

1366 4.3.3 Bayesian Model Comparisons

1367 Due to the matter resonance, this analysis has some sensitivity to the mass
1368 hierarchy of neutrino states (whether Δm_{32}^2 is positive or negative) and the
1369 octant of $\sin^2(\theta_{23})$. The Bayesian approach utilised within this analysis gives an
1370 intuitive method of model comparison by determining which hypothesis is most
1371 favourable. Taking the ratio of Equation 4.3 for the two hypotheses of normal
1372 hierarchy, NH , and inverted hierarchy, IH , gives

$$\frac{P(\vec{\theta}_{NH}|D)}{P(\vec{\theta}_{IH}|D)} = \frac{P(D|\vec{\theta}_{NH})}{P(D|\vec{\theta}_{IH})} \times \frac{P(\vec{\theta}_{NH})}{P(\vec{\theta}_{IH})}. \quad (4.9)$$

1373 The middle term defines the Bayes factor, $B(NH/IH)$, which is a data-driven
1374 interpretation of how strong the data prefers one hierarchy to the other. For this
1375 analysis, equal priors on both mass hierarchy hypotheses are chosen ($P(\vec{\theta}_{NH}) =$
1376 $P(\vec{\theta}_{IH}) = 0.5$). In practice, the MCMC chain proposes a value of $|\Delta m_{32}^2|$ and
1377 then applies a 50% probability that the value is sign flipped. Consequently,
1378 the Bayes factor can be calculated from the ratio of the probability density in
1379 either hypothesis. This equates to counting the number of steps taken in the
1380 normal and inverted hierarchies and taking the ratio. The same approach can be
1381 taken to compare the upper octant (UO) compared to the lower octant (LO)
1382 hypothesis of $\sin^2(\theta_{23})$.

$\log_{10}(B_{AB})$	B_{AB}	Strength of Preference
< 0.0	< 1	No preference for hypothesis A (Supports hypothesis B)
$0.0 - 0.5$	$1.0 - 3.16$	Preference for hypothesis A is weak
$0.5 - 1.0$	$3.16 - 10.0$	Preference for hypothesis A is substantial
$1.0 - 1.5$	$10.0 - 31.6$	Preference for hypothesis A is strong
$1.5 - 2.0$	$31.6 - 100.0$	Preference for hypothesis A is very strong
> 2.0	> 100.0	Decisive preference for hypothesis A

Table 4.1: Jeffreys scale for strength of preference for two models A and B as a function of the calculated Bayes factor ($B_{AB} = B(A/B)$) between the two models [133]. The original scale is given in terms of $\log_{10}(B(A/B))$ but converted to linear scale for easy comparison throughout this thesis.

1383 Whilst the value of the Bayes factor should always be shown, the Jeffreys scale
1384 [133] (highlighted in Table 4.1) gives an indication of the strength of preference

1385 for one model compared to the other. Other interpretations of the strength of
1386 preference of a model exist, e.g. the Kass and Raferty Scale [134].

1387 4.3.4 Comparison of MCMC Output to Expectation

1388 To ensure the fit is performing well, a best-fit spectrum is produced using the
1389 posterior probability distribution and compared with the data, allowing easy
1390 by-eye comparisons to be made. A simple method of doing this is to perform a
1391 comparison in the fitting parameters (e.g. the reconstructed neutrino energy for
1392 T2K far detector beam samples) of the spectra generated by the MCMC chain to
1393 ‘data’. This ‘data’ could be true data or some variation of Monte Carlo prediction.
1394 This allows easy comparison of the MCMC probability distribution to the data. To
1395 perform this, N steps from the post-burnin MCMC chain are randomly selected.
1396 From these, the Monte Carlo prediction at each step is generated by reweighting
1397 the model parameters to the values specified at that step. Due to the probability
1398 density being directly correlated with the density of steps in a certain region,
1399 parameter values close to the best fit value are most likely to be selected.

1400 In practice, for each bin of the fitting parameters has a probability distribution
1401 of event rates, with one entry per sampled MCMC step. This distribution is
1402 binned where the bin with the highest probability is selected as the mean and an
1403 error on the width of this probability distribution is calculated using the approach
1404 highlighted in subsection 4.3.2. Consequently, the best fit distribution in the fit
1405 parameter is not necessarily that which would be attained by reweighting the
1406 Monte Carlo prediction to the most probable parameter values.

1407 A similar study can be performed to illustrate the freedom of the model
1408 parameter space prior to the fit. This can be done by throwing parameter values
1409 from the prior uncertainty of each parameter.

5

1410

1411

1412

Simulation, Reconstruction, and Event Reduction

1413 As a crucial part of the oscillation analysis, an accurate prediction of the expected
1414 neutrino spectrum at the far detector is required. This includes modeling the
1415 flux generation, neutrino interactions, and detector effects. All of the simulation
1416 packages required to do this are briefly described in section 5.1. The reconstruc-
1417 tion of neutrino events in the far detector, including the `fitQun` algorithm, is
1418 documented in section 5.2. This also includes data quality checks of the SK-V
1419 data which the author performed for the T2K oscillation analysis presented at the
1420 Neutrino 2020 conference [72]. Finally, section 5.3 describes the steps taken in the
1421 SK detector to trigger on events of interest whilst removing the comparatively
1422 large rate of cosmic ray muon events.

1423

5.1 Simulation

1424 In order to generate a Monte Carlo prediction of the expected event rate at
1425 the far detector, all the processes in the beam and atmospheric fluxes, neutrino
1426 interaction, and detector need to be modeled.

5.1.1 Neutrino Flux

The beamline simulation consists of three distinct parts: the initial hadron interaction modeled by FLUKA [135], the target station geometry and particle tracking performed by JNUBEAM, [37, 136] and any hadronic re-interactions simulated by GCALOR [137]. The primary hadronic interactions are $O(10)\text{GeV}$, where FLUKA matches external cross-section data better than GCALOR [138]. However, FLUKA is not very adaptable so a small simulation is built to model the interactions in the target and the output is then passed to JNUBEAM and GCALOR for propagation. The hadronic interactions are tuned to data from the NA61/SHINE [139–141] and HARP [142] experiments. The tuning is done by reweighting the FLUKA and GCALOR predictions to match the external data multiplicity and cross-section measurements, based on final state particle kinematics [138]. The culmination of this simulation package generates the predicted flux for neutrino and antineutrino beam modes which are illustrated in Figure 3.7.

The atmospheric neutrino flux is simulated by the HKKM model [49, 51]. The primary cosmic ray flux is tuned to AMS [143] and BESS [144] data assuming the US-standard atmosphere '76 [145] density profile and includes geomagnetic field effects. The primary cosmic rays interact to generate pions and muons. The interaction of these secondary particles to generate neutrinos is handled by DPMJET-III [146] for energies above 32GeV and JAM [51, 147] for energies below that value [47]. These hadronic interactions are tuned to BESS and L3 data [148, 149] using the same methodology as the tuning of the beamline simulation. The energy and cosine zenith predictions of $\nu_e, \bar{\nu}_e, \nu_\mu, \bar{\nu}_\mu$ flux are given in Figure 2.3 and Figure 2.5, respectively. The flux is approximately symmetrical and peaked around the horizon ($\cos(\theta_Z) = 0.0$). This is because horizontally-going pions and kaons can travel further than their vertically-going counterparts resulting in a larger probability of decaying to neutrinos. The symmetry is broken in lower-energy neutrinos due to geomagnetic effects, which modify the track of the primary cosmic rays. Updates to the HKKM model are currently ongoing [150].

1456 5.1.2 Neutrino Interaction

1457 Once a flux prediction has been made for all three detectors, NEUT 5.4.0 [151, 152]
 1458 models the interactions of the neutrinos in the detectors. For the purposes of this
 1459 analysis, quasi-elastic (QE), meson exchange (MEC), single meson production
 1460 (PROD), coherent pion production (COH), and deep inelastic scattering (DIS)
 1461 interactions are simulated. These interaction categories can be further broken
 1462 down by whether they were propagated via a W^\pm boson in Charged Current
 1463 (CC) interactions or via a Z^0 boson in Neutral Current (NC) interactions. CC
 1464 interactions have a charged lepton in the final state, which can be flavour-tagged
 1465 in reconstruction to determine the flavour of the neutrino. In contrast, NC
 1466 interactions have a neutrino in the final state so no flavour information can be
 1467 determined from the observables left in the detector after an interaction. This
 1468 is the reason why neutrinos that interact through NC modes are assumed to
 1469 not oscillate within this analysis. Both CC and NC interactions are modeled
 1470 for all the above interaction categories, other than MEC interactions which are
 1471 only modeled for CC events.

1472 As illustrated in Figure 5.1, CCQE interactions dominate the cross-section of
 1473 neutrino interactions around $E_\nu \sim 0.5\text{GeV}$. The NEUT implementation adopts
 1474 the Llewellyn Smith [153] model for neutrino-nucleus interactions, where the
 1475 nuclear ground state of any bound nucleons (neutrino-oxygen interactions) is
 1476 approximated by a spectral-function [154] model that simulates the effects of
 1477 Fermi momentum and Pauli blocking. The cross-section of QE interactions is
 1478 controlled by vector and axial-vector form factors parameterised by the BBBA05
 1479 [155] model and a dipole form factor with $M_A^{QE} = 1.21\text{GeV}$ fit to external data
 1480 [156], respectively. NEUT implements the Valencia [157] model to simulate MEC
 1481 events, where two nucleons and two holes in the nuclear target are produced
 1482 (often called 2p2h interactions).

1483 For neutrinos of energy $O(1)\text{GeV}$, PROD interactions become dominant.
 1484 These predominantly produce charged and neutral pions although γ , kaon,

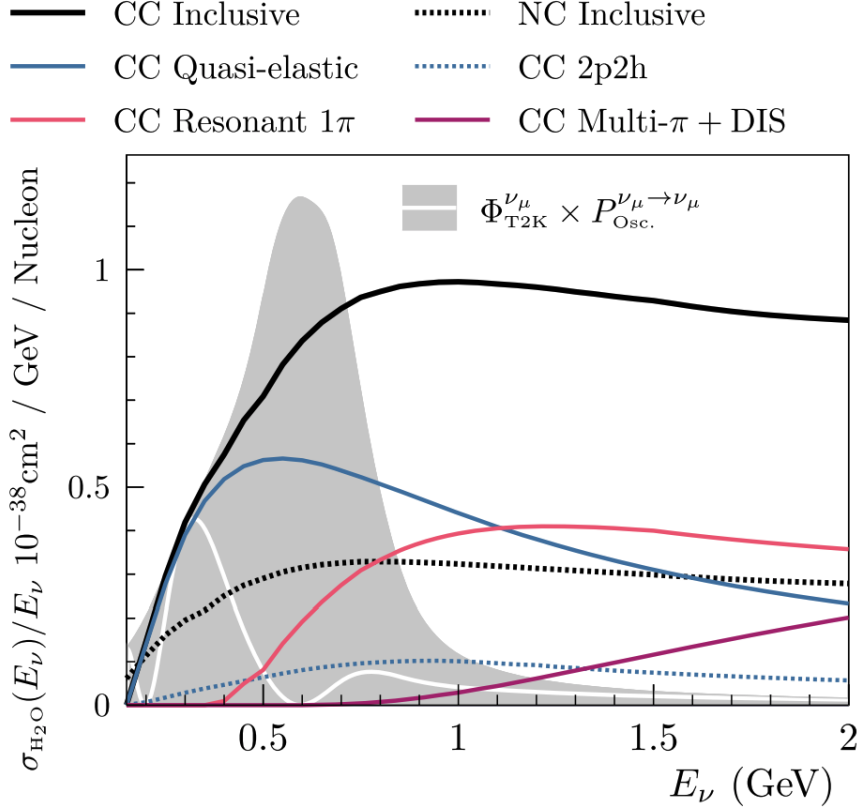


Figure 5.1: The NEUT prediction of the ν_μ -H₂O cross-section overlaid on the T2K ν_μ flux. The charged current (black, solid) and neutral current (black, dashed) inclusive, charged current quasi-elastic (blue, solid), charged current 2p2h (blue, dashed), charged current single pion production (pink), and charged current multi- π and DIS (Purple) cross-sections are illustrated. Figure taken from [151].

and η production is also considered. To simulate these interactions, the Berger-Sehgal [158] model is implemented within NEUT. It simulates the excitation of a nucleon from a neutrino interaction, production of an intermediate baryon, and the subsequent decay to a single meson or γ . Pions can also be produced through COH interactions, which occur when the incoming neutrino interacts with the entire oxygen nucleus leaving a single pion outside of the nucleus. NEUT utilises the Berger-Sehgal [159] model to simulate these COH interactions.

DIS and multi- π producing interactions become the most dominant for energies $> O(5)\text{GeV}$. PYTHIA [160] is used to simulate any interaction with invariant mass $W > 2\text{GeV}/c^2$, which produces at least one meson. For any interaction which produces at least two mesons but has $W < 2\text{GeV}/c^2$, the

¹⁴⁹⁶ Bronner model is used [161]. Both of these models use Parton distribution
¹⁴⁹⁷ functions based on the Bodek-Yang model [162–164].

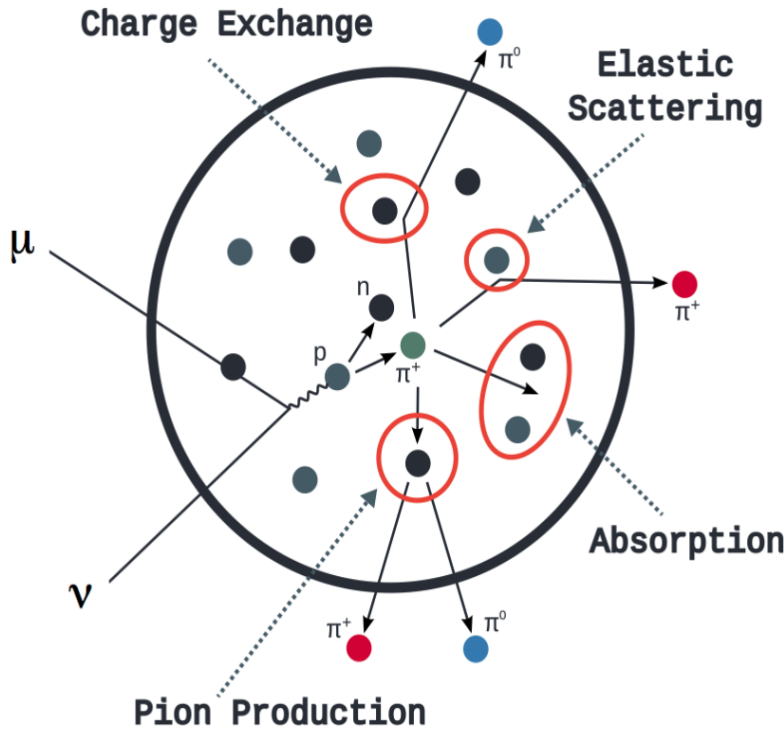


Figure 5.2: Illustration of the various processes which a pion can undergo before exiting the nucleus. Taken from [165].

¹⁴⁹⁸ Any pion that is produced within the nucleus can re-interact through final
¹⁴⁹⁹ state interactions before it exits, as illustrated by the scattering, absorption,
¹⁵⁰⁰ production, and exchange interactions in Figure 5.2. These re-interactions alter
¹⁵⁰¹ the observable particles within the detector. For instance, if the charged pion
¹⁵⁰² from a CC PROD interaction is absorbed, the observables would mimic a CC QE
¹⁵⁰³ interaction. To simulate these effects, NEUT uses a semi-classical intranuclear
¹⁵⁰⁴ cascade model [151]. This cascade functions by stepping the pion through the
¹⁵⁰⁵ nucleus in fixed-length steps equivalent to $dx = R_N/100$, where R_N is the radius
¹⁵⁰⁶ of the nucleus. At each step, the simulation allows the pion to interact through
¹⁵⁰⁷ scattering, charged exchange, absorption, or production with an interaction-
¹⁵⁰⁸ dependent probability calculated from a fit to external data [166]. This cascade
¹⁵⁰⁹ continues until the pion is absorbed or exits the nucleus.

1510 5.1.3 Detector

1511 Once the final state particle kinematics have been determined by NEUT, they
1512 are passed into the detector simulation. The near detectors, ND280 and INGRID,
1513 are simulated using a GEANT4 package [41, 167] to simulate the detector geom-
1514 etry, particle tracking, and energy deposition. The response of the detectors is
1515 simulated using the elecSim package [41].

1516 The far detector simulation is based upon the original Kamiokande experi-
1517 ment software which uses the GEANT3-based SKDETSIM [41, 168] package. This
1518 simulates the interactions of particles in the water as well as Cherenkov light
1519 production. The water quality and PMT calibration measurements detailed in
1520 subsection 3.1.2 are also used within this simulation to make accurate predictions
1521 of the detector response.

1522 Any event which generates optical photons that occurs in SK will be observed
1523 by the PMT array, where each PMT records the time and accumulated charge.
1524 This recorded information is shown in event displays similar to those illustrated
1525 in Figure 5.3 for simulated Monte Carlo events. To be useful for physics analyses,
1526 this series of PMT hit information needs to be reconstructed to determine the
1527 number and identity of particles and their kinematics (or track parameters): four-
1528 vertex, direction, and momentum. The reconstruction uses the fact that the charge
1529 and timing distribution of photons generated by a particular particle in an event is
1530 dependent upon its initial kinematics. Electron and muon rings are distinguished
1531 by their “fuzziness”. Muons are heavier and less affected by scattering or
1532 showering meaning they typically produce “crisp” rings. Electrons are more
1533 likely to interact via electromagnetic showering or scattering which results in
1534 larger variations of their direction from the initial direction. Consequently,
1535 electrons typically produce “fuzzier” rings compared to muons.

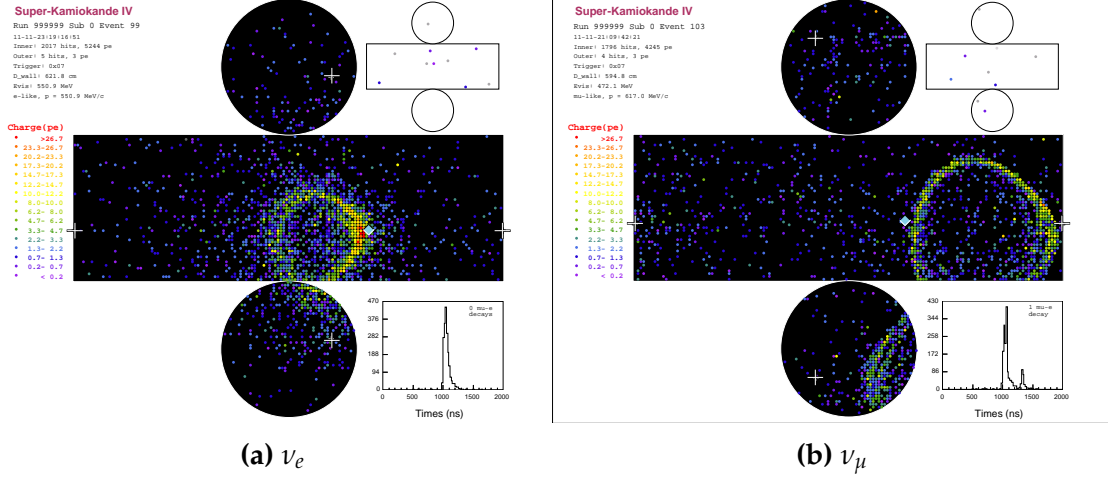


Figure 5.3: Event displays from Monte Carlo simulation at Super Kamiokande illustrating the “crisp” ring from a muon and the typically “fuzzy” electron ring. Each pixel represents a PMT and the color scheme denotes the accumulated charge deposited on that PMT. Figures taken from [169].

5.2 Event Reconstruction at SK

For the purposes of this analysis, the `fitQun` reconstruction algorithm [170] is utilised. Its core function is to compare a prediction of the accumulated charged and timing distribution from each PMT, generated for a particular particle identity and track parameters, to that observed in the neutrino event. It determines the preferred values by maximising a likelihood function (or minimising a log-likelihood function) which includes information from PMTs which were hit and those that were not hit. The `fitQun` algorithm is based on the key concepts of the MiniBooNE reconstruction algorithm [171].

The `fitQun` algorithm improves upon the previous `APFit` algorithm [172] which has been used for many previous SK analyses. `APFit` fits the vertex from timing information and then fits the direction of the particle from PMT hits within a 43 deg Cherenkov cone (assuming an ultra-relativistic particle) using a fitting estimator. A Hough transformation is used to find the radius of a ring (related to the momentum through Equation 3.2) as well as the number of rings contained within the event. The analysis presented here uses the `fitQun` algorithm as it improves both the accuracy of the fit parameters and the rejection of neutral

1553 current π^0 events as compared to APFit [173, 174].

1554 Any event in SK can consist of prompt (or primary) and decay (or secondary)
1555 particles. For example, a charged current muon neutrino interaction can gen-
1556 erate two particles that have the potential of generating Cherenkov photons
1557 (assuming the proton is below the Cherenkov threshold): the prompt muon,
1558 and the secondary decay-electron from the muon, approximately $2\mu\text{s}$ later. To
1559 reconstruct all particles within an event, it is divided into time clusters which are
1560 called “subevents”. Subevents after the primary subevent are considered to
1561 be decay electrons.

1562 The main steps of the `fitQun` reconstruction algorithm are:

- 1563 • **Vertex pre-fitting:** An estimate of the vertex is made using a goodness-of-fit
1564 metric based on PMT hit times
- 1565 • **Peak finding:** The initial time of each subevent is determined by clustering
1566 events by time residuals
- 1567 • **Single-ring fits:** Given the pre-fit vertex and estimated time of interaction,
1568 a maximum likelihood technique searches for a single particle generating
1569 light. Electron, muon, charged pion, and proton hypotheses are considered
- 1570 • **Multi-ring fits:** Seeded from the single-ring fits, hypotheses with multiple
1571 light-producing particles are considered using the same maximum likeli-
1572 hood technique. Electron-like or charged pion-like rings are added until
1573 the likelihood stops improving

1574 To find all the subevents in an event, a vertex goodness metric is calculated
1575 for some vertex position \vec{x} and time t ,

$$G(\vec{x}, t) = \sum_i^{\text{hit PMTs}} \exp \left(-\frac{1}{2} \left(\frac{T_{Res}^i(\vec{x}, t)}{\sigma} \right)^2 \right), \quad (5.1)$$

1576 where

$$T_{Res}^i(\vec{x}, t) = t^i - t - |R_{PMT}^i - \vec{x}| / c_n, \quad (5.2)$$

1577 is the residual hit time. It is the difference in time between the PMT hit time
 1578 t^i , of the i^{th} PMT, and the expected time of the PMT hit if the photon was at
 1579 the vertex. R_{PMT}^i is the position of the i^{th} PMT, c_n is the speed of light in water
 1580 and $\sigma = 4\text{ns}$ which is comparable to the time resolution of the PMT. When the
 1581 proposed fit values of time and vertex are close to the true values, $T_{Res}^i(\vec{x}, t)$ tends
 1582 to zero resulting in subevents appearing as spikes in the goodness metric. The
 1583 proposed fit vertex and time are grid-scanned, and the values which maximise
 1584 the goodness metric are selected as the “pre-fit vertex”. Whilst this predicts a
 1585 vertex for use in the clustering algorithm, the final vertex is fit using the higher-
 1586 precision maximum likelihood method described below.

1587 Once the pre-fit vertex has been determined, the goodness metric is scanned as
 1588 a function of t to determine the number of subevents. A peak-finding algorithm
 1589 is then used on the goodness metric, requiring the goodness metric to exceed
 1590 some threshold and drop below a reduced threshold before any subsequent
 1591 additional peaks are considered. The thresholds are set such that the rate of
 1592 false peak finding is minimised while still attaining good data to Monte Carlo
 1593 agreement. To improve performance, the pre-fit vertex for each delayed subevent
 1594 is re-calculated after PMT hits from the previous subevent are masked. This
 1595 improves the decay-electron tagging performance. Once all subevents have
 1596 been determined, the time window around each subevent is then defined by the
 1597 earliest and latest time which satisfies $-180 < T_{Res}^i < 800\text{ns}$. The subevents and
 1598 associated time windows are then used as seeds for further reconstruction.

1599 For a given subevent, the `fitQun` algorithm constructs a likelihood based on
 1600 the accumulated charge q_i and time information t_i from the i^{th} PMT,

$$L(\Gamma, \vec{\theta}) = \prod_j^{\text{unhit}} P_j(\text{unhit}|\Gamma, \vec{\theta}) \prod_i^{\text{hit}} \{1 - P_i(\text{unhit}|\Gamma, \vec{\theta})\} f_q(q_i|\Gamma, \vec{\theta}) f_t(t_i|\Gamma, \vec{\theta}). \quad (5.3)$$

1601 Where $\vec{\theta}$ defines the track parameters; vertex position, direction vector and
 1602 momenta, and Γ represents the particle hypothesis. $P_i(\text{unhit}|\Gamma, \vec{\theta})$ is the proba-
 1603 bility of the i^{th} tube to not register a hit given the track parameters and particle
 1604 hypothesis. The charge likelihood, $f_q(q_i|\Gamma, \vec{\theta})$, and time likelihood, $f_t(t_i|\Gamma, \vec{\theta})$,
 1605 represents the probability density function of observing charge q_i and time t_i on
 1606 the i^{th} PMT given the specified track parameters and particle hypothesis.

1607 The predicted charge is calculated based on contributions from both the
 1608 direct light and the scattered light. The direct light contribution is determined
 1609 based on the integration of the Cherenkov photon profile along the track. PMT
 1610 angular acceptance, water quality, and calibration measurements discussed in
 1611 subsection 3.1.2 are included to accurately predict the charge probability density
 1612 at each PMT. The scattered and reflected light is calculated in a similar way,
 1613 although it includes a scattering function that depends on the vertex of the
 1614 particle and the position of the PMT. The charge likelihood is calculated by
 1615 comparing the prediction to the observed charge in the PMT which is tuned
 1616 to the PMT simulation.

1617 The time likelihood is approximated to depend on the vertex \vec{x} , direction \vec{d} ,
 1618 and time t of the track as well as the particle hypothesis. The expected time
 1619 for PMT hits is calculated by assuming unscattered photons being emitted from
 1620 the midpoint of the track, S_{mid} ,

$$t_{\text{exp}}^i = t + S_{\text{mid}}/c + |R_{\text{PMT}}^i - \vec{x} - S_{\text{mid}}\vec{d}|/c_n, \quad (5.4)$$

1621 where c is the speed of light in a vacuum. The time likelihood is then expressed
 1622 in terms of the residual difference between the PMT hit time and the expected
 1623 hit time, $t_{\text{Res}}^i = t^i - t_{\text{exp}}^i$. The particle hypothesis and momentum also affect the
 1624 Cherenkov photon distribution. These parameters modify the shape of the time
 1625 likelihood density since in reality not all photons are emitted at the midpoint of
 1626 the track. As with the charge likelihood, the contributions from both the direct
 1627 and scattered light to the time likelihood density are calculated separately, which
 1628 are both calculated from particle gun Monte Carlo studies.

The track parameters and particle identity which maximise $L(\Gamma, \vec{\theta})$ are defined as the best-fit parameters. In practice MINUIT [175] is used to minimise the value of $-\ln L(\Gamma, \vec{\theta})$. The `fitQun` algorithm considers an electron-like, muon-like, and charged pion-like hypothesis for events with a single final state particle, denoted “single-ring events”. The particle’s identity is determined by taking the ratio of the likelihood of each of the hypotheses. For instance, electrons and muons are distinguished by considering the value of $\ln(L(e, \vec{\theta}_e)/L(\mu, \vec{\theta}_\mu))$ in comparison to the reconstructed momentum of the electron hypothesis, as illustrated by Figure 5.4. The coefficients of the discriminator between electron-like and muon-like events are determined from Monte Carlo studies [170]. Similar distributions exist for distinguishing electron-like events from π^0 -like events, and muon-like events from pion-like events. The cuts are defined as,

$$\begin{aligned} \text{Electron/Muon} : & \ln(L_e/L_\mu) > 0.2 \times p_e^{rec} [\text{MeV}], \\ \text{Electron}/\pi^0 : & \ln(L_e/L_{\pi^0}) < 175 - 0.875 \times m_{\gamma\gamma} [\text{MeV}], \\ \text{Muon/Pion} : & \ln(L_\mu/L_{\pi^\pm}) < 0.15 \times p_\mu^{rec} [\text{MeV}], \end{aligned} \quad (5.5)$$

as taken from [176], where p_e^{rec} and p_μ^{rec} are the reconstructed momentum of the single-ring electron and muon fits, respectively. $m_{\gamma\gamma}$ represents the reconstructed invariant mass of the two photons emitted from π^0 decay. Typically, the distance between a particular entry in these two-dimensional distributions and the cut-line is termed the PID parameter and is illustrated in Figure 5.5.

The `fitQun` algorithm also considers a π^0 hypothesis. To do this, it performs a fit looking for two standard electron-hypothesis tracks which point to the same four-vertex. This assumes the electron tracks are generated from photon-conversion so the electron tracks actually appear offset from the proposed π^0 vertex. For these fits, the conversion length, direction, and momentum of each photon are also considered as track parameters which are then fit in the same methodology as the standard single-ring hypotheses.

Whilst lower energy events are predominantly single-ring events, higher energy neutrino events can generate final states with multiple particles which

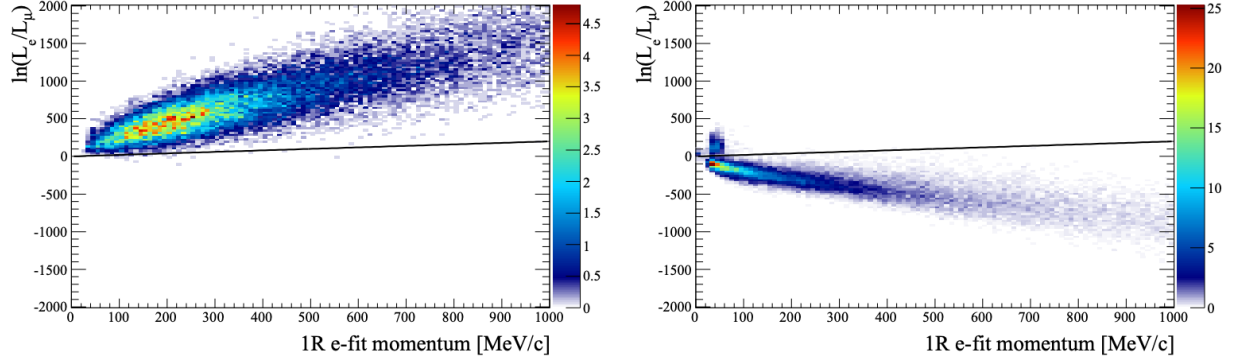


Figure 5.4: The difference of the electron-like and muon-like log-likelihood compared to the reconstructed single-ring fit momentum for atmospheric ν_e (left) and ν_μ (right) samples. The black line represents the cut used to discriminate electron-like and muon-like events, with coefficients obtained from Monte Carlo studies. Figures from [170].

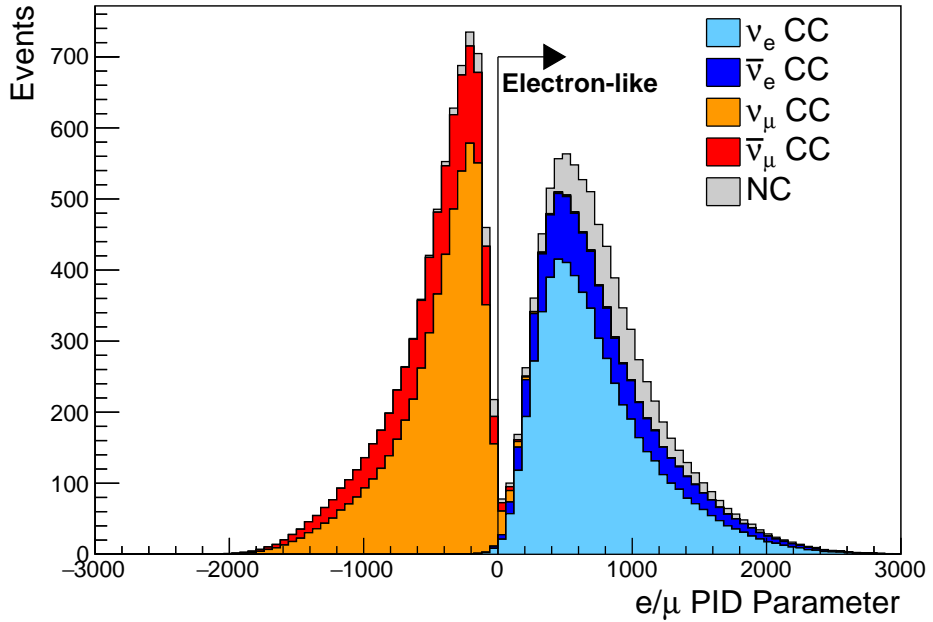


Figure 5.5: The electron/muon PID separation parameter for all sub-GeV single-ring events in SK-IV. The charged current (CC) component is broken down in four flavours of neutrino (ν_μ , $\bar{\nu}_\mu$, ν_e and $\bar{\nu}_e$). Events with positive values of the parameter are determined to be electron-like.

1655 generate Cherenkov photons. These “multi-ring” hypotheses are also considered
 1656 in the `fitQun` algorithm. When calculating the charge likelihood density, the
 1657 predicted charge associated with each ring is calculated separately and then
 1658 summed to calculate the total accumulated charge on each PMT. Similarly, the
 1659 time likelihood for the multi-ring hypothesis is calculated assuming each ring

is independent. Each track is time-ordered based on the time of flight from the center of the track to the PMT and the direct light from any ring incident on the PMT is assumed to arrive before any scattered light. To reduce computational resource usage, the multi-ring fits only consider electron-like and charged pion-like rings as the pion fit can be used as a proxy for a muon fit due to their similar mass. Due to the pions ability to interact through the strong force, they are more likely to hard-scatter. That means a single charged pion can produce multiple rings in different directions. There is an additional freedom, the fraction of kinetic energy lost in a single ring segment, which is added into the `fitQun` pion fit to cover this difference. Pion and muon rings are indistinguishable when this fraction tends to unity.

Multi-ring fits proceed by proposing another ring to the previous fit and then fitting the parameters in the method described above. Typically, multi-ring fits have the largest likelihood because of the additional degrees of freedom introduced. A likelihood value is calculated for the n -ring and $(n + 1)$ -ring hypotheses, where the additional ring is only included if the likelihood value is above 9.35, based on Monte Carlo studies in [177].

5.2.1 Validation of Reconstruction in SK-V

Understanding how the modelling of the detector conditions and stability effects the reconstruction is critical for ensuring accurate measurements. It is important to note that the detector systematics used in the 2020 T2K-only [72] oscillation analysis are determined using data-to-Monte Carlo comparisons of the SK-IV data [178]. Due to tank-open maintenance occurring between SK-IV and SK-V, the dark rate of each PMT was observed to increase in SK-V due to light exposure for a significant time during the repairs. This increase can be seen in Figure 5.6. Run-10 of the T2K experiment was conducted in the SK-V period, so the consistency of SK-IV and SK-V data needs to be studied to determine whether the SK-IV-defined systematics can be applied to the run-10 data. Consequently, the author of this thesis assessed the quality of `fitQun` event reconstruction for SK-V data.

This comparison study was performed using the stopping muon data set for both the SK-IV and SK-V periods. This data sample is used due to the high rate of interactions ($O(200)$ events per hour) as well as having similar energies to muons from CCQE ν_μ interactions from beam interactions. The rate of cosmic muons does depend on the solar activity cycle [179] but has been neglected in this comparison study. This is because the shape of the distributions is most important for the purposes of being compared to the detector systematics. The SK-IV and SK-V data samples consist of 2398.42 and 626.719 hours of data which equates to 686k and 192k events respectively. These samples do not correspond to the full data sets of either period but do contain enough events to be systematics limited rather than statistics limited.

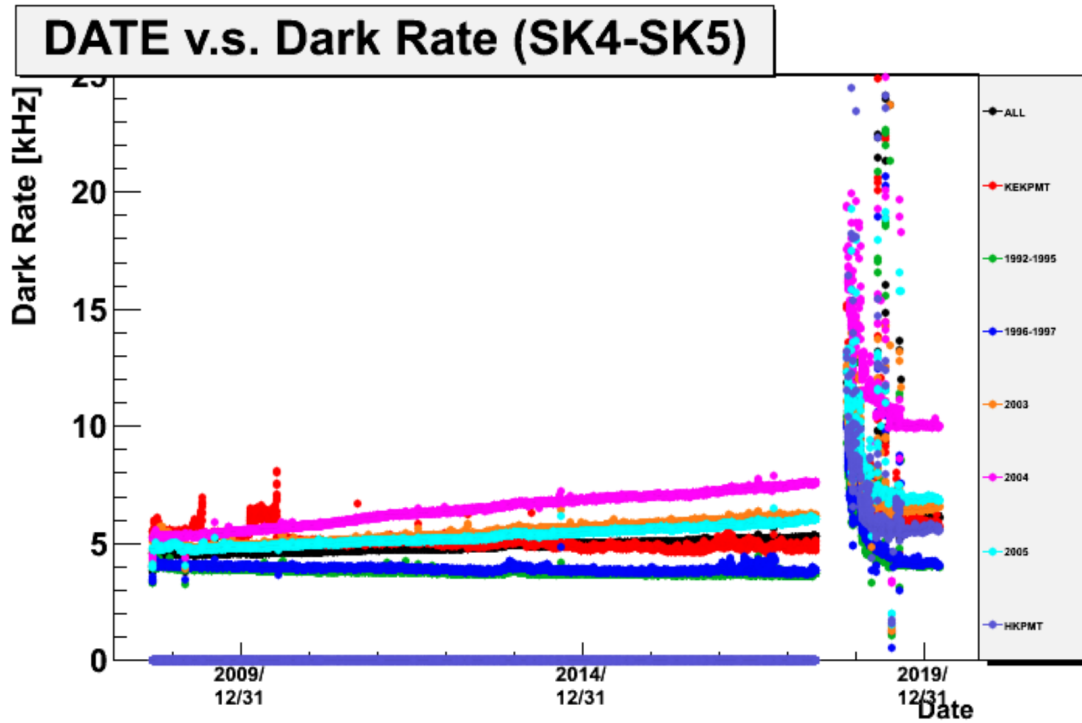


Figure 5.6: The variation of the measured dark rate as a function of date, broken down by PMT type. The SK-IV and SK-V periods span September 2008 to May 2018 and January 2019 to July 2020, respectively. The break in measurement in 2018 corresponds to the period of tank repair and refurbishment. Figure adapted from [178].

The predicted charge calculated in the `fitQun` algorithm includes a contribution from the photoelectron emission due to dark noise. Therefore, the increase

in the SK-V dark rate needs to be accounted for. In practice, the average dark rate in each SK period is calculated and used as an input in the reconstruction. This is calculated by averaging the dark rate per run for each period separately, using the calibration measurements detailed in subsection 3.1.2. The average dark rate from SK-IV and SK-V were found to be 4.57kHz and 6.30kHz, respectively. The charges associated with the muon and decay electron subevents are illustrated in Figure 5.7. The photoelectron emission from dark noise is more significant for events that have lower energy. This is because this contribution becomes more comparable to the number of photoelectrons emitted from incident photons in lower-energy events. This behaviour is observed in the data, where the charge deposited by the muon subevent is mostly unaffected by the increase in dark rate, whilst the charge associated with the decay-electron is clearly affected.

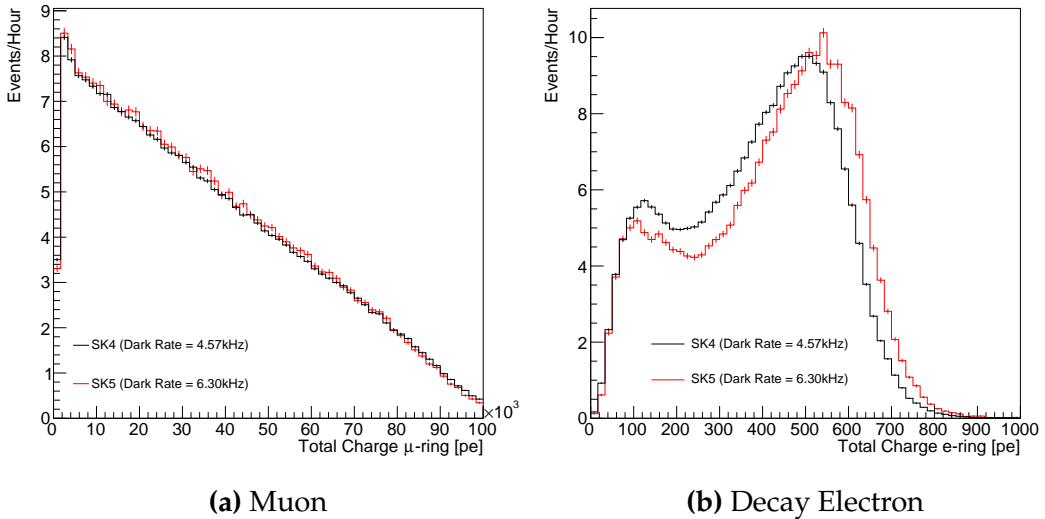


Figure 5.7: Comparison of the measured raw charge deposited per event from the stopping muon data samples between SK-IV (Blue) and SK-V (Red), split by the primary muon subevent (left) and the associated decay electron subevent (right).

The energy scale systematic is estimated from data-to-Monte Carlo differences in the stopping muon sample in [58] and found to be 2.1%. To determine the consistency of SK-IV and SK-V with respect to the energy scale systematic, the muon momentum distribution is compared between the two SK periods. As the total number of Cherenkov photons is integrated across the track length,

₁₇₁₉ the reconstructed momentum divided by track length (or range) is compared
₁₇₂₀ between SK-IV and SK-V as illustrated in Figure 5.8.

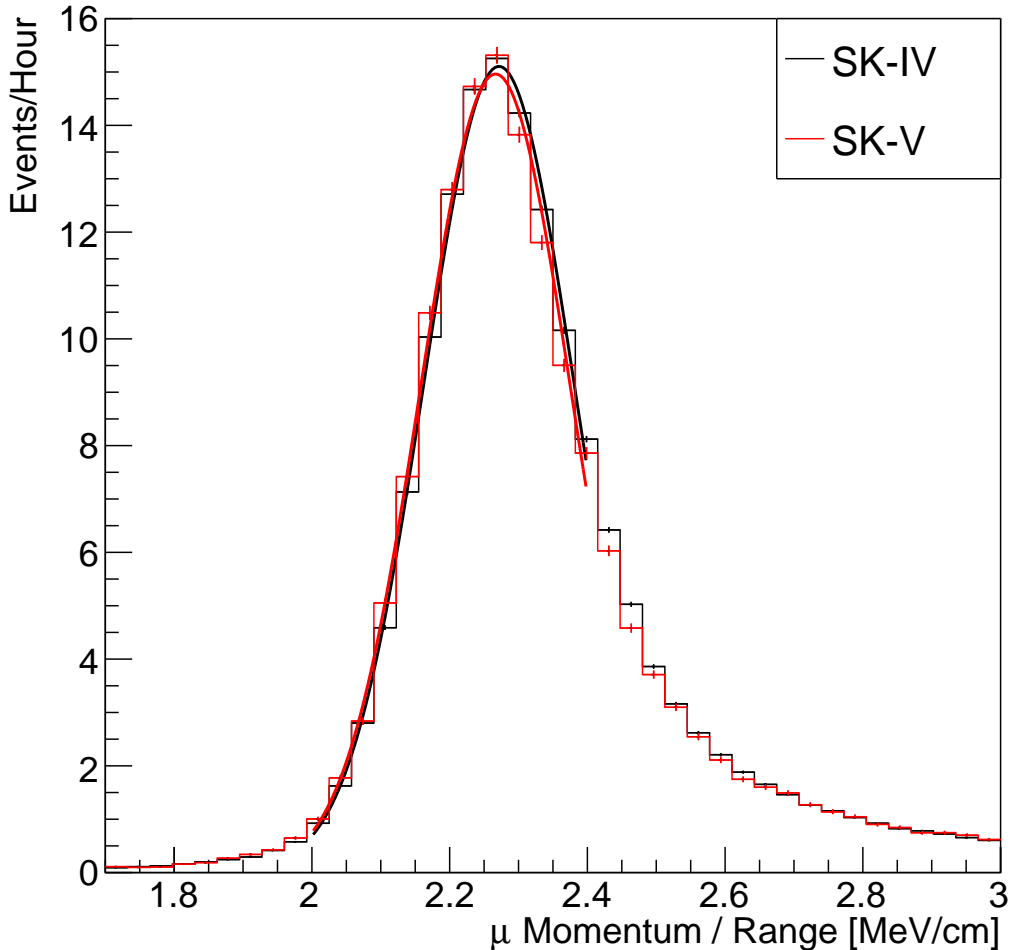


Figure 5.8: The distribution of the reconstructed momentum from the muon ring divided by the distance between the reconstructed muon and decay electron vertices as found in the stopping muon data sets of SK-IV (Black) and SK-IV (Red). Only events with one tagged decay electron are considered. A Gaussian fit is considered in the range $[2.0, 2.4]\text{MeV}/\text{cm}$ and illustrated as the solid curve.

₁₇₂₁ The consistency between these muon distributions has been computed in two
₁₇₂₂ ways. Firstly, a Gaussian is fit to the peak of each distribution separately, whose
₁₇₂₃ mean is found to be $(2.272 \pm 0.003)\text{MeV}/\text{cm}$ and $(2.267 \pm 0.006)\text{MeV}/\text{cm}$ for SK-
₁₇₂₄ IV and SK-V respectively. The ratio of these is equal to 1.002 ± 0.003 . The means of
₁₇₂₅ the Gaussian fits are consistent with the expected stopping power of a minimum

ionising muon for a target material (water) with $Z/A \sim 0.5$ [180]. The second consistency check is performed by introducing a nuisance parameter, α , which modifies the SK-V distribution. The value of α which minimises the χ^2 value between the SK-IV and SK-V is determined by scanning across a range of values. This is repeated by applying the nuisance parameter as both a multiplicative factor and an additive shift. The χ^2 distributions for different values of α is illustrated in Figure 5.9. The values which minimise the χ^2 are found to be 0.0052 and 1.0024 for the additive and multiplicative implementations, respectively. No evidence of shifts larger than the 2.1% uncertainty on the energy scale systematic has been found in the reconstructed momentum distribution of SK-IV and SK-V.

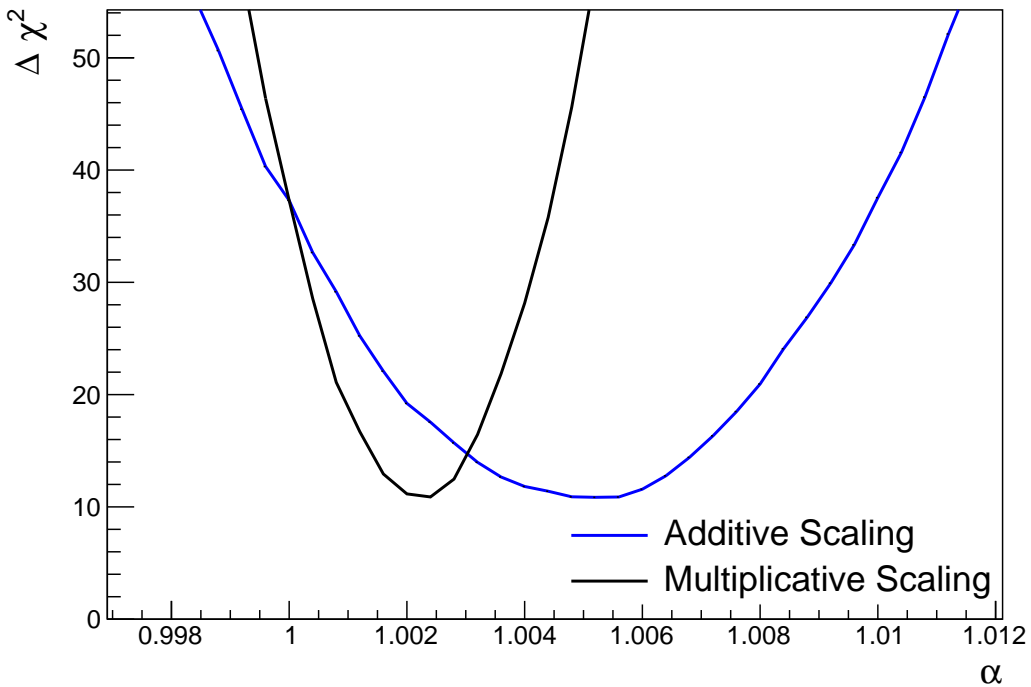


Figure 5.9: The χ^2 difference between the SK-IV and SK-V reconstructed muon momentum divided by range when the SK-V is modified by the scaling parameter α . Both additive (Blue) and multiplicative (Black) scaling factors have been considered. In practice, the additive scaling factor actually uses the value of $(\alpha - 1.0)$ but is illustrated like this so the results can be shown on the same axis range.

5.3 Event Reduction at SK

1736 In normal data-taking operations, the SK detector observes many background
1738 events alongside the beam and atmospheric neutrino signal events of physics
1739 interest for this thesis. Cosmic ray muons and flasher events, which are the spon-
1740 taneous discharge of a given PMT, contribute the largest amount of background
1741 events in the energy range relevant to this thesis. Therefore the data recorded
1742 is reduced with the aim of removing these background events. The reduction
1743 process is detailed in [53, 84] and briefly summarised below.

1744 Atmospheric neutrino events observed in the SK detector are categorised
1745 into three different types of samples: fully contained (FC), partially contained
1746 (PC) and up-going muon (Up- μ), using PMT hit signatures in the inner and
1747 outer detector (ID and OD, respectively). To identify FC neutrino events, it is
1748 required that the neutrino interacts inside the fiducial volume of the ID and that
1749 no significant OD activity is observed. For this analysis, an event is defined to be
1750 in the fiducial volume provided the event vertex is at least 0.5m away from the
1751 ID walls. PC events have the same ID requirements but can have a larger signal
1752 present inside the OD. Typically, only high energy muons from ν_μ interactions can
1753 penetrate the ID wall. The Up- μ sample contains events where muons are created
1754 from neutrino interactions in the OD water or rock below the tank. They then
1755 propagate upwards through the detector. Downward-going muons generated
1756 from neutrino interactions above the tank are neglected because of the difficulty
1757 in separating their signature from the cosmic muon shower background. The
1758 sample categories are visually depicted in Figure 5.10.

1759 Based on the event characteristics, as defined by the `fitQun` event reconstruc-
1760 tion software, the FC events are categorised by

- 1761 • **Visible Energy:** equal to the sum of the reconstructed kinetic energy of
1762 particles above the Cerenkov threshold for all rings present in the event.
1763 The purpose is to separate events into sub-GeV and multi-GeV categories.

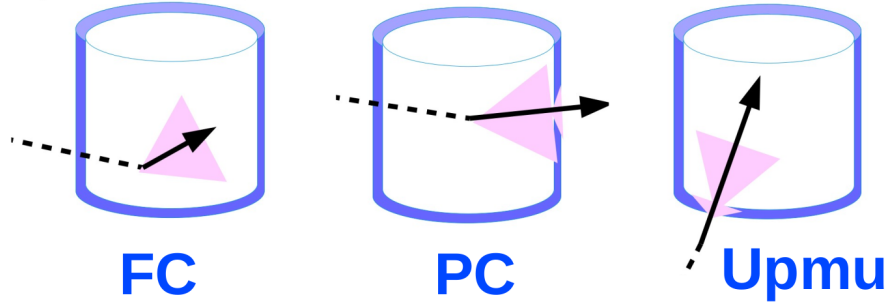


Figure 5.10: A depiction of the topology patterns for fully-contained (FC), partially-contained (PC), and up-going muon ($\text{Up-}\mu$) samples included in this analysis.

1764 • **Number of observed Cerenkov rings.** The purpose is to separate single-
 1765 ring and multi-ring events, where single-ring events predominantly consist
 1766 of quasi-elastic interactions and multi-ring events are typically resonant
 1767 pion production or deep inelastic scattering events.

1768 • **Particle identification parameter of the most energetic ring:** A value de-
 1769 termined from the maximum likelihood value based on `fitQun`'s electron,
 1770 muon, or pion hypothesis. The purpose is to separate electron-like and
 1771 muon-like events.

1772 • **Number of decay electrons:** The purpose is to separate quasi-elastic events
 1773 (which have one decay electron emitted from the muon decay) and resonant
 1774 pion production events (which have two decay electrons emitted from the
 1775 muon and pion).

1776 The PC and Up- μ categories are broken down into “through-going” and
 1777 “stopping” samples depending on whether the muon leaves the detector. This is
 1778 because the PC stopping events deposit the entire energy of the interaction into
 1779 the detector, resulting in better reconstruction. The energy of events that exit the
 1780 detector has to be estimated, with a typically worse resolution, which introduces
 1781 much larger systematic uncertainties. Through-going Up- μ samples are further
 1782 broken down by whether any hadronic showering was observed in the event
 1783 which typically indicates DIS interactions. The expected neutrino energy for the
 1784 different categories is given in Figure 5.11. FC sub-GeV and multi-GeV events

1785 peak around 0.7GeV and 3GeV respectively, with slightly different peak energies
1786 for ν_e and ν_μ oscillation channels. PC and Up- μ are almost entirely comprised
1787 of ν_μ events and peak around 7GeV and 100GeV, respectively.

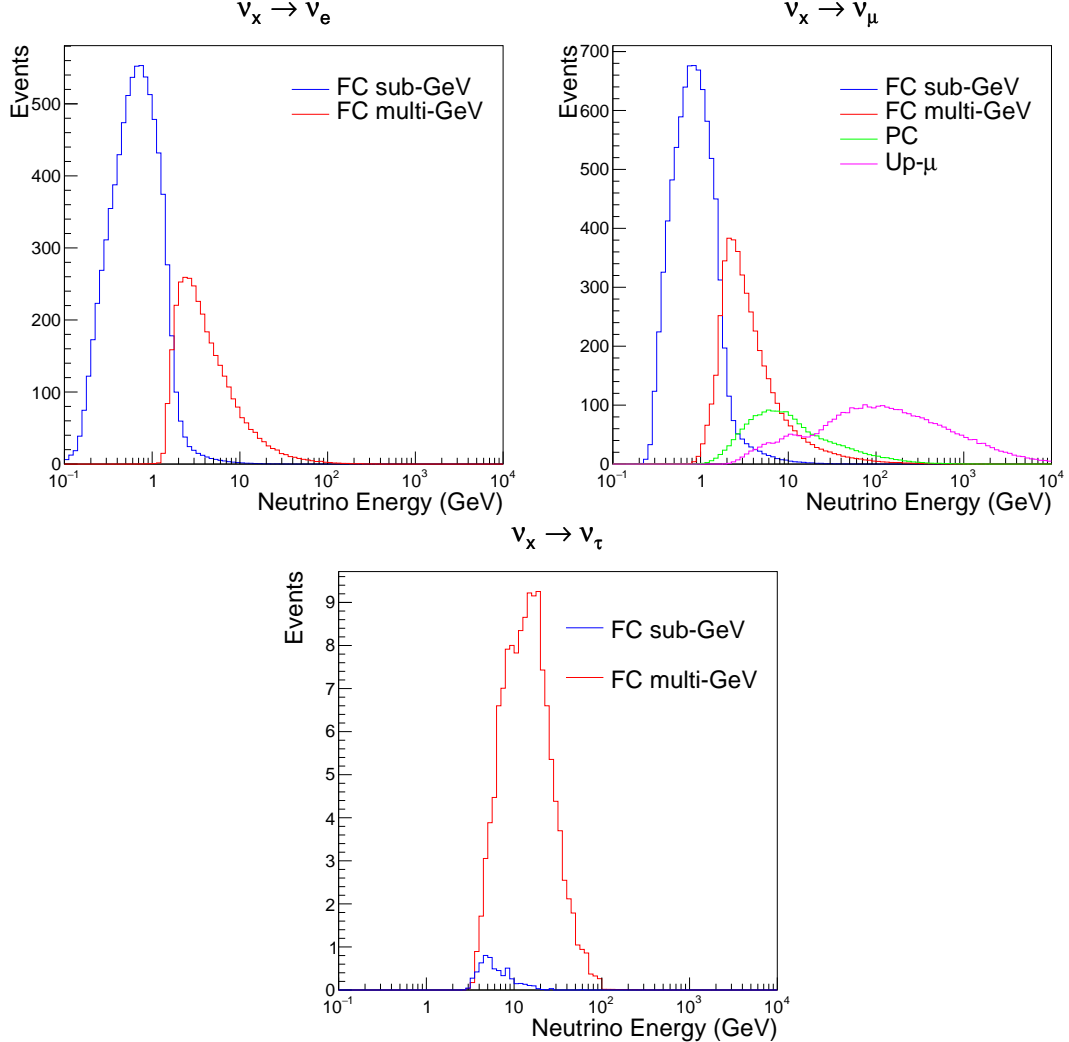


Figure 5.11: The predicted neutrino flux of the fully contained (FC) sub-GeV and multi-GeV, partially contained (PC), and upward-going muon (Up- μ) events. The prediction is broken down by the $\nu_x \rightarrow \nu_e$ prediction (top left), $\nu_x \rightarrow \nu_\mu$ prediction (top right) and $\nu_x \rightarrow \nu_\tau$ prediction (bottom). ν_x represents the flavours of neutrinos produced in the cosmic ray showers (electron and muon). Asimov A oscillation parameters are assumed (given in Table 2.2).

1788 The first two steps in the FC reconstruction remove the majority of cosmic
1789 ray muons by requiring a significant amount of ID activity compared to that
1790 measured in the OD. Events that pass this cut are typically very high momentum
1791 muons or events that leave very little activity in the OD. Consequently, a third

reduction step is then applied to select cosmic-ray muons that pass the initial reduction step. A purpose-built cosmic muon fitter is used to determine the entrance (or exit) position of the muon and a cut is applied to OD activity contained within 8m of this position. Flasher events are removed in the fourth reduction step which is based on the close proximity of PMT hits surrounding the PMT producing the flash. Events that pass all these reduction steps are reconstructed with the APFit algorithm. The fifth step of the reduction uses information from the more precise fitter to repeat the previous two steps with tighter cuts. Muons below the Cherenkov threshold can not generate optical photons in the ID but the associated decay electron can due to its lower mass. These are the types of events targeted in the fifth reduction step. The final cuts require the event vertex to be within the fiducial volume (0.5m from the wall although the nominal distance is 2.0m), visible energy $E_{vis} > 30\text{MeV}$ and fewer than 16 hits within the higher energy OD cluster. The culmination of the fully contained reduction results in 8.09 events/day in the nominal fiducial volume [81]. The uncertainty in the reconstruction is calculated by comparing Monte Carlo prediction to data. The largest discrepancy is found to be 1.3% in the fourth reduction step.

The PC and Up- μ events are processed through their own reduction processes detailed in [53]. Both of these samples are reconstructed with the APFit algorithm rather than `fiTQun`. This is because the efficiency of reconstructing events that leave the detector has not been sufficiently studied for reliable systematic uncertainties with `fiTQun`. The PC and Up- μ samples acquire events at approximately 0.66 and 1.44 events/day.

Beam neutrinos events undergo the same reduction steps as FC events and are then subject to further cuts [181]. The GPS system that links the timing between the beam facility and SK needs to be operating correctly and there should be no activity within the detector in the previous $100\mu\text{s}$ before the trigger. The events then need to triggered between $-2\mu\text{s}$ and $10\mu\text{s}$ of the expected spill timing.

1821 The beam neutrino samples are not split by visible energy since their energy
 1822 range is smaller than the atmospheric neutrino events. Following the T2K
 1823 analysis in [72], only single-ring beam neutrino events are considered. Similar to
 1824 atmospheric event selection, the number of decay electrons is used as a proxy for
 1825 distinguishing CCQE and CCRES events. The expected neutrino energy, broken
 1826 down by the number of decay electrons, is given in Figure 5.12.

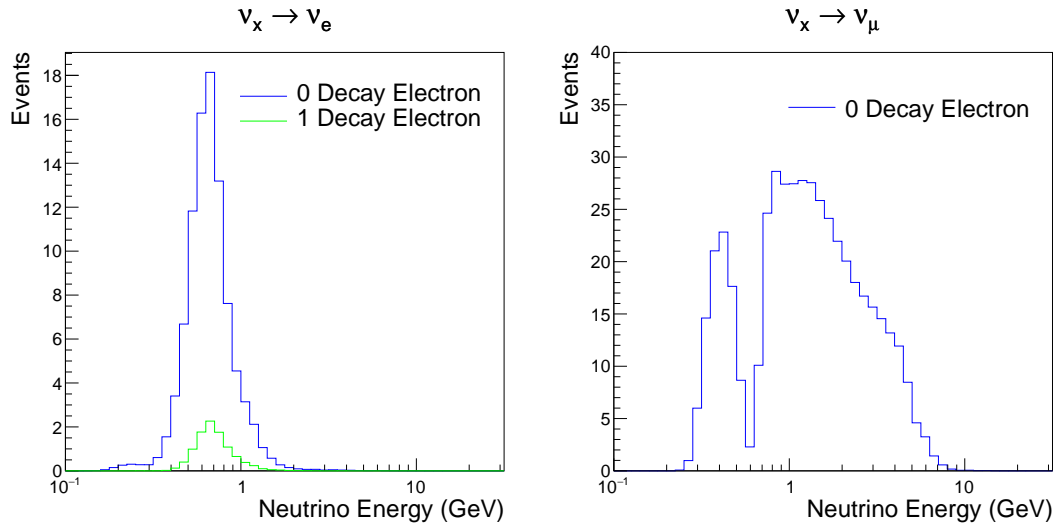


Figure 5.12: The predicted flux of beam neutrinos, as a function of neutrino energy. The predictions are broken down by the number of decay electrons associated with the particular events. Asimov A oscillation parameters are assumed (given in Table 2.2).

6

1827

1828

Sample Selections and Systematics

1829 The oscillation analysis presented within this thesis is built upon a simultaneous
1830 fit to atmospheric samples at SK, neutrino beam samples in the near detector,
1831 and beam samples at SK. This is the first simultaneous oscillation analysis of
1832 beam and atmospheric samples supported by the T2K and SK collaborations.
1833 Notably, the author of this thesis has been responsible for the building and
1834 developing the MaCh3 framework to support all sets of samples simultaneously.
1835 The definitions of the samples are documented in section 6.1, section 6.2, and
1836 section 6.3, respectively. The data collected and used within this analysis is
1837 detailed in Table 6.1. The near and far detector data corresponds to T2K runs
1838 2-9 and runs 1-10, respectively. The accumulated POT and beam power for runs
1839 1 – 10 are illustrated in Figure 6.1.

Data Type	Total
Near Detector FHC	1.15×10^{21} POT
Near Detector RHC	8.34×10^{20} POT
Far Detector FHC	1.97×10^{21} POT
Far Detector RHC	1.63×10^{21} POT
Atmospheric SK-IV	3244.4 days

Table 6.1: The amount of data collected in each detector used within this analysis. The data collected at the near and far detector, for both neutrino beam (FHC) and antineutrino beam (RHC), is measured as the number of protons on target (POT).

1840 The difference in POT recorded at the near and far detector is due to the
 1841 difference in downtime. The SK detector is very stable with almost 100% of
 1842 data recorded during beam operation. Due to various technical and operational
 1843 issues, the downtime of the near detector is significantly higher due to its more
 1844 complex design and operating requirements.

1845 The systematic parameters invoked within the flux, detector, and interaction
 1846 models used within this analysis are documented in section 6.4. The standard
 1847 configuration of the joint beam and atmospheric data fit utilises far detector sys-
 1848 tematics provided in the official inputs from the two experiments. Additionally,
 1849 a correlated detector model which fits the parameters used in sample selections
 1850 to data has been developed and documented in subsection 6.4.5.

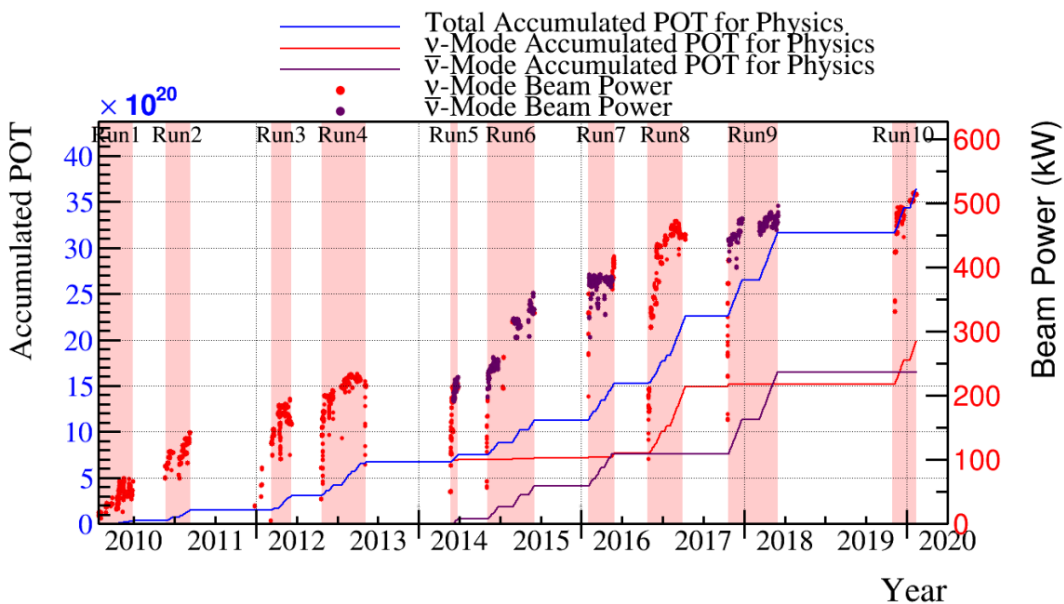


Figure 6.1: The accumulated beam data, measured as the number of protons on target (POT). The total data (blue) is given which comprises of the neutrino beam (red) and antineutrino (purple) components. The beam power for neutrino and antineutrino beams is given as the markers using the same colour scheme. The timescale runs from Run 1 which started in January 2010 until Run 10 which ended in February 2020. The ratio of accumulated data in neutrino and antineutrino beam is 54.7% : 45.3%.

1851 6.1 Atmospheric Samples

1852 The atmospheric event selection follows the official SK-IV analysis presented
1853 in [84] and is documented below. The Monte Carlo prediction used within this
1854 analysis corresponds to 500 years worth of neutrino events, which is scaled down
1855 to match the SK-IV livetime of 3244.4 days.

1856 The fully contained (FC), partially contained (PC), and upward going muon
1857 events ($\text{up-}\mu$) which pass the reduction cuts discussed in section 5.3 are further
1858 broken down into different samples based on reconstruction information. This
1859 section details the samples used within this oscillation analysis, alongside the
1860 chosen binning.

1861 FC events are first separated by the visible energy deposited within the
1862 detector. This is calculated as the sum of the reconstructed kinetic energy
1863 above the Cherenkov threshold for all rings present in the event. Events are
1864 separated by whether they were above or below $E_{\text{vis}} = 1.33\text{GeV}$. This separates
1865 “subGeV” and “multiGeV” events. Typically, lower energy events consist of
1866 charged current quasi-elastic (CCQE) interactions which are better understood
1867 and simpler to reconstruct resulting in smaller systematic uncertainties. Events
1868 are further separated by the number of rings associated with the event due to
1869 similar reasoning. As the oscillation probability is dependant upon the flavour
1870 of neutrino, electron and muon events are separated using a similar likelihood
1871 method to that discussed in section 5.2. To reduce computational resources
1872 required for the reconstruction, only electron and pion hypotheses are considered
1873 so this separation cut depends on the ratio of the electron to pion likelihoods,
1874 $\log(L_e/L_\pi)$. Finally, the number of decay electrons is used to classify events.
1875 Charged current resonant pion production (CCRES) interactions generate a final-
1876 state pion. This can decay, mostly likely through a muon, into a decay electron.
1877 Therefore any electron-like event with one decay electron or muon-like event
1878 with two decay electrons was most likely produced by a CCRES interaction.
1879 Consequently, the number of decay electrons can be used to distinguish CCQE

1880 and CCRES interaction modes. Ultimately, FC subGeV events are separated
1881 into the samples listed in Table 6.2.

Sample Name	Description
SubGeV- <i>e</i> like-0dcy	Single ring <i>e</i> -like events with zero decay electrons
SubGeV- <i>e</i> like-1dcy	Single ring <i>e</i> -like events with one or more decay electrons
SubGeV- <i>μ</i> like-0dcy	Single ring <i>μ</i> -like events with zero decay electrons
SubGeV- <i>μ</i> like-1dcy	Single ring <i>μ</i> -like events with one decay electrons
SubGeV- <i>μ</i> like-2dcy	Single ring <i>μ</i> -like events with two or more decay electrons
SubGeV- <i>π</i> 0like	Two <i>e</i> -like ring events with zero decay electrons and reconstructed π^0 mass $85 \leq m_{\pi^0} < 215$ MeV

Table 6.2: The fully contained subGeV samples, defined as events with visible energy $E_{vis} < 1.33$ GeV, used within this oscillation analysis.

1882 In addition to the cuts discussed above, multiGeV samples also have addi-
1883 tional cuts to separate samples which target neutrino and antineutrino events.
1884 As discussed in section 2.5, the matter resonance only occurs for neutrinos in the
1885 normal hierarchy and antineutrinos in the inverted mass hierarchy. Therefore,
1886 having flavour-enriched samples aids in the determination of the mass hierarchy.
1887 For a CCRES interaction,

$$\begin{aligned}
 \bar{\nu}_e + N &\rightarrow e^+ + N' + \pi^-, \\
 \nu_e + N &\rightarrow e^- + N' + \pi^+ \\
 &\quad \downarrow \mu^+ + \nu_\mu \\
 &\quad \downarrow e^+ + \nu_e + \bar{\nu}_\mu.
 \end{aligned} \tag{6.1}$$

1888 The π^- emitted from a $\bar{\nu}_e$ interaction is more likely to be captured by an
1889 oxygen nucleus than the π^+ from ν_e interactions [182]. These pions then decay,
1890 mostly through muons, to electrons. Therefore the number of tagged decay
1891 electrons associated with an event gives an indication of whether the interaction
1892 was due to a neutrino or antineutrino: zero for $\bar{\nu}_e$ events, and one for ν_e events.
1893 The ability to separate neutrino from antineutrino events is illustrated in Table 6.4,
1894 where the MultiGeV-*e*like-nue has 78% purity of CC neutrino interactions with
1895 only 7% antineutrino background, the rest consisting of NC backgrounds.

1896 The number of decay electrons discriminator works reasonably well for single-
 1897 ring events. However, this is not the case for multi-ring events. A multiGeV
 1898 multiring electron-like (MME) likelihood cut was introduced in [183, 184]. This
 1899 is a two-stage likelihood selection cut. Four observables are used in the first
 1900 likelihood cut to distinguish $CC\nu_e$ and $CC\bar{\nu}_e$ events from background:

- 1901 • The number of decay electrons
 1902 • The maximum distance between the vertex of the neutrino and the decay
 1903 electrons
 1904 • The energy deposited by the highest energy ring
 1905 • The particle identification of that highest energy ring

1906 Background events consist of $CC\nu_\mu$ and NC interactions. Typically, the
 1907 majority of the energy in these background events is carried by the hadronic
 1908 system. Additionally, muons tend to travel further than the pions from $CC\nu_e$
 1909 before decaying. Thus, the parameters used within the likelihood cut target these
 1910 typical background interaction kinematics.

Sample Name	Description
MultiGeV-elike-nue	Single ring e -like events with zero decay electrons
MultiGeV-elike-nuebar	Single ring e -like events with one or more decay electrons
MultiGeV-mulike	Single ring μ -like events
MultiRing-elike-nue	Two or more ring events with leading energy e -like ring and passed both MME and $\nu/\bar{\nu}$ separation cuts
MultiRing-elike-nuebar	Two or more ring events with leading energy e -like ring and passed MME and failed $\nu/\bar{\nu}$ separation cuts
MultiRing-mulike	Two or more ring events with leading energy μ -like ring and only requires $E_{vis} > 0.6\text{GeV}$
MultiRing-Other1	Two or more ring events with leading energy e -like ring and failed the MME likelihood cut

Table 6.3: The fully contained multiGeV samples used within this oscillation analysis. Both the sample name and description are given.

1911 Neutrino and antineutrino events are then separated by a second likelihood
 1912 method ($\nu/\bar{\nu}$ separation) detailed in [58]. This uses the number of decay electrons,

1913 the number of reconstructed rings, and the event’s transverse momentum. The
1914 last two parameters are used because higher-energy samples tend to have more
1915 pions produced above the Cherenkov threshold which results in more rings
1916 compared to an antineutrino interaction. Furthermore, the angular distribution
1917 also tends to be more forward peaked in antineutrino interactions as compared
1918 to neutrino interactions [84]. These FC multiGeV sample definitions are de-
1919 tailed in Table 6.3.

1920 The PC and up- μ samples are split by the amount of energy deposited within
1921 the outer detector, into “stopping” and “through-going” samples. If an event
1922 leaves the detector, the energy it takes with it has to be estimated which increases
1923 the systematic uncertainty compared to events entirely contained within the
1924 inner detector. This estimation is particularly poor at high energies, thus the
1925 up- μ through-going events are not binned in reconstructed momentum. The
1926 through-going up- μ are further separated by the presence of any electromagnetic
1927 showering in the event, as the assumption of non-showering muon does not give
1928 reliable reconstruction for these types of events [53]. In total, 13 FC, 2 PC, and
1929 3 up- μ atmospheric samples are included within this analysis.

1930 The atmospheric samples are binned in direct observables: reconstructed
1931 lepton momentum and direction, as given by Table 6.5. The distribution of
1932 the reconstructed lepton momentum (for samples that only have one bin in
1933 reconstructed zenith angle) and reconstructed direction for each atmospheric
1934 sample used within this analysis is illustrated in Figure 6.2.

1935 The reconstructed lepton momemtum, illustrated by interaction mode break-
1936 down, of some representative atmospheric samples is given in Figure 6.3. The
1937 equivalent distributions of all atmospheric samples used within this analy-
1938 sis can be found in [185]. The low energy samples tend to be dominated by
1939 the interaction mode they target (CCQE for SubGeV-elike-0dcy and CC1 π for
1940 SubGeV-elike-1dcy samples). The higher energy samples include much more
1941 CCOther interactions, especially at larger reconstructed lepton momentum.

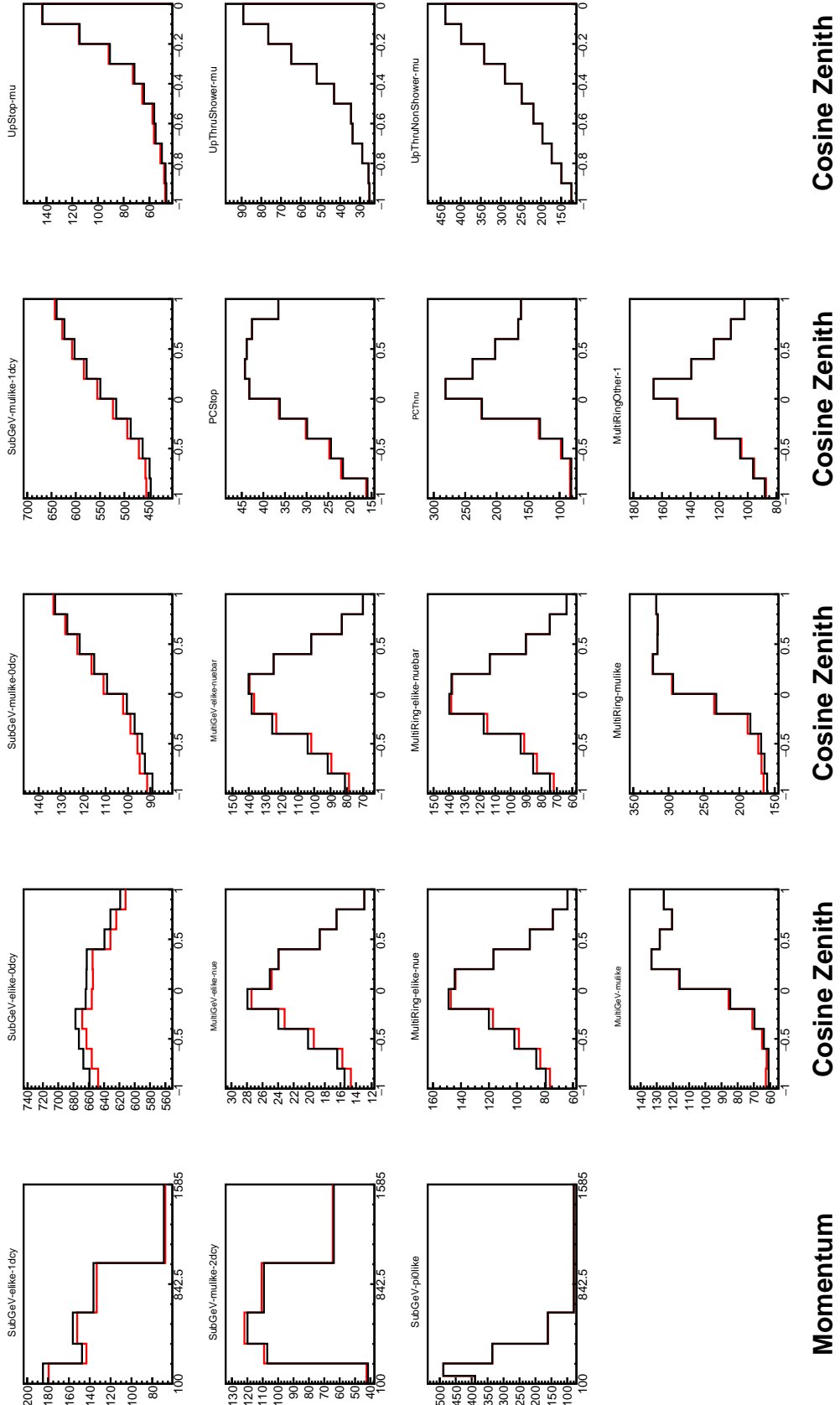


Figure 6.2: Comparison of the SK-IV atmospheric samples between predictions made with the CP-violating Asimov A (Black) and CP-conserving Asimov B (Red) oscillation parameter sets (given in Table 2.2). The subGeV samples CCRES and π^0 -like samples are given in their reconstructed lepton momentum. All other samples are presented in their reconstructed zenith angle projection.

Sample	$CC\nu_e$	$CC\bar{\nu}_e$	$CC(\nu_\mu + \bar{\nu}_\mu)$	$CC(\nu_\tau + \bar{\nu}_\tau)$	NC
SubGeV- <i>elike</i> -0dcy	72.17	23.3	0.724	0.033	3.77
SubGeV- <i>elike</i> -1dcy	86.81	1.773	7.002	0.062	4.351
SubGeV- <i>mulike</i> -0dcy	1.003	0.380	90.07	0.036	8.511
SubGeV- <i>mulike</i> -1dcy	0.023	0.	98.46	0.029	1.484
SubGeV- <i>mulike</i> -2dcy	0.012	0.	99.25	0.030	0.711
SubGeV- <i>pi0like</i>	6.923	2.368	0.928	0.011	89.77
MultiGeV- <i>elike</i> -nue	78.18	7.041	3.439	1.886	9.451
MultiGeV- <i>elike</i> -nuebar	56.68	37.81	0.174	0.614	4.718
MultiGeV- <i>mulike</i>	0.024	0.005	99.67	0.245	0.058
MultiRing- <i>elike</i> -nue	59.32	12.39	4.906	3.385	20
MultiRing- <i>elike</i> -nuebar	52.39	31.03	1.854	1.585	13.14
MultiRing- <i>mulike</i>	0.673	0.080	97.33	0.342	1.578
MultiRingOther-1	27.98	2.366	34.93	4.946	29.78
PCStop	8.216	3.118	84.45	0.	4.214
PCThru	0.564	0.207	98.65	0.	0.576
UpStop-mu	0.829	0.370	98.51	0.	0.289
UpThruNonShower-mu	0.206	0.073	99.62	0.	0.103
UpThruShower-mu	0.128	0.054	99.69	0.	0.132

Table 6.4: The purity of each atmospheric sample used within this analysis, broken down by charged current (CC) and neutral current (NC) interactions and which neutrino flavour interacted within the detector. Each row sums to 100% by definition. Asimov A oscillation parameter sets are assumed (given in Table 2.2). Electron neutrino and antineutrino events are separated to illustrate the ability of the separation likelihood cuts used within the multiGeV and multiring sample selections.

Sample	$\cos(\theta_Z)$ Bins	Momentum Bin Edges ($\log_{10}(P)$ MeV)
SubGeV- <i>elike</i> -0dcy	10	2.0, 2.4, 2.6, 2.8, 3.0, 3.2
SubGeV- <i>elike</i> -1dcy	1	2.0, 2.4, 2.6, 2.8, 3.0, 3.2
SubGeV- <i>mulike</i> -0dcy	10	2.0, 2.4, 2.6, 2.8, 3.0, 3.2
SubGeV- <i>mulike</i> -1dcy	10	2.0, 2.4, 2.6, 2.8, 3.0, 3.2
SubGeV- <i>mulike</i> -2dcy	1	2.0, 2.4, 2.6, 2.8, 3.0, 3.2
SubGeV- <i>pi0like</i>	1	2.0, 2.2, 2.4, 2.6, 2.8, 3.2
MultiGeV- <i>elike</i> -nue	10	3.0, 3.4, 3.7, 4.0, 5.0
MultiGeV- <i>elike</i> -nuebar	10	3.0, 3.4, 3.7, 4.0, 5.0
MultiGeV- <i>mulike</i>	10	3.0, 3.4, 5.0
MultiRing- <i>elike</i> -nue	10	3.0, 3.4, 3.7, 5.0
MultiRing- <i>elike</i> -nuebar	10	3.0, 3.4, 3.7, 5.0
MultiRing- <i>mulike</i>	10	2.0, 3.124, 3.4, 3.7, 5.0
MultiRing- <i>Other1</i>	10	3.0, 3.4, 3.7, 4.0, 5.0
PC-Stop	10	2.0, 3.4, 5.0
PC-Through	10	2.0, 3.124, 3.4, 3.7, 5.0
Upmu-Stop	10	3.2, 3.4, 3.7, 8.0
Upmu-Through-Showering	10	2.0, 8.0
Upmu-Through-NonShowering	10	2.0, 8.0

Table 6.5: The reconstructed cosine zenith and lepton momentum binning assigned to the atmospheric samples. The “ $\cos(\theta_Z)$ Bins” column illustrates the number of bins uniformly distributed over the $-1.0 \leq \cos(\theta_Z) \leq 1.0$ region for fully and partially contained samples and $-1.0 \leq \cos(\theta_Z) \leq 0.0$ region for up- μ samples.

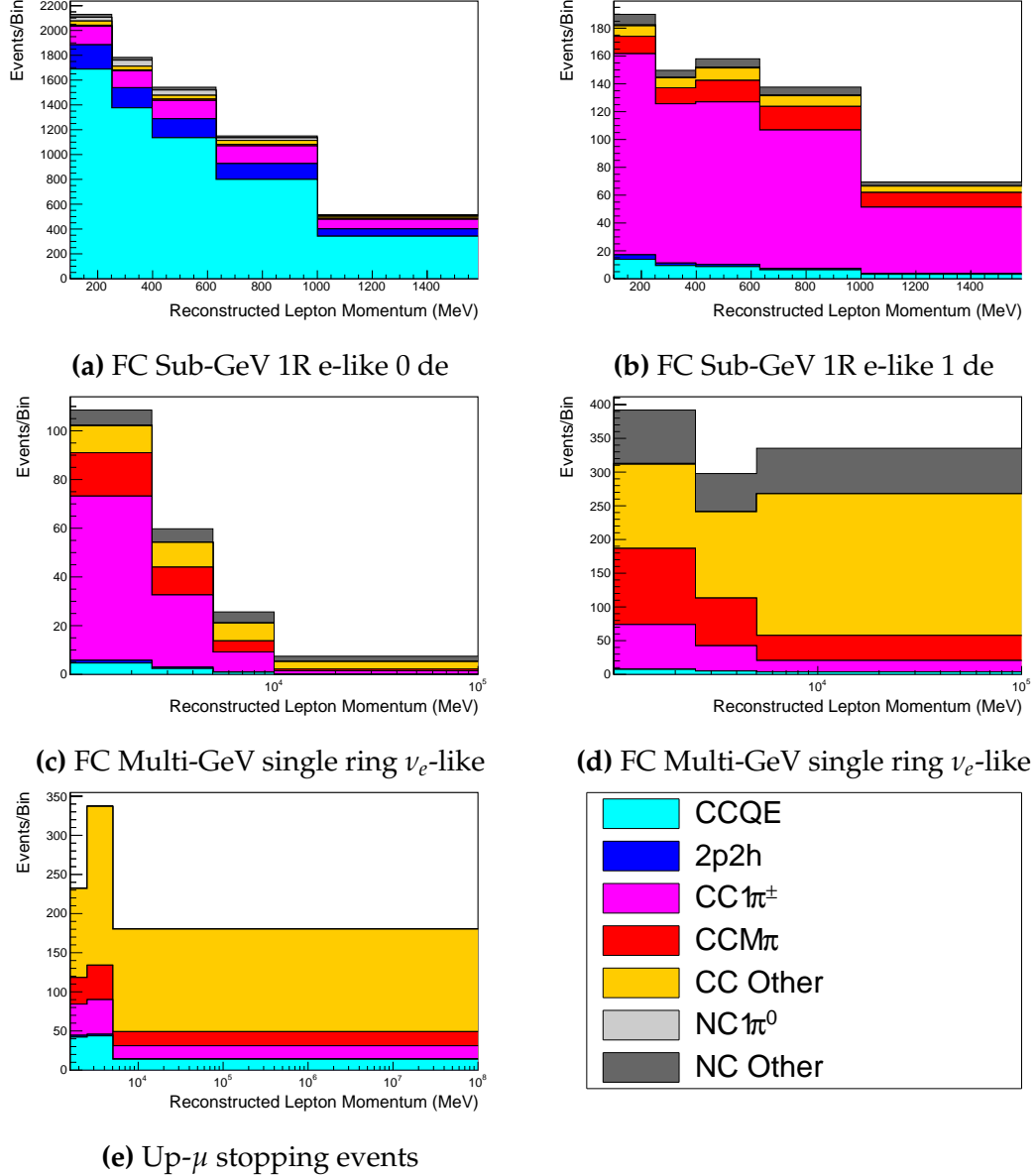


Figure 6.3: Breakdown by interaction mode of some representative atmospheric samples used within this analysis, illustrated as a function of reconstructed lepton momentum. The binning is provided in Table 6.5. Asimov A oscillation parameters are used to generate these plots. The interaction mode breakdown of all atmospheric samples used within this analysis can be found in [185].

6.2 Near Detector Beam Samples

The near detector sample selections are documented in detail within [186] and summarised below. Samples are selected based upon which of the two Fine Grained Detectors (FGD) the vertex is reconstructed in as well as the operating mode of the beam: FHC or RHC. Wrong-sign neutrino background samples are considered in the RHC mode in order to add additional constraints on model parameters. Samples from the wrong-sign component of the FHC beam mode are not included as they are statistically insignificant compared to those samples already listed.

The reconstruction algorithm uses a clustering algorithm to group hits within the TPC. It then adds information from the upstream FGD to form a track that passes through both sub-detectors. In FHC(RHC), the highest momentum negative(positive) curvature track is defined as the muon candidate. Before being assigned a sample, these candidate muon events must pass CC-inclusive cuts, as defined in [187]:

- Event Timing: The DAQ must be operational and the event must occur within the expected beam time window consistent with the beam spill
- TPC Requirement: The muon-candidate track path must intercept one or more TPCs
- Fiducial volume: The event must originate from within the fiducial volume defined in [188]
- Upstream Background: Remove events that have muon tracks that originate upstream of the FGDs by requiring no high-momentum tracks within 150mm upstream of the candidate vertex. Additionally, events that occur within the downstream FGD are vetoed if a secondary track starts within the upstream FGD

- Broken track removal: All candidates where the muon candidate is broken in two are removed

- Muon PID: Measurements of dE/dx in a TPC are used to distinguish muon-like events, from electron-like or proton-like, using a likelihood cut

In addition to these cuts, RHC neutrino events also have to undergo the following cuts to aid in the separation of neutrino and antineutrino [189]:

- TPC Requirement: The track path must intercept TPC2

- Positive Track: The highest momentum track must have a positive reconstructed charge

- TPC1 Veto: Remove any events originating upstream of TPC1

Once all CC-inclusive events have been determined, they are further split by pion multiplicity: CC0 π , CC1 π , and CCOther. Pions in the TPCs are selected by requiring a second track to be observed, which is separate from the muon track and is in the same beam spill window and sub-detector. The number of FGD pions is equal to the number of Michel electrons which were tagged within the same sub-detector and spill window. If this value is equal to zero, the number of FGD pions is equivalent to the number of pion-like tracks which have dE/dx measurements consistent with the pion hypothesis. The pion tracks from both FGD and TPC events are required to have a vertex consistent with that of the muon candidate. The Michel electron tagging is preferential as a delayed Michel is almost always a pion meaning this cut has a higher purity [187, 190], whereas a track in the FGD that is consistent with a pion could be another particle resulting in a lower purity. Michel electrons are neglected in the TPC as the pions very rarely stop due to the low density.

CC0 π , CC1 π , and CCOther samples are defined with the following cuts:

- ν_μ CC0 π Selection: No electrons in TPC and no charged pions or decay electrons within the TPC or FGD

- 1995 • ν_μ **CC1 π Selection:** Exactly one charged pion in either the TPC or FGD
- 1996 • ν_μ **CCOther Selection:** All events which are not classified into the above
- 1997 two selections

1998 Counting the three selections for each FGD in FHC and RHC running, includ-

1999 ing the wrong-sign background in RHC, 18 near detector samples are used within

2000 this analysis. These samples are binned in reconstructed lepton momentum

2001 (illustrated in Figure 6.4) and direction with respect to the beam. The binning

2002 is chosen such that each event has at least 20 Monte Carlo events in each bin

2003 [188]. This is to ensure that the bins are coarse enough to ensure the reduction

2004 of statistical errors, whilst also being fine enough to sample the high-resolution

2005 peak regions. The exact binning is detailed in [188].

2006 6.3 Far Detector Beam Samples

2007 The beam neutrino events which occur at the SK detector, which pass the

2008 reduction cuts detailed in section 5.3, are separated based on whether the beam

2009 was operating in FHC or RHC mode. The events are then separated into three

2010 samples: electron-like (1Re), muon-like (1R μ), and CC1 π^+ -like (1Re1de) which

2011 are observed as electron-like events with an associated decay electron [178].

2012 As discussed in section 6.1, positively charged pions emitted from neutrino

2013 interactions are more likely to produce decay electrons than negatively charged

2014 pions. Consequently, the CC1 π^+ -like sample is only selected when the beam is

2015 operating in FHC mode. Therefore, five beam samples measured at SK are

2016 used in this analysis.

2017 The fiducial volume definition for beam samples is slightly different from that

2018 used for the atmospheric samples. It uses both the distance to the closest wall

2019 (dWall) and the distance to the wall along the trajectory of the particle (toWall).

2020 This allows events that originate close to the wall but are facing into the tank to be

2021 included within the analysis, which would have otherwise been removed. These

2022 additional events are beneficial for a statistics-limited experiment. The exact

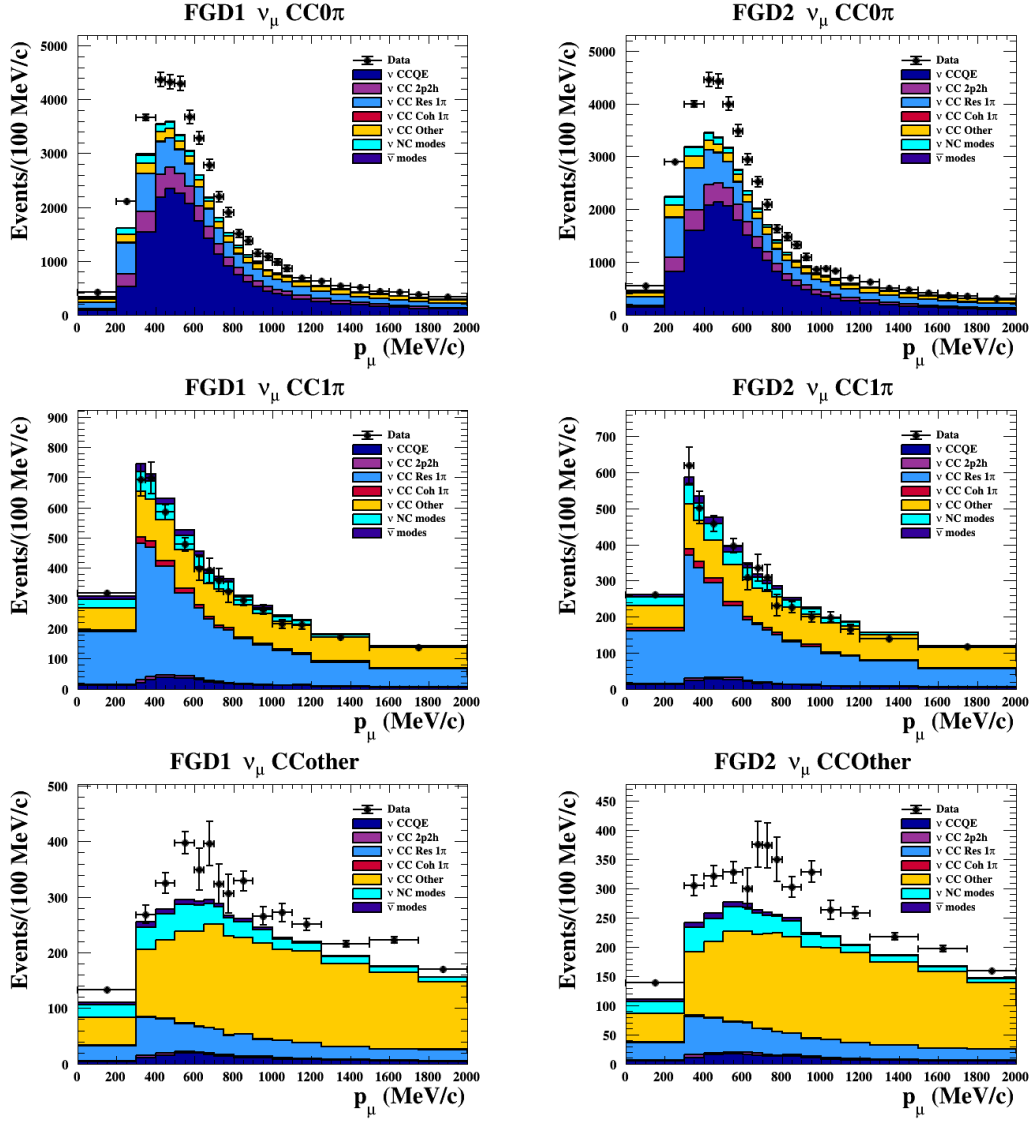


Figure 6.4: The nominal Monte Carlo predictions compared to data for the FGD1 and FGD2 samples in neutrino beam mode, broken down into the $CC\nu_\mu 0\pi$, $CC\nu_\mu 1\pi$ and $CC\nu_\mu$ Other categories. Figures taken from [186].

2023 cut values for both `dWall` and `tWall` are different for each of the three types of
 2024 sample and are optimised based on T2K sensitivity to δ_{CP} [176, 191]. They are:

2025 **1Re event selection** For an event to be classified as a 1Re-like, the event must sat-
 2026 isfy:

- 2027
 - Fully-contained and have $dWall > 80\text{cm}$ and $tWall > 170\text{cm}$
 - Total of one ring which is reconstructed as electron-like with reconstructed

2029 momentum $P_e > 100\text{MeV}$

2030 • Zero decay electrons are associated with the event

2031 • Passes π^0 rejection cut discussed in section 5.2

2032 The zero decay electron cut removes non-CCQE interactions and the π^0
 2033 rejection cut is designed to remove neutral current π^0 background events which
 2034 can be easily reconstructed as 1Re-like events.

2035 The zero decay electron cut removes non-CCQE interactions and the π^0
 2036 rejection cut is designed to remove neutral current π^0 background events which
 2037 can be easily reconstructed as 1Re-like events.

2038 **CC1 π^+ event selection** This event selection is very similar to that of the 1Re
 2039 sample. The only differences are that the dWall and toWall criteria are changed
 2040 to $> 50\text{cm}$ and $> 270\text{cm}$, respectively, and exactly one decay electron is required
 2041 from the π^+ decay.

2042 **1R μ event selection** A 1R μ -like event is determined by the following cuts:

2043 • Fully-contained and have $\text{dWall} > 50\text{cm}$ and $\text{toWall} > 250\text{cm}$

2044 • Total of one ring which is reconstructed as muon-like with reconstructed
 2045 momentum $P_\mu > 200\text{MeV}$

2046 • Fewer than two decay electrons are associated with the event

2047 • Passes π^+ rejection cut discussed in section 5.2

2048 All of these samples are binned in reconstructed neutrino energy. This is
 2049 possible under a particular interaction mode assumption, as the direction from
 2050 the source is known extremely well. For the 1Re-like and 1R μ -like samples,

$$E_\nu^{rec} = \frac{(M_N - V_{nuc})E_l - m_l^2/2 + M_N V_{nuc} - V_{nuc}^2/2 + (M_P^2 + M_N^2)/2}{M_N - V_{nuc} - E_l + P_l \cos(\theta_{beam})}. \quad (6.2)$$

2051 Where M_N , M_P and m_l are the masses of the neutron, proton and outgoing
 2052 lepton, respectively. $V_{nuc} = 27\text{MeV}$ is the binding energy of the oxygen nucleus
 2053 [178], θ_{beam} is the angle between the beam and the direction of the outgoing
 2054 lepton, and E_l and P_l are the energy and momentum of that outgoing lepton.

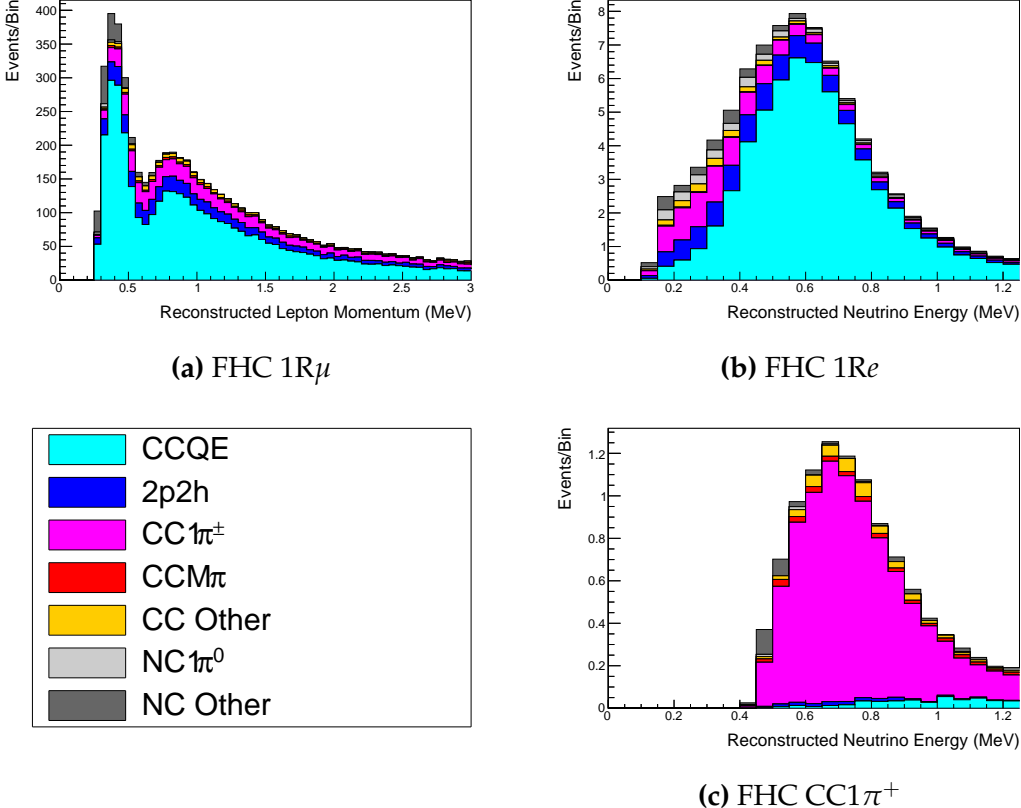


Figure 6.5: The reconstructed neutrino energy, as defined by Equation 6.2 and Equation 6.3, for the 1R μ -like, 1Re-like, and CC1 π^+ -like samples. The AsimovA oscillation parameters are assumed (given in Table 2.2). These samples are the FHC mode samples. For ease of viewing, the 1R μ sample only shows the $0 \leq E_\nu^{rec} < 3.0\text{GeV}$ but the binning extends to 30.0GeV .

2055 The reconstructed neutrino energy of the CC1 π^+ -like events also accounts
 2056 for the delta resonance produced within the interaction,

$$E_\nu^{rec} = \frac{2M_N E_l + M_{\Delta^{++}}^2 - M_N^2 - m_l^2}{2(M_N - E_l + P_l \cos(\theta_{beam}))}. \quad (6.3)$$

2057 Where $M_{\Delta^{++}}$ is the mass of the delta baryon. Binding energy effects are not
 2058 considered as a two-body process, with the delta baryon, is assumed. This follows
 2059 the T2K oscillation analysis presented in [72], although recent developments of

2060 the interaction model in the latest T2K oscillation analysis do include effects
2061 from binding energy in this calculation [192].

2062 The reconstructed neutrino energy for the FHC samples is illustrated in
2063 Figure 6.5. As expected, the $1R\mu$ -like and $1Re$ -like samples are heavily dominated
2064 by CCQE interactions, with smaller contributions from $2p2h$ meson exchange and
2065 resonant pion production interactions. The $CC1\pi^+$ -like sample predominantly
2066 consists of charged current resonant pion production interactions. The $1Re$ -like
2067 and $CC1\pi^+$ -like samples are also binned by the angle between the neutrino beam
2068 and the reconstructed lepton momentum. This is to aid in charged current and
2069 neutral current separation, as indicated in Figure 6.6. This is because the neutral
2070 current backgrounds are predominantly due to π^0 -decays, which decay into two
2071 γ rays. The opening angle of which (alongside the different final state kinematics)
2072 can produce a slightly broader angular distribution compared to the final state
2073 particles originating from charged current ν_e interactions.

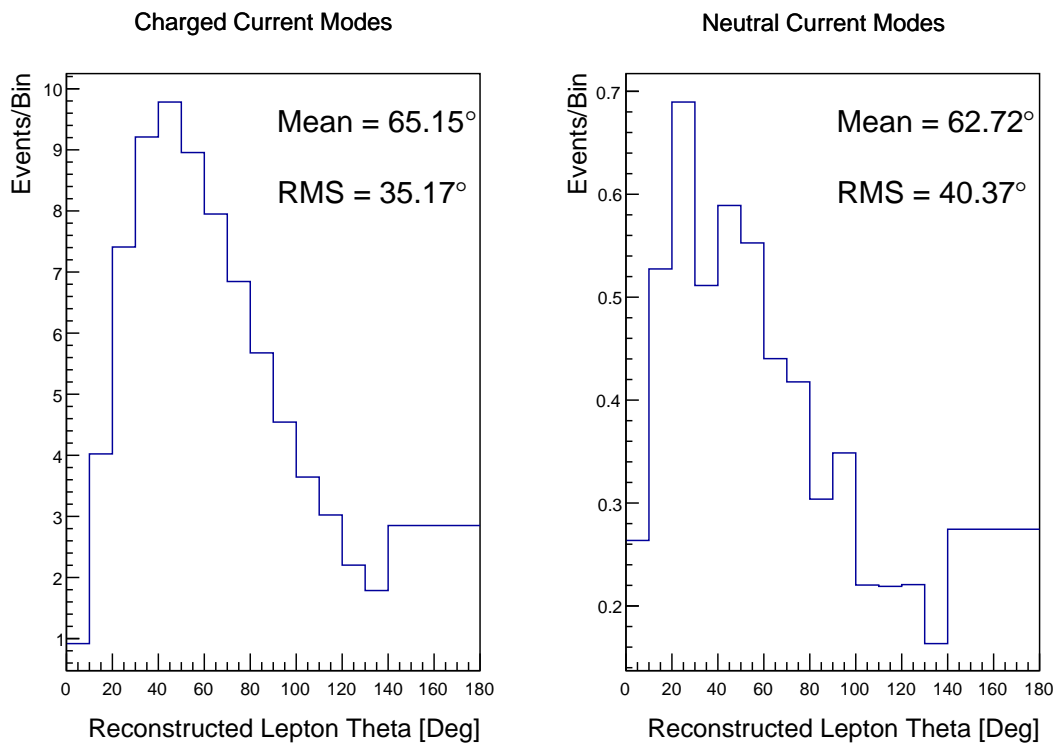


Figure 6.6: The distribution of the angle between the neutrino beam direction and the reconstructed final state lepton, for the FHC 1Re-like sample. The distribution is broken down by neutrino interaction mode into charged current (left) and neutral current (right) components. Asimov A oscillation parameter sets are assumed (given in Table 2.2). The RMS of the charged and neutral current plots are 35.17° and 40.37° , respectively.

2074 6.4 Systematic Uncertainties

2075 The systematic model parameters for this analysis are split into groups, or blocks,
2076 depending on their purpose. They consist of flux uncertainties, neutrino-matter
2077 interaction systematics, and detector efficiencies. There are also uncertainties on
2078 the oscillation parameters to which this analysis is not sensitive, namely Δm_{21}^2
2079 and $\sin^2(\theta_{12})$. These oscillation parameter uncertainties are taken from the 2020
2080 PDG measurements [73]. As described in chapter 4, each model parameter used
2081 within this analysis requires a prior uncertainty. This is provided via separate
2082 covariance matrices for each block. The covariance matrices can include prior
2083 correlations between parameters within a single block, but the separate treatment
2084 means prior correlations can not be included for parameters in different groups.
2085 Some parameters in these models have no reasonably motivated uncertainties
2086 and are assigned flat priors which do not modify the likelihood penalty. In
2087 practice, these flat prior parameters are actually assigned a Gaussian with a
2088 very large width to ensure the covariance matrix is positive definite. They are
2089 then checked at run time to determine if they contribute to the likelihood. The
2090 flux, neutrino interaction, and detector modeling simulations have already been
2091 discussed in section 5.1 and section 5.2. The uncertainties invoked within each
2092 of these models are described below.

2093 6.4.1 Beam Flux

2094 The neutrino beam flux systematics are based upon the uncertainty in the mod-
2095 eling of the components of the beam simulation. This includes the model of
2096 hadron productions and reinteractions, the shape, intensity, and alignment of
2097 the beam with respect to the target, and the uniformity of the magnetic field
2098 produced by the horn, alongside other effects. The uncertainty, as a function
2099 of neutrino energy, is illustrated in Figure 6.7 which includes a depiction of
2100 the total uncertainty as well as the contribution from individual components.
2101 The uncertainty around the peak of the energy distribution ($E_\nu \sim 0.6\text{GeV}$) is

2102 dominated by uncertainties in the beam profile and alignment. Outside of this
2103 region, uncertainties on hadron production dominate the error.

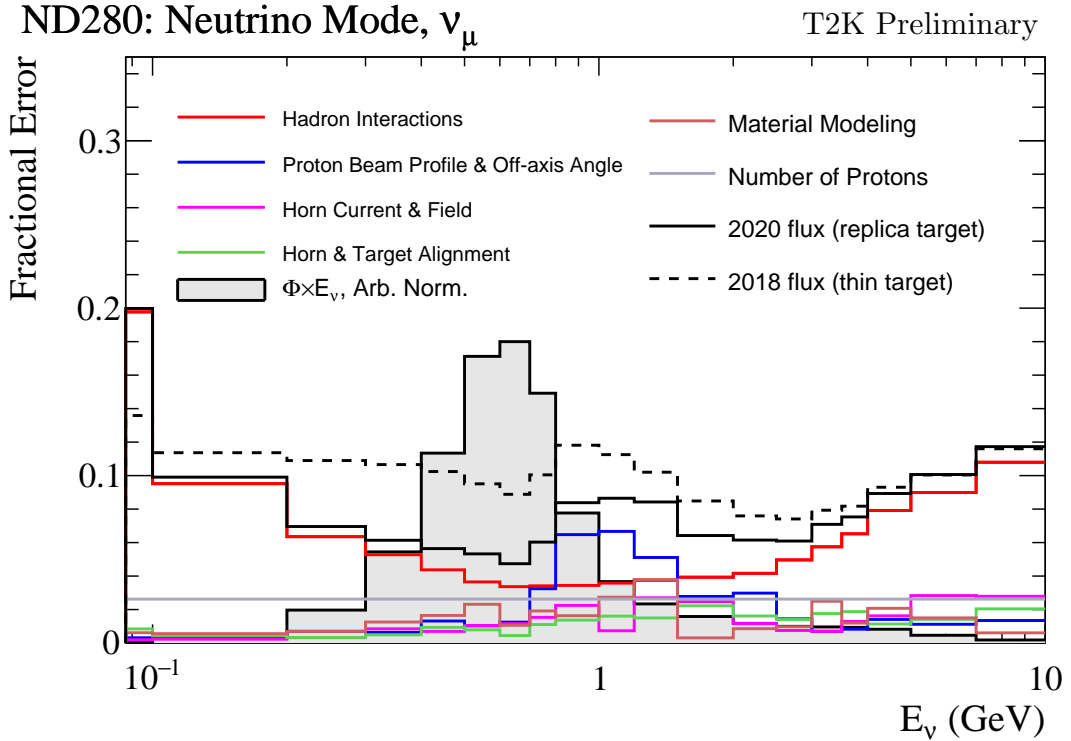


Figure 6.7: The total uncertainty evaluated on the near detector ν_μ flux prediction constrained by the replica-target data, illustrated as a function of neutrino energy. The solid(dashed) line indicates the uncertainty used within this analysis(the T2K 2018 analysis [193]). The solid histogram indicates the neutrino flux as a function of energy. Figure taken from [194].

2104 The beam flux uncertainties are described by one hundred parameters. They
2105 are split between the ND280 and SK detectors and binned by neutrino flavour:
2106 ν_μ , $\bar{\nu}_\mu$, ν_e and $\bar{\nu}_e$. The response is then broken down as a function of neutrino
2107 energy. The bin density in the neutrino energy is the same for the ν_μ in FHC
2108 and $\bar{\nu}_\mu$ in RHC beams, and narrows for neutrino energies close to the oscillation
2109 maximum of $E_\nu = 0.6\text{GeV}$. This binning is specified in Table 6.6. All of these
2110 systematic uncertainties are applied as normalisation parameters with Gaussian
2111 priors centered at 1.0 and error specified from a covariance matrix provided
2112 by the T2K beam group [194].

Neutrino Flavour	Sign	Neutrino Energy Bin Edges (GeV)
μ	Right	0., 0.4, 0.5, 0.6, 0.7, 1., 1.5, 2.5, 3.5, 5., 7., 30.
μ	Wrong	0., 0.7, 1., 1.5, 2.5, 30.
e	Right	0., 0.5, 0.7, 0.8, 1.5, 2.5, 4., 30.
e	Wrong	0., 2.5, 30.

Table 6.6: The neutrino energy binning for the different neutrino flavours. “Right” sign indicates neutrinos in the FHC beam and antineutrinos in the RHC beam. “Wrong” sign indicates antineutrinos in the FHC beam and neutrinos in the RHC beam. The binning of the detector response is identical for the FHC and RHC modes as well as at ND280 and SK.

2113 6.4.2 Atmospheric Flux

2114 The atmospheric neutrino flux is modeled by the HKKM model [49]. 16 systematic
 2115 uncertainties are applied to control the normalisation of each neutrino flavour,
 2116 energy, and direction. They are summarised below:

- 2117 • **Absolute Normalisation:** The overall normalisation of each neutrino flavour
 2118 is controlled by two independent systematic uncertainties, for $E_\nu < 1\text{GeV}$
 2119 and $E_\nu > 1\text{GeV}$, respectively. This is driven mostly by hadronic interaction
 2120 uncertainties for the production of pions and kaons [49]. The strength of
 2121 the response is dependent upon the neutrino energy. The uncertainty is
 2122 parameterized following Figure 11 in [49].
- 2123 • **Relative Normalisation:** Uncertainties on the ratio of $(\nu_\mu + \bar{\nu}_\mu) / (\nu_e + \bar{\nu}_e)$
 2124 are controlled by the difference between the HKKM model [49], FLUKA
 2125 [52] and Bartol models [48]. Three independent parameters are applied in
 2126 the energy ranges: $E_\nu < 1\text{GeV}$, $1\text{GeV} < E_\nu < 10\text{GeV}$, and $E_\nu > 10\text{GeV}$.
- 2127 • **$\nu/\bar{\nu}$ Normalisation:** The uncertainties in the π^+/π^- (and kaon equivalent)
 2128 production uncertainties in the flux of $\nu/\bar{\nu}$. The response is applied using
 2129 the same methodology as the relative normalisation parameters.
- 2130 • **Up/Down and Vertical/Horizontal Ratio:** Similar to the above two sys-
 2131 tematics, the difference between the HKKM, FLUKA, and Bartol model

2132 predictions, as a function of $\cos(\theta_Z)$, is used to control the normalisation of
2133 events as a function of zenith angle.

- 2134 • **K/ π Ratio:** Higher energy neutrinos ($E_\nu > 10\text{GeV}$) mostly originate in
2135 kaon decay. Measurements of the ratio of K/ π production [195] are used to
2136 control the systematic uncertainty of the expected ratio of pion and kaon
2137 production.
- 2138 • **Solar Activity:** As the 11-year solar cycle can affect the Earth's magnetic
2139 field, the flux of primary cosmic rays varies across the same period. The
2140 uncertainty is calculated by taking a ± 1 year variation, equating to a 10%
2141 uncertainty for the SK-IV period.
- 2142 • **Atmospheric Density:** The height of the interaction of the primary cosmic
2143 rays is dependent upon the atmospheric density. The HKKM assumes the
2144 US standard 1976 [145] profile. This systematic controls the uncertainty in
2145 that model.

2146 The total uncertainty is dominated by the absolute and relative normalisation
2147 parameters. The effect of which is illustrated in Figure 6.8. Generally, the
2148 uncertainty is large at low energy, reducing to $O(10\%)$ around the peak of the
2149 flux distribution and then increasing once the neutrino energy exceeds 10GeV.

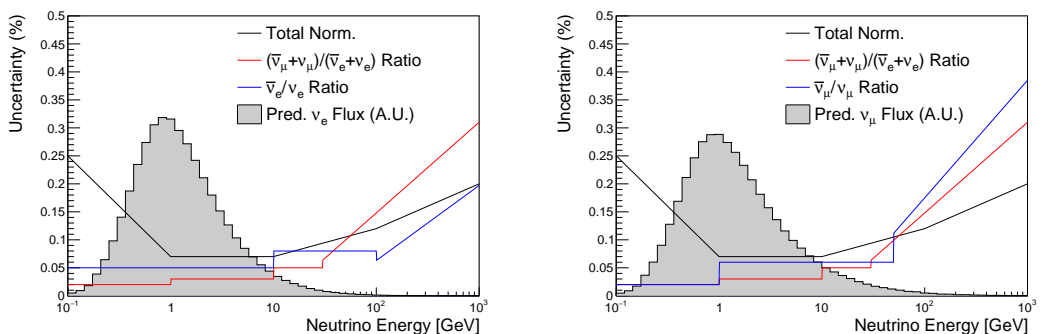


Figure 6.8: The uncertainty evaluated on the atmospheric ν_e (left) and ν_μ (right) flux predictions. The absolute normalisation and flavour ratio uncertainties are given. The solid histogram indicates the neutrino flux as a function of energy.

2150 Updates to the HKKM and Bartol models are underway [150] to use a similar
2151 tuning technique to that used in the beam flux predictions. After those updates,
2152 it may be possible to include correlations in the hadron production uncertainty
2153 systematics for beam and atmospheric flux predictions.

2154 6.4.3 Neutrino Interaction

2155 Neutrino interactions in the detectors are modeled by NEUT. The two indepen-
2156 dent oscillation analyses, T2K-only [196] and the SK-only [58], have developed
2157 separate interaction models. To maximise sensitivity out of this simultaneous
2158 beam and atmospheric analysis, a correlated interaction model has been defined
2159 in [185]. Where applicable, correlations allow the systematic uncertainties applied
2160 to the atmospheric samples to be constrained by near detector neutrino beam
2161 measurements. This can lead to stronger sensitivity to oscillation parameters
2162 as compared to an uncorrelated model.

2163 The low-energy T2K systematic model has a more sophisticated treatment
2164 of CCQE, 2p2h, and CCRES uncertainties, where extensive comparisons of
2165 this model have been performed to external data [196]. However, the model
2166 is not designed for high-energy atmospheric events, like those illustrated in
2167 Figure 5.11. Therefore the high energy systematic model from the SK-only
2168 analysis is implemented for the relevant multi-GeV, PC, and up- μ samples.
2169 The T2K CCQE model is more sophisticated so it has been implemented for
2170 all samples within this analysis, where separate low-energy and high-energy
2171 dials have been implemented. The low-energy dials are constrained by the near
2172 detector measurements and are uncorrelated to their high-energy counterparts.
2173 The author of this thesis was responsible for implementing and validating the
2174 combined cross-section model as documented in [185, 197].

2175 The high energy systematic model includes parameters developed from
2176 comparisons of Nieves and Rein-Seghal models which affect resonant pion
2177 producing interactions, comparisons of the GRV98 and CKMT models which
2178 control DIS interactions, and hadron multiplicity measurements which modulate

the normalisation of multi-pion producing events. The uncertainty on the ν_τ cross-section is particularly large and is controlled by a 25% normalisation uncertainty. These uncertainties are applied via normalisation or shape parameters. The former linearly scales the weight of all affected Monte-Carlo events, whereas the latter can increase or decrease a particular event's weight depending on its neutrino energy and mode of interaction. The response of the shape parameters is defined by third-order polynomial splines which return a weight for a particular neutrino energy. To reduce computational resources for the far detector fit, the response is binned by neutrino energy and sample binning: lepton momentum and cosine zenith binning for atmospheric splined responses and reconstructed neutrino energy and direction binning for beam samples. In total, 17 normalisation and 15 shape parameters are included in the high-energy model within this analysis.

Figure 6.9 indicates the predicted neutrino energy distribution for both beam and subGeV atmospheric samples. There is clearly significant overlap in neutrino energy between the subGeV atmospheric and beam samples, allowing similar kinematics in the final state particles. Figure 6.10 illustrates the fractional contribution of the different interaction modes per sample.

Comparing beam and atmospheric samples which target CCQE interactions (S.G. e-like 0de, S.G. μ -like [0,1]de, [FHC,RHC] 1R μ -like and [FHC,RHC] 1R e-like samples), there is a very similar contribution of CCQE, CC 2p2h, and CC1 π^\pm interactions. The samples which target CC1 π^\pm interactions, (S.G. e-like 0de, S.G. μ -like 2de and FHC 1R+1d.e e-like) also consist of very similar mode interactions.

As a consequence of the similarity in energy and mode contributions, correlating the systematic model between the beam and subGeV atmospheric samples ensures that this analysis attains the largest sensitivity to oscillation parameters while still ensuring neutrino interaction systematics are correctly accounted for. Due to its more sophisticated CCQE and 2p2h model, the T2K systematic model was chosen as the basis of the correlated model.

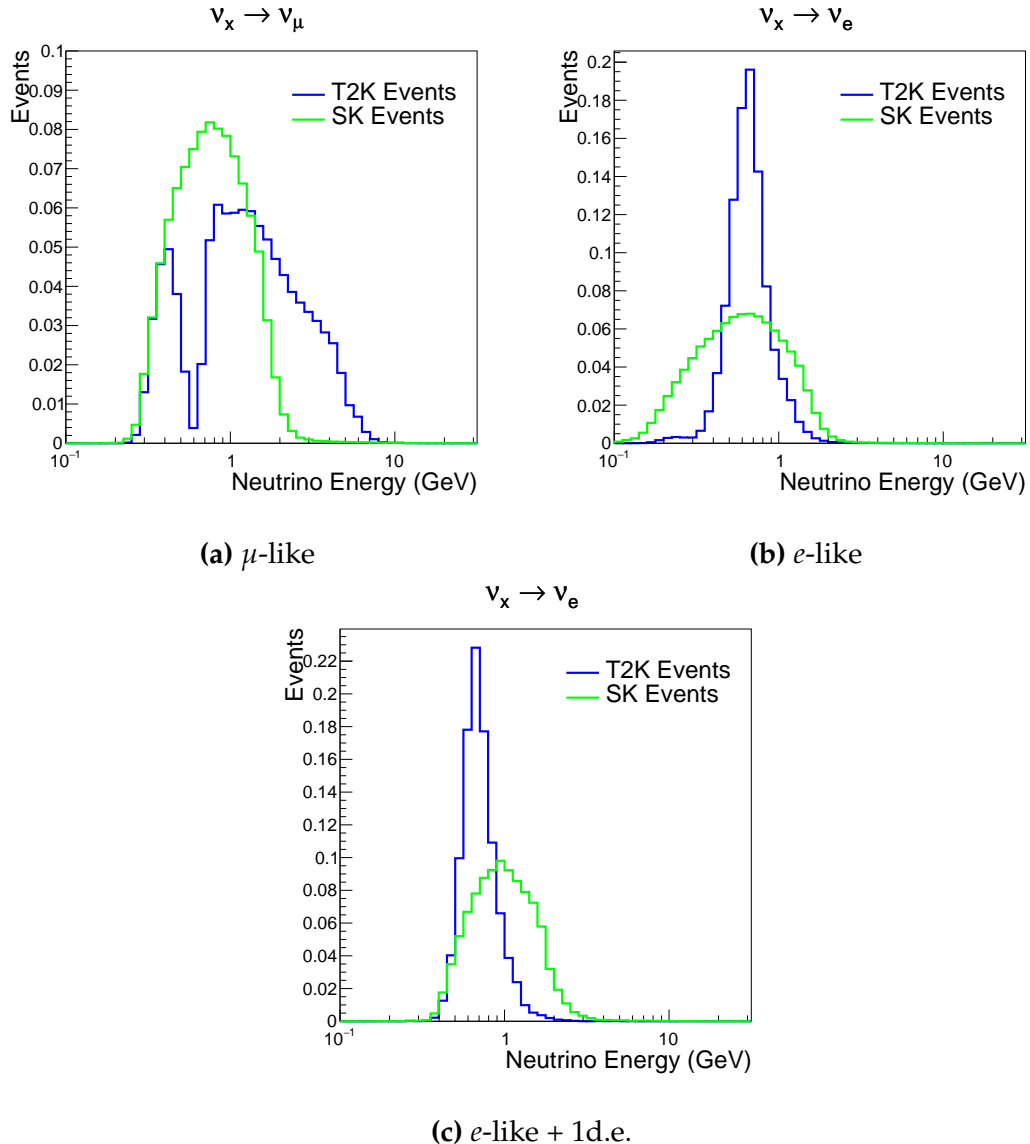


Figure 6.9: The predicted neutrino energy distribution for subGeV atmospheric and beam samples. FHC and RHC beam samples are summed together Asimov A oscillation parameters are assumed (given in Table 2.2). Beam and atmospheric samples with similar cuts are compared against one another.

The T2K systematic model [196] is applied in a similar methodology to the SK model parameters. It consists of 19 shape parameters and 24 normalisation parameters. Four additional parameters, which model the uncertainty in the binding energy, are applied in a way to shift the momentum of the lepton emitted from a nucleus. This controls the uncertainty specified on the 27MeV binding energy assumed within Equation 6.2. The majority of these parameters are

	CC QE	CC 2p2h	CC $1\pi^\pm$	CC $M\pi$	CC Other	NC $1\pi^0$	NC $1\pi^\pm$	NC $M\pi$	NC Coh.	NC Other
FHC 1R+1d.e. e-like	0.04	0.02	0.83	0.03	0.04	0.01	0.01	0.01	0.00	0.01
RHC 1R e-like	0.62	0.12	0.11	0.01	0.02	0.06	0.01	0.01	0.01	0.04
FHC 1R e-like	0.68	0.12	0.10	0.00	0.02	0.04	0.01	0.00	0.00	0.02
RHC 1R μ -like	0.62	0.13	0.17	0.02	0.03	0.00	0.02	0.00	0.00	0.00
FHC 1R μ -like	0.62	0.12	0.16	0.02	0.03	0.00	0.03	0.00	0.00	0.00
S.G. π^0 -like	0.05	0.01	0.02	0.00	0.01	0.68	0.06	0.07	0.06	0.04
S.G. μ -like 2de	0.04	0.01	0.80	0.10	0.04	0.00	0.00	0.00	0.00	0.00
S.G. μ -like 1de	0.72	0.11	0.12	0.01	0.02	0.00	0.01	0.00	0.00	0.00
S.G. μ -like 0de	0.68	0.11	0.10	0.01	0.02	0.01	0.05	0.01	0.00	0.02
S.G. e-like 1de	0.05	0.01	0.75	0.10	0.05	0.00	0.01	0.02	0.00	0.01
S.G. e-like 0de	0.73	0.11	0.10	0.01	0.02	0.02	0.00	0.00	0.00	0.00

Figure 6.10: The interaction mode contribution of each sample given as a fraction of the total event rate in that sample. Asimov A oscillation parameters are assumed (given in Table 2.2). The Charged Current (CC) modes are broken into quasi-elastic (QE), 2p2h, resonant charged pion production ($1\pi^\pm$), multi-pion production ($M\pi$), and other interaction categories. Neutral Current (NC) interaction modes are given in interaction mode categories: π^0 production, resonant charged pion production, multi-pion production, and others.

2215 assigned a Gaussian prior uncertainty. Those that have no reasonably motivated
 2216 uncertainty, or those which have not been fit to external data, are assigned a
 2217 flat prior which does not affect the penalty term.

2218 On top of the combination of the SK and T2K interaction models, several
 2219 other parameters have been specifically developed for the joint oscillation anal-
 2220 ysis. The majority of the atmospheric samples' δ_{CP} sensitivity comes from the
 2221 normalisation of subGeV electron-like events. These are modeled using a spectral
 2222 function to approximate the nuclear ground state. However, the near detector is
 2223 not able to constrain the model so an additional systematic is introduced which
 2224 models an alternative Continuous Random Phase Approximation (CRPA) nuclear
 2225 ground state. This dial approximates the event weights if a CRPA model had

been assumed rather than a spectral function. This dial only applies to ν_e and $\bar{\nu}_e$ as the near detector does not constraint ν_e cross-section measurements. It is applied as a shape parameter.

Further additions to the model have been introduced due to the inclusion of the subGeV π^0 atmospheric sample. This particularly targets charged current and neutral current π^0 producing interactions to help constrain the systematic uncertainties. Therefore, an uncertainty that affects neutral current resonant π^0 production is incorporated into this analysis. Comparisons of NEUT's NC resonant pion production predictions have been made to MiniBooNE [198] data and a consistent 16% to 21% underprediction is observed [185]. Consequently, a conservative 30% normalisation parameter is invoked.

Down-going events are mostly insensitive to oscillation parameters and can act similar to the near detector within an accelerator experiment (Details will be discussed in chapter 7). This region of phase space can act as a sideband and allows the cross-section model and near detector constraint to be studied. The distribution of events in this region is calculated using the technique outlined in subsection 4.3.4. The results are illustrated in Figure 6.11. For CCQE-targeting samples, the application of the near detector constraint is well within the statistical fluctuation of the down-going data. This means there is no significant tension is observed between the data and the Monte Carlo prediction after the near detector constraint is applied. This is not the case for samples with target CCRES interactions. The electron-like data is consistent with the constrained prediction at high reconstructed momenta but diverges at lower momentum, whereas the muon-like sample is under-predicted throughout the range of momenta. To combat this disagreement, an additional cross-section systematic dial, specifically designed to inflate the low pion momentum systematics was developed in [185]. This is a shape parameter implemented through a splined response.

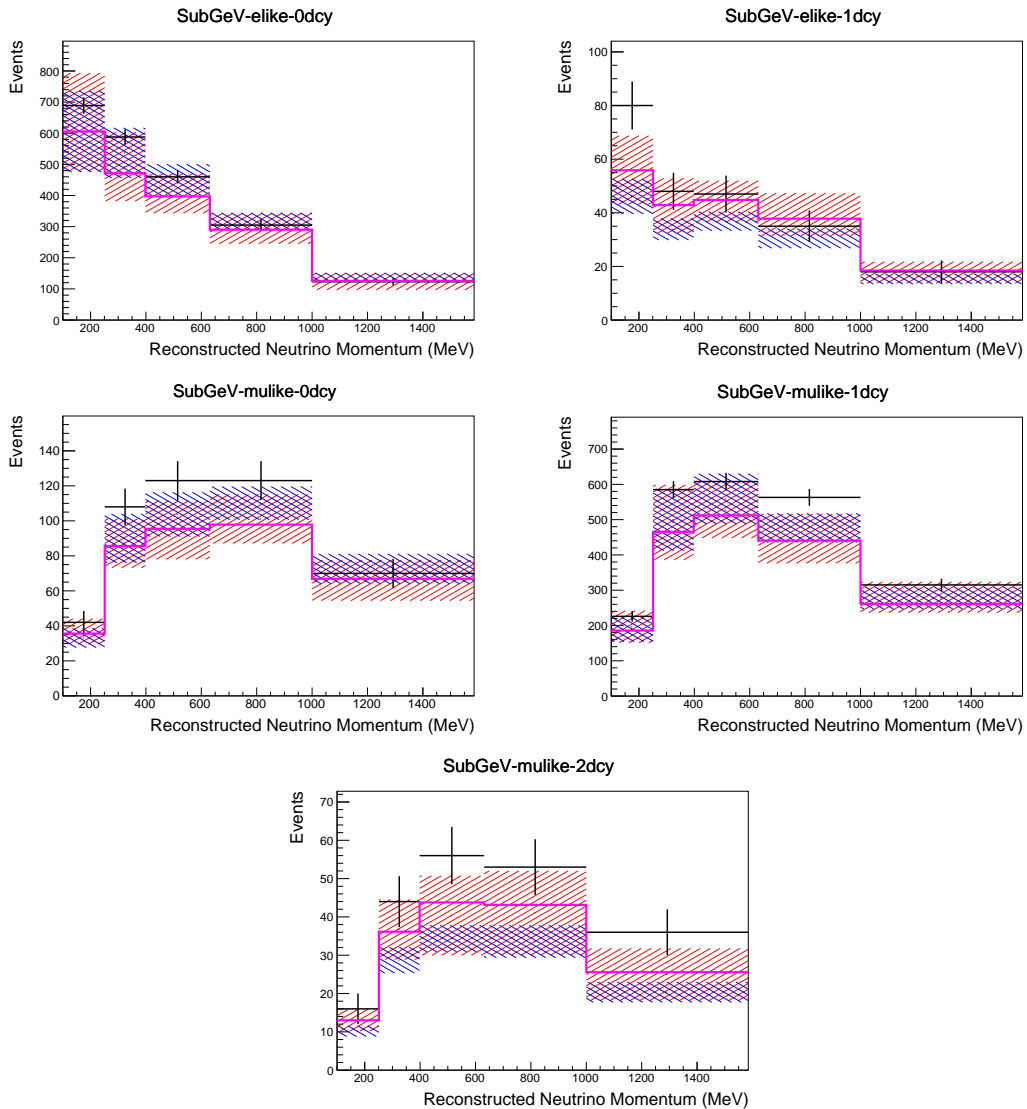


Figure 6.11: Down-going atmospheric subGeV single-ring samples comparing the mean and error of the pre-fit and post-fit Monte Carlo predictions in red and blue, respectively. The magenta histogram illustrates the Monte Carlo prediction using the generated dial values. The black points illustrate the down-going data with statistical errors given. The mean and errors of the Monte Carlo predictions are calculated by the techniques documented in subsection 4.3.4. The pre-fit spectrum is calculated by throwing the cross-section and atmospheric flux dial values from the pre-fit covariance matrix. The post-fit spectrum is calculated by sampling the cross-section dial values from an ND fit MCMC chain, whilst still throwing the atmospheric flux dials from the pre-fit covariance.

2253 6.4.4 Near Detector

2254 The systematics applied due to uncertainties arising from the response of the near
 2255 detector is documented in [125]. The response is described by 574 normalisation
 2256 parameters binned in the selected sample as well as momentum and angle,

2257 P_μ and $\cos(\theta_\mu)$, of the final-state muon. These are applied via a covariance
2258 matrix with each parameter being assigned a Gaussian prior from that covariance
2259 matrix. These normalisation parameters are built from underlying systematics,
2260 e.g. pion secondary interaction systematics, which are randomly thrown and
2261 the variation in each $P_\mu \times \cos(\theta_\mu)$ bin is determined. Two thousand throws are
2262 evaluated and a covariance matrix response is created. This allows significant
2263 correlations between FGD1 and FGD2 samples, as well as adjacent $P_\mu \times \cos(\theta_\mu)$
2264 bins. Statistical uncertainties are accounted for by including fluctuations of each
2265 event's weight from a Poisson distribution.

2266 Similar to the cross-section systematics, MaCh3 and BANFF are used to
2267 constrain the uncertainty of these systematics through independent validations.
2268 Each fitter generates a post-fit covariance matrix which is compared and passed
2269 to the far-detector oscillation analysis working group. As the analysis presented
2270 within this thesis uses the MaCh3 framework, a joint oscillation analysis fit of all
2271 three sets of samples and their respective systematics is performed.

2272 6.4.5 Far Detector

2273 Two configurations of the far detector systematic model implementation have
2274 been considered. Firstly, the far detector systematic uncertainties for beam and
2275 atmospheric samples are taken from their respective analysis inputs, denoted
2276 “official inputs” analysis, with no correlations assumed between the beam and at-
2277 mospheric samples. The beam- and atmospheric-specific inputs are documented
2278 in subsubsection 6.4.5.1 and subsubsection 6.4.5.2. Secondly, an alternative
2279 detector model has been developed which correlates the response of the SK
2280 detector systematics between the beam and atmospheric samples. Here, the
2281 distribution of parameters used for applying event cuts (e.g. electron-muon
2282 PID separation) is modified within the fit. It follows a similar methodology to
2283 the beam far detector systematics implementation but performs a joint fit of
2284 the beam and atmospheric data. This alternative implementation is detailed
2285 in subsubsection 6.4.5.3.

2286 **6.4.5.1 Beam Samples**

2287 There are 45 systematics which describe the response of the far detector to
 2288 beam events [178], split into 44 normalisation parameters and one energy scale
 2289 systematic. The energy scale systematic is applied as a multiplicative scaling
 2290 of the reconstructed neutrino energy. It is estimated from data-to-Monte Carlo
 2291 differences in the stopping muon sample in [58] and found to be 2.1%. The
 2292 normalisation parameters are assigned a Gaussian error centered at one with
 2293 width taken from a covariance matrix. A detailed breakdown of the generation
 2294 of the covariance matrix is found in [191]. To build the covariance matrix, a fit
 2295 is performed on atmospheric data which has been selected using beam sample
 2296 selection cuts. These cuts use the variables, L^i , where the index i is detailed in
 2297 Table 6.7. Each L^i is a smear, α , and shift, β parameter such that,
 2298

$$L_j^i \rightarrow \bar{L}_j^i = \alpha_j^i L + \beta_j^i. \quad (6.4)$$

2298 Where L_j^i (\bar{L}_j^i) correspond to nominal(varied) PID cut parameters given in
 2299 Table 6.7. The shift and smear parameters are nuisance parameters with no prior
 2300 constraints. They are binned by final-state topology, j , where the binning is given
 2301 in Table 6.8. The final-state topology binning is because the detector will respond
 2302 differently to events that have one or multiple rings. For example, the detector
 2303 will be able to distinguish single-ring events better than two overlapping ring
 2304 events, resulting in different systematic uncertainty for one-ring events compared
 2305 to two-ring events. This approach is used to allow the cut parameter distributions
 2306 to be modified within the fit, allowing for better data to Monte Carlo agreement.

Cut Variable	Parameter Name
0	<code>fitQun e/μ PID</code>
1	<code>fitQun e/π⁰ PID</code>
2	<code>fitQun μ/π PID</code>
3	<code>fitQun Ring-Counting Parameter</code>

Table 6.7: List of cut variables that are included within the shift/smear fit documented in [191].

Category	Description
1e	Only one electron above Cherenkov threshold in the final state
1 μ	Only one muon above Cherenkov threshold in the final state
1e+other	One electron and one or more other charged particles above Cherenkov threshold in the final state
1 μ +other	One muon and one or more other charged particles above Cherenkov threshold in the final state
1 π^0	Only one π^0 in the final state
1 π^\pm or 1p	Only one hadron (typically charged pion or proton) in the final state
Other	Any other final state

Table 6.8: Reconstructed event topology categories on which the SK detector systematics [191] are based.

2307 The mis-modeling of π^0 events is also considered. If one of the two rings
 2308 from a π^0 event is missed, this will be reconstructed as a CC ν_e -like event. This
 2309 is one of the largest systematics hindering the electron neutrino appearance
 2310 analyses. Consequently, additional systematics have been introduced to con-
 2311 strain the mis-modeling of π^0 events in SK, binned by reconstructed neutrino
 2312 energy. To evaluate this systematic uncertainty, a set of “hybrid- π^0 ” samples is
 2313 constructed. These events are built by overlaying one electron-like ring from
 2314 the SK atmospheric neutrino samples or decay electron ring from a stopping
 2315 cosmic ray muon with one simulated photon ring. Both rings are chosen so
 2316 that momenta and opening angle follow the decay kinematics of NC π^0 events
 2317 from the T2K-MC. Hybrid- π^0 Monte Carlo samples with both rings from the
 2318 SK Monte Carlo are produced to compare with the hybrid- π^0 data samples and
 2319 the difference in the fraction of events that pass the ν_e selection criteria is used
 2320 to assign the systematic errors. In order to investigate any data to Monte Carlo
 2321 differences that may originate from either the higher energy ring or lower energy
 2322 ring, two samples are built; a sample in which the electron constitutes the higher
 2323 energy ring from the π^0 decay (called the primary sample) and another one in
 2324 which it constitutes the lower energy ring (called the secondary sample). The
 2325 standard T2K ν_e fitQun event selection criteria are used to select events.

2326 Final contributions to the covariance matrix are determined by supplemen-
 2327 tary uncertainties obtained by comparing stopping muon data to Monte Carlo

prediction, as first introduced in section 5.2. The efficiency of tagging decay electrons is estimated by the stopping muon data to Monte Carlo differences by comparing the number of one decay electron events to the number of events with one or fewer decay electrons. Similarly, the rate at which fake decay electrons are reconstructed by `fiTQun` is estimated by comparing the number of two decay electron events to the number of events with one or two reconstructed decay electrons. The two sources of systematics are added in quadrature weighted by the number of events with one true decay electron yielding a 0.2% systematic uncertainty. A fiducial volume systematic of $\pm 2.5\text{cm}$ which corresponds to a 0.5% shift in the normalisation of events is also applied. Additional normalisation uncertainties based on neutrino flavour and interaction mode are also defined in [178, 199, 200].

Two additional sources of uncertainty are included: secondary and photoneuclear interactions. These are estimated by varying the underlying parameters are building a distribution of sample event rates. These contributions are then added in quadrature to the above covariance matrix. The final uncertainty on the SK detector systematics are provided in Figure 6.12.

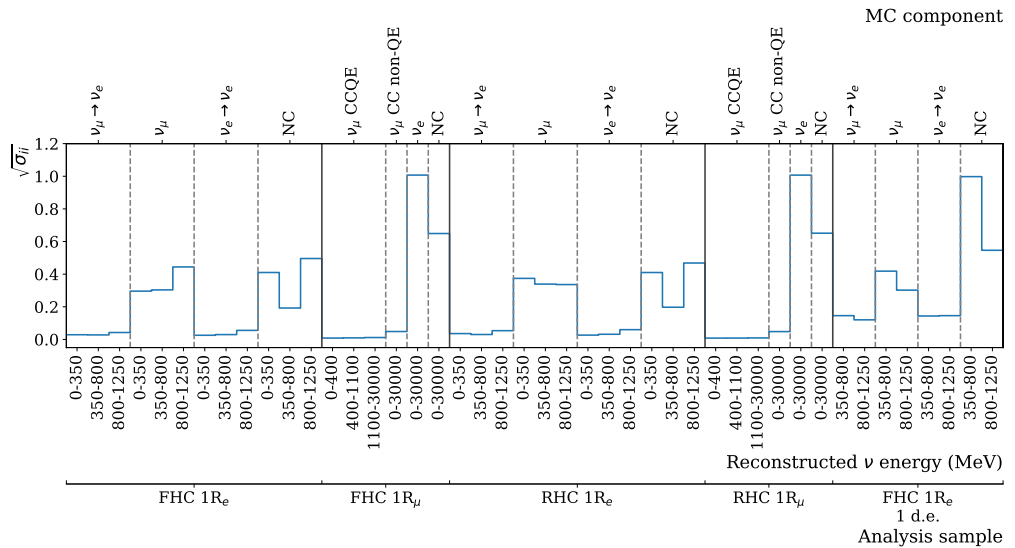


Figure 6.12: The fractional uncertainty on each of the 44 parameters describing the SK detector systematics (The energy scale systematic is neglected). The parameters are split by sample, oscillation channel, interaction mode and reconstructed neutrino energy.

2345 6.4.5.2 Atmospheric Samples

2346 The detector systematics for atmospheric samples, documented in [84], are split
2347 into two sub-groups: those which are related to particle identification and ring
2348 counting systematics, and those which are related to calibration, separation,
2349 and reduction uncertainties.

2350 The particle identification systematics consist of five parameters. The ring sep-
2351 aration systematic enforces an anti-correlated response between the single-ring
2352 and multi-ring samples. This is implemented as a fractional increase/decrease
2353 in the overall normalisation of each sample, depending on the distance to the
2354 nearest wall from an event's vertex. The coefficients of the normalisation are
2355 estimated prior to the fit and depend on the particular atmospheric sample. Two
2356 electron-muon separation systematics are included within this model which
2357 anti-correlates the response of the electron-like and muon-like samples: one for
2358 single-ring events and another for multi-ring events.

2359 The multi-ring electron-like separation likelihood, discussed in section 6.1,
2360 encodes the ability of the detector to separate neutrino from anti-neutrino events.
2361 Two normalisation parameters vary the relative normalisation of multi-ring ν_e
2362 and $\bar{\nu}_e$ samples whilst keeping a consistent overall event rate.

2363 There are 22 systematics related to calibration measurements, including effects
2364 from backgrounds, reduction, and showering effects. They are documented in
2365 [84] and are briefly summarised in Table 6.9. They are applied via normalisation
2366 parameters, with the separation systematics requiring the conservation of event
2367 rate across all samples.

2368 6.4.5.3 Correlated Detector Model

2369 A complete uncertainty model of the SK detector would be able to determine
2370 the systematic shift on the sample spectra for a variation of the underlying
2371 parameters, e.g. PMT angular acceptance. However, this is computationally
2372 intensive, requiring Monte Carlo predictions to be made for each plausible
2373 variation. Consequently, an effective parameter model has been utilised for

Index	Description
0	Partially contained reduction
1	Fully contained reduction
2	Separation of fully contained and partially contained events
3	Separation of stopping and through-going partially contained events in top of detector
4	Separation of stopping and through-going partially contained events in barrel of detector
5	Separation of stopping and through-going partially contained events in bottom of detector
6	Background due to cosmic rays
7	Background due to flasher events
8	Vertex systematic moving events into and out of fiducial volume
9	Upward going muon event reduction
10	Separation of stopping and through-going in upward going muon events
11	Energy systematic in upward going muon events
12	Reconstruction of the path length of upward going muon events
13	Separation of showering and non-showering upward going muon events
14	Background of stopping upward going muon events
15	Background of non-showering through-going upward going muon events
16	Background of showering through-going upward going muon events
17	Efficiency of tagging two rings from π^0 decay
18	Efficiency of decay electron tagging
19	Background from downgoing cosmic muons
20	Asymmetry of energy deposition in tank
21	Energy scale deposition

Table 6.9: Sources of systematic errors specified within the grouped into the “calibration” systematics model.

2374 a correlated detector model following from the T2K-only model implementation
2375 documented in subsubsection 6.4.5.1. It correlates the detector systematics
2376 between the far-detector beam and subGeV atmospheric samples due to their
2377 similar energies and interaction types. As there are no equivalent beam samples,
2378 the multi-GeV, multiring, PC, and Up- μ samples will be subject to the particle
2379 identification systematics implementation as described in subsubsection 6.4.5.2
2380 rather than using this correlated detector model. The calibration systematics also
2381 described in the aforementioned chapter still apply to all atmospheric samples.
2382 The correlated detector model utilises the same smear and shift parameters
2383 documented in subsubsection 6.4.5.1, split by final state topology. Beyond this,

2384 the shift and smear parameters are split by visible energy deposited within the
 2385 detector, with binning specified in Table 6.10. This is because atmospheric events
 2386 are categorised by subGeV and multi-GeV events based on visible energy, so
 2387 this splitting is required when correlating the systematic model for beam and
 2388 atmospheric events. Alongside the technical requirement, higher energy events
 2389 will be better reconstructed due to fractionally less noise within the detector. As
 2390 a result of the inclusion of visible energy binning, Equation 6.4 becomes

$$L_{jk}^i \rightarrow \bar{L}_{jk}^i = \alpha_{jk}^i L + \beta_{jk}^i, \quad (6.5)$$

2391 where k is the visible energy bin.

Index	Range (MeV)
0	$30 \geq E_{vis} > 300$
1	$300 \geq E_{vis} > 700$
2	$700 \geq E_{vis} > 1330$
3	$E_{vis} \geq 1330$

Table 6.10: Visible energy binning for which the correlated SK detector systematics are based

2392 The implementation of this systematic model takes the events reconstructed
 2393 values of the cut parameters, modifies them by the particular shift and smear
 2394 parameter for that event, and then re-applies event selection. This causes event
 2395 migration, which is a new feature incorporated into the MaCh3 framework which
 2396 is only achievable due to the event-by-event reweighting scheme.

2397 Particular care has to be taken when varying the ring counting parameter.
 2398 This is because the number of rings is a finite value (one-ring, two-ring, etc.)
 2399 which can not be continuously varied through this shift and smear technique.
 2400 Consequently a continuous ring counting parameter, RC_i , is calculated for the
 2401 i^{th} event, following the definition in [177]: the preferred likelihoods from all
 2402 considered one-ring (L_{1R}) and two-ring (L_{2R}) fits are determined. The difference

2403 is computed as $\Delta_{LLH} = \log(L_{1R}) - \log(L_{2R})$. The ring counting parameter is
 2404 then defined as

$$RC_i = \text{sgn}(\Delta_{LLH}) \times \sqrt{|\Delta_{LLH}|}, \quad (6.6)$$

2405 where $\text{sgn}(x) = x/|x|$. This ring counting parameter corresponds to an
 2406 intermediate likelihood value used within the `fitQun` algorithm to decide the
 2407 number of rings associated with a particular event. However, fake-ring merging
 2408 algorithms are applied after this likelihood value is used. Consequently, this
 2409 ring counting parameter does not always exactly correspond to the number of
 2410 reconstructed rings. This can be seen in Figure 6.13.

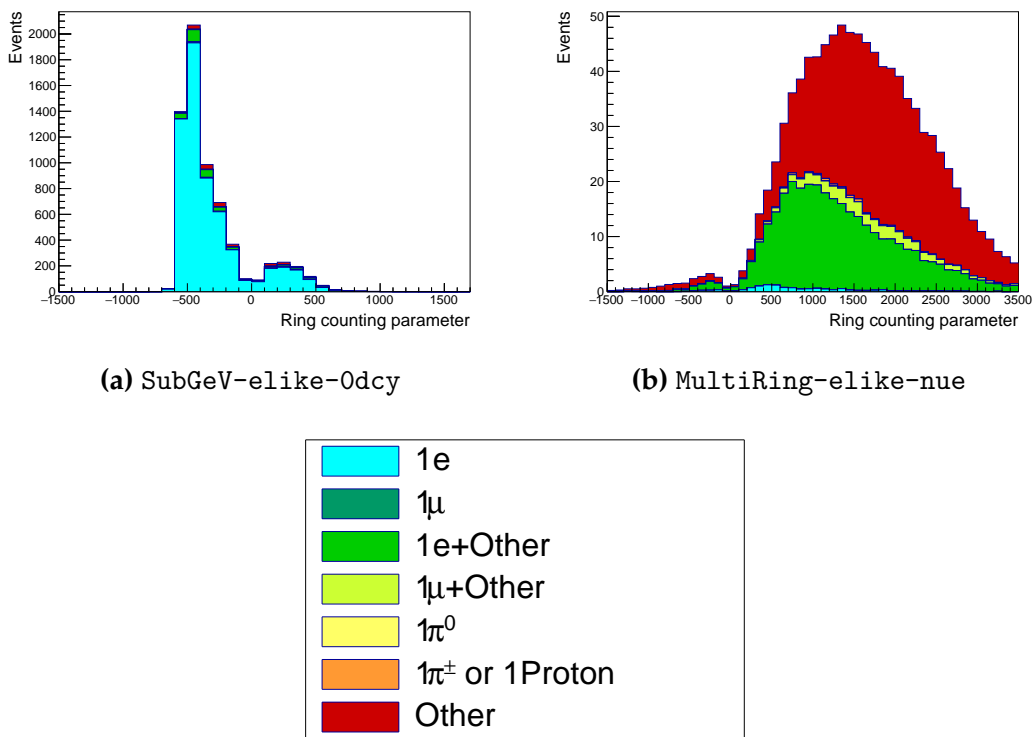


Figure 6.13: The ring counting parameter as defined in Equation 6.6 for the SubGeV-elike-0dcy and MultiRing-elike-nue samples.

2411 As the `fitQun` algorithm does not provide a likelihood value after the fake-
 2412 ring algorithms have been applied, the ring counting parameter distribution is
 2413 correlated to the final number of reconstructed rings through “maps”. These

2414 are two-dimensional distributions of the ring counting parameter and the final
 2415 number of reconstructed rings. An example is illustrated in Figure 6.14. In
 2416 principle, the `fitQun` reconstruction algorithm should be re-run after the variation
 2417 in the ring counting parameter. However, this is not computationally viable.
 2418 Therefore the “maps” are used as a reweighting template.

2419 The maps are split by final state topology and true neutrino flavour and
 2420 all `fitQun`-reconstructed Monte Carlo events are used to fill them. The maps
 2421 are row-normalised to represent the probability of X rings for a given RC_i
 2422 value. Prior to the oscillation fit, an event’s nominal weight is calculated as
 2423 $W^i(N_{Rings}^i, L_{jk}^i)$, where N_{Rings}^i is the reconstructed number of rings for the i^{th}
 2424 event and $W^i(x, y)$ is the bin content in map associated with the i^{th} event, where
 2425 x number of rings and y is ring counting parameter. Then during the fit, the
 2426 value of $R = W^i(N_{Rings}^i, \bar{L}_{jk}^i) / W^i(N_{Rings}^i, L_{jk}^i)$ is calculated as the event weight
 2427 for the i^{th} event. This is the only cut variable that uses a reweighting technique
 2428 rather than event migration.

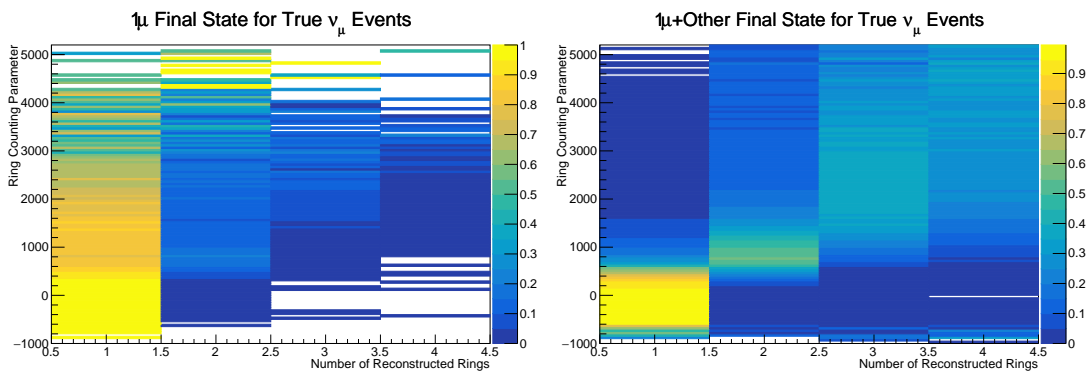


Figure 6.14: The ring counting parameter, defined in Equation 6.6, as a function of the number of reconstructed rings as found by the `fitQun` reconstruction algorithm. Left: true ν_μ events with only one muon above the Cherenkov threshold in the final state. Right: true ν_μ events with one muon and at least one other charged particle above the Cherenkov threshold in the final state.

2429 The π^0 systematics introduced in subsection 6.4.4 are applied via a covariance
 2430 matrix. This is not possible in the alternative model as no covariance matrix
 2431 is used. Thus, the implementation of the π^0 systematics has been modified.
 2432 The inputs from the hybrid π^0 sample are included via the use of “ χ^2 maps”,

which are two-dimensional histograms in α_{jk}^i and β_{jk}^i parameters over some range. Illustrative examples of the χ^2 maps are given in Figure 6.15. Due to their nature, the shift and smear parameters are typically very correlated. A map is produced for each cut parameter given in Table 6.7 and for each visible energy bin given in Table 6.10.

The maps are filled through the χ^2 comparison of the hybrid π^0 Monte Carlo and data in the particle identification parameters documented in Table 6.7. The Monte Carlo distribution is modified by the α_{jk}^i and β_{jk}^i scaling, whilst cross-section and flux nuisance parameters are thrown from their prior uncertainties. The χ^2 between the scaled Monte Carlo and data is calculated and the relevant point in the χ^2 map is filled.

The implementation within this alternative detector model is to add the bin contents of the maps, for the relevant values of the α_{jk}^i and β_{jk}^i parameters, to the likelihood penalty. Only $1\pi^0$ final state topology shift and smear parameters use this prior uncertainty.

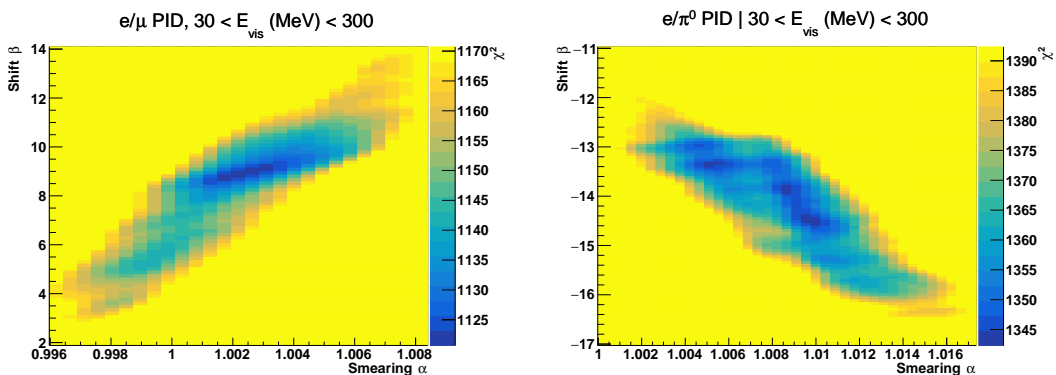


Figure 6.15: The χ^2 between the hybrid- π^0 Monte Carlo and data samples, as a function of smear (α) and shift (β) parameters, for events which have $1\pi^0$ final state topology. Left: Electron-muon separation PID parameter for events with $30 \leq E_{\text{vis}}(\text{MeV}) < 300$. Right: Electron- π^0 separation PID parameter for events with $30 \leq E_{\text{vis}}(\text{MeV}) < 300$.

Similarly, the implementation of the supplementary systematics documented in subsubsection 6.4.5.1 needs to be modified. A new framework [201] was built in tandem between the author of this thesis and the T2K-SK working group [178] so the additional parameters can be incorporated into the MaCh3 framework. These are applied as normalisation parameters, depending on the particular

2453 interaction mode, number of tagged decay electrons, and whether the primary
2454 particle generated Cherenkov light. They are assigned Gaussian uncertainties
2455 with widths described by a covariance matrix. Furthermore, the secondary
2456 interaction and photo-nuclear effects need to be accounted for in this detector
2457 model using a different implementation than that in subsubsection 6.4.5.1. This
2458 was done by including a shape parameter for each of the secondary interactions
2459 and the photo-nuclear systematic parameters.

2460 There are a total of 224 α_{jk}^i and β_{jk}^i parameters, of which 32 have prior
2461 constraints from the hybrid π^0 samples.

2462 One final complexity of this correlated detector model is that the two sets
2463 of samples, beam and subGeV atmospheric, use slightly different parameters
2464 to distinguish electron and muon-like events. The T2K samples use the value
2465 of $\log(L_e/L_\mu)$ whereas the atmospheric samples use the value of $\log(L_e/L_\pi)$,
2466 where L_X is the likelihood for hypothesis X. This is because the T2K fits use
2467 single-ring f iTQun fitting techniques, whereas multi-ring fits are applied to the
2468 atmospheric samples where only the electron and pion hypothesis are considered.
2469 The correlation between the two likelihood ratios is illustrated in Figure 6.16. As
2470 discussed in section 5.2, the pion hypothesis is a very good approximation of the
2471 muon hypothesis due to their similar mass. Consequently, using the same shift
2472 and smear parameters correlated between the beam and subGeV atmospheric
2473 samples is deemed a good approximation.

2474 6.5 Likelihood Calculation

2475 This analysis performs a joint oscillation parameter fit of the ND280 beam
2476 samples, the T2K far detector beam samples, and the SK atmospheric samples
2477 introduced in this chapter.

2478 Once the Monte Carlo predictions of each beam and atmospheric sample
2479 have been built, a likelihood needs to be constructed. This is done by comparing
2480 the binned Monte Carlo prediction to binned data. The Monte Carlo prediction
2481 is calculated at a particular point, $\vec{\theta}$, in the model parameter space such that

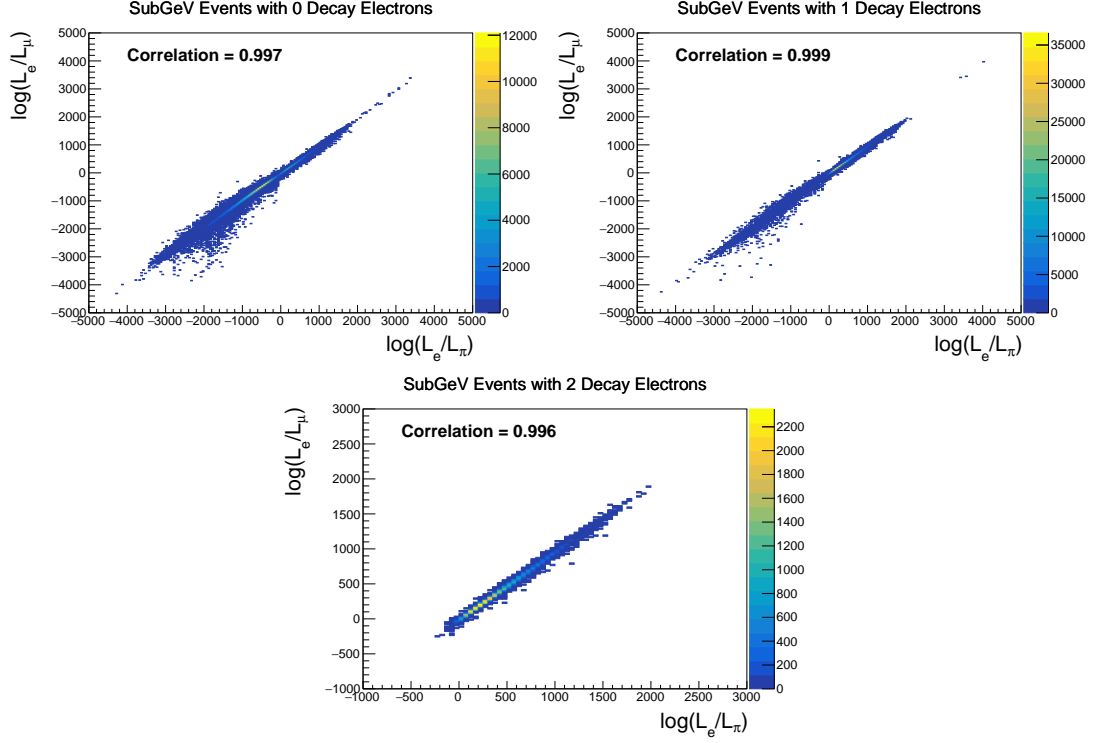


Figure 6.16: The distribution of $\log(L_e/L_\mu)$ compared to $\log(L_e/L_\pi)$ for subGeV events with zero (top left), one (top right) or two (bottom) decay electrons. The correlation in the distribution is calculated as 0.997, 0.999 and 0.996, respectively.

2482 $N_i^{MC} = N_i^{MC}(\vec{\theta})$, where N_i represents the bin content of the i^{th} bin. The data
 2483 and Monte Carlo spectra are represented by N_i^D and N_i^{MC} , respectively. The bin
 2484 contents for the beam near detector, beam far detector and atmospheric samples
 2485 are denoted with ND , FD , and Atm , respectively. Taking the FHC1Rmu far detector
 2486 sample as an example, the binning index runs over all the reconstructed neutrino
 2487 energy bins. The likelihood calculation between the data and the Monte Carlo
 2488 prediction for a particular bin follows a Poisson distribution, where the data
 2489 is treated as a fluctuation of the simulation.

2490 The data can consist of either real data or an ‘Asimov’ Monte Carlo prediction,
 2491 which is typically used for sensitivity studies and denoted ‘Asimov data’. The
 2492 process for building Asimov data is as follows. The Monte Carlo prediction is
 2493 reweighted using a particular set of oscillation parameters (potentially those
 2494 listed in Table 2.2) and systematic parameter tune. The resulting spectra for each
 2495 sample is then defined to be the Asimov data for that sample. Whilst this results

in unphysical non-integer data predictions, it eliminates statistical fluctuations from the data. Therefore, the results of a fit to Asimov data should not include any biases from statistical fluctuations. Furthermore, these results should produce posterior probability distributions consistent with the parameters which were used to make the data prediction. That is to say, the fit results should return the known parameters. Any biases seen would be attributed to correlations between each oscillation parameter and correlations between oscillation and systematic parameters. Consequently, Asimov fit results present the maximum precision at which the oscillation parameters could be measured to.

Following the T2K analysis presented in [72], the likelihood contribution for the near detector samples also includes a Monte Carlo statistical uncertainty term, derived from the Barlow and Beeston statistical treatment [202, 203]. It includes a contribution to the likelihood that treats the generated Monte Carlo prediction as a statistical fluctuation of the actual true simulation assuming an infinite amount of statistics had been created. The technical implementation of this additional likelihood term is documented in [186] and briefly summarised as follows. The term is defined as,

$$\frac{(\beta_i - 1)^2}{2\sigma_{\beta_i}^2}, \quad (6.7)$$

where β_i represents a scaling parameter for the i^{th} bin that relates the bin content for the amount of Monte Carlo actually generated N_i^{MC} to the bin content if an infinite amount of Monte Carlo statistics had been generated $N_{i,true}^{MC}$, such that $N_{i,true}^{MC} = \beta_i \times N_i^{MC}$. In the case where a sufficient amount of Monte Carlo statistics had been generated, $\beta_i = 1$. An analytical solution for β_i is given in [186]. Additionally, $\sigma_{\beta_i} = \sqrt{\sum_i w_i^2} / N_i^{MC}$ where $\sqrt{\sum_i w_i^2}$ represents the sum of the square of the weights of the Monte Carlo events which fall into bin i .

DB: Giles did not understand this - Address An additional contribution to the likelihood comes from the variation of the systematic model parameters. For those parameters with well-motivated uncertainty estimates, a covariance matrix, V , describes the prior knowledge of each parameter as well as any

correlations between the parameters. Due to a technical implementation, a single covariance matrix describes each “block” of model parameters, e.g. beam flux systematics. The covariance matrix associated with the k^{th} block is denoted V^k . This substitution results in $\vec{\theta} = \sum_k^{N_b} \vec{\theta}^k$ and $V = \sum_k^{N_b} V^k$ where N_b denotes the number of blocks. A single covariance matrix is provided for: the oscillation parameters, the beam flux parameters, the atmospheric flux parameters, the neutrino interaction systematics, the near detector parameters, the beam far detector systematics, and the atmospheric far detector systematics. The number of parameters in the k^{th} block is defined as $n(k)$.

The equation for the likelihood \mathcal{L} includes all the terms discussed above. It is defined as,

$$\begin{aligned}
-\ln(\mathcal{L}) = & \\
& \sum_i^{\text{NDbins}} N_i^{\text{ND},MC}(\vec{\theta}) - N_i^{\text{ND},D} + N_i^{\text{ND},D} \times \ln \left[N_i^{\text{ND},D} / N_i^{\text{ND},MC}(\vec{\theta}) \right] + \frac{(\beta_i - 1)^2}{2\sigma_{\beta_i}^2} \\
& + \sum_i^{\text{FDbins}} N_i^{\text{FD},MC}(\vec{\theta}) - N_i^{\text{FD},D} + N_i^{\text{FD},D} \times \ln \left[N_i^{\text{FD},D} / N_i^{\text{FD},MC}(\vec{\theta}) \right] \\
& + \sum_i^{\text{Atmbins}} N_i^{\text{Atm},MC}(\vec{\theta}) - N_i^{\text{Atm},D} + N_i^{\text{Atm},D} \times \ln \left[N_i^{\text{Atm},D} / N_i^{\text{Atm},MC}(\vec{\theta}) \right] \\
& + \frac{1}{2} \sum_k^{N_b} \sum_i^{n(k)} \sum_j^{n(k)} (\vec{\theta}^k)_i (V^k)_{ij}^{-1} (\vec{\theta}^k)_j.
\end{aligned} \tag{6.8}$$

The negative log-likelihood value is determined at each step of the MCMC to build the posterior distribution defined in chapter 4. This value is minimised when the Monte Carlo prediction tends towards the data spectrum.

7

2538

2539

Oscillation Probability Calculation

2540 It is important to understand how and where the sensitivity to the oscillation parameters comes from for both atmospheric and beam samples. An
2541 overview of how these samples respond to changes in δ_{CP} , Δm_{32}^2 , and $\sin^2(\theta_{23})$
2542 is given in section 2.5. This section also explains the additional complexities
2543 involved when performing an atmospheric neutrino analysis as compared to
2544 a beam-only analysis.

2546 Without additional techniques, atmospheric sub-GeV upward-going neutrinos ($E_\nu < 1.33\text{GeV}, \cos(\theta_Z) < 0.$) can artificially inflate the sensitivity to $\delta_{CP,zaza}$
2547 due to the quickly varying oscillation probability in this region. Therefore, a
2548 “sub-sampling” approach has been developed to reduce these biases ensuring
2549 accurate and reliable sensitivity measurements. This technique ensures that small-
2550 scale unresolvable features of the oscillation probability have been averaged over
2551 whilst the large-scale features in the oscillation probability are unaffected. The
2552 documentation and validation of this technique are found in section 7.1. The
2553 oscillation probability calculation is computationally intensive due to the large
2554 number of matrix multiplications needed. Consequently, the CUDAProb3 imple-
2555 mentation choice made within the fitting framework, as detailed in section 7.2,
2556 ensures that the analysis can be done in a timely manner.

Whilst the beam neutrinos are assumed to propagate through a constant density slab of material, the density variations through the Earth result in more complex oscillation patterns for atmospheric neutrinos. Furthermore, the uncertainty in the electron density can modify the oscillation probability for the denser core layers of the Earth. The model of the Earth used within this analysis is detailed in section 7.3. This includes information about the official SK-only methodology as well as improvements that have been made to remove some of the approximations used in that analysis. Another complexity of atmospheric neutrino oscillation studies is that the height of production in the atmosphere is not known on an event-by-event basis. An analytical averaging technique that approximates the uncertainty of the oscillation probability has been followed, with the author of this thesis being responsible for the implementation and validation. This implementation of an external technique is described in section 7.4.

7.1 Treatment of Fast Oscillations

As shown in Figure 7.1, atmospheric neutrino oscillations have a significantly more complex structure for upgoing neutrinos with energy below 1GeV. This is because the L/E dependence of the oscillation probability in this region induces rapid variations for small changes in L or E . As discussed in section 2.5, this is also the region in which atmospheric neutrinos have sensitivity to δ_{CP} . In practice, the direction of the neutrino is inferred from the direction of the final state particles traveling in the detector. The correlation between these two directions can be particularly weak for low-energy neutrino interactions. This creates a distinct difference from the beam neutrinos where the position of the source is very precisely known.

As a consequence of the unresolvable structure, an event rate consistent with the averaged oscillation probability is observed in the subGeV upgoing region. This creates a computational problem: A significantly large amount of Monte Carlo statistics would be required to accurately predict the number of events if Monte Carlo averaging was the only technique used. This section describes

2587 the ‘sub-sampling’ approach developed for this analysis and compares it to the
2588 methodology used within the SK-only analysis.

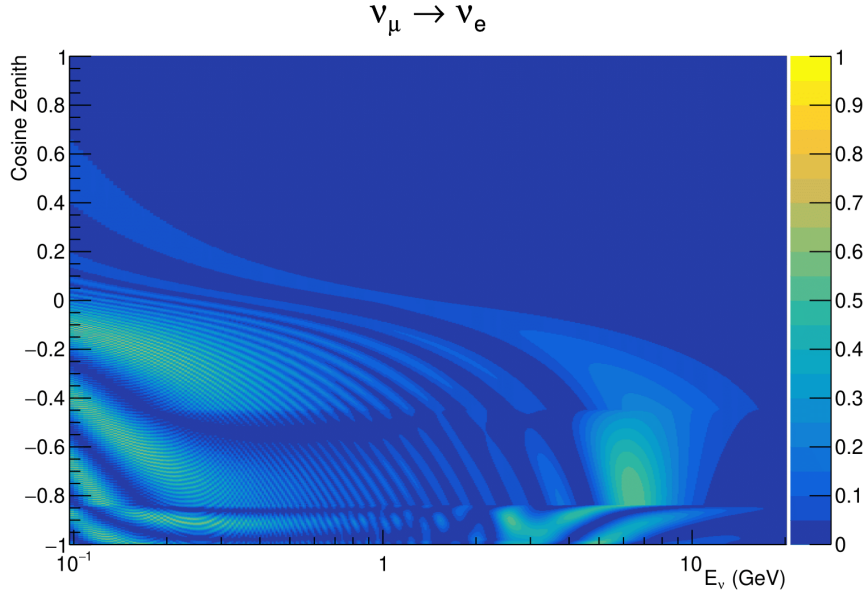


Figure 7.1: The oscillation probability $P(\nu_\mu \rightarrow \nu_e)$, given as a function of neutrino energy and zenith angle, which highlights an example of the “fast” oscillations in the sub-GeV upgoing region.

2589 The official SK-only analysis uses the osc3++ oscillation parameter fitter
2590 [76]. To perform the fast oscillation averaging, it uses a ‘nearest-neighbour’
2591 technique. For a given Monte Carlo neutrino event, the nearest twenty Monte
2592 Carlo neighbours in reconstructed lepton momentum and zenith angle are
2593 found and a distribution of their neutrino energies is built. The RMS, σ , of
2594 this distribution is then used to compute an average oscillation probability for
2595 the given neutrino Monte Carlo event.

2596 For the i^{th} event, the oscillation weight is calculated as

$$W_i = \frac{1}{5}P(E_i, \bar{L}_i) + \frac{1}{5}\sum_{\beta=-1, -0.5, 0.5, 1}P(E_i + \beta\sigma_i, L_\beta), \quad (7.1)$$

2597 where $P(E, L)$ is the oscillation probability calculation for neutrino energy E
2598 and path length L and the two path lengths, \bar{L}_i and L_β are described below. All
2599 of the oscillation probability calculations are performed with a fixed zenith angle
2600 such that the same density profile is used. The uncertainty in the production

height is controlled by using an “average” production height, \bar{L}_i , which represents the average path length computed using twenty production heights taken from the Honda flux model’s prediction [51]. These inputs are provided in 5% intervals of the cumulative distribution function. The value of \bar{L}_i is calculated as:

$$\bar{L}_i = \frac{1}{20} \sum_{j=1}^{20} \sqrt{(R_E + h_j)^2 - R_E^2 (1 - \cos^2 \theta_i)} - R_E \cos \theta_i. \quad (7.2)$$

Where R_E is the Earth’s radius and θ_i is the zenith angle of the i^{th} event. The production heights h_j represent the $(j \times 5)^{th}$ percentile of the cumulative distribution function. L_β values (where the values of β are given in Equation 7.1) are similarly calculated but instead use different combinations of four production heights,

$$\begin{aligned} L_{-1.0} &= \frac{1}{4} L(45, 50, 55, 60), \\ L_{-0.5} &= \frac{1}{4} L(35, 40, 65, 70), \\ L_{+0.5} &= \frac{1}{4} L(25, 30, 75, 68), \\ L_{+1.0} &= \frac{1}{4} L(15, 20, 85, 89). \end{aligned} \quad (7.3)$$

Where $L(i, j, k, l)$ represents the sum of the path lengths with fixed zenith angle and production heights corresponding to the i^{th} , j^{th} , k^{th} and l^{th} percentile of the cumulative distribution function. The values that are taken as β (and values for L_β) are chosen to smooth the oscillation contours in Δm_{32}^2 without incurring loss of sensitivity [204].

This averaging technique works because of the inference between the zenith angle and the reconstructed direction of final state particles in the detector. For low-energy neutrinos, where the resolution of the true neutrino direction is poor, σ_i will be large, resulting in significant averaging effects. Contrary to this, the inferred direction of high-energy neutrinos will be much closer to the true value, meaning that σ_i will be smaller, culminating in small averaging effects.

In practice, these calculations are performed prior to the fit as only oscillation parameters at fixed points are considered. The MCMC technique used in this thesis requires oscillation probabilities to be evaluated at arbitrary parameter values, not known *a priori*. Calculating the five oscillation probabilities per event required by the SK technique is computationally infeasible, so a different averaging technique is used. However, the concept of the averaging technique can be taken from it.

To perform a similar averaging as the SK analysis, a sub-sampling approach using binned oscillograms has been devised. A coarsely binned oscillogram is defined in $\cos(\theta_Z)$ and E_ν . For a given set of oscillation parameters, a single oscillation probability will be assigned to each coarse bin. This value will then apply to all Monte Carlo events which fall into that bin. To assign these oscillation probabilities, the probability is calculated at $N \times N$ points on a grid within a particular bin. This ensemble of oscillation probabilities is averaged to define the coarse bin's oscillation probability, assuming a flat prior in E_ν and $\cos(\theta_Z)$ within the bin. Figure 7.2 illustrates the $N = 2$ example where the assigned value to a coarse bin is the average of the four fine bins which fall in that coarse bin. Whilst the coarse bin edges do not have to be linear on either axis, the sub-division of the fine bins is linear within the range of a coarse bin.

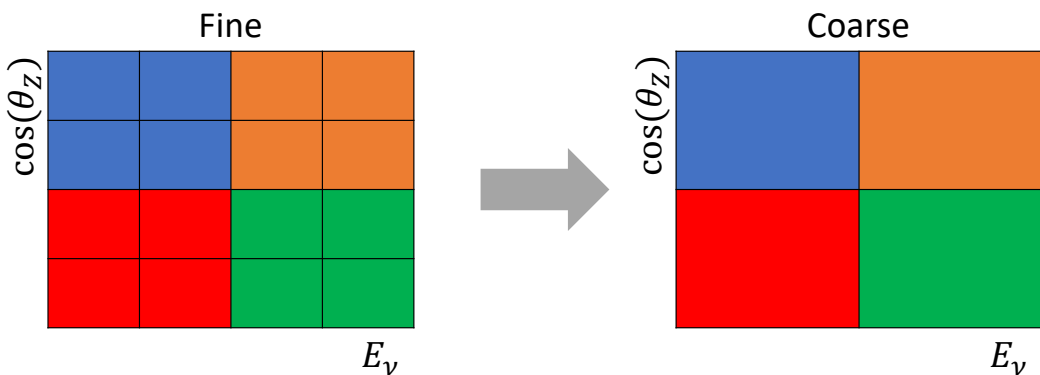


Figure 7.2: Illustration of the averaging procedure for $N = 2$. The oscillation probabilities calculated on the finer left binning are averaged to obtain the oscillation probabilities in the coarser right binning. These averaged oscillation probabilities with the coarser binning are then applied to each event during the fit.

2640 The coarse binning is defined with 67×52 bins in true neutrino energy \times
 2641 cosine zenith. It is picked to be identical to that provided in [204]. In general, the
 2642 binning is logarithmically spaced in neutrino energy but has some hand-picked
 2643 bin edges around the matter resonance to smoothly increased the bin density.
 2644 This is to avoid smearing this region which can be well sampled by the Monte
 2645 Carlo. The cosine zenith binning is approximately linearly spaced across the
 2646 allowable range but the values of layer transitions are hit precisely: -0.8376 (core-
 2647 mantle) and -0.4464 (mantle/transition zone). Bins are spread further apart for
 2648 downgoing events as this is a region unaffected by the fast oscillation wavelengths
 2649 and reduces the total number of calculations required to perform the calculation.

2650 The choice of N is justified based on two studies. Firstly, the variation of event
 2651 rates of each sample is studied as a function of N . For a given set of oscillation
 2652 parameters thrown from the PDG prior constraints (detailed in Table 2.1), the
 2653 oscillation probabilities are calculated using a given value of N . Each sample
 2654 is re-weighted and the event rate is stored. The value of N is scanned from
 2655 1, which corresponds to no averaging, to 19, which corresponds to the largest
 2656 computationally viable subdivision binning. The event rate of each sample at
 2657 large N is expected to converge to a stationary value due to the fine binning fully
 2658 sampling the small-scale structure. Figure 7.3 illustrates this behaviour for the
 2659 SubGeV_elike_0dcy sample for 9 different throws of the oscillation parameters.

2660 Denoting the event rate for one sample for a given throw t at each N by λ_t^N ,
 2661 the average over all considered N values ($\bar{\lambda}_t = \frac{1}{24} \sum_{N=1}^{24} \lambda_t^N$) is computed. The
 2662 variance in the event rate at each N is then calculated as

$$\text{Var}[\lambda^N] = \frac{1}{N_{\text{throws}}} \sum_{t=1}^{N_{\text{throws}}} \left(\lambda_t^N - \bar{\lambda}_t \right)^2 - \left[\frac{1}{N_{\text{throws}}} \sum_{t=1}^{N_{\text{throws}}} \left(\lambda_t^N - \bar{\lambda}_t \right) \right]^2. \quad (7.4)$$

2663 In practice, the following procedure is undertaken. For a particular throw,
 2664 the difference between the event rate at a particular choice of N and the mean
 2665 of the distribution is calculated. This is illustrated in Figure 7.4. This value
 2666 is then calculated for all the 2000 throws, generating a distribution of $\lambda_t^N - \bar{\lambda}_t$.

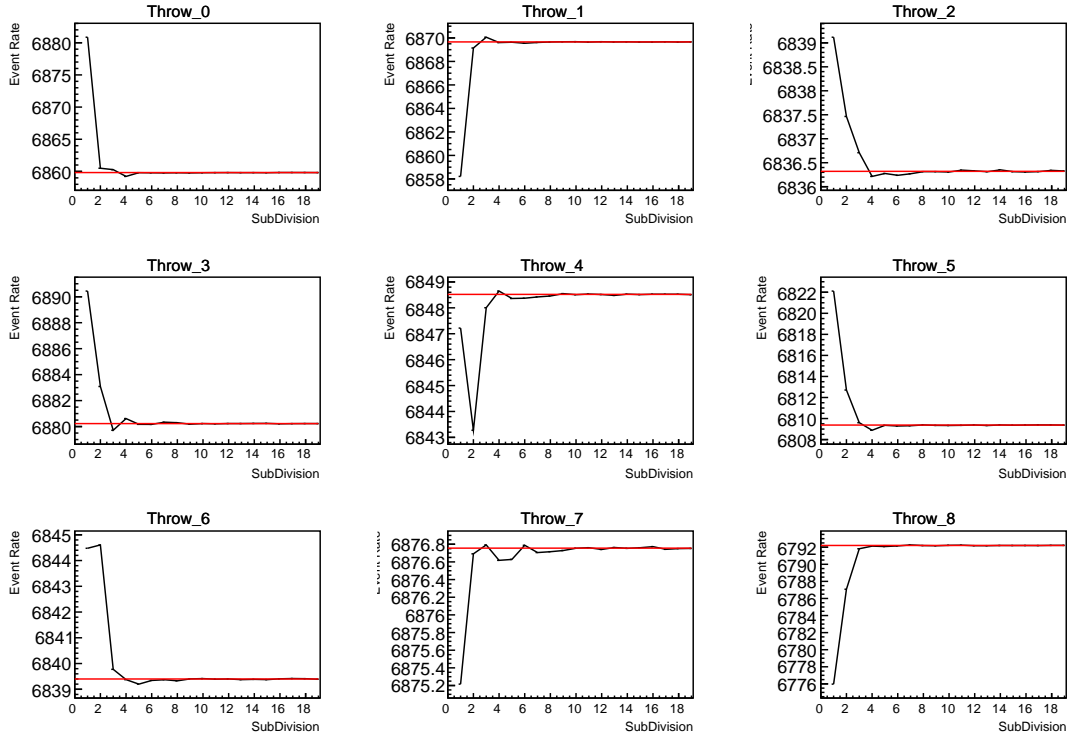


Figure 7.3: Event rate of the SubGeV_elike_0dcy sample as a function of the number of sub-divisions per coarse bin. Each subplot represents the event rate of the sample at a different oscillation parameter set thrown from the PDG priors detailed in Table 2.1. The red line in each subplot represents the mean of the event rate over the different values of sub-divisions for that particular oscillation parameter throw.

2667 This is repeated for each of the values of N considered within this study. The
 2668 distributions of this value, for $N = \{1, 5\}$, are given in Figure 7.5. As expected,
 2669 the distribution gets narrower and tends towards zero for the higher values of N .

2670 The aim of the study is to find the lowest value of N such that this variance
 2671 is below 0.001. This utilises the width of the distributions given in Figure 7.5.
 2672 This is the typical threshold used by T2K fitters to validate systematic imple-
 2673 mentation so has been set as the same criteria. The results of this study for
 2674 each atmospheric sample used within this thesis are illustrated in Figure 7.6 for
 2675 2000 throws of the oscillation parameters. As can be seen, the variance is below
 2676 the threshold at $N = 10$, and is driven primarily by the SubGeV_mulike_1dcy
 2677 and SubGeV_elike_0dcy samples.

2678 The second study to determine the value of N is as follows. The likelihood
 2679 for each sample is computed against an Asimov data set created with Asimov A

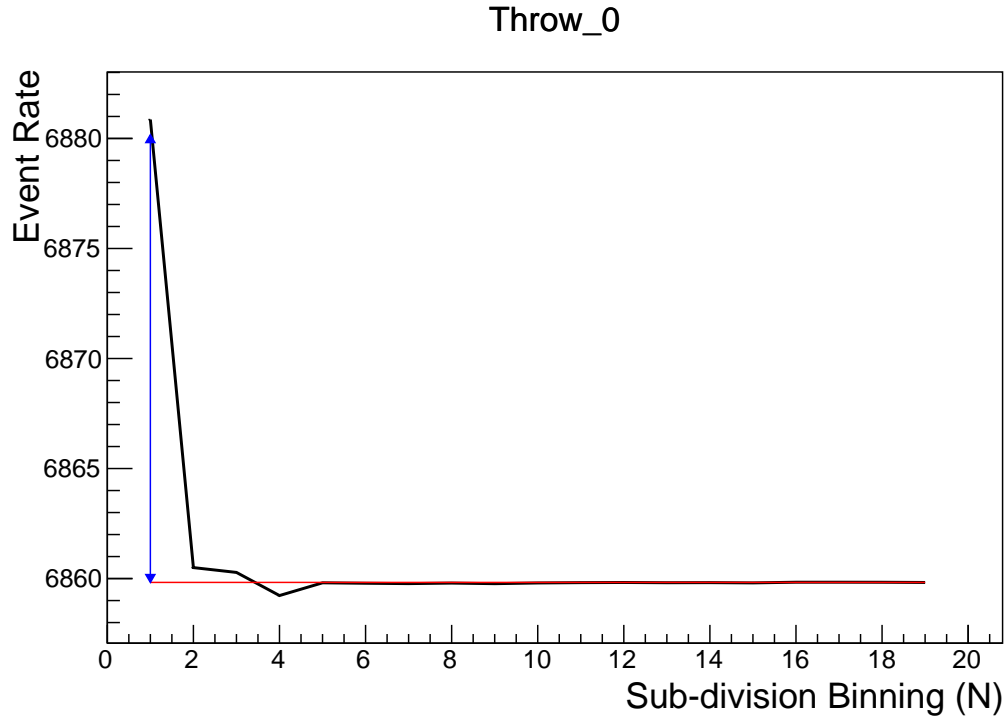


Figure 7.4: Event rate of the SubGeV_elike_0dcy sample, for a particular oscillation parameter throw, as a function of the number of sub-divisions, N , per coarse bin. The difference between the mean event rate (red), $\bar{\lambda}$, and the event rate at $N = 1$, $\lambda^{N=1}$ is defined as $\lambda^N - \bar{\lambda}$ and illustrated by the blue arrow.

oscillation parameters (Table 2.2). Following Equation 7.4, the variance of the log-likelihood over all considered N is computed. The results are shown in Figure 7.7.

A choice of $N = 10$ sub-divisions per coarse bin has a variance in both event rate and log-likelihood residuals less than the required threshold of 0.001. The largest value of the likelihood variance is of order 10^{-7} , corresponding to an error on the log-likelihood of about 3×10^{-4} which is small enough to be negligible for the oscillation analysis.

Figure 7.8 illustrates the effect of the smearing using $N = 10$. The fast oscillations in the sub-GeV upgoing region have been replaced with a normalisation effect whilst the large matter resonance structure remains.

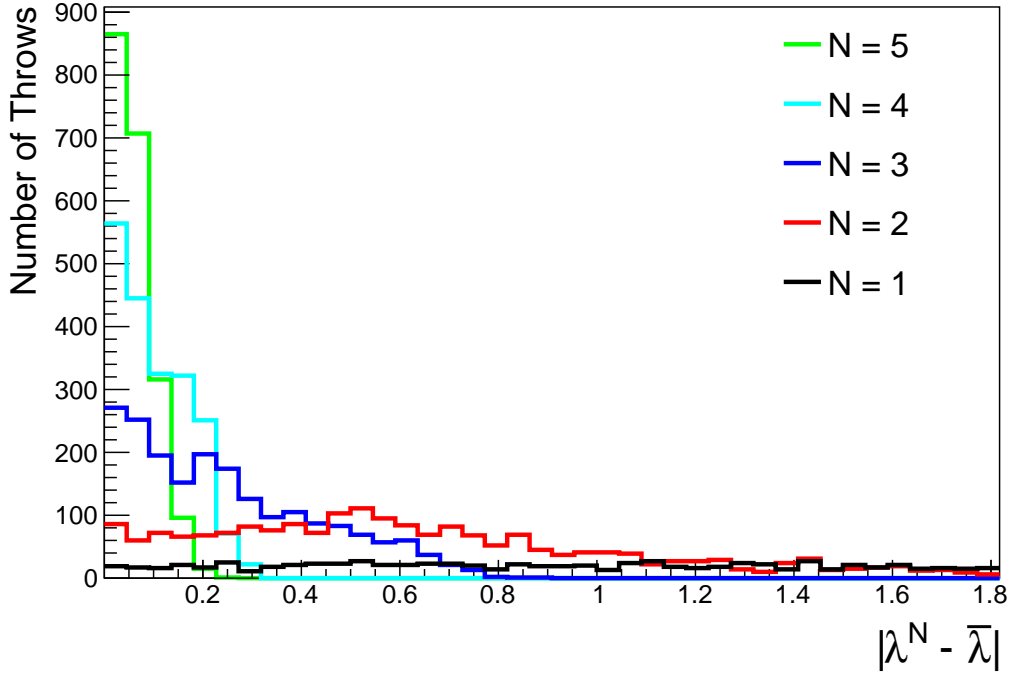


Figure 7.5: The distribution of $\lambda^N - \bar{\lambda}$ for various values of N . As expected, the distribution gets narrower for larger values of N .

2690 7.2 Calculation Engine

2691 As previously discussed in section 7.1, the calculation of oscillation probabilities
 2692 is performed at run-time. Consequently, the time per calculation is crucial for fit
 2693 performance. The initial fitting framework used for this analysis was developed
 2694 with ProbGPU [205]. This is a GPU-only implementation of the prob3 engine
 2695 [206]. It is primarily designed for neutrino propagation in a beam experiment
 2696 (single layer of constant density) with the atmospheric propagation code not
 2697 being used prior to the analysis in this thesis.

2698 Another engine, CUDAProb3 [207], has been interfaced with the fitting frame-
 2699 work used in this analysis. This interfacing was done by the author of this
 2700 thesis. It has been specifically optimised for atmospheric neutrino oscillation
 2701 calculation so does not contain the code to replace the beam oscillation calculation.
 2702 The engine utilises object-orientated techniques as compared to the functional
 2703 implementation of ProbGPU. This allows the energy and cosine zenith arrays to

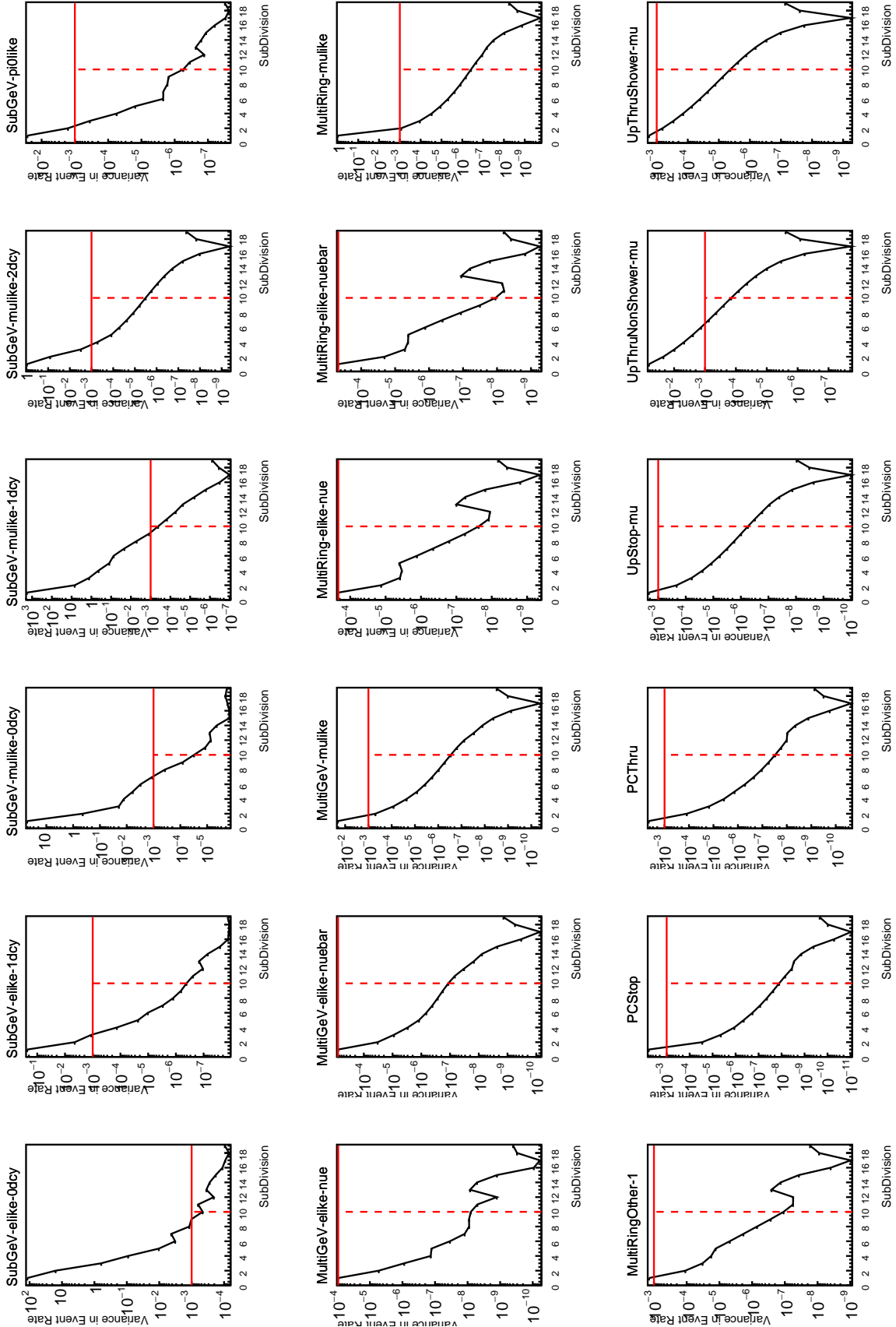


Figure 7.6: Variance of event rate for each atmospheric sample as a function of the number of sub-divisions per coarse bin. The solid red line indicates the 0.1% threshold and the dashed red line indicates the variance at a sub-division $N = 10$.

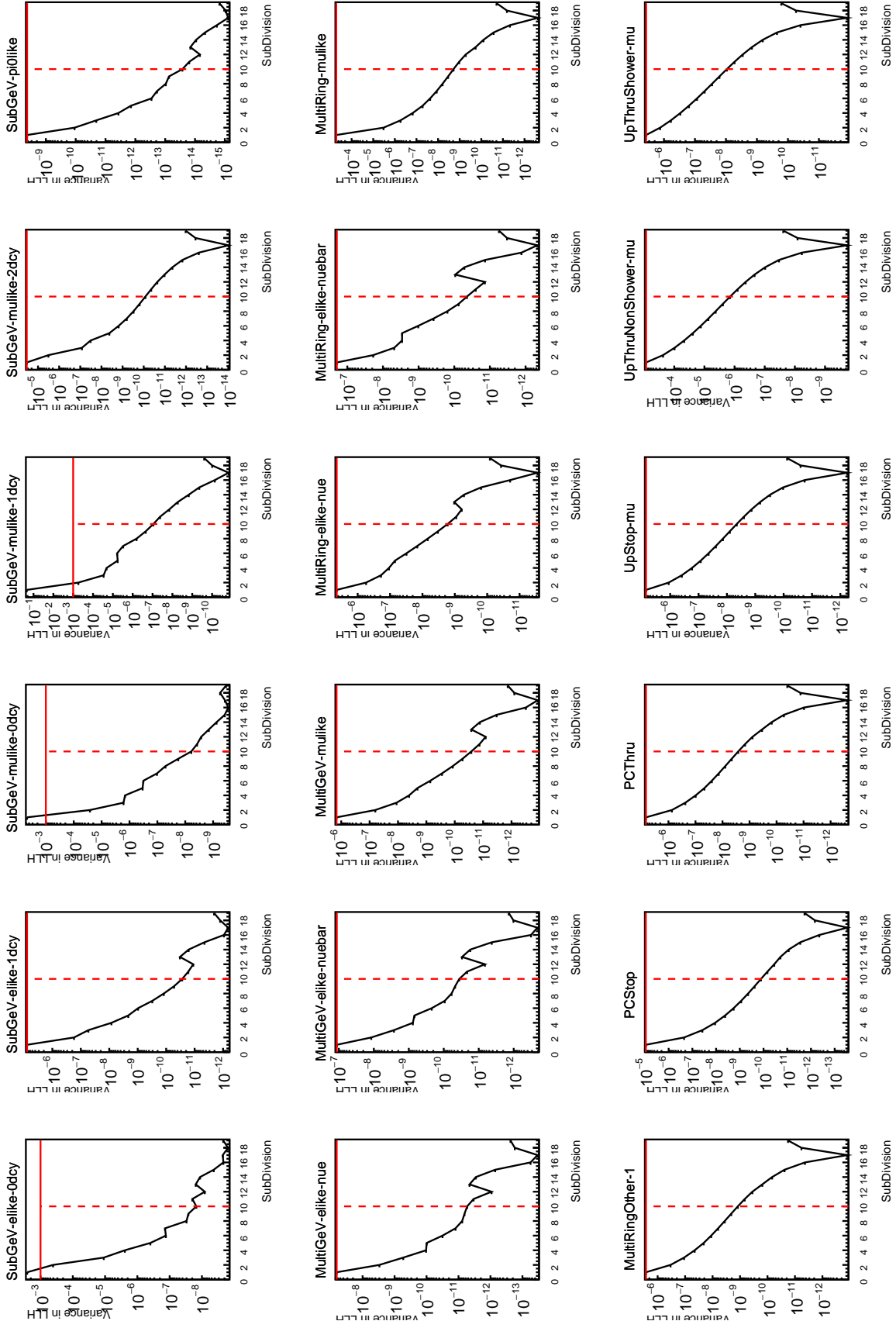


Figure 7.7: Variance of sample likelihood, when compared to 'Asimov data' set at Asimov A, for each atmospheric sample as a function of the number of sub-divisions per coarse bin. The solid red line indicates the 0.1% threshold and the dashed red line is a graphical indication of the variance at a sub-division $N = 10$.

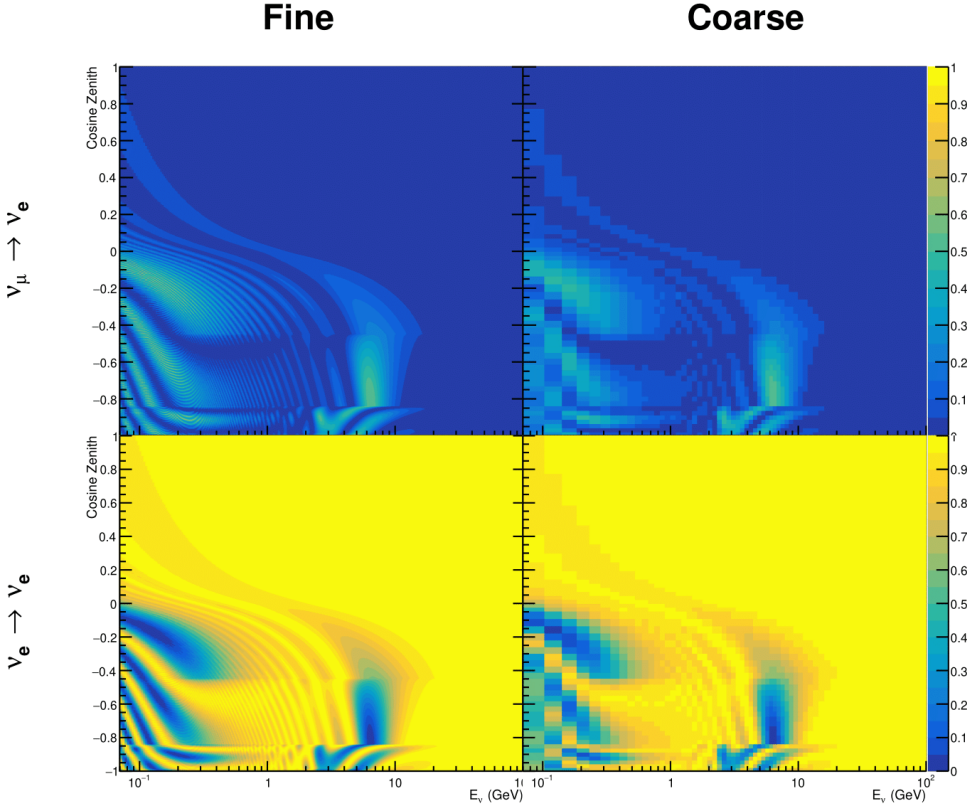


Figure 7.8: The oscillation probability, $P(\nu_\mu \rightarrow \nu_e)$ (top row) and $P(\nu_e \rightarrow \nu_e)$ (bottom row), given as a function of neutrino energy and zenith angle. The left column gives the “fine” binning used to calculate the oscillation probabilities and the right column illustrates the “coarse” binning used to reweight the Monte Carlo events. The fine binning choice is given with $N = 10$, which was determined to be below the threshold from Figure 7.6 and Figure 7.7.

2704 be kept on GPU memory, rather than having to load these arrays onto GPU
 2705 memory for each calculation. Reducing the memory transfer between CPU and
 2706 GPU significantly reduces the time required for calculation. This can be seen
 2707 in Figure 7.9, where the GPU implementation of CUDAProb3 is approximately
 2708 three times faster than the ProbGPU engine.

2709 Another significant advantage of CUDAProb3 is that it contains a CPU multi-
 2710 threaded implementation which is not possible with the ProbGPU or prob3 engines.
 2711 This eliminates the requirement for GPU resources when submitting jobs to batch
 2712 systems. As illustrated in Figure 7.9, the calculation speed depends on the number

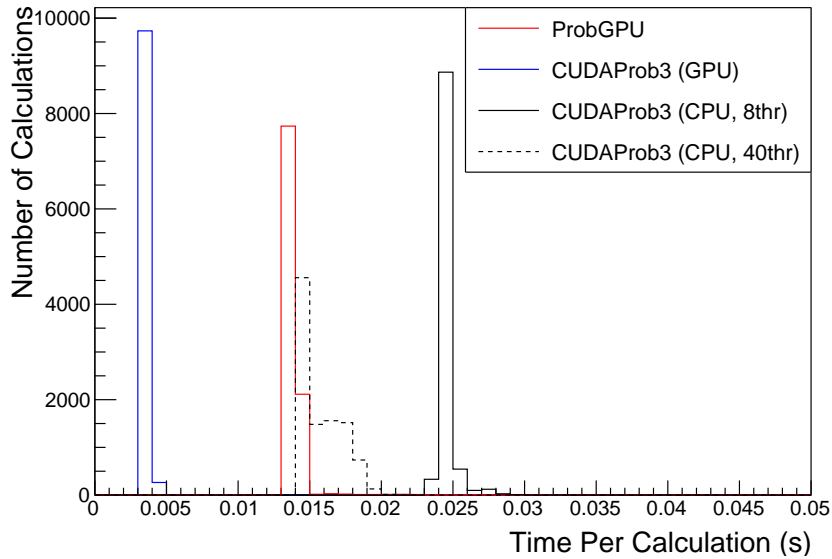


Figure 7.9: The calculation time taken to both calculate the oscillation probabilities and fill the “coarse” oscillograms, following the technique given in section 7.1, for the CUDAProb3 and ProbGPU (Red) calculation engines. CUDAProb3 has both a GPU (Blue) and CPU (Black) implementation, where the CPU implementation is multi-threaded. Therefore, 8-threads (solid) and 40-threads (dashed) configurations have been tested. Prob3, which is a CPU single-thread implementation has a mean step time of 1.142s.

of available threads. Using 8 threads (which is typical of the batch systems being used) is approximately twice as slow as the ProbGPU engine implementation, but would allow the fitting framework to be run on many more resources. This fact is utilised for any SK-only fits but GPU resources are required for any fits which include beam samples due to the ProbGPU requirement. Based on the benefits shown by the implementation in this section, efforts are being placed into including linear propagation for beam neutrino propagation into the engine [208].

7.3 Matter Density Profile

For an experiment observing neutrinos propagating through the Earth, a model of the Earth’s density profile is required. The model used within this analysis is based on the Preliminary Reference Earth Model (PREM) [77], as illustrated in Figure 2.8. Table 2.3 documents the density and radii of the layers used within the constant density approximation used by the SK-only analysis [76]. The

density measurements provided in the PREM model are provided in terms of mass density, whereas neutrino oscillations are sensitive to the electron number density. This value can be computed as the product of the chemical composition, or the Z/A value, and the mass density of each layer. Currently, the only way to measure the chemical composition value for layers close to the Earth's core is through neutrino oscillations. The chemical composition of the upper layers of the Earth's Mantle and the Transition zone is well known due to it being predominantly pyrolite which has a chemical composition value of 0.496 [209]. The chemical composition dial for the core layers is set to a value of 0.468, as calculated in [210]. As this value is less well known, it is assigned a Gaussian error with a standard deviation equivalent to the difference in chemical composition in core and mantle layers. Figure 7.10 illustrates the effect of moving from the $Z/A = 0.5$ method which is used in the official SK-only analysis to these more precise values.

The beam oscillation probability in this thesis uses a baseline of 295km, density $2.6\text{g}/\text{cm}^3$, and chemical composition 0.5 as is done by the official T2K-only analysis [211].

For a neutrino with given $E_\nu, \cos(\theta_Z)$, the oscillation probability calculation engine must be passed a list of the matter regions that the neutrino traversed, with the path length and fixed density in each region. However, a neutrino passing through the earth experiences a range of radii, and thus a range of densities, in each region. In the SK-only analysis, the earth density model used is piecewise-constant, thereby ignoring this effect. For this thesis, the density values for the calculation engine are found by averaging the earth density along the neutrino's path in each layer,

$$\langle \rho \rangle_i = \frac{1}{t_{i+1} - t_i} \int_{t_i}^{t_{i+1}} \rho(t) dt, \quad (7.5)$$

where t_i are the intersection points between each layer and t is the path length of the trajectory across the layer. This leads to an improved approximation. For this averaging, the simplification of the PREM model developed in [212] is

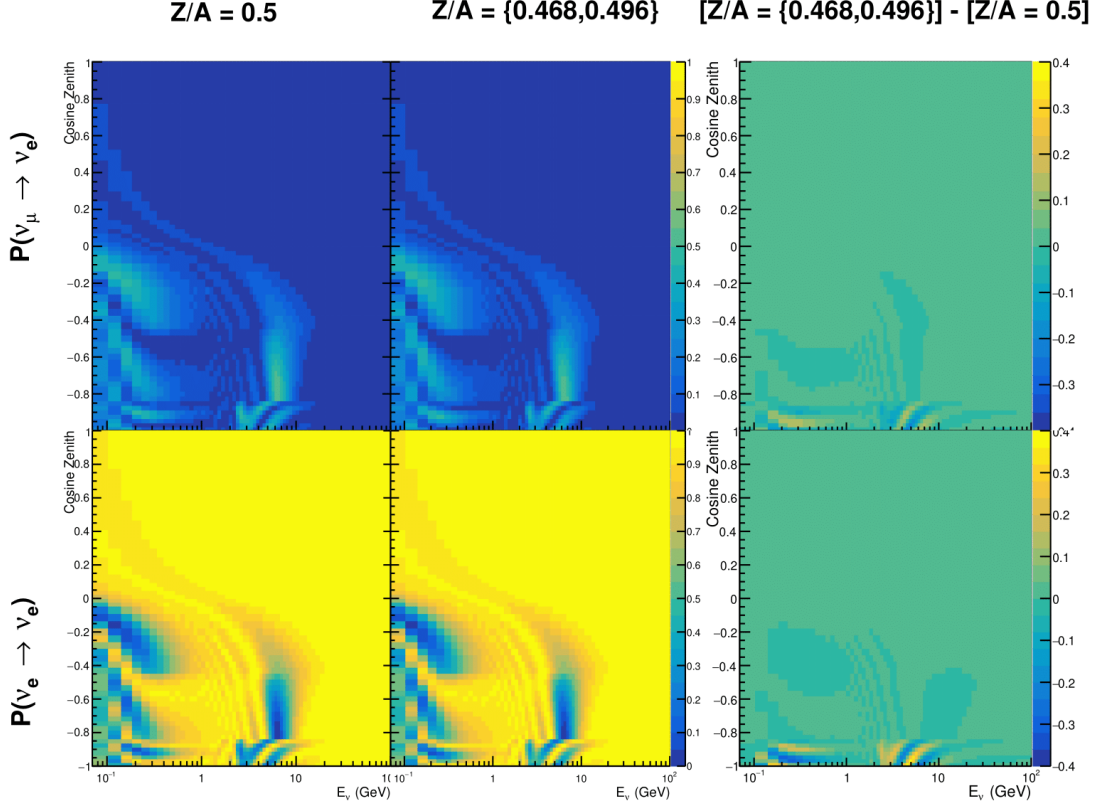


Figure 7.10: The oscillation probability, $P(\nu_\mu \rightarrow \nu_e)$ (top row) and $P(\nu_e \rightarrow \nu_e)$ (bottom row), given as a function of neutrino energy and zenith angle. The left column gives probabilities where the constant $Z/A = 0.5$ approximation which is used in the official SK-only analysis. The middle column gives the probabilities where $Z/A = [0.468, 0.498]$ values are used, as given in Table 2.3. The right column illustrates the difference in oscillation probability between the two different techniques.

used. The layers of the prem model are combined into four to reduce calculation time, with a quadratic fit to each section. This fit was not performed by the author of the thesis and is documented in [204]. The coefficients of the quadratic fit to each layer are given in Table 7.1 with the final distribution illustrated in Figure 7.11. The quadratic approximation is clearly much closer to the PREM model as compared to the constant density approximation.

The effect of using the quadratic density per $\cos(\theta_Z)$ model is highlighted in Figure 7.12. The slight discontinuity in the oscillation probability around $\cos(\theta_Z) \sim -0.45$ in the fixed density model, which is due to the transition to

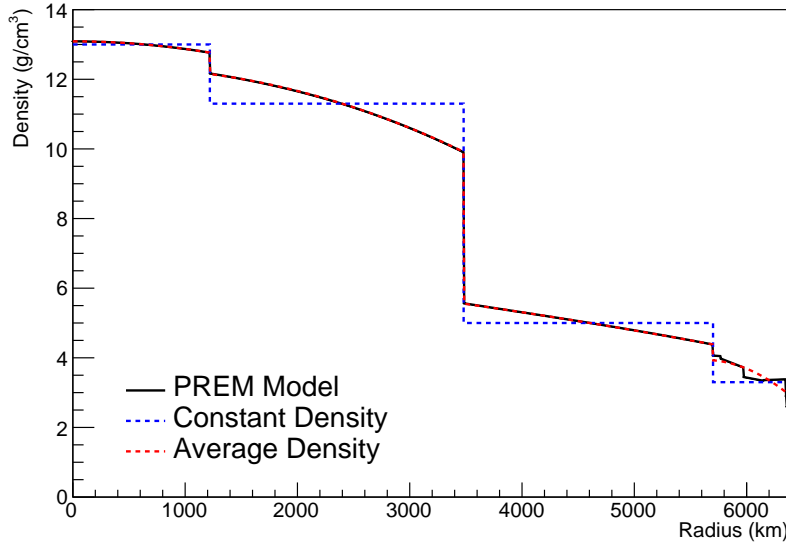


Figure 7.11: The density of the Earth given as a function of the radius, as given by the PREM model (Black), the constant density four-layer approximation (Blue), as used in the official SK-only analysis, and the quadratic approximation of the PREM model (Red).

Layer	Outer Radius [km]	Density [g/cm ³]
Inner Core	1220	$13.09 - 8.84x^2$
Outer Core	3480	$12.31 + 1.09x - 10.02x^2$
Lower Mantle	5701	$6.78 - 1.56x - 1.25x^2$
Transition Zone	6371	$-50.42 + 123.33x - 69.95x^2$

Table 7.1: The quadratic polynomial fits to the PREM model for four assumed layers of the PREM model. The fit to calculate the coefficients is given in [204], where $x = R / R_{\text{Earth}}$.

mantle layer boundary, has been reduced. This is expected as the difference in the density across this boundary is significantly smaller in the quadratic density model as compared to the constant density model. Whilst the difference in density across the other layer transitions is reduced, there is still a significant difference. This means the discontinuities in the oscillation probabilities remain but are significantly reduced. However, as the quadratic density approximation matches the PREM model well in this region, these discontinuities are due to the Earth model rather than an artifact of the oscillation calculation.

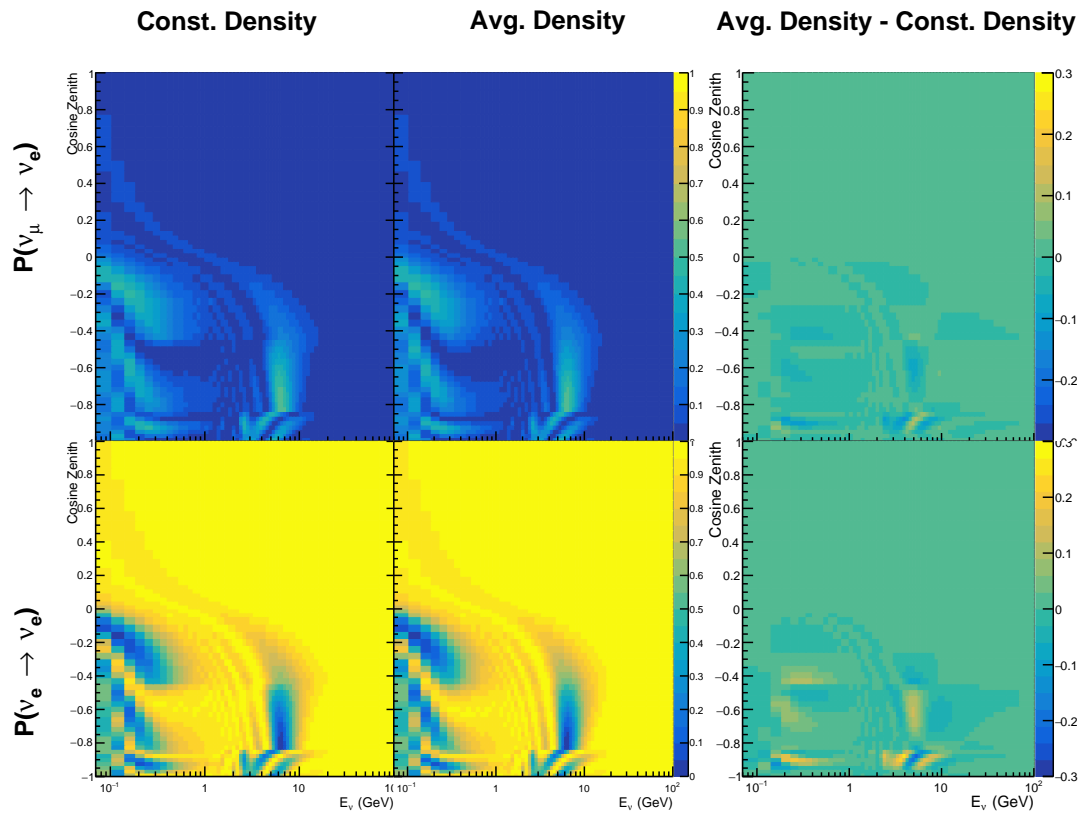


Figure 7.12: The oscillation probability, $P(\nu_\mu \rightarrow \nu_e)$ (top row) and $P(\nu_e \rightarrow \nu_e)$ (bottom row), given as a function of neutrino energy and zenith angle. The left column gives probabilities where the four-layer constant density approximation is used. The middle column gives the probabilities where the density is integrated over the trajectory, using the quadratic PREM approximation, for each $\cos(\theta_Z)$ is used. The right column illustrates the difference in oscillation probability between the two different techniques.

²⁷⁷¹ 7.4 Production Height Averaging

²⁷⁷² As discussed in section 2.5, the height at which the cosmic ray flux interacts
²⁷⁷³ in the atmosphere is not known on an event-by-event basis. The production
²⁷⁷⁴ height can vary from the Earth’s surface to $\sim 50\text{km}$ above that. The SK-only
²⁷⁷⁵ analysis methodology (described in section 7.1) for including the uncertainty
²⁷⁷⁶ on the production height is to include variations from the Honda model when
²⁷⁷⁷ pre-calculating the oscillation probabilities prior to the fit. This technique is not
²⁷⁷⁸ possible for this analysis which uses continuous oscillation parameters that can
²⁷⁷⁹ not be known prior to the fit. Consequently, an analytical averaging technique
²⁷⁸⁰ was developed in [204]. The author of this thesis was not responsible for the
²⁷⁸¹ derivation of the technique but has performed the implementation and validation
²⁷⁸² of the technique for this analysis alone.

²⁷⁸³ Using the 20 production heights per Monte Carlo neutrino event, provided
²⁷⁸⁴ as 5% percentiles from the Honda flux model, a production height distribution
²⁷⁸⁵ $p_j(h|E_\nu, \cos \theta_Z)$ is built for each neutrino flavour $j = \nu_e, \bar{\nu}_e, \nu_\mu, \bar{\nu}_\mu$. In practice, a
²⁷⁸⁶ histogram is filled with 20 evenly spaced bins in production height h between
²⁷⁸⁷ 0 and 50km. The neutrino energy and cosine zenith binning of the histogram
²⁷⁸⁸ are the same as that provided in section 7.1. The average production height,
²⁷⁸⁹ $\bar{h} = \int dh \frac{1}{4} \sum_j p_j(h|E_\nu, \cos(\theta_Z))$, is calculated. This assumes a linear average over
²⁷⁹⁰ the four flavours of neutrino which are considered to be generated in cosmic
²⁷⁹¹ ray showers. The production height binning of this histogram is then translated
²⁷⁹² into $\delta t(h) = t(\bar{h}) - t(h)$, where $t(x)$ is the distance travelled along the trajectory
²⁷⁹³ in the atmosphere from some production height, x .

²⁷⁹⁴ For the i^{th} traversed layer, the transition amplitude, $D_i(t_{i+1}, t_i)$, is computed.
²⁷⁹⁵ The time-ordered product of these is then used as the overall transition amplitude
²⁷⁹⁶ via

$$A(t_{n+1}, t_0) = D_n(t_{n+1}, t_n) \dots D_1(t_2, t_1) D_0(t_1, t_0), \quad (7.6)$$

2797 where,

$$\begin{aligned} D_n(t_{n+1}, t_n) &= \exp[-iH_n(t_{n+1} - t_n)] \\ &= \sum_{k=1}^3 C_k \exp[ia_k(t_{n+1} - t_n)] \end{aligned} \quad (7.7)$$

2798 is expressed as a diagonalised time-dependent solution to the Schrodinger
 2799 equation. The 0th layer is the propagation through the atmosphere and is the
 2800 only term that depends on the production height. Using the substitution $t_0 =$
 2801 $t(\bar{h}) - \delta t(h)$, it can be shown that

$$D_0(t_1, t_0) = D_0(t_1, \bar{h})D_0(\delta t). \quad (7.8)$$

2802 Thus Equation 7.6 becomes

$$\begin{aligned} A(t_{n+1}, t_0) &= D_n(t_{n+1}, t_n) \dots D_1(t_2, t_1)D_0(t_1, \bar{h})D(\delta t) \\ &= A(t_{n+1}, \bar{h}) \sum_{k=1}^3 C_k \exp[ia_k \delta t], \\ &= \sum_{k=1}^3 B_k \exp[ia_k \delta t]. \end{aligned} \quad (7.9)$$

2803 The oscillation probability averaged over production height is then calculated
 2804 as

$$\begin{aligned} \bar{P}(\nu_j \rightarrow \nu_i) &= \int d(\delta t) p_j(\delta t | E_\nu, \cos \theta_Z) P(\nu_j \rightarrow \nu_i) \\ &= \int d(\delta t) p_j(\delta t | E_\nu, \cos \theta_Z) A(t_{n+1}, t_0) A^*(t_{n+1}, t_0) \\ &= \sum_{km} (B_k)_{ij} (B_m)_{ij}^* \int d(\delta t) p_j(\delta t | E_\nu, \cos \theta_Z) \exp[i(a_k - a_m) \delta t]. \end{aligned} \quad (7.10)$$

2805 It is important to note that the exact value of \bar{h} used does not matter as the
 2806 values of δt would change to compensate for any modification to the value of \bar{h} .

2807 In practice, implementation in CUDAProb3 [207] is relatively straightforward
 2808 as the majority of these terms are already calculated in the standard oscillation
 2809 calculation. Figure 7.13 illustrates the results of the production height averaging.

2810 As expected, the main effect is observed in the low-energy downward-going
 2811 and horizontal-going events. Upward-going events have to travel the radius
 2812 of the Earth, $R_E = 6371\text{km}$, where the production height uncertainty is a small
 2813 fraction of the total path length.

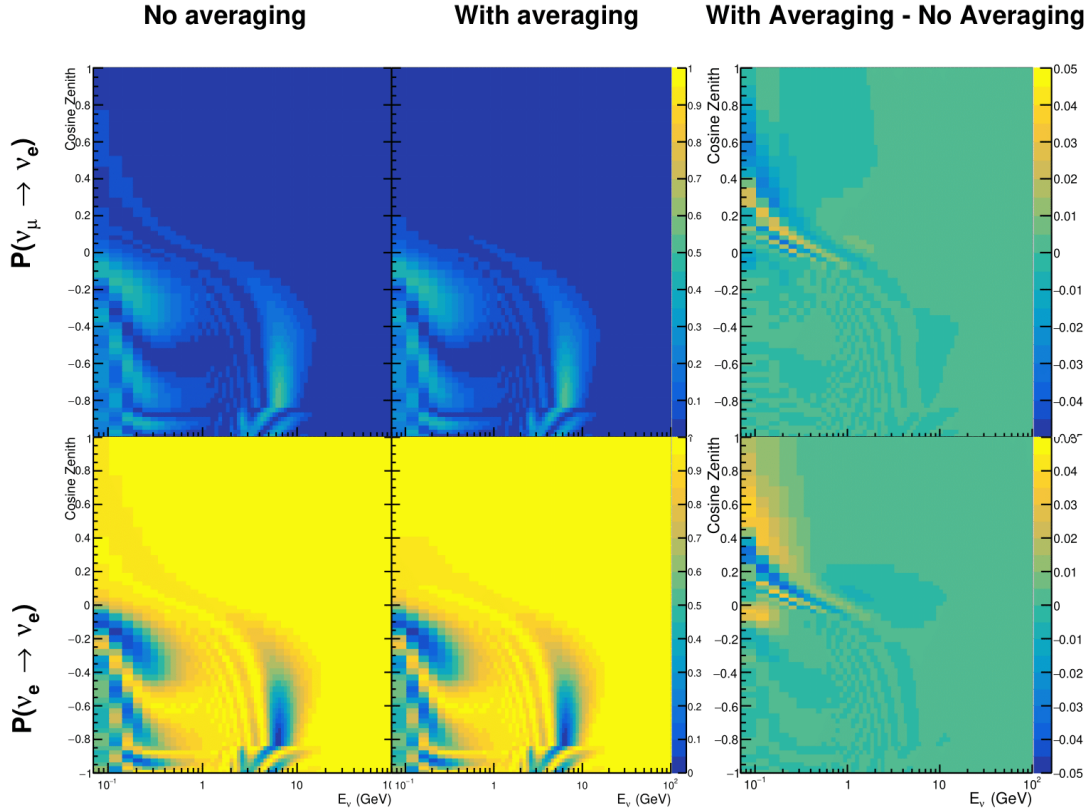


Figure 7.13: The oscillation probability, $P(\nu_\mu \rightarrow \nu_e)$ (top row) and $P(\nu_e \rightarrow \nu_e)$ (bottom row), given as a function of neutrino energy and zenith angle. The left column gives probabilities where a fixed production height of 25km is used. The middle column gives the probabilities where the production height is analytically averaged. The right column illustrates the difference in oscillation probability between the two different techniques.

8

2814

2815

Oscillation Analysis

2816 Using the samples and systematics defined in chapter 6, this chapter documents
2817 a simultaneous beam and atmospheric oscillation analysis from the T2K and SK
2818 experiments. The MaCh3 Bayesian MCMC framework introduced in chapter 4
2819 is used for all studies performed within this thesis.

2820 The MaCh3 framework has been validated through many tests. The code
2821 that handles the beam far detector samples was developed by the author and
2822 validated by comparison to the 2020 T2K analysis [72]. The sample event rates and
2823 likelihood evaluations of beam samples generated by the framework used within
2824 this thesis were compared to those from the T2K analysis by the author of this
2825 thesis. Variations of the sample predictions were compared at $\pm 1\sigma$ and $\pm 3\sigma$ and
2826 good agreement was found in all cases. A similar study, led by Dr. C. Wret was
2827 used to validate the near detector portion of the code [197]. The implementation
2828 of the atmospheric samples within MaCh3 was completed and cross-checked by
2829 the author of this thesis against the P-Theta framework (introduced in section 3.2).
2830 Both fitters are provided with the same inputs and can therefore cross-validate
2831 each other. These validations compared the event rate and likelihood calculation.
2832 Documentation of all the above validations can be found in [197]. These stringent
2833 validations ensure that the code is doing as intended.

2834 8.1 Monte Carlo Prediction

- 2835 Using the three sets of dial values (generated, pre-fit, and post-fit tunes) defined
 2836 in subsection 6.4.3, the predicted event rates for each sample are given in Table 8.1.
 2837 The oscillated and un-oscillated event rates are calculated for each tune.

Sample	Total Predicted Events					
	Generated		Pre-fit		Post-fit	
	Osc	UnOsc	Osc	UnOsc	Osc	UnOsc
SubGeV- <i>elike</i> -0dcy	7121.0	7102.6	6556.8	6540.0	7035.2	7015.7
SubGeV- <i>elike</i> -1dcy	704.8	725.5	693.8	712.8	565.7	586.0
SubGeV- <i>mulike</i> -0dcy	1176.5	1737.2	1078.6	1588.1	1182.7	1757.1
SubGeV- <i>mulike</i> -1dcy	5850.7	8978.1	5351.7	8205.1	5867.0	9009.9
SubGeV- <i>mulike</i> -2dcy	446.9	655.2	441.6	647.7	345.9	505.6
SubGeV- <i>pi0like</i>	1438.8	1445.4	1454.9	1461.1	1131.1	1136.2
MultiGeV- <i>elike</i> -nue	201.4	195.6	201.1	195.3	202.6	196.7
MultiGeV- <i>elike</i> -nuebar	1141.5	1118.3	1060.7	1039.5	1118.5	1095.7
MultiGeV- <i>mulike</i>	1036.7	1435.8	963.1	1334.1	1015.2	1405.9
MultiRing- <i>elike</i> -nue	1025.1	982.2	1026.8	984.3	1029.8	986.4
MultiRing- <i>elike</i> -nuebar	1014.8	984.5	991.0	962.0	1008.9	978.5
MultiRing- <i>mulike</i>	2510.0	3474.4	2475.6	3425.8	2514.6	3480.4
MultiRingOther-1	1204.5	1279.1	1205.8	1280.3	1207.4	1281.0
PCStop	349.2	459.2	338.4	444.7	346.8	456.1
PCThrus	1692.8	2192.5	1661.5	2149.8	1689.2	2187.8
UpStop-mu	751.2	1295.0	739.7	1271.6	750.4	1293.0
UpThruNonShower-mu	2584.4	3031.6	2577.9	3019.4	2586.8	3034.0
UpThruShower-mu	473.0	488.6	473.2	488.7	473.8	489.4
FHC1Rmu	328.0	1409.2	301.1	1274.7	345.1	1568.0
RHC1Rmu	133.0	432.3	122.7	396.2	135.0	443.9
FHC1Re	84.6	19.2	77.4	18.2	93.7	19.7
RHC1Re	15.7	6.4	14.6	6.1	15.9	6.3
FHC1Re1de	10.5	3.2	10.3	3.1	8.8	2.9

Table 8.1: The Monte Carlo predicted event rate of each far detector sample used within this analysis. Three model parameter tunes are considered, as defined in subsection 6.4.3. Un-oscillated and oscillated predictions are given, where the oscillated predictions assume Asimov A oscillation parameters provided in Table 2.2.

- 2838 Generally, the samples that target CCQE interaction modes observe a decrease
 2839 in prediction when comparing the generated values with the pre-fit dial values.
 2840 This is in accordance with the Monte Carlo being produced at $M_A^{QE} = 1.21\text{GeV}$
 2841 [156] whilst the pre-fit dial value is set to $M_A^{QE} = 1.03\text{GeV}$ as suggested by [196].

Furthermore, the predicted event rates of samples that target CCRES interaction modes are significantly reduced when considering the post-BANFF fit. This follows the observations in subsection 6.4.3. The strength of the accelerator neutrino experiment can be seen in the remarkable difference between the oscillated and unoscillated predictions in the FHC1Rmu and RHC1Rmu samples. There is a very clear decrease in the expected event rate between the oscillated and un-oscillated predictions which is not as obvious as in the atmospheric samples. This is due to the fact that the beam energy is tuned to the maximum disappearance probability, which is not the case for the naturally generated atmospheric neutrinos.

8.2 Likelihood Scans

Using the definition of the likelihood presented in section 6.5, the contribution of each sample to the likelihood from a variation of a particular parameter can be studied. This process identifies which samples drive the determination of the oscillation parameters in the joint fit. Figure 8.1 presents the variation of all the samples (beam and atmospheric) at the far detector to the oscillation parameters of interest: δ_{CP} , $\sin^2(\theta_{13})$, $\sin^2(\theta_{23})$, and Δm_{32}^2 . These plots are colloquially called ‘likelihood scans’ (or ‘log-likelihood scans’). The process of making these plots is as follows. An Asimov data set is built using the AsimovA oscillation parameters and pre-fit systematic tune. The Monte Carlo is then reweighted using the value of the oscillation parameter at each point on the x-axis of the scan. The likelihood is then calculated between the Asimov data and Monte Carlo prediction and plotted.

Due to the caveat of fixed systematic parameters and the correlations between oscillation parameters being ignored when creating these likelihood scans, the value of $\chi^2 = 1$ (or $-2 \times \ln(\text{Likelihood}) = 1$) does not equate to the typical 1σ sensitivity. However, it does give an indication of which samples respond most strongly to variations in a particular oscillation parameter. The point at

2870 which the likelihood tends to zero illustrates the value of the parameter used
 2871 to build the Asimov data prediction.

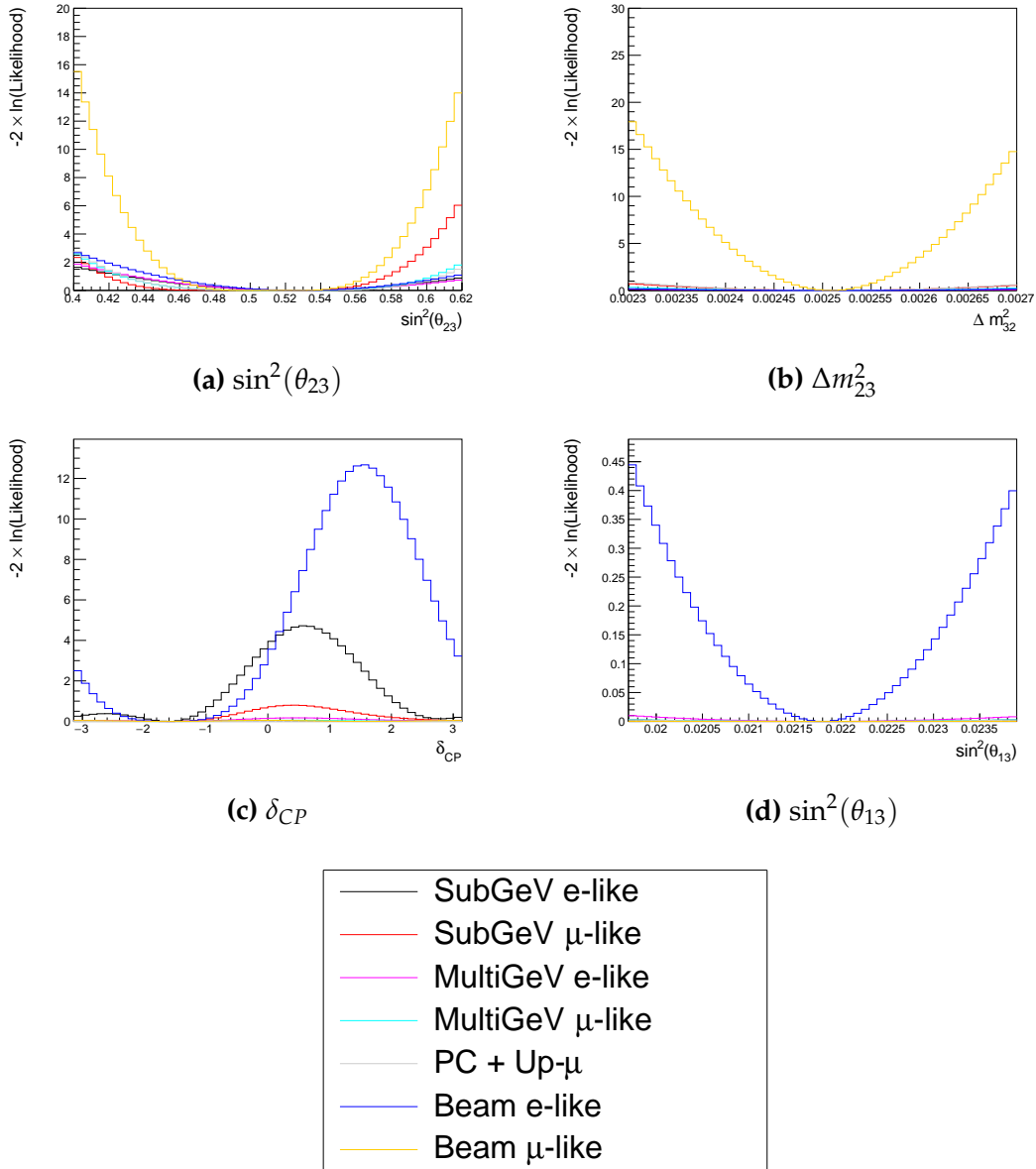


Figure 8.1: The response of the likelihood, as defined in section 6.5, illustrating the response of the samples to a variation of an oscillation parameter.

2872 The sensitivity to $\sin^2(\theta_{23})$ is mostly dominated by the beam muon-like
 2873 samples. The response of an individual atmospheric sample is small but non-
 2874 negligible such that the summed response over all atmospheric samples becomes
 2875 comparable to that of the muon-like beam samples. Consequently, the sensitivity

of the joint fit to $\sin^2(\theta_{23})$ would be expected to be greater than the beam-only analysis. The only sample that responds to the $\sin^2(\theta_{13})$ oscillation parameter is the electron-like beam sample. Consequently, no increase in sensitivity beyond that of the T2K-only analysis would be expected from the joint fit. Regardless, the sensitivity of the beam sample is significantly weaker than the external reactor constraint so prior knowledge will dominate any sensitivity to $\sin^2(\theta_{13})$ which is included within this thesis. The Δm_{21}^2 and $\sin^2(\theta_{12})$ parameters are not considered as there is simply no sensitivity in any sample considered within this analysis. The response to Δm_{32}^2 is completely dominated by the beam muon-like samples. This is because the beam neutrino energy is specifically tuned to match the maximal disappearance probability. Despite this, improvements to the $|\Delta m_{32}^2|$ sensitivity may be expected due to additional mass hierarchy determination added by the atmospheric samples.

Two-dimensional scans of the appearance ($\sin^2(\theta_{13}) - \delta_{CP}$) and disappearance ($\sin^2(\theta_{23}) - \Delta m_{32}^2$) parameters are illustrated in Figure 8.2 and Figure 8.3, respectively. The caveat of fixed systematic parameters and correlations between other oscillation parameters being neglected still apply.

The appearance log-likelihood scans show the distinct difference in how the beam and atmospheric samples respond. The beam samples have an approximately constant width of the 2σ and 3σ contours, throughout all ranges of δ_{CP} . Whereas, the response of the atmospheric samples to $\sin^2(\theta_{13})$ is very strongly correlated to the value of δ_{CP} . At higher values of $\sin^2(\theta_{13})$, two lobes appear around $\delta_{CP} \sim -\pi/2$ and $\delta_{CP} \sim 2.4$. Consequently, this difference allows some of the degeneracy in a beam-only fit to be broken. Comparing the beam-only and joint fit likelihood scans, the 2σ continuous contour in δ_{CP} for beam samples becomes closed when the atmospheric samples are added. This may result in a stronger sensitivity to δ_{CP} . Similarly, the width of the 3σ contours also becomes dependent upon the value of δ_{CP} . Furthermore, atmospheric samples have little sensitivity to $\sin^2(\theta_{13})$ on their own, as evidenced in Figure 8.1, but may improve sensitivity to the parameter when combined within the simultaneous

2906 fit. It is important to remember that these likelihood scans are not sensitivity
2907 measurements as the systematic parameters are fixed and the correlation between
2908 oscillation parameters is neglected. However, they are a very encouraging result
2909 for the joint fit.

2910 The disappearance log-likelihood scans in $\sin^2(\theta_{23}) - \Delta m_{32}^2$ space (Figure 8.3)
2911 show the expected behaviour when considering the one-dimensional scans
2912 already discussed. The uncertainty on the width of $|\Delta m_{32}^2|$ is mostly driven by the
2913 beam samples. However, the width of this contour in the inverted mass region
2914 ($\Delta m_{32}^2 < 0$) is significantly reduced due to the ability of the atmospheric samples
2915 to select the correct (normal) mass hierarchy. The width of the uncertainty
2916 in $\sin^2(\theta_{23})$ is also reduced compared to the beam-only sensitivities, with a
2917 further decrease in the inverted hierarchy region due to the better mass hierarchy
2918 determination.

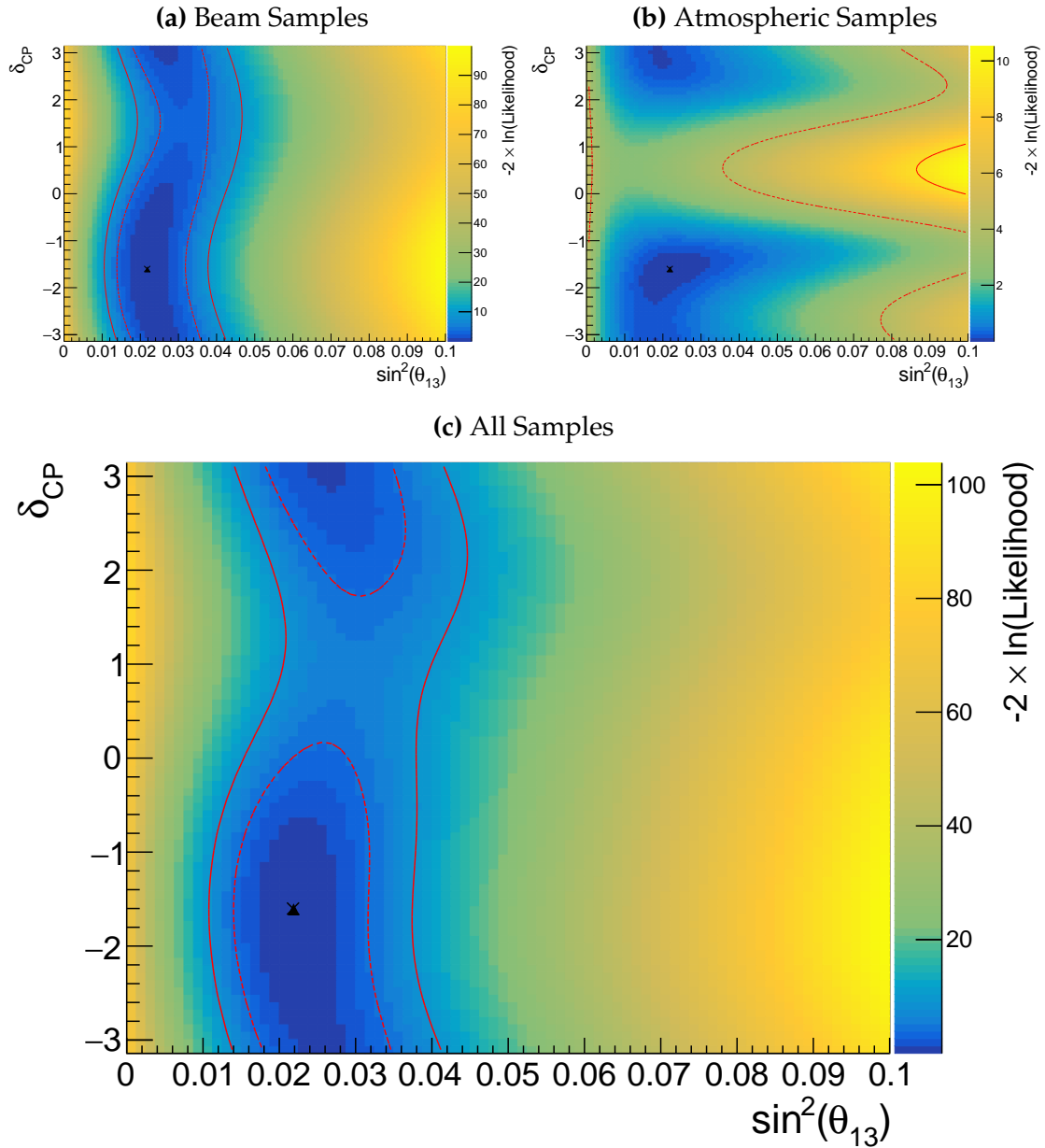


Figure 8.2: Two-dimensional log-likelihood scan of the appearance ($\sin^2(\theta_{13})$)– δ_{CP}) parameters showing the response of the beam samples (top left), atmospheric samples (top right) and the summed response (bottom). The Asimov A oscillation parameters, defined in Table 2.2, are known to be the true point (Black Cross). The position of the smallest log-likelihood is highlighted with the triangle. Prior uncertainty terms of the oscillation parameters are neglected. The two(three) sigma contour levels are illustrated with the dashed(solid) red line.

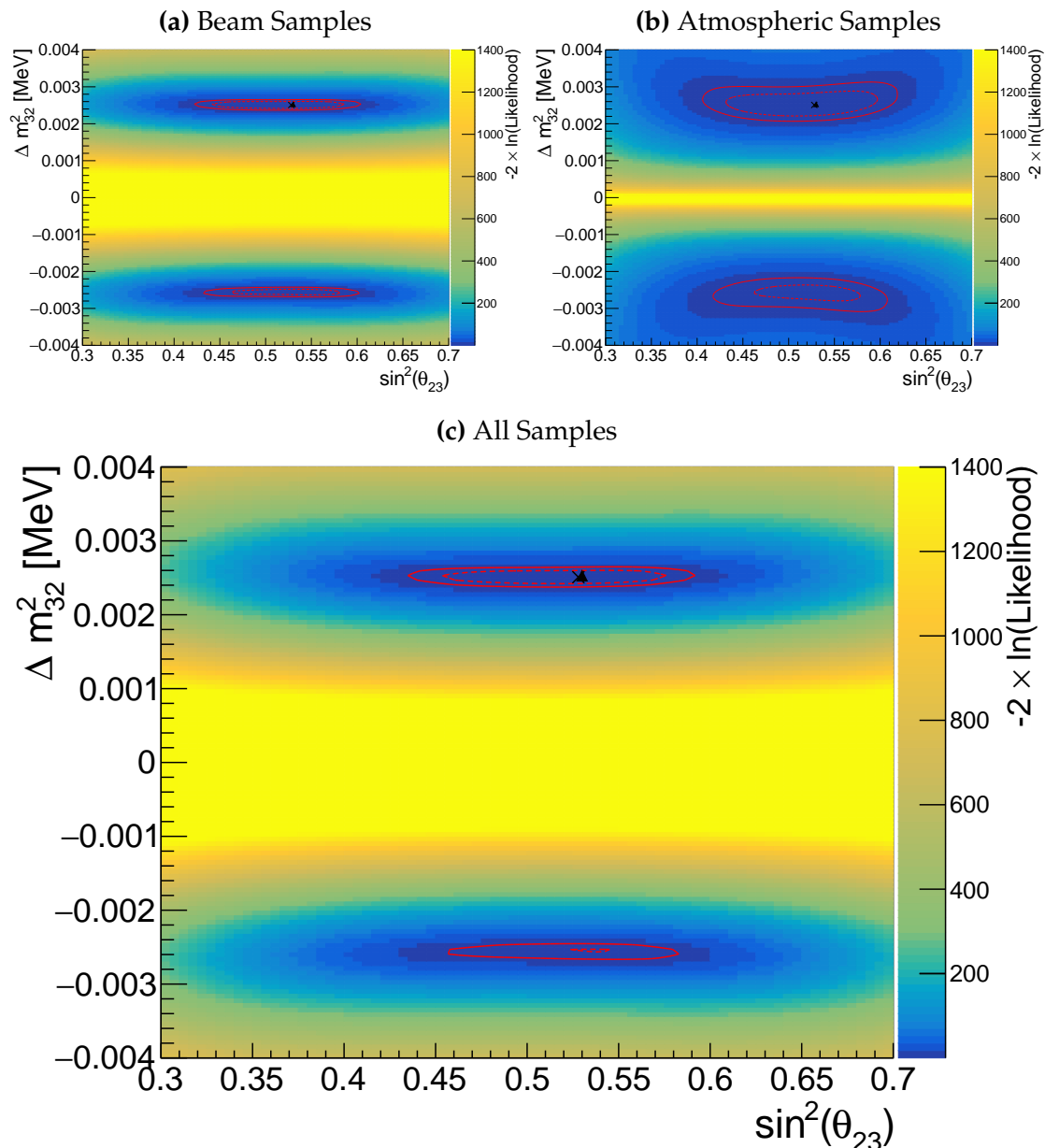


Figure 8.3: Two-dimensional log-likelihood scan of the disappearance ($\sin^2(\theta_{23}) - \Delta m_{32}^2$) parameters showing the response of the beam samples (top left), atmospheric samples (top right) and the summed response (bottom). The Asimov A oscillation parameters, defined in Table 2.2, are known to be the true point (Black Cross). The position of the smallest log-likelihood is highlighted with the triangle. Prior uncertainty terms of the oscillation parameters are neglected. The two(three) sigma contour levels are illustrated with the dashed(solid) red line.

The likelihood scans illustrated thus far only consider the sensitivity of this analysis for a fixed set of true oscillation parameters, namely Asimov A defined in Table 2.2. Whilst computationally infeasible to run many fits at different parameter sets, it is possible to calculate the likelihood response to different Asimov data sets. Figure 8.4 and Figure 8.5 illustrate how the sensitivity changes for differing true values of δ_{CP} and $\sin^2(\theta_{23})$, respectively. For both of these plots, the other oscillation parameters are fixed at their Asimov A values. Consequently, the caveat of fixed systematic parameters and correlations between other oscillation parameters being neglected still applies.

To explain how these plots are made, consider Figure 8.4. This plot is built by considering multiple one-dimensional log-likelihood scans, each creating an Asimov data set with the value of δ_{CP} taken from the x-axis. The likelihood to this particular Asimov data set is calculated after reweighting the Monte Carlo prediction to each value of δ_{CP} on the y-axis.

Figure 8.4 illustrates the sensitivity to δ_{CP} . To interpret this plot, larger contours result in more phase space being excluded from the 1σ region. The 1σ intervals contain regions where the beam and atmospheric samples have discontinuous contours. For example, for the x-axis value of $\delta_{CP} = 0$, the beam samples sensitivity would include two discontinuous regions excluded from the 1σ interval: $\delta_{CP} \sim 0$ and $\delta_{CP} \sim \pi$. This behaviour is also seen in atmospheric samples response but at a value of $\delta_{CP} \sim -1$. This difference allows the joint fit to have increased sensitivity to these regions. Consequently, the difference between the beam-only and joint beam-atmospheric fit should be studied using multiple Asimov data sets.

Despite the increased sensitivity at 1σ , the 2σ intervals from the joint fit are more similar to the two independent sensitivities and the off-diagonal degeneracies mostly remain. This indicates that the joint fit has the strength to aid parameter determination but can not entirely break the degeneracies in δ_{CP} at higher confidence levels.

2948 Figure 8.5 illustrates a similar analysis as above, although the value of $\sin^2(\theta_{23})$
2949 is varied and δ_{CP} is fixed to the Asimov A parameter value. Due to the beam
2950 parameters and baseline being tuned to specifically target this oscillation parame-
2951 ter, the average sensitivity of the beam samples is stronger than the atmospheric
2952 samples. However, the degeneracy around maximal mixing ($\sin^2(\theta_{23}) = 0.5$) is
2953 significantly more peaked in the beam samples compared to the atmospheric
2954 samples. This means that a value of $\sin^2(\theta_{23}) \sim 0.56$ would be contained within
2955 the 1σ confidence interval for a true value of $\sin^2(\theta_{23}) \sim 0.46$ if using the beam-
2956 only analysis, whereas it would be excluded in the joint analysis.

2957 This behaviour is strengthened when considering the 2σ intervals, to the
2958 point where two distinct discontinuous regions of the 2σ intervals exist around
2959 the Asimov point $\sin^2(\theta_{23}) \sim 0.41, 0.6$. Given the caveat of only considering
2960 likelihood scans, the joint analysis would mostly eliminate the discontinuous
2961 intervals in these regions. This means that the joint fit could feasibly have an
2962 increased preference for the correct octant hypothesis.

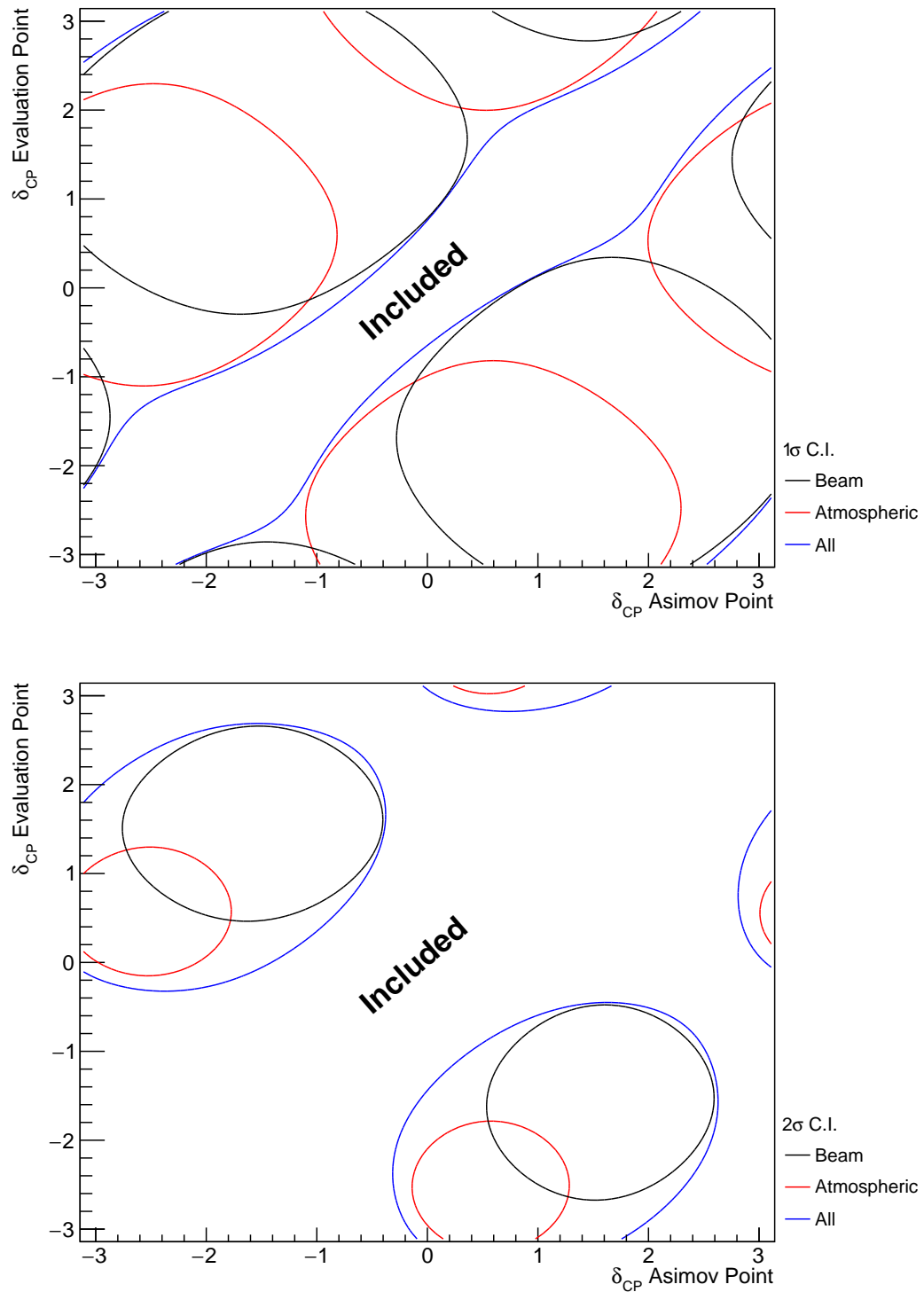


Figure 8.4: A series of one-dimensional likelihood scans over δ_{CP} , where an Asimov data set is built for each value of δ_{CP} on the x-axis and the likelihood is evaluated for each value of δ_{CP} on the y-axis. The diagonal represents the minimum log-likelihood and defines the region included within the 1σ (Top) and 2σ (Bottom) confidence intervals. The beam (black) and atmospheric (red) samples are individually plotted and the joint fit (blue) is the sum of the two.

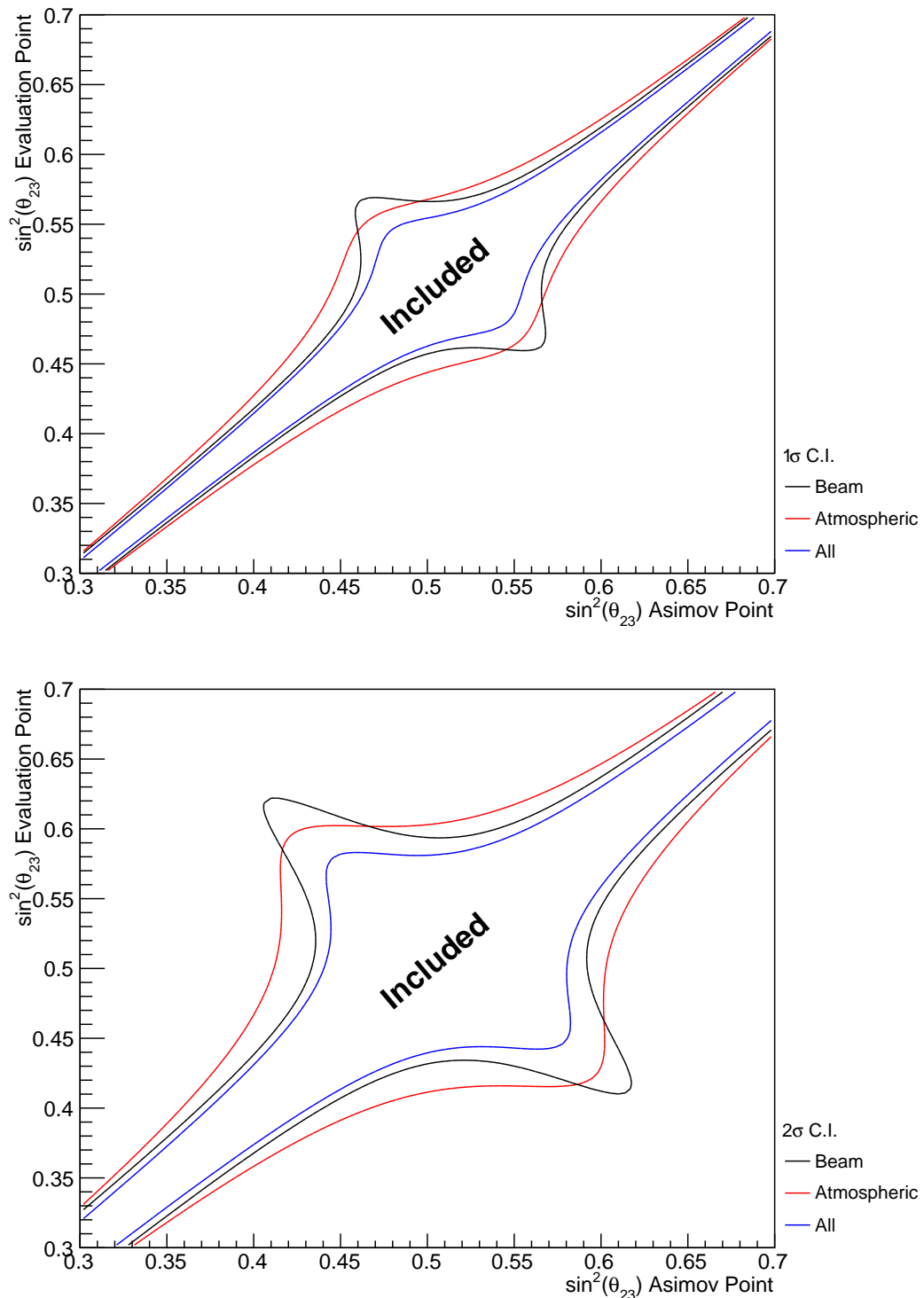


Figure 8.5: A series of one-dimensional likelihood scans over $\sin^2(\theta_{23})$, where an Asimov data set is built for each value of $\sin^2(\theta_{23})$ on the x-axis and the likelihood is evaluated for each value of $\sin^2(\theta_{23})$ on the y-axis. The diagonal represents the minimum log-likelihood and defines the region included within the 1σ (Top) and 2σ (Bottom) confidence intervals. The beam (black) and atmospheric (red) samples are individually plotted and the joint fit (blue) is the sum of the two.

Alongside oscillation parameters (Figure 8.1), the sensitivity to systematic parameters can also be studied for the joint fit. As some of these parameters are correlated between the beam and atmospheric events, the response of the atmospheric samples can modify the constraint. This means the systematics can have additional constraints than they would from a beam-only analysis. Therefore, the response from the beam and the atmospheric samples to various systematic parameters has been compared in Figure 8.6. The Asimov data set has been created using the AsimovA oscillation parameter and the pre-fit systematic tune. For example, the systematic parameter controlling the effective axial mass coupling in CCQE interactions, M_A^{QE} , is clearly dominated by the ND constraint. An example where the response of the atmospheric sample is approximately similar to the near detector constraint is the 2p2h CtoO normalisation systematic. This systematic models the scaling of the 2p2h interaction cross-section on a carbon target to an oxygen target. There are also systematics that have no near detector constraint. For example, the systematic parameters which describe the normalisation of the NC1Gamma and NCOther interaction modes. The atmospheric and beam samples can have similar sensitivity to these systematics due to their similar composition in energy and interaction mode. As an example of how the atmospheric samples can help constrain systematic parameters used within the T2K-only analysis, these NC background events in beam electron-like samples will be more constrained with the additional sensitivity of atmospheric samples. This would be expected to reduce the overall uncertainty of the beam electron-like event rates in the joint analysis compared to the beam-only studies. This could modify the sensitivity of the beam samples due to the more constrained background events.

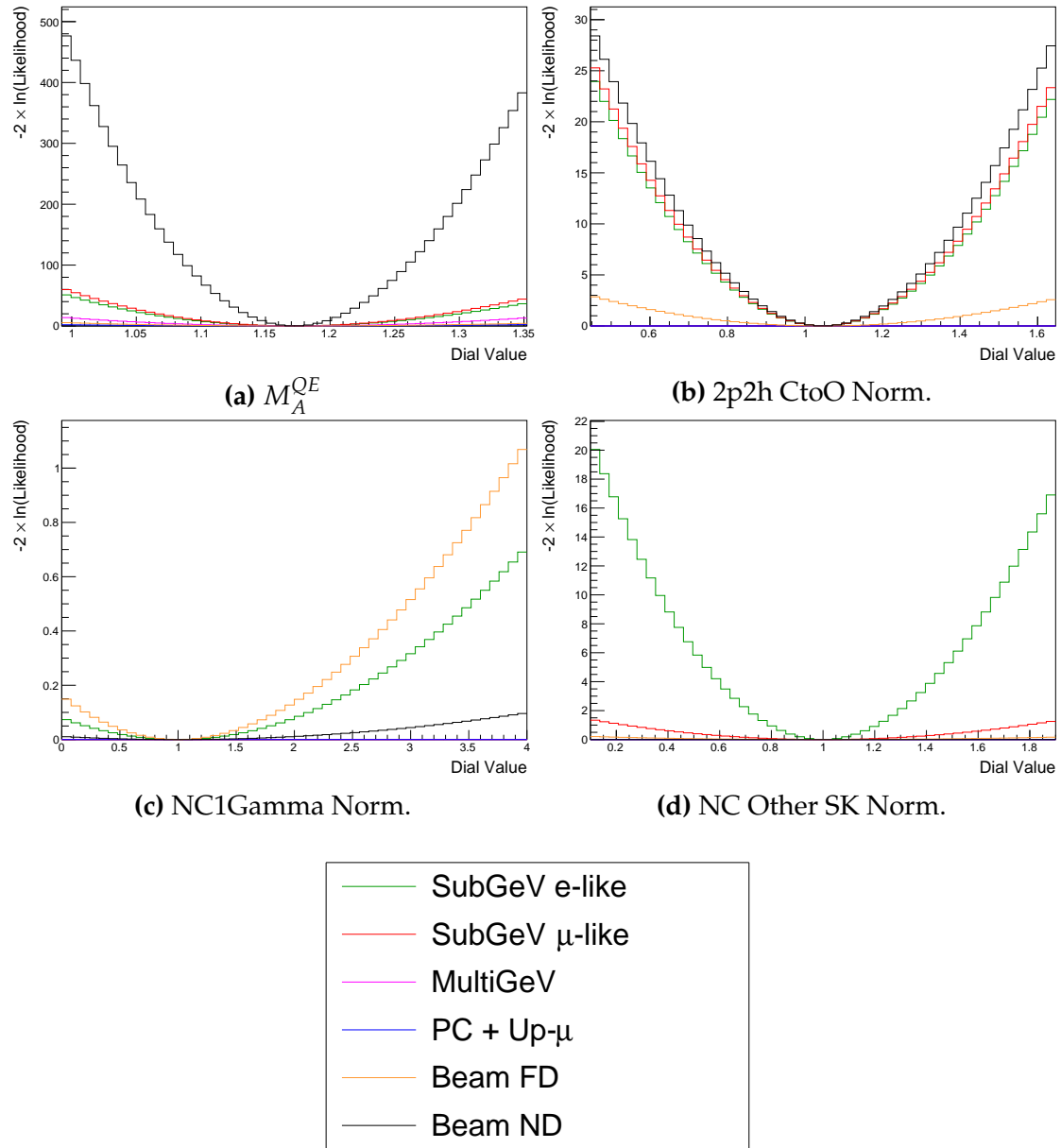


Figure 8.6: The response of the likelihood, as defined in section 8.2, illustrating the response of the samples to the various cross-section systematic parameters.

2988 8.3 Sensitivity Studies

2989 DB: Statistics vs Systematics dominated

2990 The sensitivities of the joint T2K and SK oscillation analysis are presented
2991 in the form of Asimov fits. These fits consider beam samples from the near
2992 and far detector alongside atmospheric samples at SK. This technique builds an
2993 Asimov data set (following section 6.5) using the AsimovA oscillation parameters
2994 and post-BANFF systematic tune, which is then fit. This technique eliminates
2995 statistical fluctuations from the data, therefore, providing the maximum sen-
2996 sitivity of the analysis.

2997 In practice, the Asimov fits presented within this analysis are modified from
2998 the above definition. An Asimov prediction of both beam and atmospheric far
2999 detector samples is fit whilst the true data is used for near detector samples. The
3000 Asimov predictions at the far detector are built using the post-BANFF tune (as
3001 discussed in section 3.2). These modifications mean that the results are equivalent
3002 to performing a far detector Asimov fit using inputs from the BANFF data fit.
3003 Consequently, this allows the results to be cross-checked with the results from
3004 the P-Theta analysis. The comparison has been performed and is documented in
3005 [213]. No significant discrepancies were found between the fitters.

3006 This section proceeds with the following studies. Firstly, the sensitivity
3007 of the atmospheric samples using the correlated detector model is detailed in
3008 subsection 8.3.1. This includes studying the choice of applying the 2020 PDG
3009 reactor constraint [73] to the atmospheric samples, which is documented in
3010 subsection 8.3.2. Additionally, the effect of applying the near-detector constraints
3011 onto the atmospheric samples is discussed in subsection 8.3.3. The main result is
3012 the sensitivity of the simultaneous beam and atmospheric fit. The sensitivities,
3013 both with and without the application of the reactor constraint, are presented
3014 in subsection 8.3.4 and subsection 8.3.5, respectively. To indicate the benefit
3015 of the joint analysis, the sensitivities are compared to the 2020 T2K beam-only
3016 sensitivities [72, 214] in subsection 8.3.6 and subsection 8.3.7. The T2K analysis

3017 is used as a reference as it uses the same samples and a similar systematic
 3018 model. As shown in section 8.2, the response of the beam and atmospheric
 3019 samples change depending upon the true set of oscillation parameters assumed.
 3020 Therefore, subsection 8.3.8 documents the sensitivities at an alternative oscillation
 3021 parameter set. These results have been presented at the Neutrino 2022 conference
 3022 on behalf of the T2K and SK collaborations [104].

3023 8.3.1 Atmospheric-Only Sensitivity Without Reactor Constraint

3024 This section presents the results of an Asimov fit using samples from the near
 3025 detector and only atmospheric samples from the far detector. The results are
 3026 presented as one-dimensional or two-dimensional histograms which have been
 3027 marginalised over all other parameters using the technique outlined in sub-
 3028 section 4.3.1. Each histogram displays the posterior probability density and
 3029 illustrates the credible intervals, calculated using the technique in subsection 4.3.2.
 3030 For this fit, a flat prior is used for $\sin^2(\theta_{13})$ meaning that the reactor constraint is
 3031 not applied. The Asimov data is generated assuming the AsimovA oscillation pa-
 3032 rameter set defined in Table 2.2 and the post-BANFF systematic parameter tune.

3033 Figure 8.7 illustrates the posterior probability density for δ_{CP} , marginalised
 3034 over both hierarchies. The fit favours the known oscillation parameter ($\delta_{CP} =$
 3035 -1.601) although the posterior probability is very flat through the range of
 3036 $-\pi < \delta_{CP} < -1$ and $2 < \delta_{CP} < \pi$. There is also a region around $\delta_{CP} \sim 0.4$
 3037 which is disfavoured at 2σ . This indicates that the SK samples can rule out some
 3038 parts of the CP conserving parameter space reasonably well, near $\delta_{CP} \sim 0.4$,
 3039 when the true value of $\delta_{CP} \sim -\pi/2$.

3040 The posterior probability density in Δm_{32}^2 is given in Figure 8.8. This distribu-
 3041 tion includes steps in both the normal hierarchy (NH, $\Delta m_{32}^2 > 0$) and the inverse
 3042 hierarchy (IH, $\Delta m_{32}^2 < 0$). The highest posterior probability density is found
 3043 within the NH 1σ credible interval, which agrees with the known oscillation
 3044 parameter value, $2.509 \times 10^{-3}\text{eV}^2$. However, all of the credible intervals span
 3045 both of the hierarchy hypotheses.

Without Reactor Constraint, Both Hierarchies

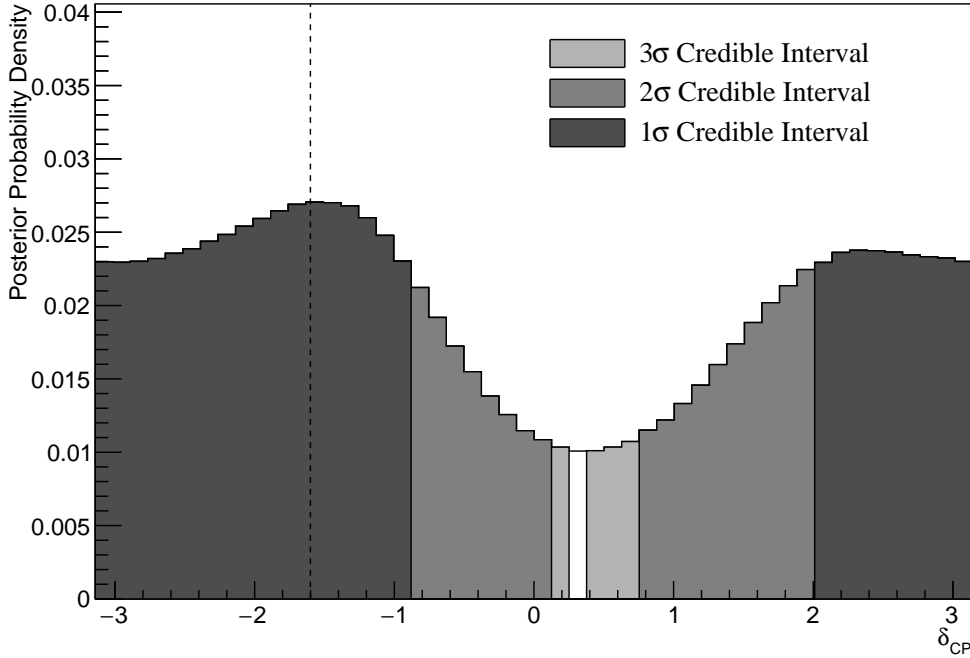


Figure 8.7: The one-dimensional posterior probability density distribution in δ_{CP} , marginalised over both hierarchies, from the SK atmospheric-only fit. The reactor constraint is not applied. The vertical dashed line represents the known value of δ_{CP} .

	LO ($\sin^2 \theta_{23} < 0.5$)	UO ($\sin^2 \theta_{23} > 0.5$)	Sum
NH ($\Delta m_{32}^2 > 0$)	0.17	0.40	0.58
IH ($\Delta m_{32}^2 < 0$)	0.13	0.29	0.42
Sum	0.31	0.69	1.00

Table 8.2: The distribution of steps in an SK atmospheric-only fit, presented as the fraction of steps in the upper (UO) and lower (LO) octants and the normal (NH) and inverted (IH) hierarchies. The reactor constraint is not applied. The Bayes factors are calculated as $B(\text{NH}/\text{IH}) = 1.37$ and $B(\text{UO}/\text{LO}) = 2.24$.

Following the discussion in subsection 4.3.3, the Bayes factor for hierarchy preference can be calculated by determining the fraction of steps that fall into the NH and the IH regions, as an equal prior is placed on both hypotheses. A similar calculation can be performed by calculating the fraction of steps which fall in the lower octant (LO, $\sin^2 \theta_{23} < 0.5$) or upper octant (UO, $\sin^2 \theta_{23} > 0.5$). The fraction of steps, broken down by hierarchy and octant, are given in Table 8.2. The Bayes factor for preferred hierarchy hypothesis is $B(\text{NH}/\text{IH}) = 1.37$. Jeffrey's

Without Reactor Constraint, Both Hierarchies

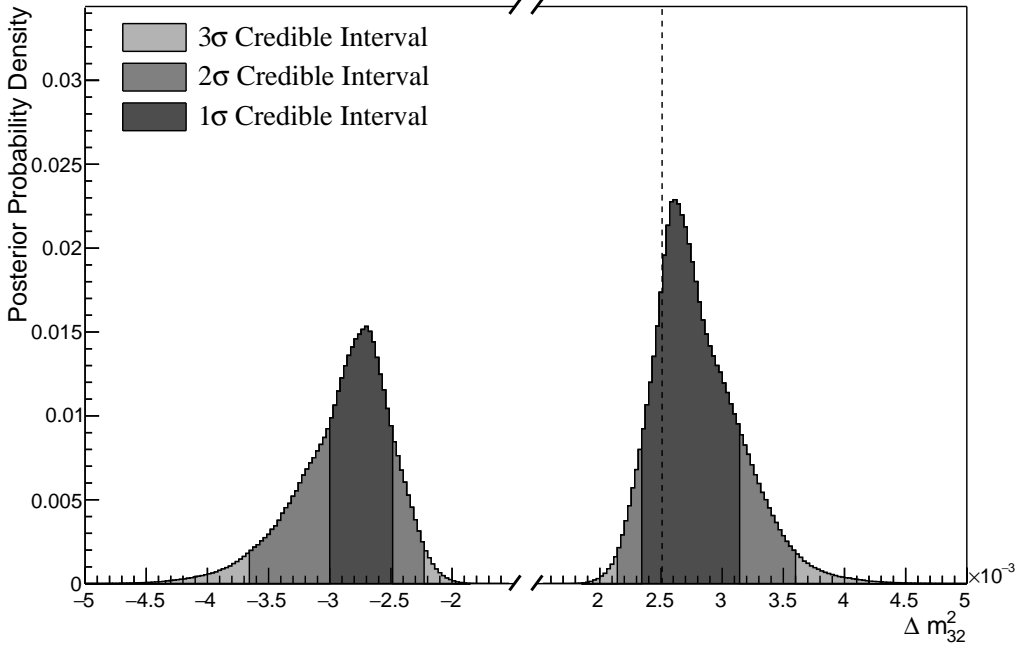


Figure 8.8: The one-dimensional posterior probability density distribution in Δm_{32}^2 , marginalised over both hierarchies, from the SK atmospheric-only fit. The reactor constraint is not applied. The vertical dashed line represents the known value of Δm_{32}^2 .

scale, given in Table 4.1, states this value of the Bayes factor indicates a weak preference for the normal hierarchy hypothesis. The Bayes factor for choice of octant is $B(\text{UO}/\text{LO}) = 2.24$. This is also classified as a weak preference for the UO. Both of these show that the fit is returning the correct choice of hypotheses (NH and UO) for the known Asimov A oscillation parameters defined in Table 2.2.

The 1 σ credible intervals, broken down by hierarchy, and position in parameter space of the highest posterior probability density is given in Table 8.3. These are taken from the one-dimensional projections of the oscillation parameters, marginalised over all other parameters within the fit. As the distribution is binned, the highest posterior density is presented as the center of the bin with the highest posterior density with an error equal to the bin width. For the known Asimov value of $\delta_{CP} = -1.601$, the 1 σ credible interval rules out a region between $\delta_{CP} = -0.88$ and $\delta_{CP} = 1.96$, when marginalising over both hierarchies. The position of the highest posterior density is $\delta_{CP} = -1.57 \pm 0.07$ which is clearly

Parameter	Interval	HPD
δ_{CP} , (BH)	$[-\pi, -0.88], [2.01, \pi]$	-1.57 ± 0.07
δ_{CP} , (NH)	$[-\pi, -0.88], [1.88, \pi]$	-1.57 ± 0.07
δ_{CP} , (IH)	$[-\pi, -0.88], [2.01, \pi]$	-1.57 ± 0.07
Δm_{32}^2 (BH) [$\times 10^{-3}\text{eV}^2$]	$[-3.00, -2.49], [2.34, 3.14]$	2.61 ± 0.02
Δm_{32}^2 (NH) [$\times 10^{-3}\text{eV}^2$]	$[2.41, 3.04]$	2.59 ± 0.03
Δm_{32}^2 (IH) [$\times 10^{-3}\text{eV}^2$]	$[-3.11, -2.41]$	-2.73 ± 0.03
$\sin^2(\theta_{23})$ (BH)	$[0.476, 0.584]$	0.542 ± 0.006
$\sin^2(\theta_{23})$ (NH)	$[0.488, 0.596]$	0.554 ± 0.006
$\sin^2(\theta_{23})$ (IH)	$[0.476, 0.584]$	0.542 ± 0.006

Table 8.3: The position of the highest posterior probability density (HPD) and width of the 1σ credible interval for the SK atmospheric-only fit. The reactor constraint is not applied. The values are presented by which hierarchy hypothesis is assumed: marginalised over both hierarchies (BH), normal hierarchy only (NH), and inverted hierarchy only (IH).

3067 compatible with the known oscillation parameter value.

3068 The sensitivity of the atmospheric samples to $\sin^2(\theta_{13})$ is presented in Fig-
 3069 ure 8.9. The likelihood scans presented in Figure 8.1 suggest that the sensitivity
 3070 to $\sin^2(\theta_{13})$ will be small. This behaviour is also seen in the fit results, where the
 3071 width of the 1σ credible intervals span the region of $\sin^2(\theta_{13}) = [0.008, 0.08]$. This
 3072 is more than an order of magnitude worse than the constraint from reactor
 3073 experiments [73].

3074 As previously discussed, the correlations between oscillation parameters are
 3075 also important to understand how the atmospheric samples respond. Figure 8.10
 3076 illustrates the two dimensional $\sin^2(\theta_{13}) \times \delta_{CP}$ sensitivity, marginalised over all
 3077 other parameters. The shape of the 1σ credible interval shows that the constrain-
 3078 ing power of the fit on δ_{CP} is dependent upon the value of $\sin^2(\theta_{13})$. Furthermore,
 3079 they show a strong resemblance to the likelihood scans illustrated in Figure 8.2.
 3080 Whilst the atmospheric samples do not strongly constrain the value of $\sin^2(\theta_{13})$,
 3081 the value of $\sin^2(\theta_{13})$ does impact the atmospheric samples' sensitivity to δ_{CP} .

Without Reactor Constraint, Both Hierarchies

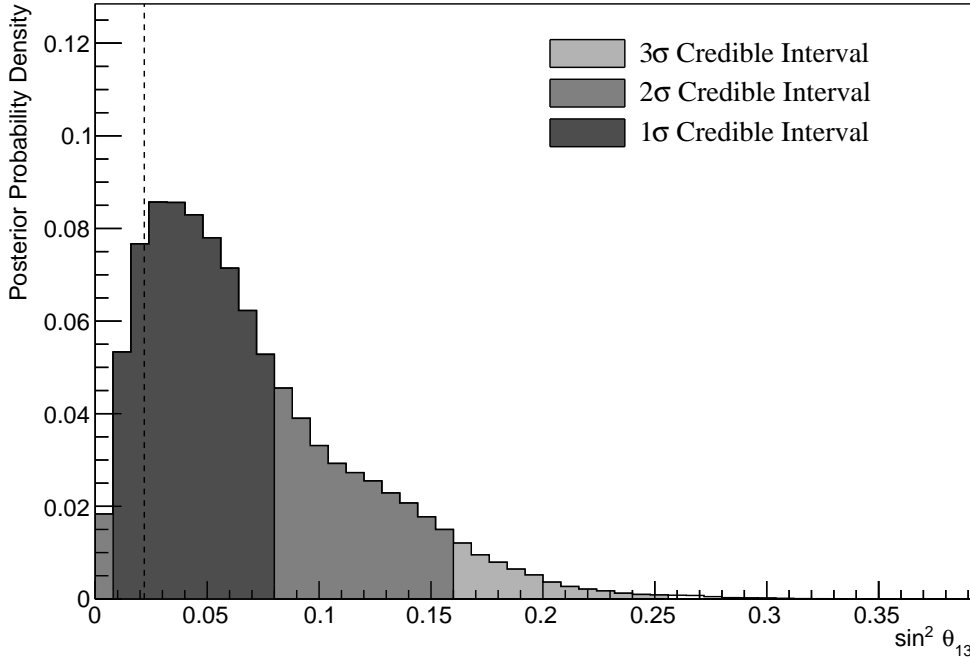


Figure 8.9: The one-dimensional posterior probability density distribution in $\sin^2(\theta_{13})$, marginalised over both hierarchies, from the SK atmospheric-only fit. The reactor constraint is not applied. The vertical dashed line represents the known value of $\sin^2(\theta_{13})$.

3082 The $\sin^2(\theta_{23}) \sim \Delta m_{32}^2$ disappearance contours are illustrated in Figure 8.11. As
 3083 expected, the area contained in the inverted hierarchy 1σ credible interval is
 3084 slightly smaller than that in the normal hierarchy. This follows from the Bayes
 3085 factor showing a weak preference for NH meaning that more of the steps will exist
 3086 in the $\Delta m_{32}^2 > 0$ region. The known oscillation parameters of $\sin^2(\theta_{23}) = 0.528$
 3087 and $\Delta m_{32}^2 = 2.509 \times 10^{-3} \text{ eV}^2$ are contained within the 1σ credible interval.

3088 Figure 8.12 illustrates the two-dimensional projections for each permutation of
 3089 oscillation parameters which this analysis is sensitive to: δ_{CP} , $\sin^2(\theta_{13})$, $\sin^2(\theta_{23})$,
 3090 and Δm_{32}^2 . The purpose of this plot is to illustrate the correlations between
 3091 the oscillation parameters. The contours are calculated whilst marginalising
 3092 over both hierarchies, however, only the NH is illustrated when plotting the
 3093 Δm_{32}^2 parameter. As expected the correlations play a significant role in these
 3094 sensitivity measurements, especially the choice of the $\sin^2(\theta_{13})$ constraint. Most
 3095 notably, the application of reactor constraint would be expected to alter both the

Without Reactor Constraint, Both Hierarchies

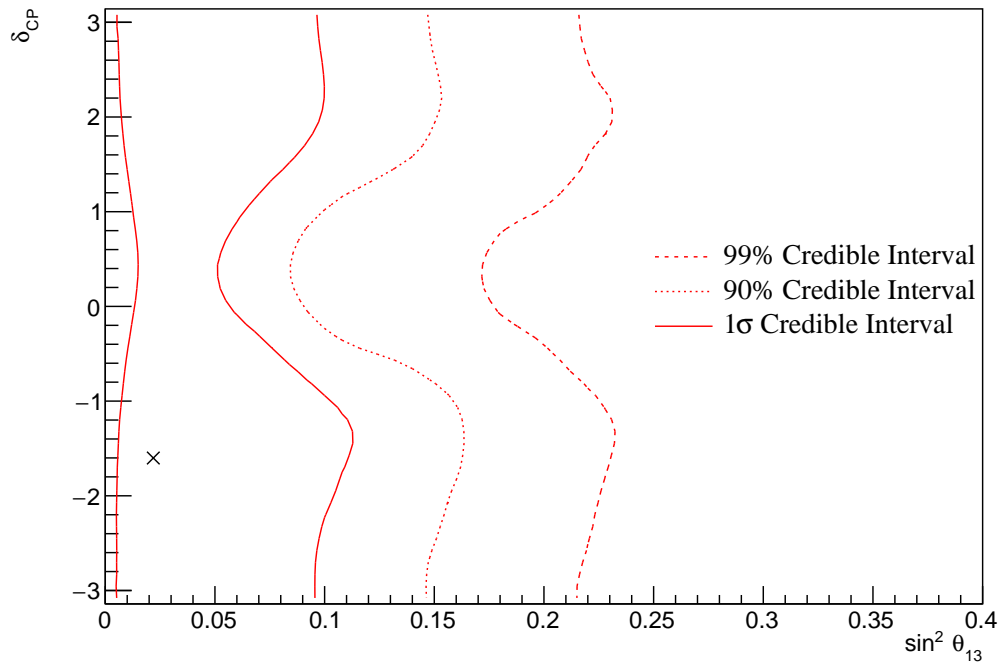


Figure 8.10: The two-dimensional posterior probability density distribution in $\delta_{CP}^\nu \sin^2(\theta_{13})$, marginalised over both hierarchies, from the SK atmospheric-only fit. The reactor constraint is not applied. The marker represents the known value of $\delta_{CP}^\nu \sin^2(\theta_{13})$.

3096 width and position of the Δm_{32}^2 intervals due to the strong correlation between
3097 the parameters.

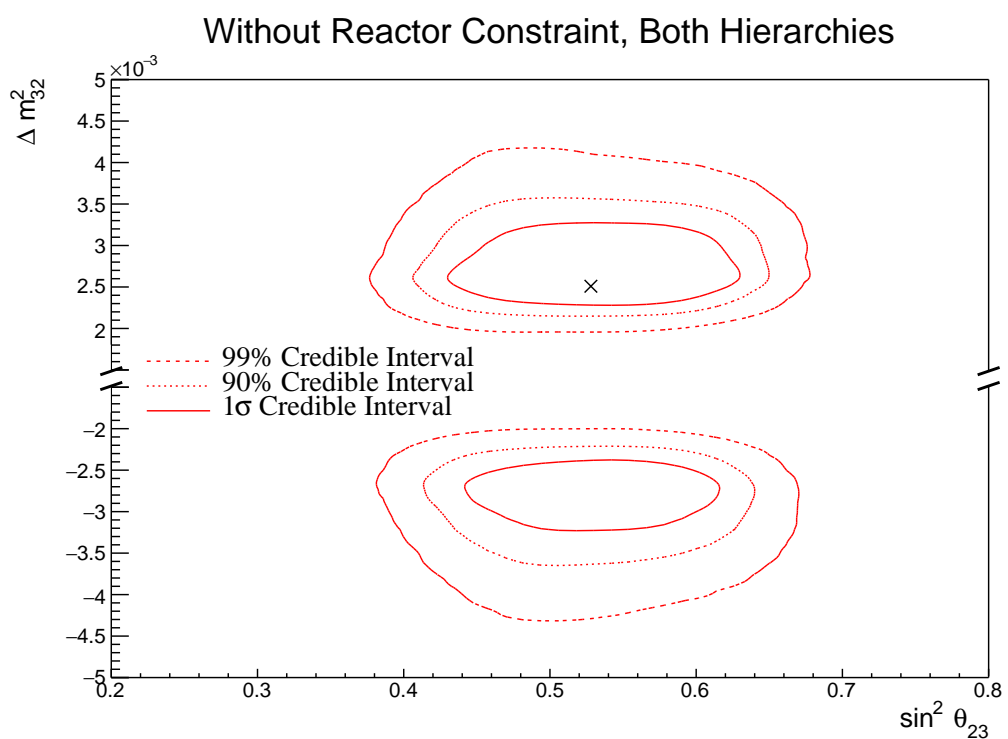


Figure 8.11: The two-dimensional posterior probability density distribution in $\Delta m_{32}^2 \sim \sin^2(\theta_{23})$, marginalised over both hierarchies, from the SK atmospheric-only fit. The reactor constraint is not applied. The marker represents the known value of $\Delta m_{32}^2 \sim \sin^2(\theta_{23})$.

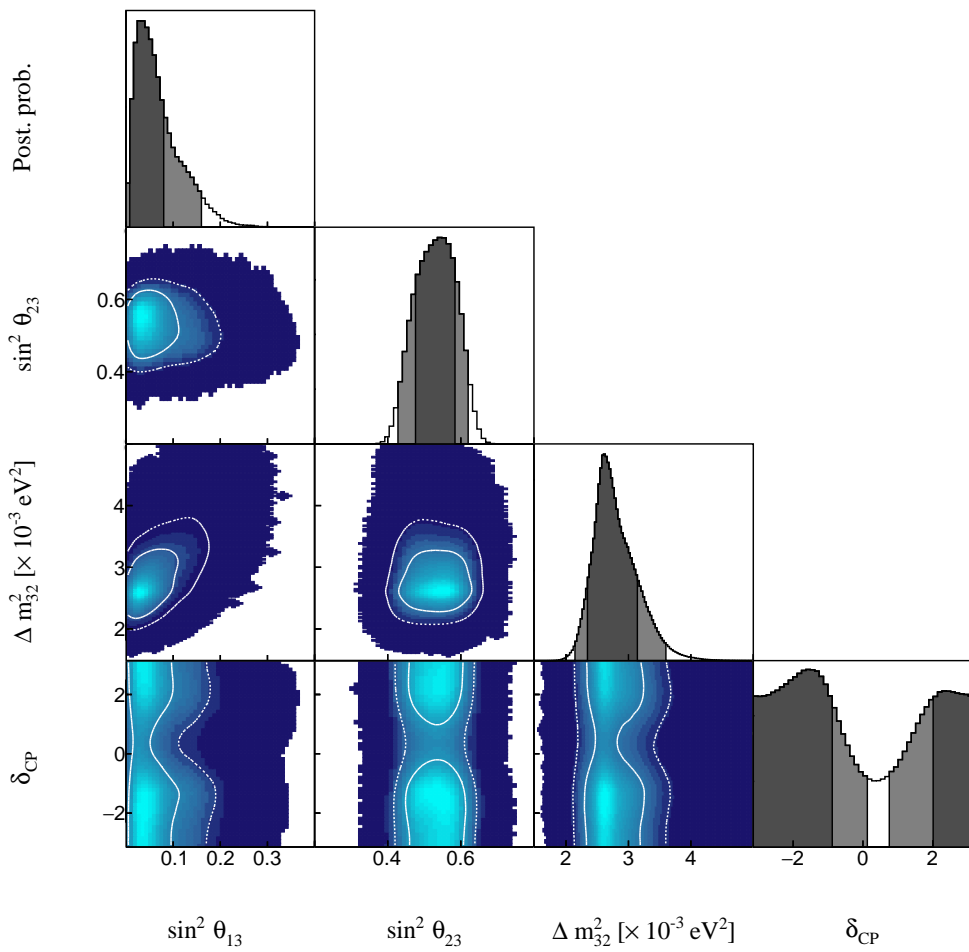


Figure 8.12: The posterior probability density distribution from the SK atmospheric-only fit. The reactor constraint is not applied. The distribution is given for each two-dimensional permutation of the oscillation parameters of interest. The one-dimensional distribution of each parameter is also given.

3098 8.3.2 Atmospheric-Only Sensitivity With Reactor Constraint

3099 The results in subsection 8.3.1 discuss the atmospheric sensitivity when the reactor
 3100 constraint is not applied. The correlations illustrated in Figure 8.12 indicate that
 3101 the marginalisation effects could contribute to differing sensitivities when the
 3102 external reactor constraint is applied. Using the technique discussed in subsec-
 3103 tion 4.1.1, the posterior distribution of the fit in subsection 8.3.1 can be reweighted
 3104 to include the reactor constraint of $\sin^2(\theta_{13}) = (2.18 \pm 0.08) \times 10^{-2}$ [73].

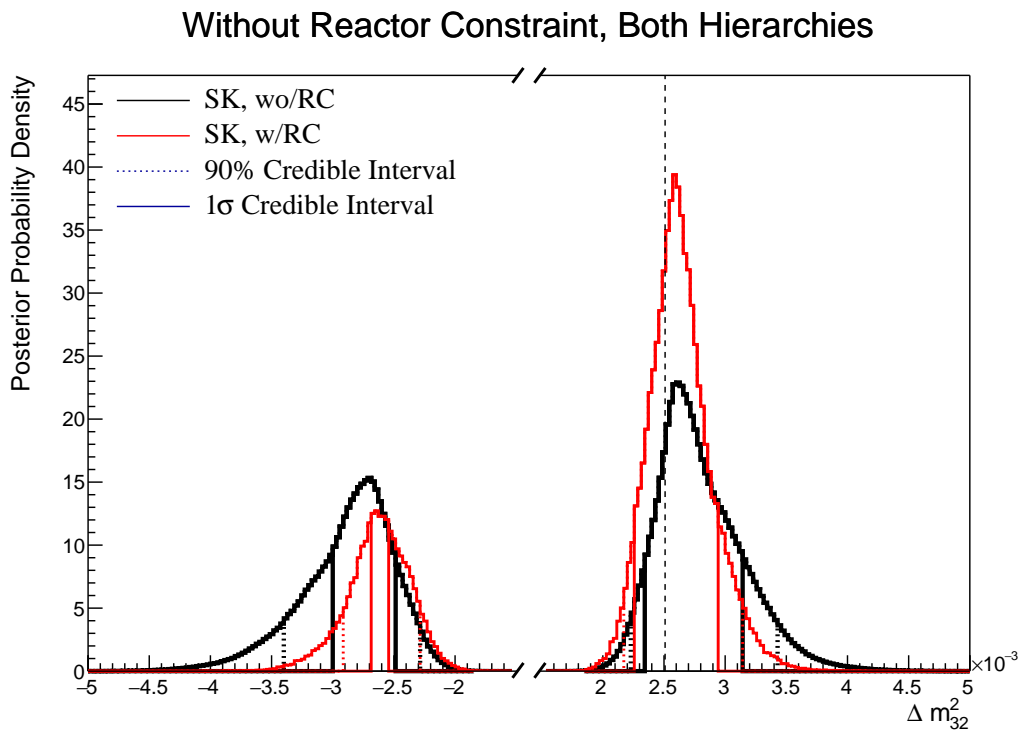


Figure 8.13: The one-dimensional posterior probability density distribution in Δm_{32}^2 compared between the SK atmospheric-only fit (Black) and the SK atmospheric fit with the reactor constraint applied (Red). The distributions are marginalised over both hierarchies. The vertical dashed line represents the known value of Δm_{32}^2 .

3105 The reactor constraint increases the sensitivity of the atmospheric samples to
 3106 Δm_{32}^2 as illustrated in Figure 8.13. The 1σ credible interval in Δm_{32}^2 is determined
 3107 to be $[-2.69, -2.54] \times 10^{-3} \text{ eV}^2$ and $[2.25, 2.94] \times 10^{-3} \text{ eV}^2$. The width of the IH
 3108 credible interval is reduced by $\sim 70\%$ when the reactor constraint is applied. Due
 3109 to the marginalisation effects observed in Figure 8.12, the favoured region of Δm_{32}^2
 3110 moves closer to zero for both hierarchies. A clear explanation of this behaviour is

illustrated in Figure 8.14, which shows the posterior distribution in the $\Delta m_{32}^2 - \sin^2(\theta_{13})$ parameters. The correlation between Δm_{32}^2 and $\sin^2(\theta_{13})$ is such that lower values of $\sin^2(\theta_{13})$ tend towards lower values of $|\Delta m_{32}^2|$. Therefore the application of the reactor constraint moves the posterior distribution towards the known oscillation parameter.

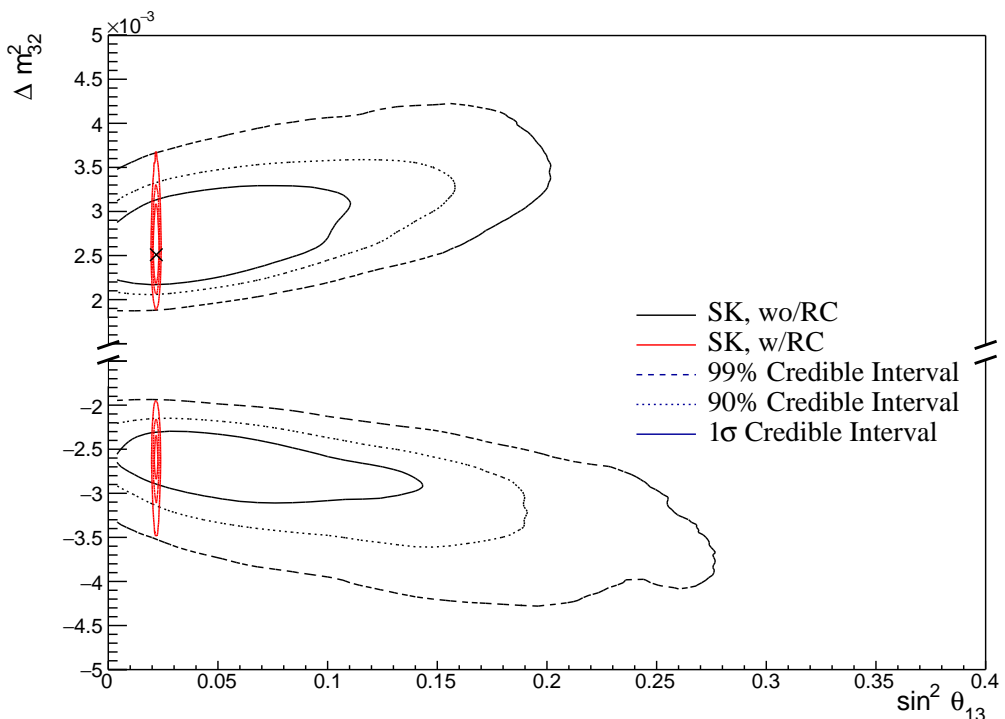


Figure 8.14: The two-dimensional posterior probability density distribution in $\Delta m_{32}^2 \times \sin^2(\theta_{13})$ compared between the SK atmospheric-only fit (Black) and the SK atmospheric fit with the reactor constraint (Red). The distributions are marginalised over both hierarchies. The marker represents the known value of $\Delta m_{32}^2 \times \sin^2(\theta_{13})$.

	LO ($\sin^2 \theta_{23} < 0.5$)	UO ($\sin^2 \theta_{23} > 0.5$)	Sum
NH ($\Delta m_{32}^2 > 0$)	0.21	0.53	0.74
IH ($\Delta m_{32}^2 < 0$)	0.08	0.18	0.26
Sum	0.29	0.71	1.00

Table 8.4: The distribution of steps in an SK atmospheric with reactor constraint fit, presented as the fraction of steps in the upper (UO) and lower (LO) octants and the normal (NH) and inverted (IH) hierarchies. The Bayes factors are calculated as $B(\text{NH}/\text{IH}) = 2.85$ and $B(\text{UO}/\text{LO}) = 2.39$.

3116 Table 8.4 presents the fraction of steps in each hierarchy and octant model
3117 for the fit after the reactor constraint has been applied. The reactor constraint
3118 significantly increases the NH preference, increasing the Bayes factor from
3119 $B(\text{NH}/\text{IH}) = 1.37$ to $B(\text{NH}/\text{IH}) = 2.85$ when the reactor constraint is applied.
3120 This is still defined as a weak preference for the NH hypothesis according to
3121 Jeffrey's scale, however, it is a stronger preference than when the constraint is
3122 not applied. The preference for the correct octant model is also slightly increased
3123 by the application of the reactor constraint.

3124 8.3.3 Impact of Near Detector Constraints for Atmospheric Sam- 3125 ples

3126 The choice of applying the near detector constraints to the low-energy atmo-
3127 spheric samples was introduced in subsection 6.4.3. This subsection illustrates the
3128 effect of removing the ND constraint on the sensitivity of the atmospheric samples
3129 to the oscillation parameters. To do this, the fit presented in subsection 8.3.1 has
3130 been compared to another fit where the constraints from the near detector have
3131 not been included. This is the only case where the near detector constraints are
3132 neglected throughout this chapter. For both fits, the Asimov data was generated
3133 assuming the ‘AsimovA’ oscillation parameter set defined in Table 2.2 and the
3134 post-BANFF systematic parameter tune.

3135 The change in sensitivity on δ_{CP} is given in Figure 8.15. The reactor constraint
3136 is not applied in either of the fits within this comparison. The fit which includes
3137 the near detector constraint is slightly more peaked at the known oscillation
3138 parameter value. The width of the 1σ credible intervals are approximately the
3139 same (identical to within a bin width) and the same conclusion holds for the
3140 higher credible intervals. The change in sensitivity to other oscillation parameters
3141 has been studied and no significant discrepancies were found. As expected, the
3142 sensitivities are statistics dominated such that the exact choice of constraint does
3143 not significantly affect the physics conclusions one would make from this analysis.

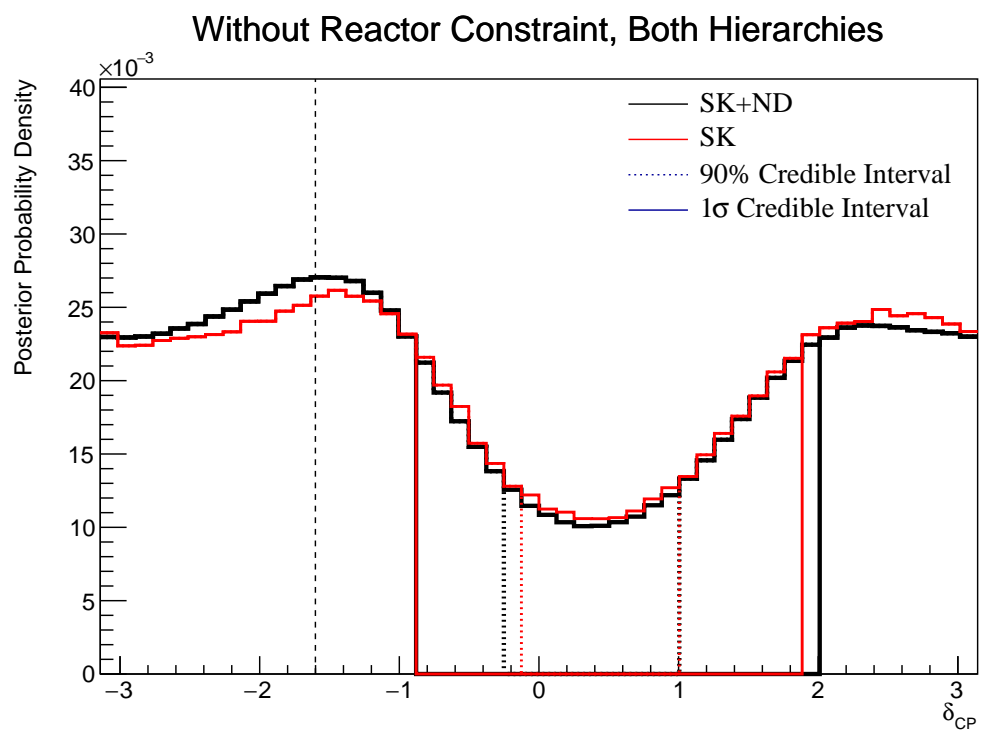


Figure 8.15: The one-dimensional posterior probability density distribution in δ_{CP} compared between the SK atmospheric-only fit where the near detector constraint is (Black) and is not (Red) applied. The distributions are marginalised over both hierarchies. The reactor constraint is not applied in either fit. The vertical dashed line represents the known value of δ_{CP} .

3144 8.3.4 Atmospheric and Beam Sensitivity without Reactor Con- 3145 straint

3146 This section presents the sensitivities of the simultaneous beam and atmospheric
 3147 analysis where the reactor constraint is not applied. Similar to the previous
 3148 studies, the Asimov data is built assuming the post-BANFF systematic tune and
 3149 Asimov A oscillation parameters defined in Table 2.2. This fit uses all 18 near
 3150 detector beam samples, 5 far detector beam samples, and 18 atmospheric samples.

Without Reactor Constraint, Both Hierarchies

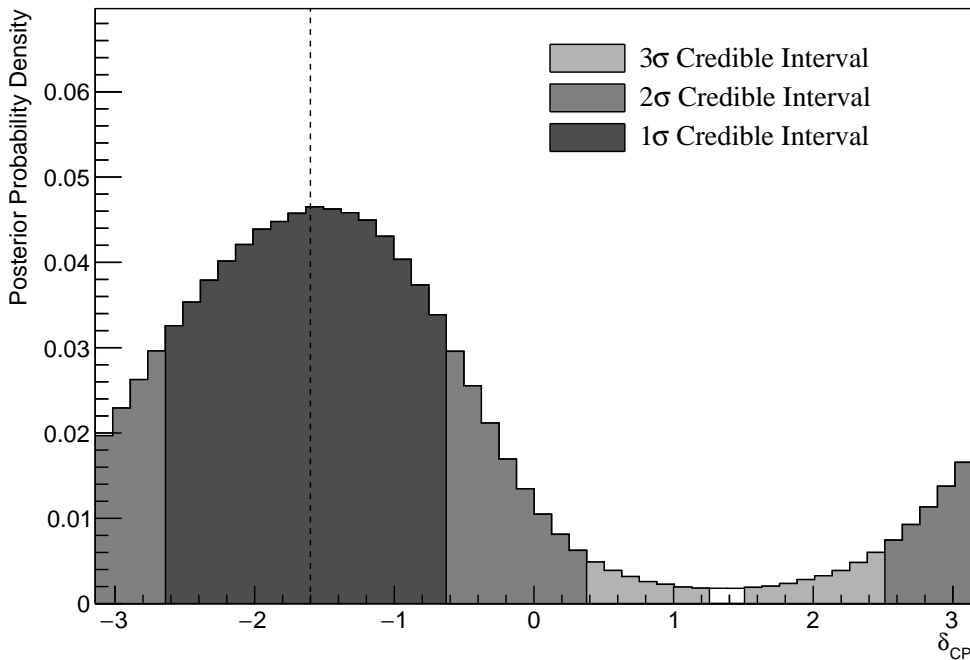


Figure 8.16: The one-dimensional posterior probability density distribution in δ_{CP} , marginalised over both hierarchies, from the joint beam-atmospheric fit. The reactor constraint is not applied. The vertical dashed line represents the known value of δ_{CP} .

3151 The sensitivity to δ_{CP} , marginalised over both hierarchies, is given in Fig-
 3152 ure 8.16. The credible intervals and highest posterior distribution for each
 3153 oscillation parameter is given in Table 8.5. The highest posterior probability
 3154 density is $\delta_{CP} = -1.57 \pm 0.07$ and is compatible with the known value of
 3155 $\delta_{CP} = -1.601$. The CP-conserving values of $\delta_{CP} = 0, \pm\pi$ are disfavoured at
 3156 1 σ credible interval. There is also a region around $\delta_{CP} = 1.4$ which is disfavoured
 3157 at more than 3 σ . Whilst these conclusions can only be made at this particular

3158 Asimov point, it does show that if the true value of δ_{CP} were CP-violating,
3159 this joint analysis would be able to disfavour CP conserving values at over 1σ
3160 without any external constraints.

Parameter	Interval	HPD
δ_{CP} , (BH)	$[-2.64, -0.63]$	-1.57 ± 0.07
δ_{CP} , (NH)	$[-2.76, -0.63]$	-1.45 ± 0.07
δ_{CP} , (IH)	$[-2.39, -0.88]$	-1.57 ± 0.07
Δm_{32}^2 (BH) [$\times 10^{-3}\text{eV}^2$]	[2.45, 2.58]	2.51 ± 0.01
Δm_{32}^2 (NH) [$\times 10^{-3}\text{eV}^2$]	[2.47, 2.56]	2.51 ± 0.01
Δm_{32}^2 (IH) [$\times 10^{-3}\text{eV}^2$]	$[-2.60, -2.51]$	-2.55 ± 0.01
$\sin^2(\theta_{23})$ (BH)	[0.480, 0.545]	0.518 ± 0.003
$\sin^2(\theta_{23})$ (NH)	[0.480, 0.545]	0.508 ± 0.003
$\sin^2(\theta_{23})$ (IH)	[0.480, 0.545]	0.513 ± 0.003

Table 8.5: The position of the highest posterior probability density (HPD) and width of the 1σ credible interval for the joint beam-atmospheric fit. The reactor constraint is not applied. The values are presented by which hierarchy hypothesis is assumed: marginalised over both hierarchies (BH), normal hierarchy only (NH), and inverted hierarchy only (IH).

3161 The sensitivity to Δm_{32}^2 is illustrated in Figure 8.17. Notably, the 1σ credible
3162 interval is entirely contained within the NH region, as further evidenced by
3163 Table 8.5. This illustrates good sensitivity to the mass hierarchy as it is correctly
3164 selecting the correct hypothesis. This is reflected in the 1σ credible intervals being
3165 approximately the same when they are constructed considering both hierarchies
3166 and when considering only the NH region. The NH distribution favours this
3167 region surrounding the known Asimov point, $\Delta m_{32}^2 = 2.509 \times 10^{-3}\text{eV}^2$, where
3168 the highest posterior probability density is at $\Delta m_{32}^2 = (2.51 \pm 0.01) \times 10^{-3}\text{eV}^2$.

3169 The fraction of steps in each of the mass hierarchy regions and octants of
3170 $\sin^2(\theta_{23})$ is given in Table 8.6. The Bayes factors are determined to be $B(\text{NH}/\text{IH}) =$
3171 3.67 and $B(\text{UO}/\text{LO}) = 1.74$. Jeffrey's scale states that this value of the mass
3172 hierarchy Bayes factor illustrates substantial evidence for the NH hypothesis.

3173 This corresponds to the correct hypothesis given the known oscillation parameters
 3174 and is a stronger statement than the atmospheric-only analysis can provide. It is
 3175 important to note that this substantial preference requires no external constraints.
 3176 The Bayes factor for octant determination represents a weak preference for the
 3177 upper octant, therefore, selecting the correct octant hypothesis.

	LO ($\sin^2 \theta_{23} < 0.5$)	UO ($\sin^2 \theta_{23} > 0.5$)	Sum
NH ($\Delta m_{32}^2 > 0$)	0.29	0.50	0.79
IH ($\Delta m_{32}^2 < 0$)	0.08	0.13	0.21
Sum	0.37	0.63	1.00

Table 8.6: The distribution of steps in a joint beam-atmospheric fit, presented as the fraction of steps in the upper (UO) and lower (LO) octants and the normal (NH) and inverted (IH) hierarchies. The reactor constraint is not applied. The Bayes factors are calculated as $B(\text{NH}/\text{IH}) = 3.67$ and $B(\text{UO}/\text{LO}) = 1.74$.

Without Reactor Constraint, Both Hierarchies

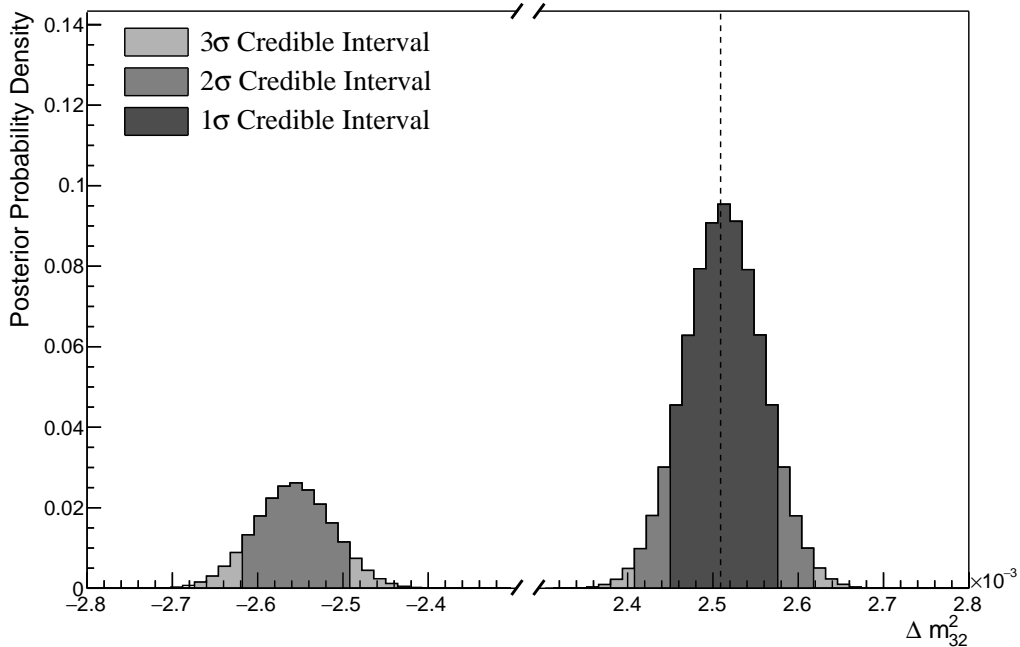


Figure 8.17: The one-dimensional posterior probability density distribution in Δm_{32}^2 , marginalised over both hierarchies, from the joint beam-atmospheric fit. The reactor constraint is not applied. The vertical dashed line represents the known value of Δm_{32}^2 .

3178 The sensitivity to $\sin^2(\theta_{23})$ is presented in Figure 8.18. There is a clear

³¹⁷⁹ preference for the upper octant but the peak of the distribution is relatively
³¹⁸⁰ flat. It peaks at $\sin^2(\theta_{23}) = 0.509 \pm 0.003$ which is in the region of the known
³¹⁸¹ value of $\sin^2(\theta_{23}) = 0.528$. The difference in the highest posterior distribution
³¹⁸² and the width of the credible interval is relatively unchanged when consid-
³¹⁸³ ering different hierarchy hypotheses showing no strong correlation between
³¹⁸⁴ $\sin^2(\theta_{23})$ and $|\Delta m_{32}^2|$.

Without Reactor Constraint, Both Hierarchies

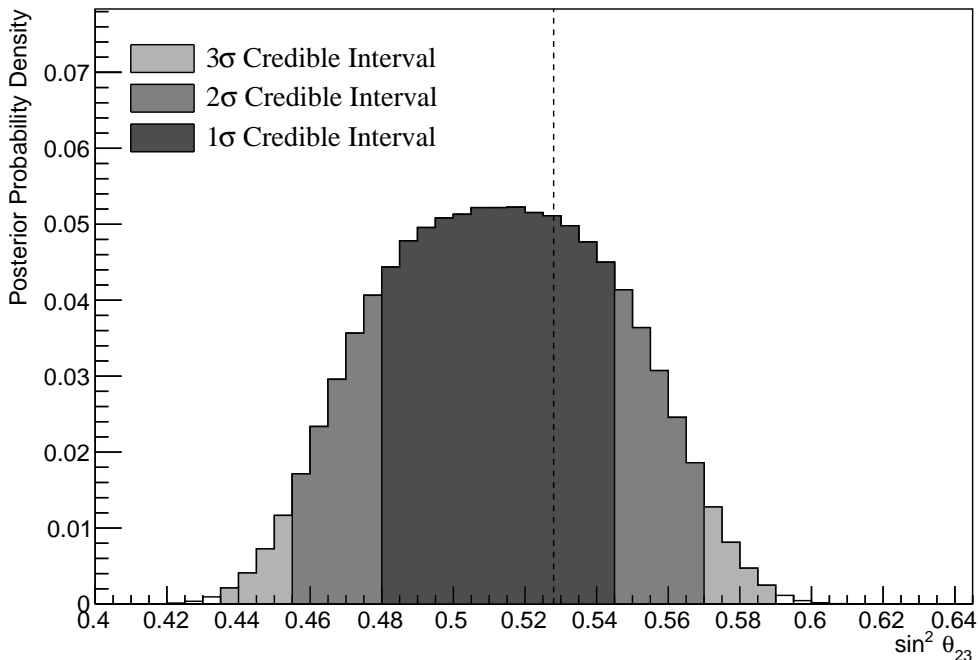


Figure 8.18: The one-dimensional posterior probability density distribution in $\sin^2(\theta_{23})$, marginalised over both hierarchies, from the joint beam-atmospheric fit. The reactor constraint is not applied. The vertical dashed line represents the known value of $\sin^2(\theta_{23})$.

³¹⁸⁵ The sensitivity presented as a function of the appearance parameters $(\sin^2(\theta_{13}), \delta_{CP})$
³¹⁸⁶ is given in Figure 8.19. As expected, the contours follow the likelihood shape
³¹⁸⁷ given in Figure 8.2, where the 2σ credible intervals have a closed contour exclu-
³¹⁸⁸ ding the region around $\delta_{CP} \sim 1.2$. The width of the 3σ credible interval in $\sin^2(\theta_{13})$
³¹⁸⁹ is dependent upon the value of δ_{CP} . Close to the Asimov point, $\delta_{CP} = -1.601$, the
³¹⁹⁰ width of the 3σ credible interval approximately spans $\sin^2(\theta_{13}) = [0.013, 0.04]$.
³¹⁹¹ This is reduced to a region of $\sin^2(\theta_{13}) = [0.023, 0.042]$ at the most disfavoured
³¹⁹² value of δ_{CP} . The 1σ credible interval is consistent with the known oscillation

parameter. Application of the reactor constraint would be expected to decrease the width of the 1σ credible intervals in δ_{CP} due to the triangular shape of the posterior probability.

The sensitivity in terms of the disappearance parameters, $\sin^2(\theta_{23}) \sim \Delta m_{32}^2$, is given in Figure 8.20. The area contained within the IH contours is significantly smaller than the area within the NH contours. The IH credible intervals are also notably tighter in the $\sin^2(\theta_{23})$ dimension. No significant correlation is observed between $\sin^2(\theta_{23})$ and $|\Delta m_{32}^2|$.

Without Reactor Constraint, Both Hierarchies

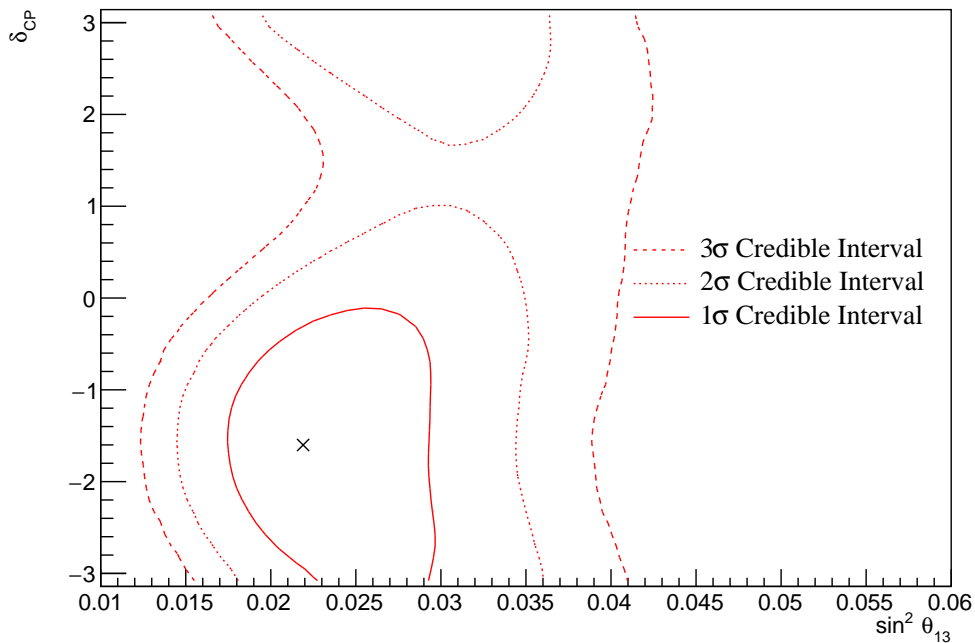


Figure 8.19: The two-dimensional posterior probability density distribution in $\delta_{CP} \sim \sin^2(\theta_{13})$, marginalised over both hierarchies, from the joint beam-atmospheric fit. The reactor constraint is not applied. The marker represents the known value of $\delta_{CP} \sim \sin^2(\theta_{13})$.

The two-dimensional posterior distribution for each permutation of the oscillation parameters of interest is given in Figure 8.21. The most notable observation is that the $\sin^2(\theta_{13})$ and $\sin^2(\theta_{23})$ are anti-correlated. If the value of $\sin^2(\theta_{13})$ was constrained closer to the known oscillation parameter value, the preferred value of $\sin^2(\theta_{23})$ would increase. This would move the highest posterior probability

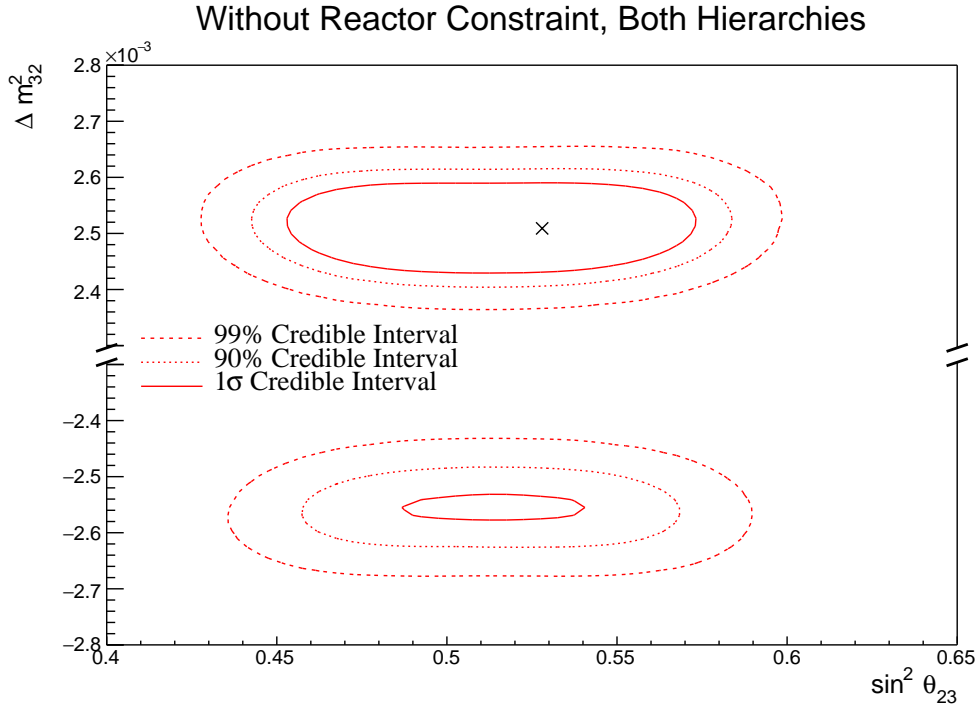


Figure 8.20: The two-dimensional posterior probability density distribution in $\Delta m_{32}^2 \sim \sin^2(\theta_{23})$, marginalised over both hierarchies, from the joint beam-atmospheric fit. The reactor constraint is not applied. The marker represents the known value of $\Delta m_{32}^2 \sim \sin^2(\theta_{23})$.

closer in line with the known value and could lead to an increase in the preference for the UO hypothesis.

Furthermore, the δ_{CP} and $|\Delta m_{32}^2|$ oscillation parameters are anti-correlated, such that higher values of $|\Delta m_{32}^2|$ prefer lower values of δ_{CP} . Whilst this is an interesting result on its own, the width of the Δm_{32}^2 contours also depend on $\sin^2(\theta_{13})$. This introduces another correlation effect that could modify the sensitivity to δ_{CP} once the reactor constraint is applied.

The correlation between $\sin^2(\theta_{13})$ and Δm_{32}^2 can be seen in Figure 8.22. A much larger fraction of the posterior distribution is contained in the NH for lower values of $\sin^2(\theta_{13})$. Consequently, the application of the reactor constraint would be expected to significantly increase the preference for NH.

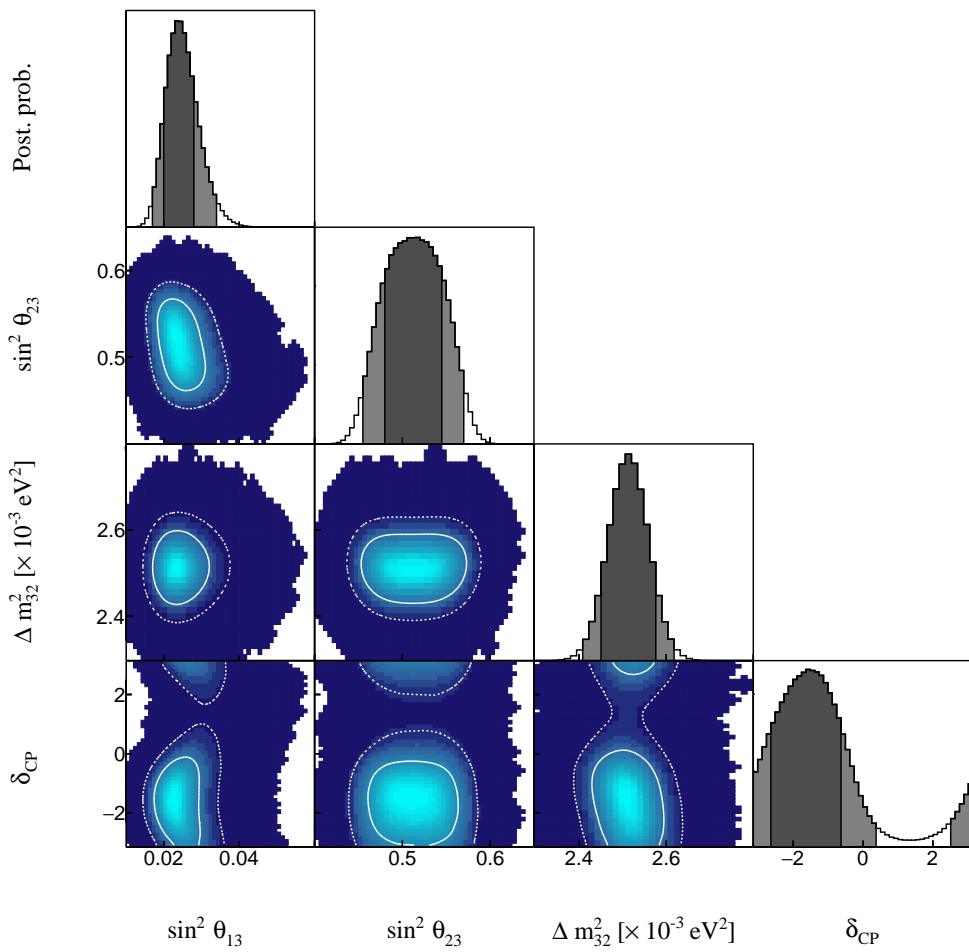


Figure 8.21: The posterior probability density distribution from the joint beam-atmospheric fit. The reactor constraint is not applied. The distribution is given for each two-dimensional permutation of the oscillation parameters of interest. The one-dimensional distribution of each parameter is also given.

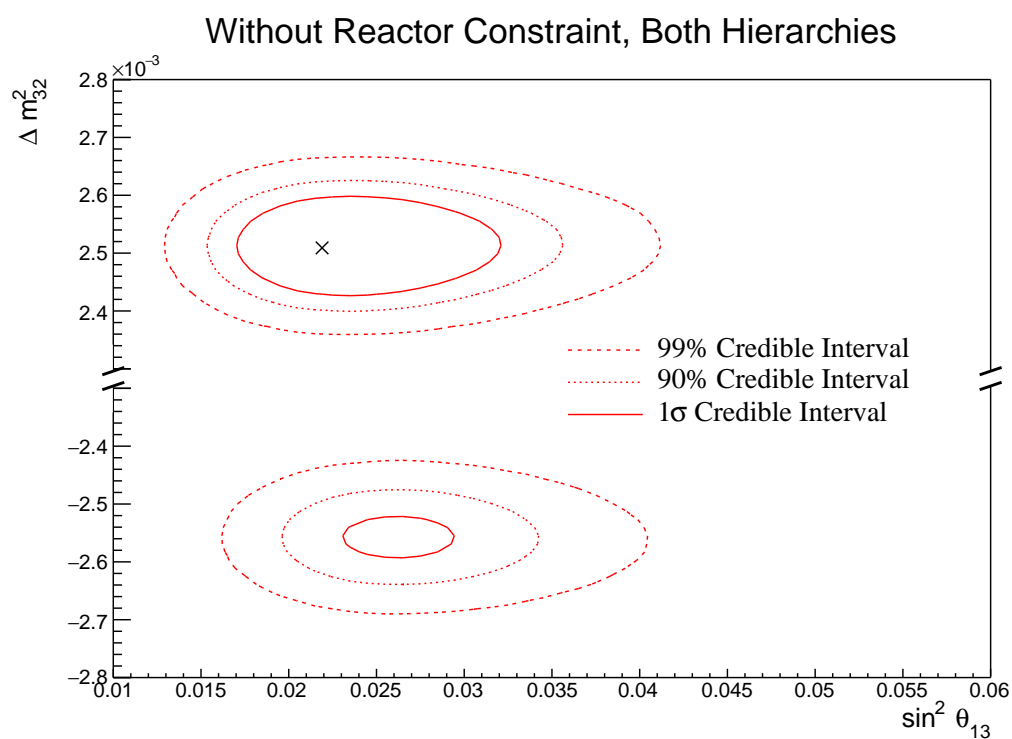


Figure 8.22: The two-dimensional posterior probability density distribution in $\Delta m_{32}^2 \sim \sin^2(\theta_{13})$, marginalised over both hierarchies, from the joint beam-atmospheric fit. The reactor constraint is not applied. The marker represents the known value of $\Delta m_{32}^2 \sim \sin^2(\theta_{13})$.

3217 8.3.5 Atmospheric and Beam Sensitivity with Reactor Constraint

3218 This section presents the sensitivities of the joint beam-atmospheric fit when
 3219 the reactor constraint is applied to $\sin^2(\theta_{13})$. As with the previous studies, the
 3220 Asimov data is made using the AsimovA oscillation parameter set defined in
 3221 Table 2.2 and the post-BANFF systematic parameter tune.

With Reactor Constraint, Both Hierarchies

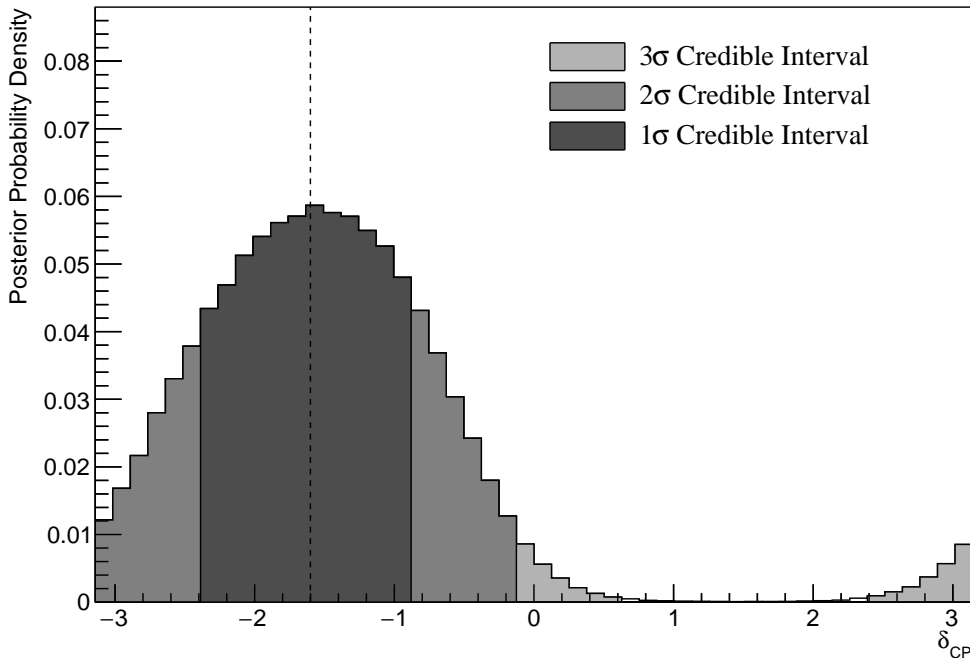


Figure 8.23: The one-dimensional posterior probability density distribution in δ_{CP} , marginalised over both hierarchies, from the joint beam-atmospheric fit where the reactor constraint is applied. The vertical dashed line represents the known value of δ_{CP} .

3222 Figure 8.23 illustrates the sensitivity to δ_{CP} , marginalised over both hierarchies.
 3223 The CP-conserving value of $\delta_{CP} = 0$ is disfavoured at 2σ whilst the value of $\delta_{CP} =$
 3224 $\pm\pi$ is very close to being disfavoured at 2σ . Furthermore, the 3σ credible interval
 3225 excludes the region of $\delta_{CP} = [0.63, 2.39]$, thus clearly disfavouring the region of
 3226 $\delta_{CP} = \pi/2$ at more than 3σ for this particular set of known oscillation parameters.
 3227 The width of the 1σ credible intervals and the position of the highest posterior
 3228 probability density is given in Table 8.7. The highest posterior probability density
 3229 in δ_{CP} is calculated as $\delta_{CP} = -1.57 \pm 0.07$ showing no significant biases in the
 3230 determination of the known oscillation parameters.

The effect of applying the reactor constraint for δ_{CP} in the joint beam-atmospheric fit is presented in Figure 8.24. The reactor constraint significantly improves the ability of the fit to select the known parameter value. This behaviour is evidenced by the tightening of the 1σ and 90% credible intervals and the disfavoured region, centered at $\delta_{CP} \sim \pi/2$, becoming wider when the reactor constraint is applied. This follows from the correlations shown in Figure 8.19, where a lower value of $\sin^2(\theta_{13})$ results in tighter constraints on δ_{CP} .

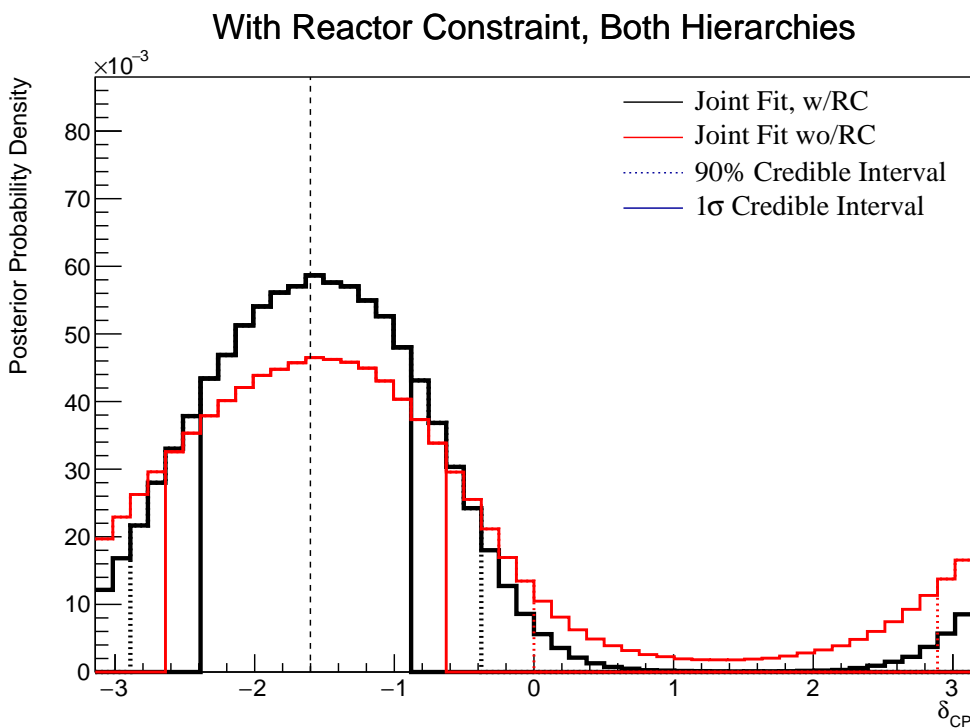


Figure 8.24: The one-dimensional posterior probability density distribution in δ_{CP} compared between the joint beam-atmospheric fit (Red) and the joint beam-atmospheric fit with the reactor constraint (Black). The distributions are marginalised over both hierarchies. The vertical dashed line represents the known value of δ_{CP} .

The sensitivity to $\sin^2(\theta_{23})$, marginalised over both hierarchies, is given in Figure 8.25. The highest posterior probability density is located at $\sin^2(\theta_{23}) = 0.528 \pm 0.03$ which agrees with the known value of $\sin^2(\theta_{23}) = 0.528$. The distribution clearly favours the UO with almost the entirety of the 1σ credible interval being contained in that region. Figure 8.26 highlights the sensitivity of the joint fit both with and without the reactor constraint. The fit where the

Parameter	Interval	HPD
δ_{CP} , (BH)	[-2.39, -0.88]	-1.57 ± 0.07
δ_{CP} , (NH)	[-2.39, -0.75]	-1.57 ± 0.07
δ_{CP} , (IH)	[-2.14, -1.01]	-1.57 ± 0.07
Δm_{32}^2 (BH) [$\times 10^{-3}\text{eV}^2$]	[2.45, 2.56]	2.51 ± 0.01
Δm_{32}^2 (NH) [$\times 10^{-3}\text{eV}^2$]	[2.47, 2.56]	2.51 ± 0.01
Δm_{32}^2 (IH) [$\times 10^{-3}\text{eV}^2$]	[-2.60, -2.51]	-2.55 ± 0.01
$\sin^2(\theta_{23})$ (BH)	[0.490, 0.555]	0.528 ± 0.03
$\sin^2(\theta_{23})$ (NH)	[0.490, 0.555]	0.528 ± 0.03
$\sin^2(\theta_{23})$ (IH)	[0.500, 0.560]	0.538 ± 0.03

Table 8.7: The position of the highest posterior probability density (HPD) and width of the 1σ credible interval for the joint beam-atmospheric fit where the reactor constraint is applied. The values are presented by which hierarchy hypothesis is assumed: marginalised over both hierarchies (BH), normal hierarchy only (NH), and inverted hierarchy only (IH).

reactor constraint is applied selects the known value much better. This is a result of the marginalisation effects between the $\sin^2(\theta_{13})$ and $\sin^2(\theta_{23})$ parameters, as observed in Figure 8.21.

The fraction of steps from the joint fit, after the reactor constraint is applied, is given in Table 8.8 and split by the two hierarchy and two octant hypotheses. The reactor constraint significantly reduces the fraction of steps that are contained within the IH-LO region from 0.08 to 0.03, whilst significantly increasing the fraction of steps within the NH-UO region from 0.50 to 0.62. The application of the reactor constraint increases the Bayes factor from $B(\text{NH}/\text{IH}) = 3.67$ to $B(\text{NH}/\text{IH}) = 6.47$. There is a very clear preference for the NH, with the Jeffreys scale stating a substantial preference for both fits. The Bayes factor for UO preference is calculated as $B(\text{UO}/\text{LO}) = 2.64$. Whilst still a weak preference, this is certainly a stronger statement than the sensitivity when the reactor constraint is not applied.

The sensitivity of the joint beam-atmospheric fit to Δm_{32}^2 , with the reactor constraint applied, is presented in Figure 8.27. The 1σ credible interval is

With Reactor Constraint, Both Hierarchies

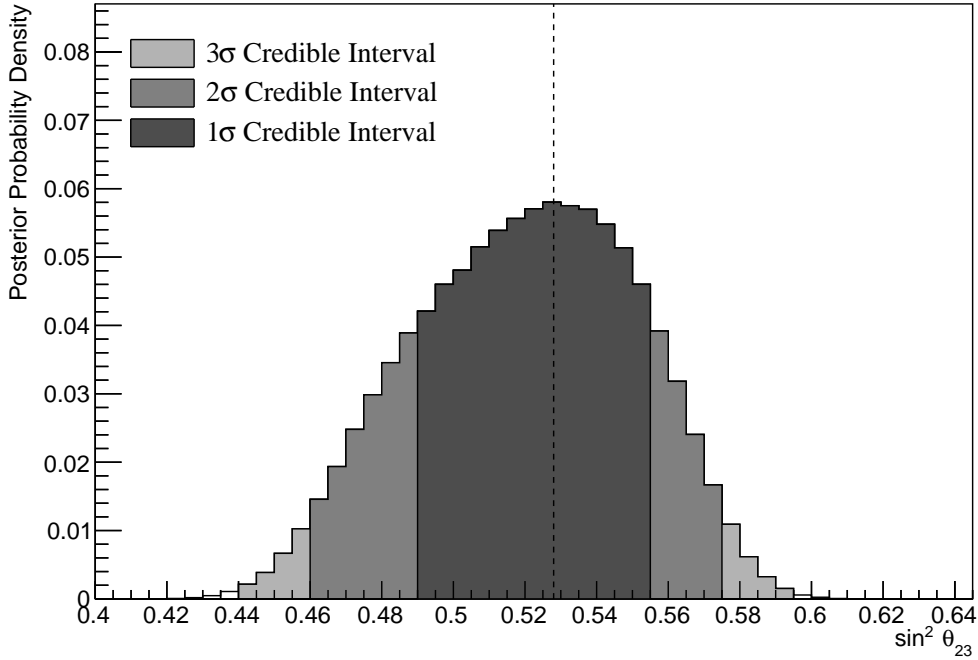


Figure 8.25: The one-dimensional posterior probability density distribution in $\sin^2(\theta_{23})$, marginalised over both hierarchies, from the joint beam-atmospheric fit where the reactor constraint is applied. The vertical dashed line represents the known value of $\sin^2(\theta_{23})$.

	LO ($\sin^2 \theta_{23} < 0.5$)	UO ($\sin^2 \theta_{23} > 0.5$)	Sum
NH ($\Delta m_{32}^2 > 0$)	0.24	0.62	0.87
IH ($\Delta m_{32}^2 < 0$)	0.03	0.10	0.13
Sum	0.27	0.73	1.00

Table 8.8: The distribution of steps in a joint beam-atmospheric with the reactor constraint fit applied, presented as the fraction of steps in the upper (UO) and lower (LO) octants and the normal (NH) and inverted (IH) hierarchies. The Bayes factors are calculated as $B(\text{NH}/\text{IH}) = 6.47$ and $B(\text{UO}/\text{LO}) = 2.64$.

3260 entirely contained within the NH region and the position of the highest posterior
 3261 probability density is given as $(2.49 \pm 0.01) \times 10^{-3} \text{ eV}^2$. This illustrates no bias
 3262 between the fit results and the known oscillation parameters. The application
 3263 of the reactor constraint does not significantly move the position or width of
 3264 the credible intervals.

3265 The sensitivity to the appearance parameters $(\sin^2(\theta_{13}) \delta_{CP})$ is given in Fig-
 3266 ure 8.28. The distribution is mostly uncorrelated between the two parameters and

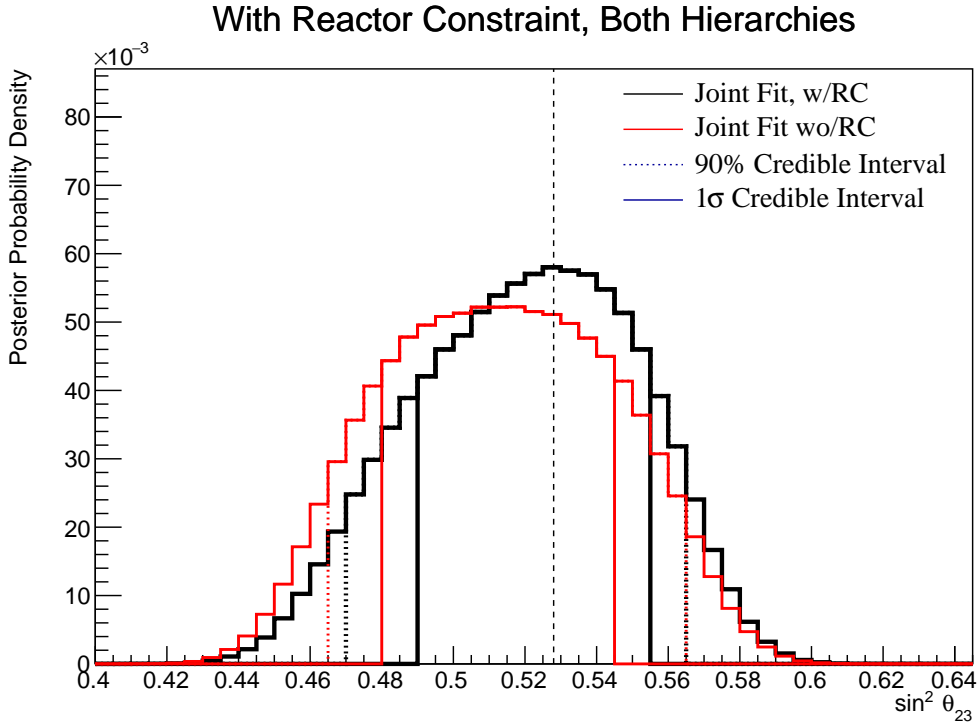


Figure 8.26: The one-dimensional posterior probability density distribution in $\sin^2(\theta_{23})$ compared between the joint beam-atmospheric fit (Red) and the joint beam-atmospheric fit with the reactor constraint (Black). The distributions are marginalised over both hierarchies. The vertical dashed line represents the known value of $\sin^2(\theta_{23})$.

is centered at the known oscillation parameters. The 1σ credible interval excludes $\delta_{CP} = 0$ and $\delta_{CP} = \pm\pi$. Furthermore, the 3σ credible intervals exclude the region of $\delta_{CP} = \pi/2$.

The sensitivity to the disappearance parameters ($\sin^2(\theta_{23}) \sim \Delta m_{32}^2$) is illustrated in Figure 8.29. The 1σ credible interval is entirely contained within the NH region reflecting the same results as the one-dimensional marginalised results in Figure 8.27. Both the NH and IH regions favour the UO, with a visually similar preference in both hierarchies. The width of the 1σ contour, in Δm_{32}^2 , does not significantly depend upon the value or octant of $\sin^2(\theta_{23})$. This shows that there are no strong correlations between these two parameters.

Figure 8.30 illustrates the posterior distribution for each permutation of two oscillation parameters of interest. The application of the reactor constraint significantly reduces the correlations previously seen in Figure 8.21.

With Reactor Constraint, Both Hierarchies

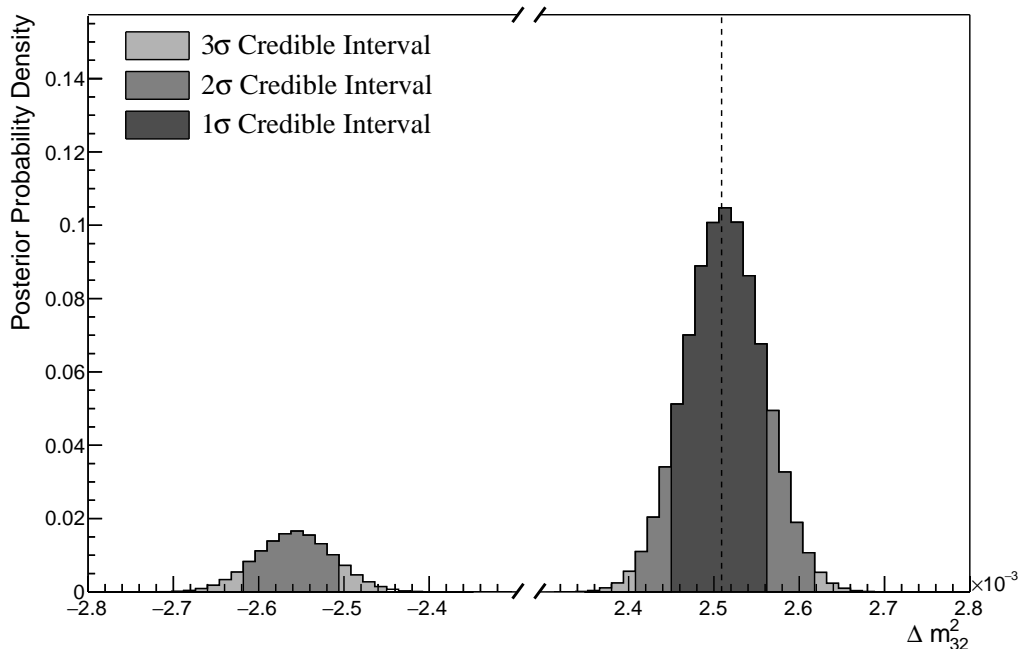


Figure 8.27: The one-dimensional posterior probability density distribution in Δm_{32}^2 from the joint beam-atmospheric fit where the reactor constraint is applied. The vertical dashed line represents the known value of Δm_{32}^2 .

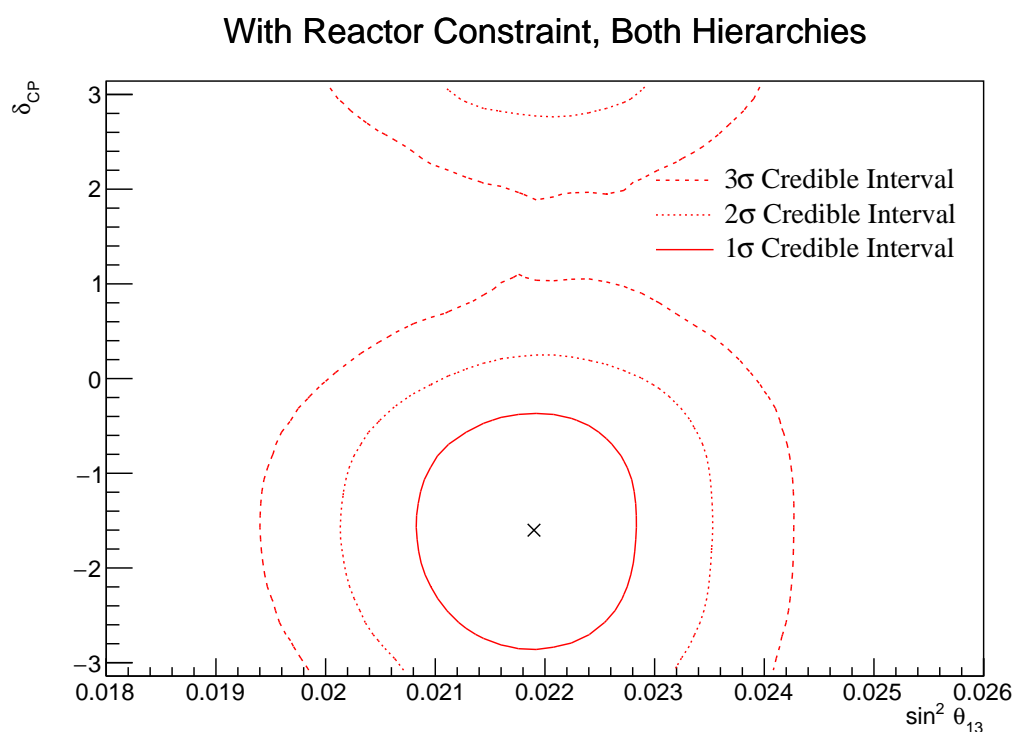


Figure 8.28: The two-dimensional posterior probability density distribution in $\delta_{CP} - \sin^2(\theta_{13})$, marginalised over both hierarchies, from the joint beam-atmospheric fit where the reactor constraint is applied. The marker represents the known value of $\delta_{CP} - \sin^2(\theta_{13})$.

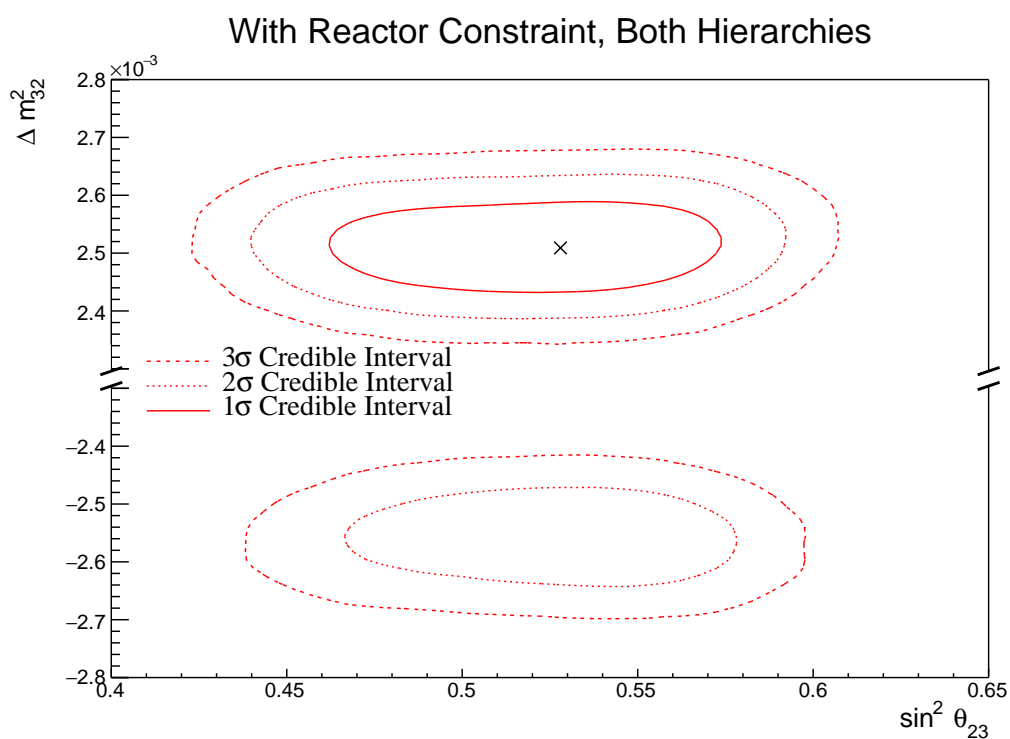


Figure 8.29: The two-dimensional posterior probability density distribution in $\Delta m_{32}^2 - \sin^2(\theta_{23})$, marginalised over both hierarchies, from the joint beam-atmospheric fit where the reactor constraint is applied. The marker represents the known value of $\Delta m_{32}^2 - \sin^2(\theta_{23})$.

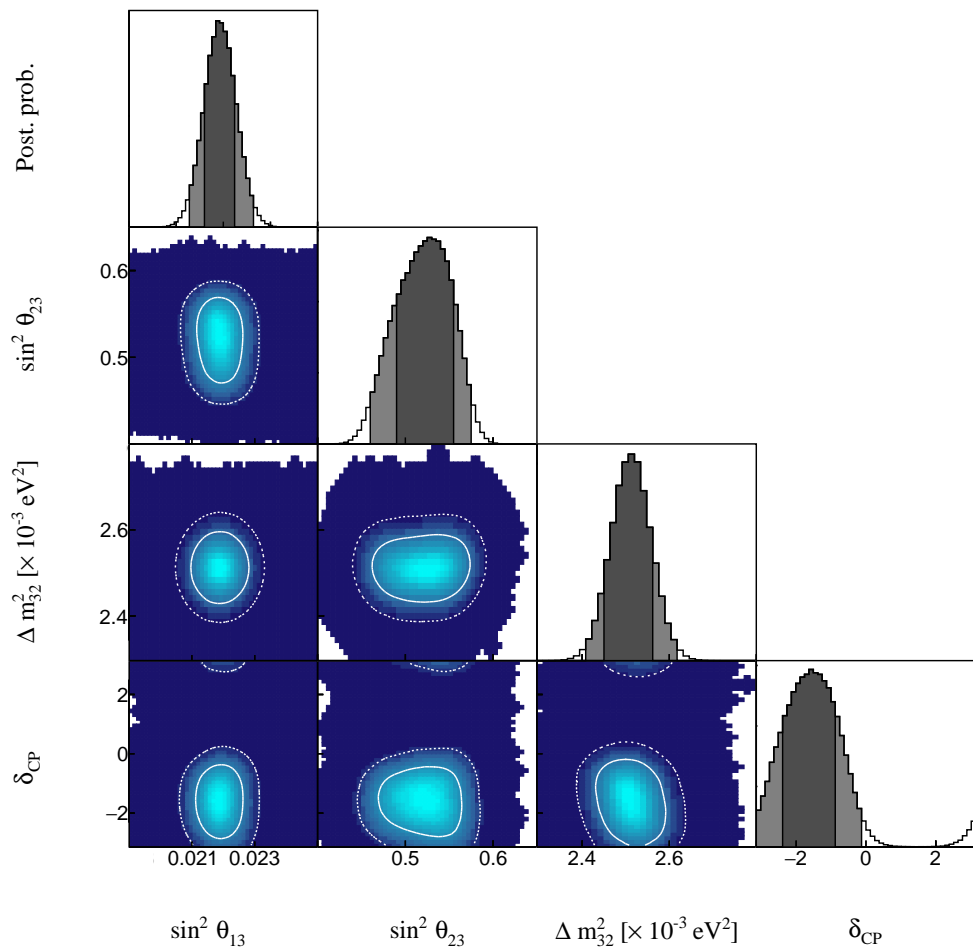


Figure 8.30: The posterior probability density distribution from the joint beam-atmospheric fit where the reactor constraint is applied. The distribution is given for each two-dimensional permutation of the oscillation parameters of interest. The one-dimensional distribution of each parameter is also given.

3280 8.3.6 Comparison to Latest T2K Sensitivities without Reactor 3281 Constraint

3282 The benefits of the joint beam-atmospheric analysis can be determined by compar-
 3283 ing the sensitivities to the beam-only analysis presented in [72, 214]. This section
 3284 presents those comparisons for sensitivities built using the Asimov A oscillation
 3285 parameters defined in Table 2.2 and the post-BANFF systematic tune. The reactor
 3286 constraint is not applied within either of the fits used in these comparisons.

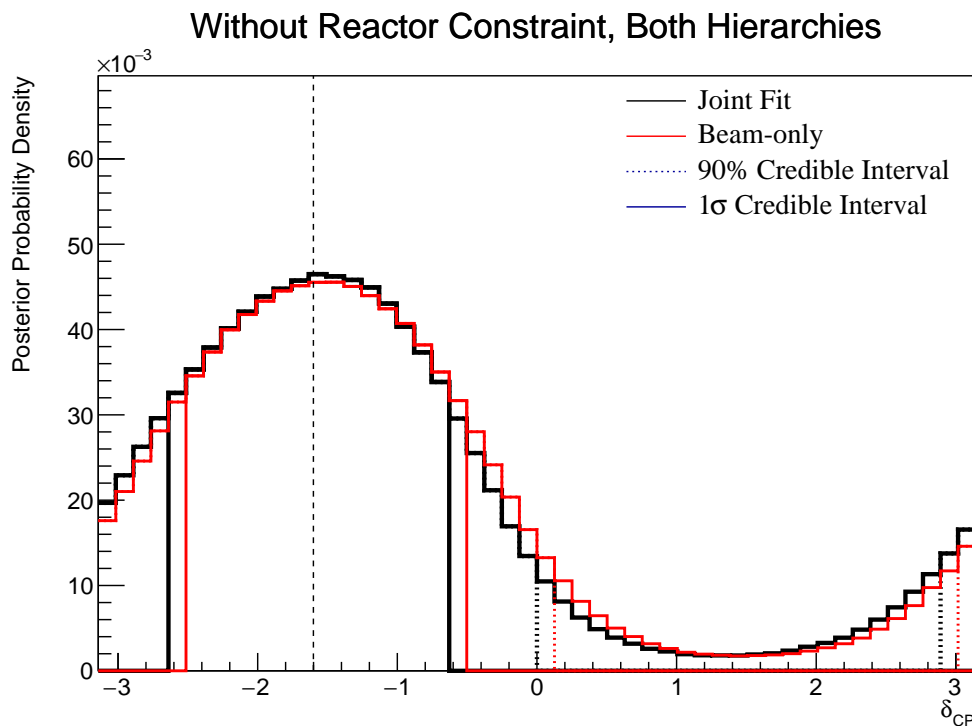


Figure 8.31: The one-dimensional posterior probability density distribution in δ_{CP} compared between the joint beam-atmospheric fit (Black) and the latest T2K sensitivities (Red) [72, 214]. The reactor constraint is not applied in either fit. The distributions are marginalised over both hierarchies. The vertical dashed line represents the known value of δ_{CP} .

3287 The sensitivity, marginalised over both hierarchies, to δ_{CP} from the joint beam-
 3288 atmospheric and beam-only fits is presented in Figure 8.31. As expected from the
 3289 likelihood scans (Figure 8.4), the sensitivity to δ_{CP} is not significantly increased.
 3290 This is because the known oscillation parameter value lies at the position where
 3291 the beam samples dominate the sensitivity compared to the SK samples.

The sensitivity to Δm_{32}^2 is compared between the joint beam-atmospheric fit and beam-only fit in Figure 8.32. The 1σ credible interval of the joint beam-atmospheric fit is entirely contained within the NH region. This shows the significant increase in the ability of the fit to determine the correct mass hierarchy, compared to the beam-only analysis. This is further evidenced by the fact that the 90% credible intervals from the joint fit are also tighter in the IH region compared to the beam-only analysis. The Bayes factor for mass hierarchy determination for the beam-only and joint beam-atmospheric fits are $B(\text{NH}/\text{IH}) = 1.91$ and $B(\text{NH}/\text{IH}) = 3.67$, respectively. According to Jeffrey's scale, the beam-only analysis represents a weak preference for the NH hypothesis whereas the joint fit returns a substantial preference for the NH hypothesis. Notably, this conclusion does not require any external constraints and clearly illustrates the benefit of the joint analysis.

Without Reactor Constraint, Both Hierarchies

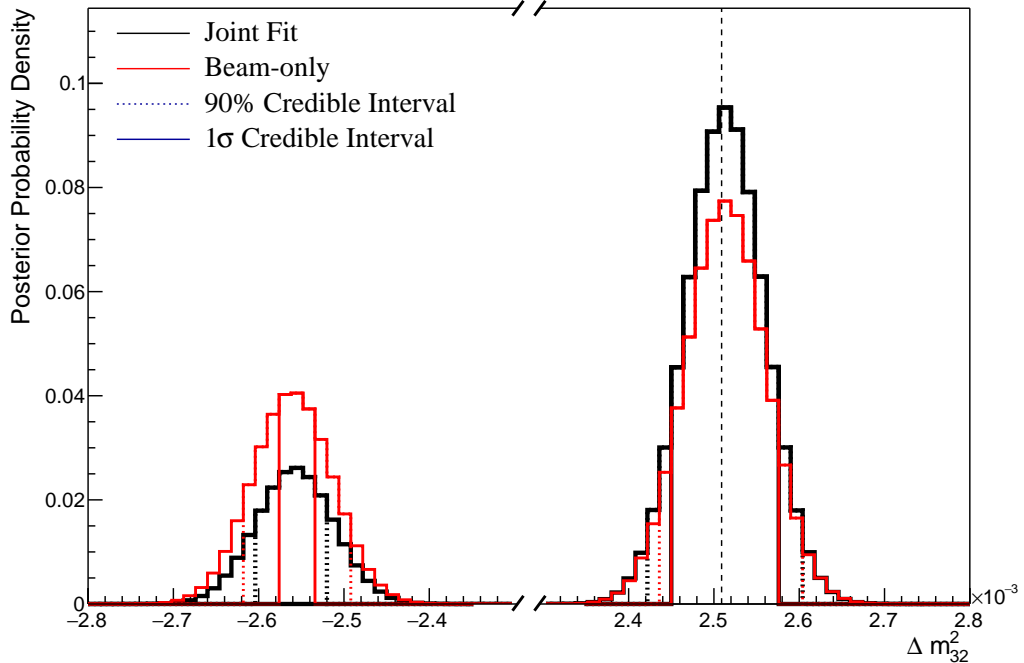


Figure 8.32: The one-dimensional posterior probability density distribution in Δm_{32}^2 compared between the joint beam-atmospheric fit (Black) and the latest T2K sensitivities (Red) [72, 214]. The reactor constraint is not applied in either fit. The vertical dashed line represents the known value of Δm_{32}^2 .

3305 The sensitivity to $\sin^2(\theta_{23})$, marginalised over both hierarchies, for both the
 3306 beam-only and joint beam-atmospheric analysis are presented in Figure 8.33. The
 3307 peak of the posterior distribution from the joint analysis is more aligned with the
 3308 known value of $\sin^2(\theta_{23}) = 0.528$ compared to the beam-only analysis. The Bayes
 3309 factors for the beam-only and joint beam-atmospheric fit are $B(\text{UO}/\text{LO}) = 1.56$
 3310 and $B(\text{UO}/\text{LO}) = 1.74$, respectively. Therefore, the joint beam-atmospheric fit
 3311 does prefer the UO more strongly than the beam-only analysis, albeit slightly.

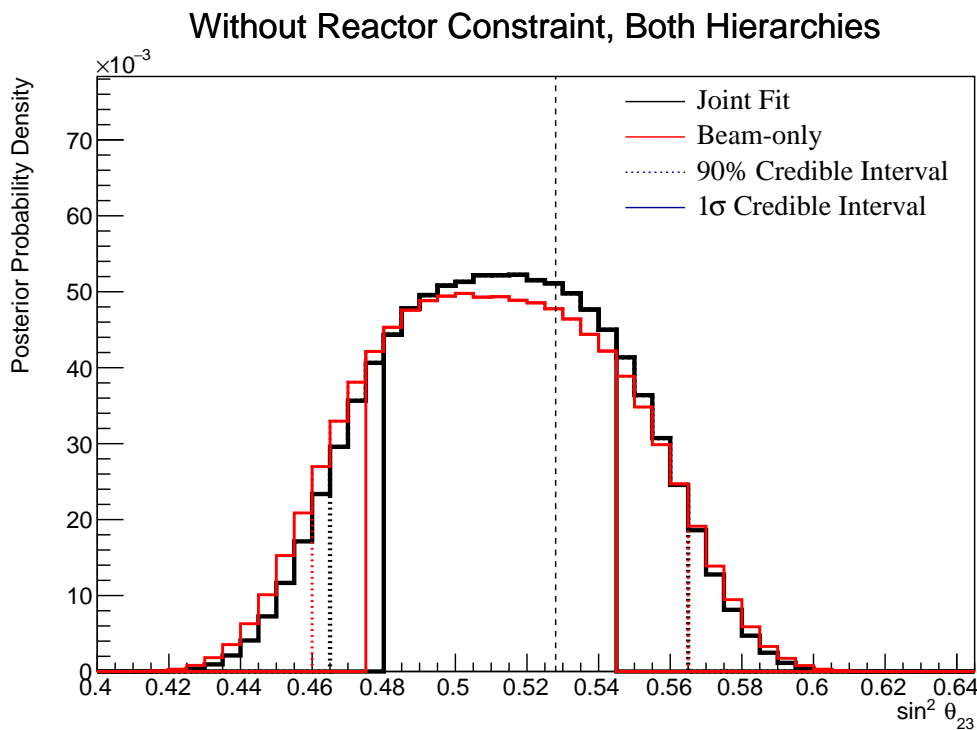


Figure 8.33: The one-dimensional posterior probability density distribution in $\sin^2(\theta_{23})$ compared between the joint beam-atmospheric fit (Black) and the latest T2K sensitivities (Red) [72, 214]. The reactor constraint is not applied in either fit. The distributions are marginalised over both hierarchies. The vertical dashed line represents the known value of $\sin^2(\theta_{23})$.

3312 Whilst the beam-only and joint beam-atmospheric fits have similar sensi-
 3313 tivity to δ_{CP} and $\sin^2(\theta_{23})$ when projected in one-dimension, the benefit of the
 3314 joint analysis becomes more obvious when the sensitivities are presented in
 3315 two-dimensions. The sensitivity of the two fits to the appearance parameters
 3316 ($(\delta_{CP}, \sin^2(\theta_{13}))$) is illustrated in Figure 8.34. The width of the 99% joint fit credible
 3317 interval in $\sin^2(\theta_{13})$ is squeezed in the region of $\delta_{CP} \sim 0$ compared to the

beam-only analysis. This is the same behaviour that is seen in the appearance likelihood scans presented in Figure 8.2. The 1σ and 90% also exhibit slightly tighter constraints on δ_{CP} . This is most prevalent in the region of $\delta_{CP} \sim 0$ and $\sin^2(\theta_{13}) \sim 0.03$. Whilst the atmospheric samples do not have significant sensitivity to $\sin^2(\theta_{13})$ (as shown in Figure 8.1), they aid in breaking the degeneracy between the oscillation parameters allowing for tighter constraints.

The sensitivity to the disappearance parameters $\sin^2(\theta_{23}) \sim \Delta m_{32}^2$ is presented in Figure 8.35 for both the beam-only and joint beam-atmospheric fits. Whilst the one-dimensional sensitivity comparisons considered so far show the improvements of the joint fit, the two-dimensional projection really shows the benefit of adding the atmospheric samples to the beam samples. The area contained within the IH credible intervals is drastically reduced in the joint fit. This follows from the better determination of the mass hierarchy seen in the Bayes factor comparisons. Even in the NH region, the widths of the credible intervals in $\sin^2(\theta_{23})$ decreases, albeit to a smaller extent.

The comparison in sensitivity to $\delta_{CP} \sim \Delta m_{32}^2$ is illustrated in Figure 8.36. The contours from the joint beam-atmospheric fit are much smaller in the IH region as compared to the beam-only analysis. This culminates in a region around $\delta_{CP} \sim \pi/2$ in the H region which is excluded at 3σ . This behaviour is not present within the beam-only analysis. Consistent with the previous observations, the area contained within the IH credible intervals is significantly reduced in comparison to the beam-only analysis.

The sensitivity to Δm_{32}^2 , as a function of $\sin^2(\theta_{13})$, is presented in Figure 8.37. Similar to previous observations, the Δm_{32}^2 contours within IH region of the joint fit are much smaller than the beam-only analysis. Notably, the joint fit IH 1σ credible intervals exclude the region around the reactor constraint. This suggests that the application of the reactor constraint would further increase the preference for NH in the joint fit compared to its effect on the beam-only analysis.

The beam-only and joint beam-atmospheric fits have a slightly different contour shape between the $\sin^2(\theta_{13})$ and $\sin^2(\theta_{23})$ parameters, as illustrated

Without Reactor Constraint, Both Hierarchies

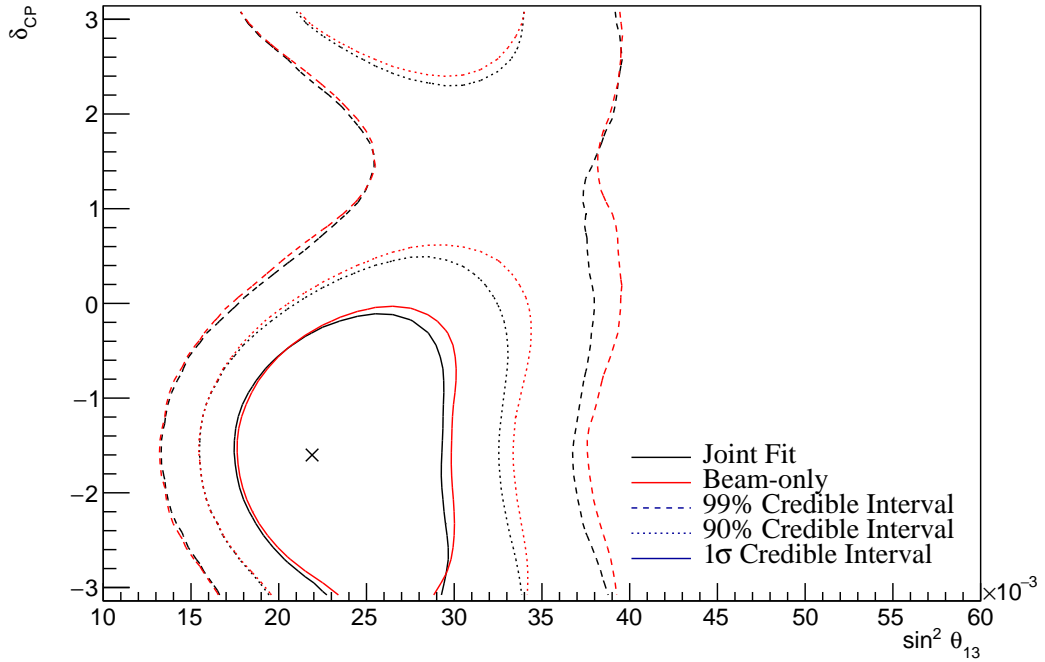


Figure 8.34: The two-dimensional posterior probability density distribution in δ_{CP} – $\sin^2(\theta_{13})$ compared between the joint beam-atmospheric fit (Black) and the latest T2K sensitivities (Red) [72, 214]. The reactor constraint is not applied in either fit. The distributions are marginalised over both hierarchies. The marker represents the known value of δ_{CP} – $\sin^2(\theta_{13})$.

³³⁴⁸ by Figure 8.38. The joint analysis disfavours the wrong octant hypothesis more
³³⁴⁹ strongly in the region of high $\sin^2(\theta_{13})$. This change in correlation means that the
³³⁵⁰ application of the reactor constraint could affect the two analyses differently.

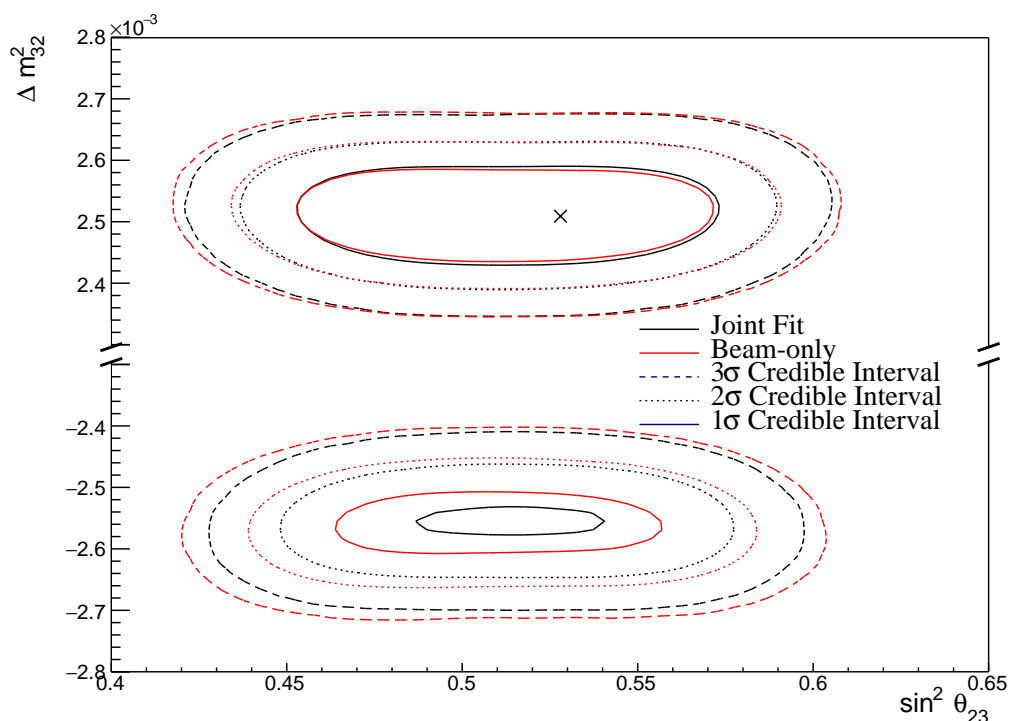


Figure 8.35: The two-dimensional posterior probability density distribution in $\Delta m_{32}^2 \sim \sin^2(\theta_{23})$ compared between the joint beam-atmospheric fit (Black) and the latest T2K sensitivities (Red) [72, 214]. The reactor constraint is not applied in either fit. The marker represents the known value of $\Delta m_{32}^2 \sim \sin^2(\theta_{23})$.

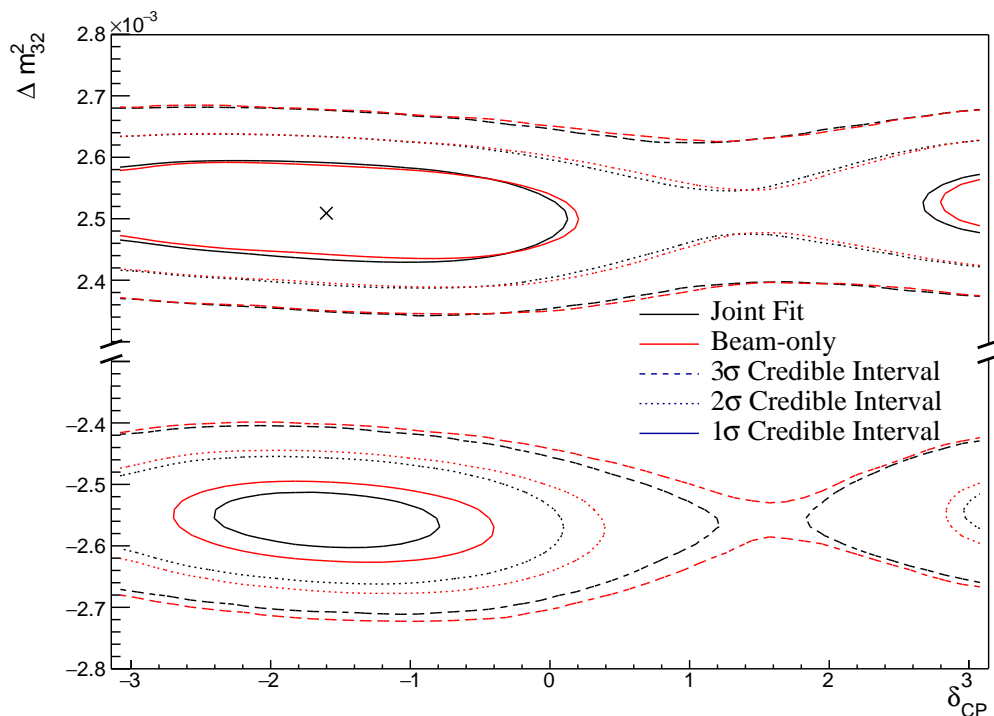


Figure 8.36: The two-dimensional posterior probability density distribution in $\Delta m_{32}^2 \sim \Delta_{CP}$ compared between the joint beam-atmospheric fit (Black) and the latest T2K sensitivities (Red) [72, 214]. The reactor constraint is not applied in either fit. The marker represents the known value of $\Delta m_{32}^2 \sim \Delta_{CP}$.

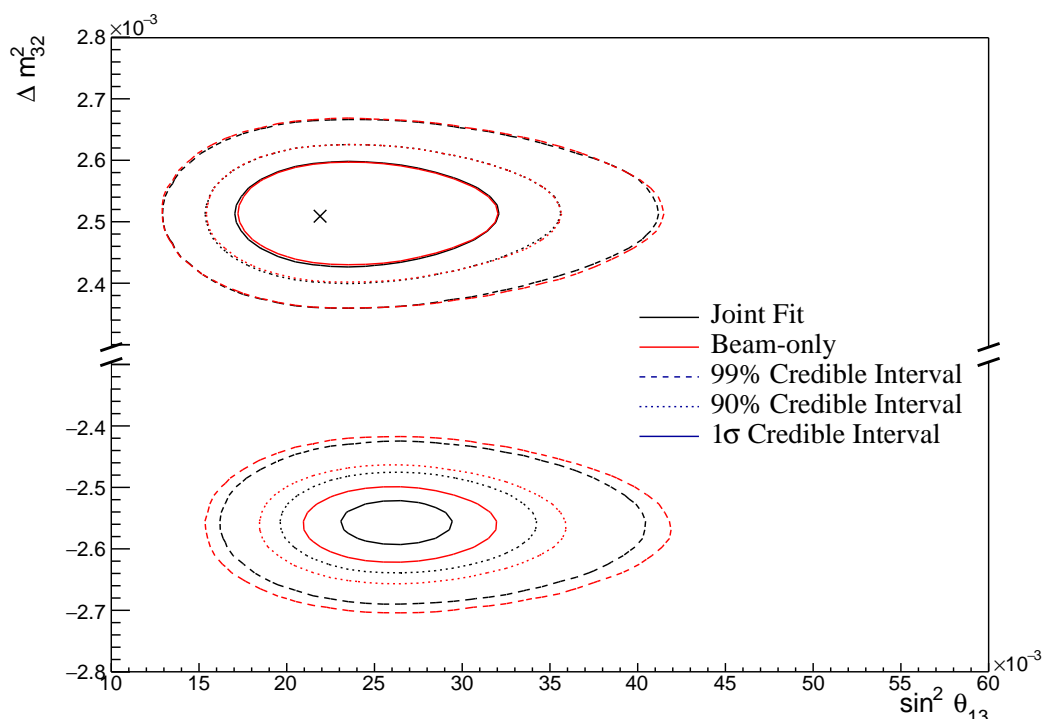


Figure 8.37: The two-dimensional posterior probability density distribution in $\Delta m_{32}^2 \times \sin^2(\theta_{23})$ compared between the joint beam-atmospheric fit (Black) and the latest T2K sensitivities (Red) [72, 214]. The reactor constraint is not applied in either fit. The marker represents the known value of $\Delta m_{32}^2 \times \sin^2(\theta_{23})$.

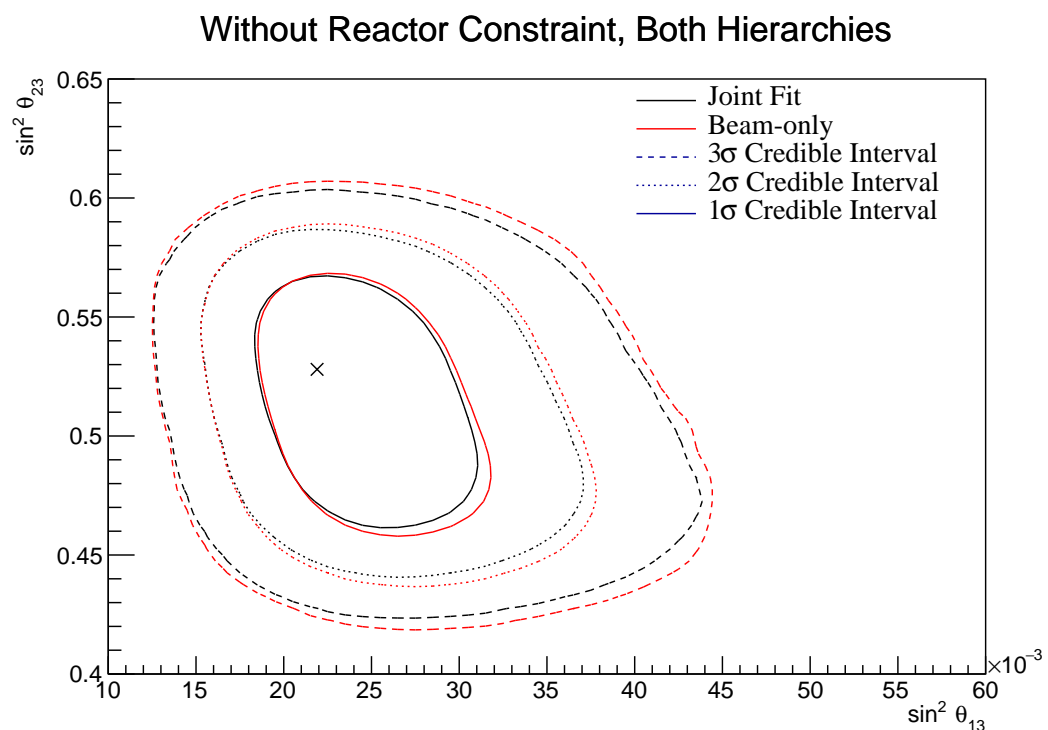


Figure 8.38: The two-dimensional posterior probability density distribution in $\sin^2(\theta_{23}) \times \sin^2(\theta_{13})$ compared between the joint beam-atmospheric fit (Black) and the latest T2K sensitivities (Red) [72, 214]. The reactor constraint is not applied in either fit. The distributions are marginalised over both hierarchies. The marker represents the known value of $\sin^2(\theta_{23}) \times \sin^2(\theta_{13})$.

3351 8.3.7 Comparison to Latest T2K Sensitivities with Reactor Con- 3352 straint

3353 This section illustrates the comparison between the joint beam-atmospheric and
 3354 beam-only fits when the reactor constraint is applied. As shown in Figure 8.37,
 3355 the application of the reactor constraint is expected to significantly increase
 3356 the joint fit's preference for the NH hypothesis, compared to the beam-only
 3357 analysis. Figure 8.39 illustrates the sensitivities of the two fits to the disappearance
 3358 parameters ($\sin^2(\theta_{23}) \sim \Delta m_{32}^2$). This plot further illustrates the benefit of the joint
 3359 beam-atmospheric analysis. The 1σ credible interval in the IH region is entirely
 3360 removed in the joint analysis but not for the beam-only analysis.

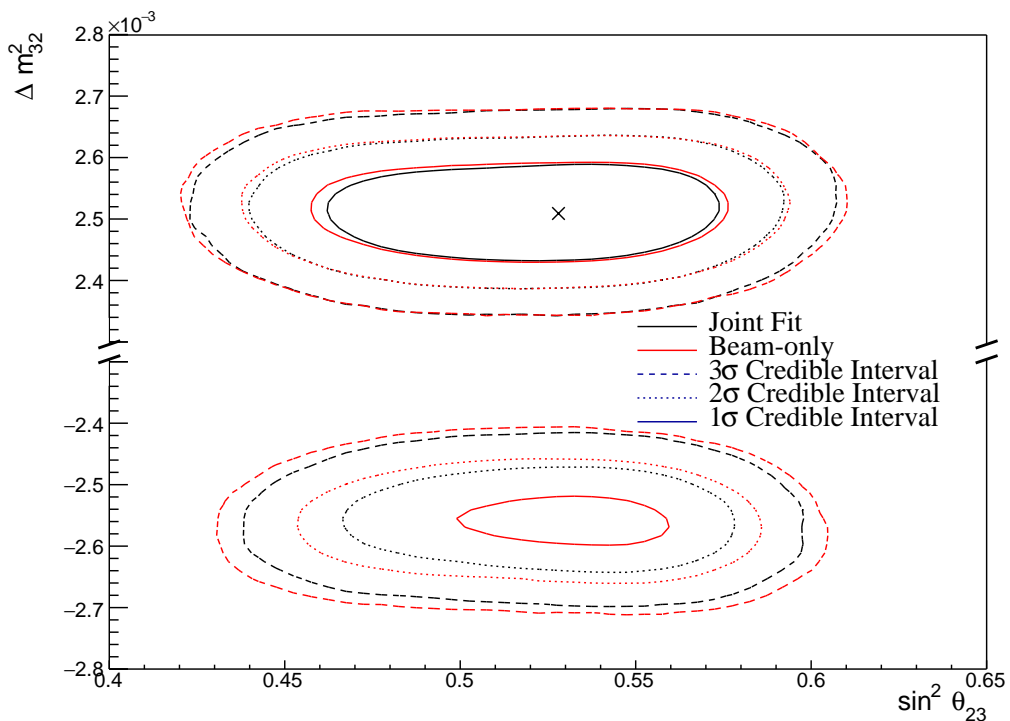


Figure 8.39: The two-dimensional posterior probability density distribution in $\Delta m_{32}^2 \sim \sin^2(\theta_{23})$ compared between the joint beam-atmospheric fit (Black) and the latest T2K sensitivities (Red) [72, 214]. The reactor constraint is applied in both fits. The marker represents the known value of $\Delta m_{32}^2 \sim \sin^2(\theta_{23})$.

3361 The credible intervals of the joint fit are also tighter in the $\sin^2(\theta_{23})$ dimension
 3362 than the beam-only analysis in both mass hierarchy regions. This shows that
 3363 beyond the ability of the joint fit to prefer the NH more strongly than the beam-

only analysis, the precision to which it can measure $\sin^2(\theta_{23})$ is also improved. The Bayes factor for NH preference is calculated as $B(\text{NH}/\text{IH}) = 6.47$ and $B(\text{NH}/\text{IH}) = 3.09$ for the joint beam-atmospheric and beam-only analysis, respectively. This important conclusion illustrates that the joint beam-atmospheric analysis can provide a substantial preference for the NH hypothesis whilst the beam-only analysis can not.

The Bayes factors for UO preference which are $B(\text{UO}/\text{LO}) = 2.86$ and $B(\text{UO}/\text{LO}) = 2.47$ for the joint beam-atmospheric and beam-only analysis, respectively. Both of these represent a mild preference for the UO but a stronger preference is observed in the joint analysis.

The sensitivity of the beam-only and joint beam-atmospheric analyses, to the appearance parameters ($\delta_{CP} \sin^2(\theta_{13})$), are compared in Figure 8.40. These results are marginalised over both hierarchies. For this particular set of known oscillation parameters (AsimovA defined in Table 2.2), the beam-only analysis dominates the sensitivity. The joint fit does slightly increase the sensitivity to δ_{CP} but it does not change any conclusions that would be made. As expected, the prior knowledge dominates any sensitivity either fit would have on $\sin^2(\theta_{13})$.

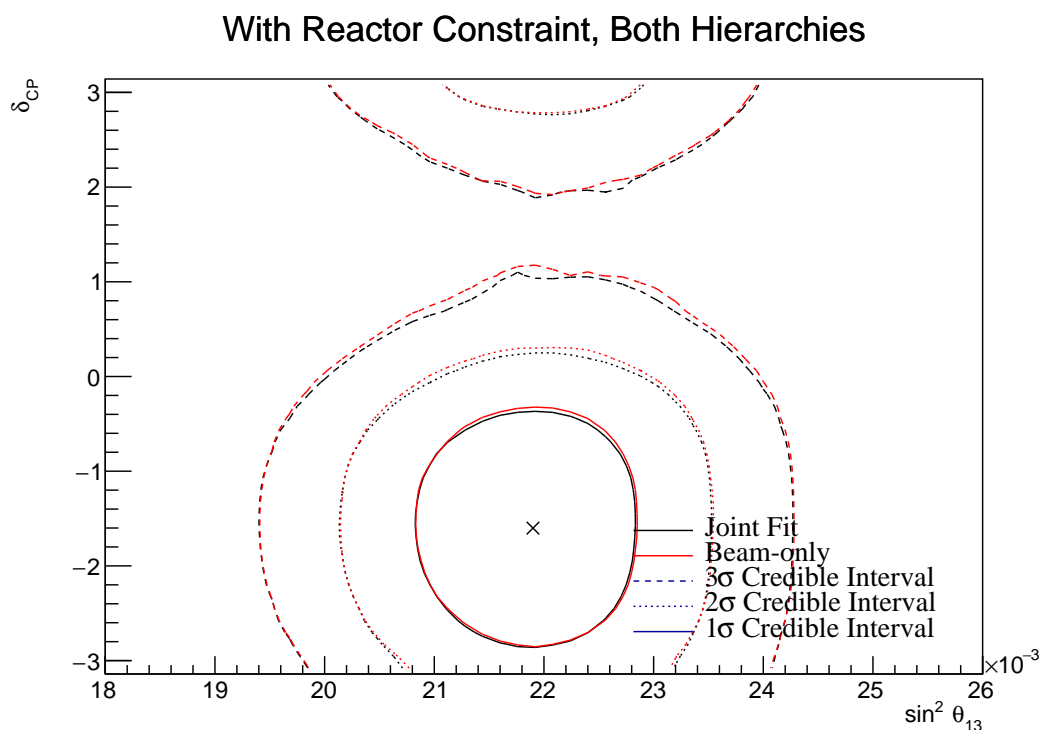


Figure 8.40: The two-dimensional posterior probability density distribution in $\delta_{CP} \sim \sin^2(\theta_{13})$ compared between the joint beam-atmospheric fit (Black) and the latest T2K sensitivities (Red) [72, 214]. The reactor constraint is applied in both fits. The distributions are marginalised over both hierarchies. The marker represents the known value of $\delta_{CP} \sim \sin^2(\theta_{13})$.

3381 8.3.8 Alternate Asimov Parameter Set

3382 Figure 8.4 and Figure 8.5 show that the choice of the parameter set at which the
 3383 Asimov data is made can affect the conclusion. ‘AsimovA’ oscillation parameters
 3384 are defined at a region of δ_{CP} which is preferred by the T2K experiment. This
 3385 explains why the addition of the atmospheric samples does not significantly in-
 3386 crease the sensitivity to δ_{CP} , as illustrated in subsection 8.3.6 and subsection 8.3.7.
 3387 This section presents the sensitivities when ‘AsimovB’ oscillation parameters,
 3388 as defined in Table 2.2, are assumed (alongside the post-BANFF tune) when
 3389 building the Asimov data.

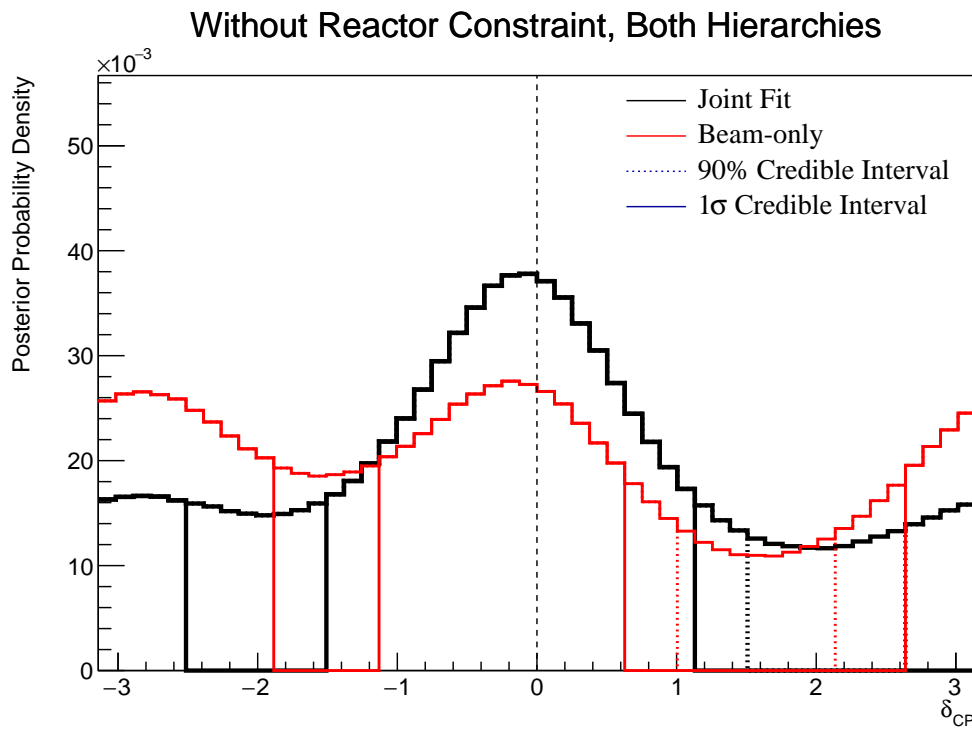


Figure 8.41: The one-dimensional posterior probability density distribution in δ_{CP} compared between the joint beam-atmospheric fit (Black) and the latest T2K sensitivities (Red) [72, 214]. The reactor constraint is not applied in either fit. The distributions are marginalised over both hierarchies. The vertical dashed line represents the known value of δ_{CP} .

3390 The sensitivity to δ_{CP} for the joint beam-atmospheric fit is presented in
 3391 Figure 8.41. The results are compared to those from the beam-only analysis
 3392 in [72, 214]. The reactor constraint is not applied in either of the fits. The

shape of the posterior distribution from the joint analysis is more peaked at the known oscillation parameter value compared to the beam-only analysis, which has approximately the same posterior probability density at $\delta_{CP} = 0$ and $\delta_{CP} = \pm\pi$. This shows the ability of the joint analysis to better determine the correct phase of δ_{CP} if the true value were CP-conserving. The 1σ credible intervals and the position of the highest posterior probability density are given in Table 8.9. The highest posterior density for the joint beam-atmospheric analysis is $\delta_{CP} = -0.06 \pm 0.06$ which is consistent with the known value.

Parameter	Interval	HPD
δ_{CP} , (BH)	$[-\pi, -2.51], [-1.51, 1.13]$	-0.06 ± 0.06
δ_{CP} , (NH)	$[-1.13, 1.63]$	0.06 ± 0.06
δ_{CP} , (IH)	$[-3.02, -1.88], [-1.76, 0.13]$	-0.44 ± 0.06
Δm_{32}^2 (BH) [$\times 10^{-3}\text{eV}^2$]	$[-2.60, -2.52], [2.46, 2.56]$	2.51 ± 0.01
Δm_{32}^2 (NH) [$\times 10^{-3}\text{eV}^2$]	$[2.47, 2.56]$	2.52 ± 0.01
Δm_{32}^2 (IH) [$\times 10^{-3}\text{eV}^2$]	$[-2.61, -2.52]$	-2.57 ± 0.01
$\sin^2(\theta_{23})$ (BH)	$[0.430, 0.480], [0.545, 0.585]$	0.453 ± 0.003
$\sin^2(\theta_{23})$ (NH)	$[0.430, 0.485], [0.550, 0.580]$	0.453 ± 0.003
$\sin^2(\theta_{23})$ (IH)	$[0.435, 0.480], [0.540, 0.585]$	0.568 ± 0.003

Table 8.9: The position of the highest posterior probability density (HPD) and width of the 1σ credible interval for the joint beam-atmospheric fit. The reactor constraint is not applied. The values are presented by which hierarchy hypothesis is assumed: marginalised over both hierarchies (BH), normal hierarchy only (NH) and inverted hierarchy only (IH).

Naively, if just the 1σ credible interval were considered without observing the shape of the distribution, it would appear that the joint analysis would have a worse sensitivity to δ_{CP} due to the larger interval around $\delta_{CP} = 0$. The 1σ credible interval for the beam-only analysis is given as the range $\delta_{CP} = [-\pi, -1.88], [-1.13, 0.63]$ and $[2.64, \pi]$ which contains 56% of all values of δ_{CP} . Whereas, the joint beam-atmospheric analysis contains 52% of all δ_{CP} values within the 1σ credible interval. Therefore, if the area within the 1σ credible

3408 interval were to be compared between the two fits, the joint analysis would
3409 be shown to have better precision.

3410 This apparent contradiction stems from the methodology in which the credible
3411 interval is calculated. The technique used in this analysis (documented in
3412 subsection 4.3.2) fills the credible interval by selecting bins in order of probability
3413 density until 68% of the posterior density is contained. If instead, the credible
3414 interval were calculated by expanding around the highest posterior probability,
3415 the benefits of the joint fit would be more obvious. In the case where the shape
3416 of the posterior was uni-modal, these two techniques would be equivalent to
3417 statistical fluctuations.

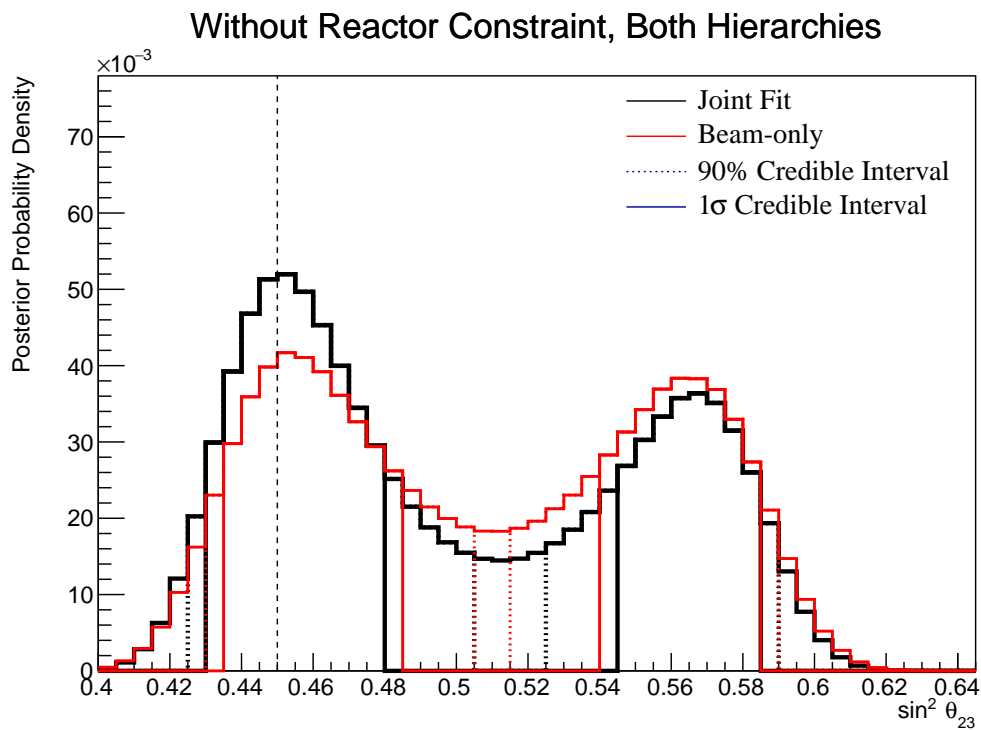


Figure 8.42: The one-dimensional posterior probability density distribution in $\sin^2(\theta_{23})$ compared between the joint beam-atmospheric fit (Black) and the latest T2K sensitivities (Red) [72, 214]. The reactor constraint is not applied in either fit. The distributions are marginalised over both hierarchies. The vertical dashed line represents the known value of $\sin^2(\theta_{23})$.

3418 The sensitivity of the joint beam-atmospheric fit to $\sin^2(\theta_{23})$ is presented in
3419 Figure 8.42. The sensitivity is compared to that of the beam-only analysis in [72,
3420 214]. The reactor constraint is not applied in either of the fits being compared.

3421 The joint beam-atmospheric fit has a much larger probability density in the region
 3422 surrounding the known oscillation parameter, $\sin^2(\theta_{23}) = 0.45$. This shows the
 3423 better octant determination of the joint analysis compared to the beam-only fit.
 3424 The ratio of the posterior density at the peak of the lower octant to the peak of
 3425 the upper octant from the joint fit is 1.43 compared to 1.09 from the beam-only
 3426 analysis. The area contained within the 1σ credible interval for the joint analysis
 3427 is $\sin^2(\theta_{23}) = [0.430, 0.480]$ and $\sin^2(\theta_{23}) = [0.545, 0.585]$, whereas the beam-
 3428 only analysis includes $\sin^2(\theta_{23}) = [0.435, 0.485]$ and $\sin^2(\theta_{23}) = [0.540, 0.585]$.
 3429 This corresponds to a $\sim 5\%$ (binning dependent) increase in precision from
 3430 the joint analysis.

	LO ($\sin^2 \theta_{23} < 0.5$)	UO ($\sin^2 \theta_{23} > 0.5$)	Sum
NH ($\Delta m_{32}^2 > 0$)	0.35	0.24	0.59
IH ($\Delta m_{32}^2 < 0$)	0.19	0.22	0.41
Sum	0.54	0.46	1.00

Table 8.10: The distribution of steps in a joint beam-atmospheric fit, presented as the fraction of steps in the upper (UO) and lower (LO) octants and the normal (NH) and inverted (IH) hierarchies. The reactor constraint is not applied. The Bayes factors are calculated as $B(\text{NH}/\text{IH}) = 1.43$ and $B(\text{LO}/\text{UO}) = 1.19$.

3431 The distribution of steps, split by hierarchy and octant hypothesis, is presented
 3432 in Table 8.10. The Bayes factor for hierarchy and octant determination are
 3433 $B(\text{NH}/\text{IH}) = 1.43$ and $B(\text{LO}/\text{UO}) = 1.19$, respectively. These values compare
 3434 to $B(\text{NH}/\text{IH}) = 1.08$ and $B(\text{LO}/\text{UO}) = 0.91$ from the beam-only analysis. This
 3435 evidences the joint analysis's ability to select the correct octant and hierarchy
 3436 hypothesis. Comparisons to the AsimovA Bayes factors presented in Table 8.6
 3437 show how the preferences for the correct octant and hierarchy depend on the
 3438 true value of δ_{CP} and $\sin^2(\theta_{23})$.

3439 The sensitivity of the beam-only and joint beam-atmospheric analysis to
 3440 Δm_{32}^2 is given in Figure 8.43. The joint analysis has a stronger preference for the
 3441 correct hierarchy (NH) which is shown by the higher Bayes factor compared
 3442 to the beam-only analysis. This is further evidenced by the width of the 90%

Without Reactor Constraint, Both Hierarchies

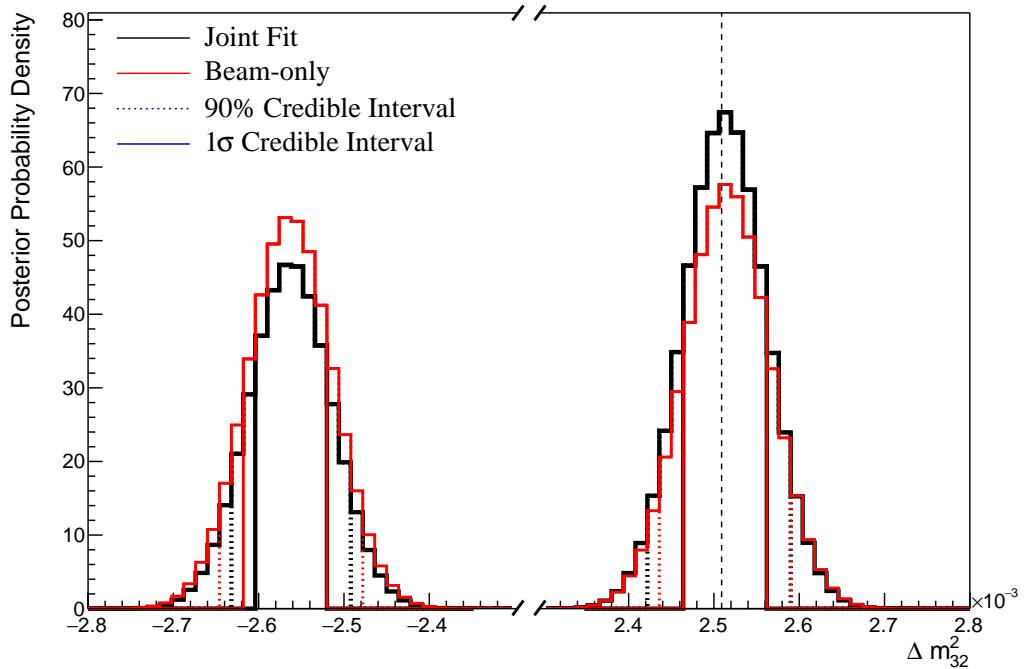


Figure 8.43: The one-dimensional posterior probability density distribution in Δm_{32}^2 compared between the joint beam-atmospheric fit (Black) and the latest T2K sensitivities (Red) [72, 214]. The reactor constraint is not applied in either fit. The vertical dashed line represents the known value of Δm_{32}^2 .

credible interval in the IH region being tighter in the joint analysis compared to the beam-only analysis.

³⁴⁴³ credible interval in the IH region being tighter in the joint analysis compared

³⁴⁴⁴ to the beam-only analysis.

3445 8.3.9 Effect of Systematics

3446 Using the posterior predictive method documented in subsection 4.3.4, the
 3447 distribution of each sample's spectrum has been generated by sampling 2000 steps
 3448 from the posterior distribution of the joint beam-atmospheric fit. This technique
 3449 reweights the Monte Carlo prediction using the systematic values given by a
 3450 particular step, stores the sample spectra, and repeats until the full distribution is
 3451 built. The oscillation parameters are always fixed at Asimov A values. Figure 8.44
 3452 illustrates the distribution for the SubGeV-*elike*-0dcy atmospheric sample. The
 3453 fit being sampled uses an Asimov data set which is created using Asimov A
 3454 oscillation parameters and the post-BANFF tune, as detailed in subsection 8.3.4.
 3455 The distribution closely resembles the Asimov data spectrum (denoted 'Post
 3456 BANFF Spectra'). This would be expected from an Asimov fit where the Monte
 3457 Carlo is fit to itself but gives more credibility to the results of the fit.

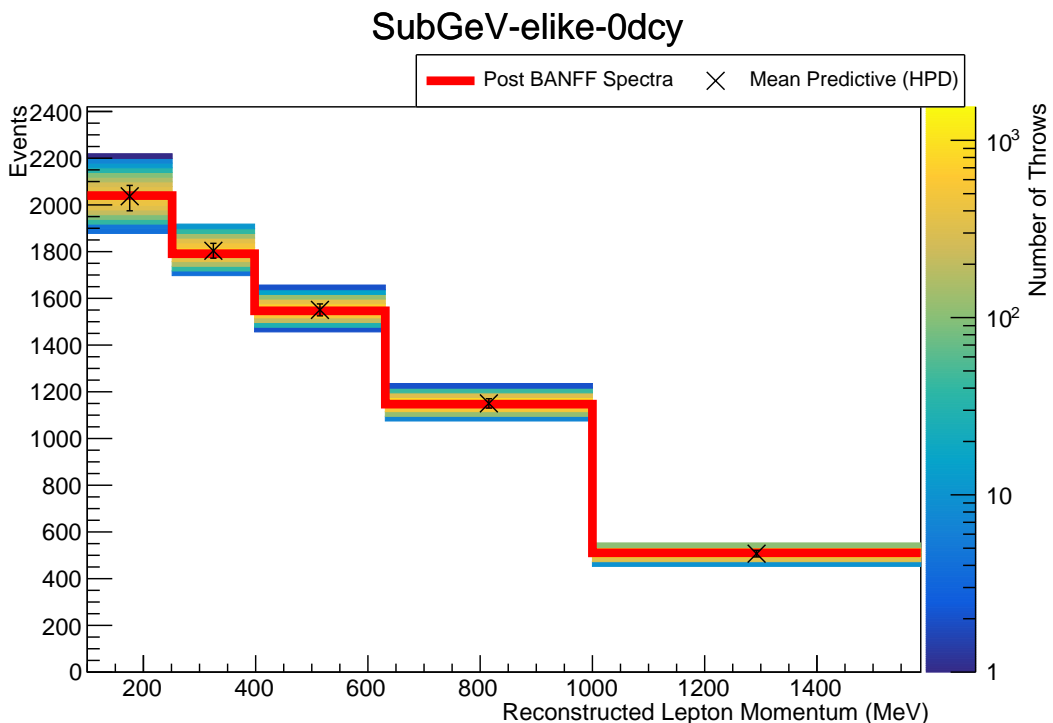


Figure 8.44: Result of the posterior predictive method for the SubGeV_elike_0dcy sample after sampling 2000 steps from the joint beam-atmospheric chain detailed in subsection 8.3.4 (Coloured histogram). The mean and uncertainty is presented for each bin. The Asimov data prediction (Red) assumes the post-BANFF tune and Asimov A oscillation parameters.

The total event rate for each sample from each of the sampled steps is calculated and the fractional uncertainty, $\Delta N_i / N_i$ where N_i is the event rate of the i^{th} sample, is calculated. These values are presented in Table 8.11. In general, the impact of the systematics has an $\sim 3\%$ uncertainty on the event rate of atmospheric samples, where CC1 π targeting samples have slightly larger uncertainties than the CCQE-like samples. The fractional uncertainties on the beam samples are compared to those from the beam-only analysis presented in [72, 214]. The uncertainties on the one-ring muon samples are mostly unchanged, whereas the uncertainties on the one-ring electron samples are different. As discussed in section 8.2, the atmospheric samples should be able to add constraints on the NC background events present in the FHC1Re and RHC1Re samples. The uncertainty reduction seen in those samples is due to those additional constraints. The reason why the FHC1Re1de has a higher uncertainty in this analysis is due to the addition of the ad-hoc systematic introduced for CC1 π interactions (see subsection 6.4.3).

Beyond the impact on the uncertainty of each sample's event rate, the post-fit constraint on each systematic parameter should be checked. Figure 8.45 illustrates the central value and uncertainty on a select group of interaction systematics, for both the joint beam-atmospheric (from subsection 8.3.4) and the beam-only analysis. From the discussion in section 8.2, the uncertainty on systematics which are strongly constrained by the near detector should not significantly change when adding the atmospheric analysis. This behaviour is evidenced by the fact that the ratio of constraints between the two fits are very similar (within a few %) for almost all systematics. The only systematic which is more constrained in the joint beam-atmospheric analysis is the *NCOtherSK* normalisation parameter, which has a $O(10\%)$ tighter constraint. As expected, the atmospheric samples have been able to constrain this systematic which leads to the reduction in uncertainty for the beam electron-like samples.

Sample	Joint Analysis	Beam-only Analysis
SubGeV- <i>elike</i> -0dcy	2.53	-
SubGeV- <i>elike</i> -1dcy	3.28	-
SubGeV- <i>mulike</i> -0dcy	2.62	-
SubGeV- <i>mulike</i> -1dcy	2.23	-
SubGeV- <i>mulike</i> -2dcy	3.96	-
SubGeV- <i>pi0like</i>	2.84	-
MultiGeV- <i>elike</i> -nue	5.14	-
MultiGeV- <i>elike</i> -nuebar	2.79	-
MultiGeV- <i>mulike</i>	2.99	-
MultiRing- <i>elike</i> -nue	2.94	-
MultiRing- <i>elike</i> -nuebar	2.83	-
MultiRing- <i>mulike</i>	2.89	-
MultiRingOther-1	2.70	-
PCStop	3.22	-
PCThru	2.99	-
UpStop-mu	2.95	-
UpThruNonShower-mu	2.70	-
UpThruShower-mu	3.19	-
FHC1Rmu	2.49	2.33
RHC1Rmu	2.89	2.93
FHC1Re	4.12	4.57
RHC1Re	5.15	5.65
FHC1Re1de	13.38	11.51

Table 8.11: The fractional uncertainty, $\Delta N / N$, as calculated from sampling 2000 throws from a joint beam-atmospheric chain. The same values for the beam samples are provided from the beam-only analysis [72, 214]. These uncertainties consider all systematic parameters to be sampled from the fit whilst the oscillation parameters are fixed at the Asimov A oscillation set.

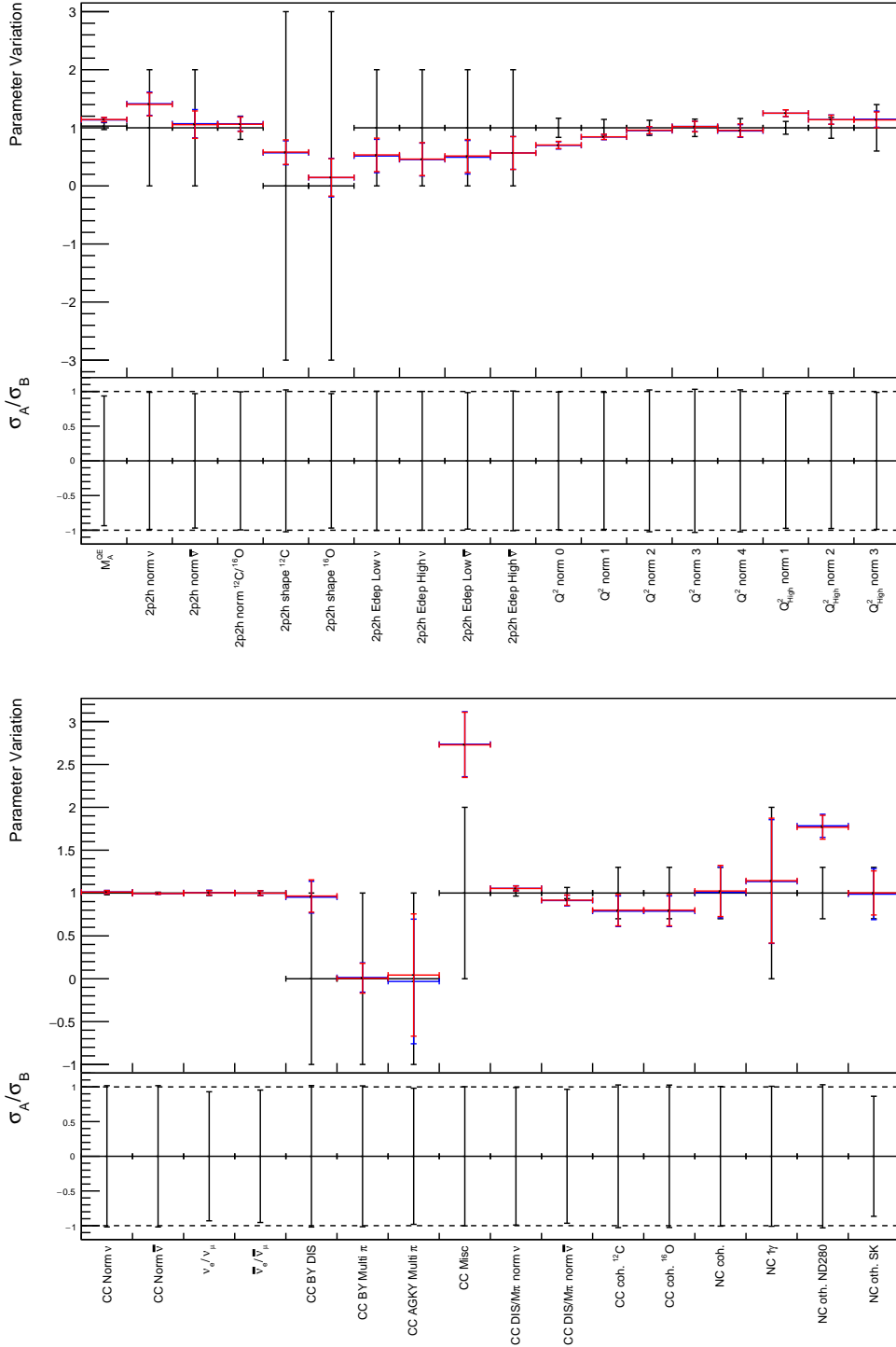


Figure 8.45: Central values and 1σ uncertainties for a select group of interaction systematics. The constraints from the prior uncertainty (Black), joint atmospheric-beam fit given in subsection 8.3.4 (Red) and beam-only analysis [72, 214] (Blue) are presented. The top pad of each plot presents the parameter variation and the bottom pad represents the ratio of the uncertainty between the joint beam-atmospheric and beam-only fits, where a value below 1.0 means the joint fit has a tighter constraint than the beam-only analysis.

3485 8.4 Summary of Sensitivity Studies

3486 The sensitivities to each oscillation parameter from the joint beam-atmospheric
 3487 and beam-only fits, which use the Asimov A oscillation parameter set, are
 3488 summarised in Table 8.12. As the posterior distribution to δ_{CP} is cyclical, only the
 3489 position of the highest posterior density is given. Furthermore, the Δm_{32}^2 reported
 3490 values only consider the NH credible interval region as the full discussion can
 3491 be found in the previous section.

Fit	δ_{CP} (HPD)	$\Delta m_{32}^2 [\times 10^{-3}\text{eV}^2]$	$\sin^2(\theta_{23})$	$\sin^2(\theta_{13}) [\times 10^{-2}]$
Asimov A	-1.601	2.509	0.528	2.19
Beam	-1.45 ± 0.06	$2.51^{+0.07}_{-0.06}$	$0.501^{+0.044}_{-0.026}$	$2.45^{+0.45}_{-0.35}$
Beam w/RC	-1.57 ± 0.06	$2.51^{+0.08}_{-0.06}$	$0.533^{+0.022}_{-0.043}$	$2.19^{+0.06}_{-0.07}$
Joint	-1.57 ± 0.06	$2.51^{+0.07}_{-0.06}$	$0.518^{+0.027}_{-0.038}$	$2.35^{+0.45}_{-0.35}$
Joint w/RC	-1.57 ± 0.06	$2.51^{+0.05}_{-0.06}$	$0.528^{+0.027}_{-0.038}$	$2.18^{+0.07}_{-0.06}$

Table 8.12: A comparison of the sensitivity to each oscillation parameter of interest, from the beam-only [72, 214] and joint atmospheric-beam fits discussed within this thesis. The results are illustrated both with and without the reactor constraint (RC). The best-fit values are taken from the highest posterior density (HPD) and the error comes from the width of the one-dimensional 1σ credible intervals. As the posterior distribution in δ_{CP} is cyclical, the highest posterior distribution is given instead.

3492 The Bayes factors from the beam-only and joint atmospheric-beam analyses,
 3493 from the Asimov A fits, are presented in Table 8.13. The strength of each
 3494 preference is, from Jeffrey's scale (Table 4.1), is also given.

3495 To summarise this information, the joint fit prefers a tighter 1σ credible
 3496 interval in $\sin^2(\theta_{23})$ along with a stronger Bayes factor for preferring the correct
 3497 octant hypothesis. The increase in sensitivity to $|\Delta m_{32}^2|$ between the two fits is
 3498 negligible but the joint analysis substantially prefers the correct mass hierarchy
 3499 hypothesis. It does not require any external constraints on $\sin^2(\theta_{13})$ to make
 3500 this statement. The joint analysis also prefers a value of $\sin^2(\theta_{13})$ closer to the
 3501 known value compared to the beam-only analysis. When the reactor constraint is

Fit	$B(\text{NH}/\text{IH})$		$B(\text{UO}/\text{LO})$	
	Value	Strength	Value	Strength
Asimov A				
Beam	1.91	Weak	1.56	Weak
Beam w/RC	3.09	Weak	2.47	Weak
Joint	3.67	Substantial	1.74	Weak
Joint w/RC	6.47	Substantial	2.64	Weak
Asimov B				
Beam	1.08	Weak	0.91	Weak
Beam w/RC	0.98	Weak	1.15	Weak
Joint	1.43	Weak	1.19	Weak
Joint w/RC	1.36	Weak	1.52	Weak

Table 8.13: A comparison of the Bayes factors for mass hierarchy and $\sin^2(\theta_{23})$ octant hypotheses, from the beam-only [72, 214] and joint atmospheric-beam fits discussed within this thesis. The results are illustrated both with and without the reactor constraint (RC). The strength of the preference for the normal mass hierarchy and upper octants are provided by Jeffrey's scale Table 8.13.

3502 applied, the preference for both the NH and UO hypotheses increases but does
 3503 not change the statement which would be made.

3504 The fits from the Asimov B comparisons show the improved ability for
 3505 the joint analysis to more precisely select the true value of δ_{CP} if it were CP-
 3506 conserving, compared to the beam-only analysis. This is evidenced by the area
 3507 contained within the 1σ credible interval decreasing by $\sim 4\%$. Furthermore,
 3508 the joint fit is able to better determine the octant of $\sin^2(\theta_{23})$ when the true
 3509 value is moved further away from the boundary as evidenced by the larger
 3510 Bayes factor. There is also a $\sim 5\%$ reduction of area contained within the 1σ
 3511 credible interval in $\sin^2(\theta_{23})$.

9

3512

3513

Conclusions and Outlook

3514 This thesis has presented the sensitivites of a joint beam and atmospheric neutrino
3515 oscillation parameter measurements from the Tokai-to-Kamioka (T2K) and Super-
3516 Kamiokande (SK) experiments. It combines the two independent analyses
3517 presented by the two collaborations [72, 84]. This analysis combines 3244.4
3518 days equivalent of SK livetime and 1.97×10^{21} (1.63×10^{21}) POT recorded at the
3519 far detector in the neutrino(antineutrino) beam operating mode. The ND280 near
3520 detector is used within this analysis to constrain the beam flux and cross-section
3521 systematics. It uses 1.15×10^{21} POT and 8.34×10^{20} POT in the neutrino and
3522 antineutrino running modes, respectively.

3523 This analysis uses a Bayesian Markov Chain Monte Carlo fitting technique
3524 implemented within the MaCh3 framework. This analysis has significantly devel-
3525 oped the fitting framework, both in terms of technical features and performance.
3526 This includes supporting new samples, systematics and oscillation channels.
3527 These developments have become the foundation of the fitters expansion into
3528 other neutrino oscillation experiments. Beyond these improvements, a novel
3529 technique of calculating the atmospheric neutrino oscillation probabilities has
3530 been developed. This calculation uses a sub-sampling linear-averaging approach
3531 to ensure that the sensitivities being calculated are not biased due to insufficient
3532 Monte Carlo statistics in a region of rapidly varying probability. It illustrates a

3533 computationally feasible method of reliably calculating oscillation probabilities
3534 which can be utilised within any fitting framework.

3535 The sensitivity of the joint beam-atmospheric analysis is presented in Table 9.1,
3536 and compared to the beam-only analysis [72]. This uses a set of known oscillation
3537 parameter values close to the results from a previous T2K analysis [75]. The
3538 joint analysis has a stronger sensitivity to $\sin^2(\theta_{23})$, as evidenced by the tighter
3539 1σ credible intervals when the reactor constraint is not applied. The joint fit's
3540 sensitivity to δ_{CP} is marginally stronger than beam-only analysis but would not
3541 change any conclusion which would be made. Whilst the sensitivity to $|\Delta m_{32}^2|$
3542 is mostly unchanged between the two analyses, the sensitivity to select the
3543 correct hierarchy given is significantly improved. This follows from substantial
3544 preference for the normal hierarchy hypothesis presented within the joint analysis,
3545 as classified by the Jeffrey's scale [133]. This is notable as the beam-only analysis
3546 can not make this statement, either with or without the application of the reactor
3547 constraint. The joint fit's preference for the correct hierarchy increases once the
3548 reactor constraint is applied. The preference for selecting the correct octant of
3549 $\sin^2(\theta_{23})$ is classified as weak by the Jeffrey's scale but is still stronger than the
3550 statement made by the beam-only analysis.

Fit	δ_{CP} (HPD)	Δm_{32}^2 [$\times 10^{-3}\text{eV}^2$]	$\sin^2(\theta_{23})$	$B(\text{NH/IH})$	$B(\text{UO/LO})$
Asimov A	-1.601	2.509	0.528	NH	UO
Beam	$-1.45^{+0.06}_{-0.06}$	$2.51^{+0.07}_{-0.06}$	$0.501^{+0.044}_{-0.026}$	1.91	1.56
Beam w/RC	$-1.57^{+0.06}_{-0.06}$	$2.51^{+0.08}_{-0.06}$	$0.533^{+0.022}_{-0.043}$	3.09	2.47
Joint	$-1.57^{+0.06}_{-0.06}$	$2.51^{+0.07}_{-0.06}$	$0.518^{+0.027}_{-0.038}$	3.67	1.74
Joint w/RC	$-1.57^{+0.06}_{-0.06}$	$2.51^{+0.05}_{-0.06}$	$0.528^{+0.027}_{-0.038}$	6.47	2.64

Table 9.1

3551 The sensitivities of the beam-only and joint atmospheric-beam fit have also
3552 been compared at a set of known oscillation parameters which are CP-conserving
3553 and in the lower octant of $\sin^2(\theta_{23})$. The joint-analysis has an $\sim 5\%$ improved

ability to select the known values more precisely compared to the beam-only analysis. This is further evidenced by the larger Bayes factor for preferring the correct hierarchy and octant hypothesis. These sensitivities have been presented by the T2K and SK collaborations at the Neutrino 2022 conference [104].

Whilst this analysis provides the first sensitivity measurement of a joint beam and atmospheric analysis, there are more improvements which could be made. Since this analysis began, T2K has released an updated oscillation analysis with additional near and far detector samples alongside a more sophisticated interaction model [104]. The overall change in oscillation parameter measurement observed by T2K was relatively minor but the stronger constraints on the systematics could impact this joint analysis to a larger extent. Further developments could consider the effect of correlating the beam and atmospheric flux uncertainties, where updates of the Bartol and Honda models may allow this to be studied [150].

Beyond these model improvements, more data is available than what is assumed for this analysis. The T2K experiment has ran an additional period of two months, corresponding to an additional 1.78×10^{20} POT in neutrino mode. Similarly, there are several SK periods which have not been considered within this analysis as the reconstruction software used in this analysis has not been validated for those periods. The SK-Gd era will also continue to accumulate statistics. Developments in the atmospheric sample selections may also benefit from the Gadolinium dopants as neutron capture will aid in neutrino/antineutrino separation leading to better mass hierarchy sensitivity. This would require including interaction systematics for neutron capture of Gadolinium which has already started [215].

Moving towards the next generation neutrino experiments, this analysis has the potential to become the basis of the oscillation analysis for future Hyper-Kamiokande experiment.

Bibliography

- [1] J. Chadwick. "Intensitätsverteilung im magnetischen Spectrum der β -Strahlen von radium B + C". In: *Verhandl. Dtsc. Phys. Ges.* 16 (1914), p. 383. URL: <http://cds.cern.ch/record/262756>.
- [2] C. D. Ellis and W. A. Wooster. "The average energy of disintegration of radium E". en. In: *Proc. R. Soc. Lond. A Math. Phys. Sci.* 117.776 (Dec. 1927), pp. 109–123.
- [3] W. Pauli. "Dear radioactive ladies and gentlemen". In: *Phys. Today* 31N9 (1978), p. 27.
- [4] E. Fermi. "An attempt of a theory of beta radiation. 1." In: *Z. Phys.* 88 (1934), pp. 161–177.
- [5] F. Reines and C. L. Cowan. "Detection of the Free Neutrino". In: *Phys. Rev.* 92 (3 1953), pp. 830–831. URL: <https://link.aps.org/doi/10.1103/PhysRev.92.830>.
- [6] C. L. Cowan et al. "Detection of the Free Neutrino: a Confirmation". In: *Science* 124.3212 (1956), pp. 103–104. URL: <http://science.sciencemag.org/content/124/3212/103>.
- [7] G. Danby et al. "Observation of High-Energy Neutrino Reactions and the Existence of Two Kinds of Neutrinos". In: *Phys. Rev. Lett.* 9 (1 1962), pp. 36–44. URL: <https://link.aps.org/doi/10.1103/PhysRevLett.9.36>.
- [8] K. Kodama et al. "Observation of tau neutrino interactions". In: *Physics Letters B* 504.3 (2001), pp. 218 –224. URL: <http://www.sciencedirect.com/science/article/pii/S0370269301003070>.
- [9] A. Aguilar-Arevalo et al. "Evidence for neutrino oscillations from the observation of anti-neutrino(electron) appearance in a anti-neutrino(muon) beam". In: *Phys. Rev.* D64 (2001), p. 112007. arXiv: hep-ex/0104049 [hep-ex].
- [10] A. A. Aguilar-Arevalo et al. "Improved Search for $\bar{\nu}_\mu \rightarrow \bar{\nu}_e$ Oscillations in the MiniBooNE Experiment". In: *Phys. Rev. Lett.* 110 (16 2013), p. 161801. URL: <https://link.aps.org/doi/10.1103/PhysRevLett.110.161801>.
- [11] Planck Collaboration. "Planck 2018 results. VI. Cosmological parameters". In: *aap* 641 (Sept. 2020).
- [12] J. A. Bagger et al. "Precision electroweak measurements on the Z resonance". In: *Physics Reports* 427.5 (2006), pp. 257 –454. URL: <http://www.sciencedirect.com/science/article/pii/S0370157305005119>.
- [13] B. Pontecorvo. "Neutrino Experiments and the Problem of Conservation of Leptonic Charge". In: *Sov. Phys. JETP* 26 (1968). [Zh. Eksp. Teor. Fiz. 53, 1717(1967)], pp. 984–988.

- [14] B. Pontecorvo. "Inverse beta processes and nonconservation of lepton charge". In: *Sov. Phys. JETP* 7 (1958). [Zh. Eksp. Teor. Fiz.34,247(1957)], pp. 172–173.
- [15] M. Kobayashi and T. Maskawa. "CP-Violation in the Renormalizable Theory of Weak Interaction". In: *Progress of Theoretical Physics* 49.2 (1973), pp. 652–657. URL: <http://dx.doi.org/10.1143/PTP.49.652>.
- [16] N. Cabibbo. "Unitary Symmetry and Leptonic Decays". In: *Phys. Rev. Lett.* 10 (12 1963), pp. 531–533. URL: <https://link.aps.org/doi/10.1103/PhysRevLett.10.531>.
- [17] A. Maio et al. "Search for Majorana neutrinos with the SNO+ detector at SNOLAB". In: *Journal of Physics: Conference Series* 587 (2015), p. 012030. URL: <https://doi.org/10.1088/1742-6596/587/1/012030>.
- [18] A. Y. Smirnov. "The MSW effect and Solar Neutrinos". In: *Arxiv* (2003). URL: <https://arxiv.org/abs/hep-ph/0305106>.
- [19] S. P. Mikheyev and A. Y. Smirnov. "Resonance enhancement of oscillations in matter and solar neutrino spectroscopy". In: *Soviet Journal of Nuclear Physics* 42 (6 1985), pp. 913–917.
- [20] L. Wolfenstein. "Neutrino oscillations in matter". In: *Phys. Rev. D* 17 (9 1978), pp. 2369–2374. URL: <https://link.aps.org/doi/10.1103/PhysRevD.17.2369>.
- [21] V. D. Barger et al. "Matter Effects on Three-Neutrino Oscillations". In: *Phys. Rev. D* 22 (1980), p. 2718.
- [22] Y. Ashie et al. "Evidence for an Oscillatory Signature in Atmospheric Neutrino Oscillations". In: *Phys. Rev. Lett.* 93 (10 2004), p. 101801. URL: <https://link.aps.org/doi/10.1103/PhysRevLett.93.101801>.
- [23] Q. R. Ahmad et al. "Direct Evidence for Neutrino Flavor Transformation from Neutral-Current Interactions in the Sudbury Neutrino Observatory". In: *Phys. Rev. Lett.* 89 (1 2002), p. 011301. URL: <https://link.aps.org/doi/10.1103/PhysRevLett.89.011301>.
- [24] Nobel Prize. *2015 Nobel prize in Physics as listed by Nobelprize.org*. https://www.nobelprize.org/nobel_prizes/physics/laureates/2015/. Accessed: 22-06-2022.
- [25] J. A. Formaggio and G. P. Zeller. "From eV to EeV: Neutrino Cross Sections Across Energy Scales". In: *Rev. Mod. Phys.* 84 (2012), pp. 1307–1341. arXiv: 1305.7513 [hep-ex].
- [26] A. Oralbaev, M. Skorokhvatov, and O. Titov. "The inverse beta decay: a study of cross section". In: *Journal of Physics: Conference Series* 675.1 (2016), p. 012003. URL: <https://doi.org/10.1088/1742-6596/675/1/012003>.
- [27] A. Bellerive. "Review of solar neutrino experiments". en. In: *Int. J. Mod. Phys. A* 19.08 (Mar. 2004), pp. 1167–1179.
- [28] R. Davis, D. S. Harmer, and K. C. Hoffman. "Search for Neutrinos from the Sun". In: *Phys. Rev. Lett.* 20 (21 1968), pp. 1205–1209. URL: <https://link.aps.org/doi/10.1103/PhysRevLett.20.1205>.
- [29] N. Vinyoles et al. "A new generation of standard solar models". In: *Astrophys. J.* 835.2 (Jan. 2017), p. 202.

- 3661 [30] V. Gribov and B. Pontecorvo. "Neutrino astronomy and lepton charge". en. In: *Phys. Lett. B* 28.7 (Jan. 1969), pp. 493–496.
- 3662 [31] K. S. Hirata et al. "Observation of ${}^8\text{B}$ solar neutrinos in the Kamiokande-II detector". In: *Phys. Rev. Lett.* 63 (1 1989), pp. 16–19. URL: <https://link.aps.org/doi/10.1103/PhysRevLett.63.16>.
- 3663 [32] W. Hampel et al. "GALLEX solar neutrino observations: results for GALLEX IV". en. In: *Phys. Lett. B* 447.1-2 (Feb. 1999), pp. 127–133.
- 3664 [33] J. N. Abdurashitov et al. "Measurement of the solar neutrino capture rate with gallium metal". In: *Phys. Rev. C* 60 (5 1999), p. 055801. URL: <https://link.aps.org/doi/10.1103/PhysRevC.60.055801>.
- 3665 [34] Borexino Collaboration. "Comprehensive measurement of pp-chain solar neutrinos". en. In: *Nature* 562.7728 (Oct. 2018), pp. 505–510.
- 3666 [35] B. Aharmim et al. "A search for neutrinos from the SolarhepReaction and the diffuse supernova neutrino background with the Sudbury neutrino observatory". en. In: *Astrophys. J.* 653.2 (Dec. 2006), pp. 1545–1551.
- 3667 [36] Borexino Collaboration. "Experimental evidence of neutrinos produced in the CNO fusion cycle in the Sun". In: *Nature* 587.7835 (2020), pp. 577–582. URL: <https://doi.org/10.1038%2Fs41586-020-2934-0>.
- 3668 [37] K. Abe et al. "T2K neutrino flux prediction". In: *Phys. Rev. D* 87 (1 2013), p. 012001. URL: <https://link.aps.org/doi/10.1103/PhysRevD.87.012001>.
- 3669 [38] D. G. Michael et al. "Observation of Muon Neutrino Disappearance with the MINOS Detectors in the NuMI Neutrino Beam". In: *Phys. Rev. Lett.* 97 (19 2006), p. 191801. URL: <https://link.aps.org/doi/10.1103/PhysRevLett.97.191801>.
- 3670 [39] M. H. Ahn et al. "Measurement of neutrino oscillation by the K2K experiment". In: *Phys. Rev. D* 74 (7 2006), p. 072003. eprint: <https://link.aps.org/doi/10.1103/PhysRevD.74.072003>.
- 3671 [40] M. A. Acero et al. "First measurement of neutrino oscillation parameters using neutrinos and antineutrinos by NOvA". In: *Phys. Rev. Lett.* 123 (15 2019), p. 151803. URL: <https://link.aps.org/doi/10.1103/PhysRevLett.123.151803>.
- 3672 [41] K. Abe et al. "The T2K experiment". In: *Nuclear Instruments and Methods in Physics Research Section A* 659.1 (2011), pp. 106 –135. eprint: <http://www.sciencedirect.com/science/article/pii/S0168900211011910>.
- 3673 [42] B. Abi et al. "Long-baseline neutrino oscillation physics potential of the DUNE experiment". en. In: *Eur. Phys. J. C Part. Fields* 80.10 (Oct. 2020).
- 3674 [43] Hyper-Kamiokande Proto-Collaboration. "Physics potential of a long-baseline neutrino oscillation experiment using a J-PARC neutrino beam and Hyper-Kamiokande". In: *Prog. Theor. Exp. Phys.* 2015.5 (May 2015), pp. 53C02–0.
- 3675 [44] C. Blanco, D. Hooper, and P. Machado. "Constraining sterile neutrino interpretations of the LSND and MiniBooNE anomalies with coherent neutrino scattering experiments". In: *Phys. Rev. D* 101.7 (2020). URL: <https://doi.org/10.1103%2Fphysrevd.101.075051>.

- 3704 [45] MicroBooNE Collaboration. "Search for an Excess of Electron Neutrino
3705 Interactions in MicroBooNE Using Multiple Final State Topologies". In: *arXiv*
3706 (2021). URL: <https://arxiv.org/abs/2110.14054>.
- 3707 [46] B. Armbruster et al. "Upper limits for neutrino oscillations $\bar{\nu}_\mu \rightarrow \bar{\nu}_e$ from muon
3708 decay at rest". In: *Phys. Rev. D* 65 (11 2002), p. 112001. URL:
3709 <https://link.aps.org/doi/10.1103/PhysRevD.65.112001>.
- 3710 [47] T. K. Gaisser and M. Honda. "Flux of Atmospheric Neutrinos". In: *Annual Review
3711 of Nuclear and Particle Science* 52.1 (2002), pp. 153–199. URL:
3712 <https://doi.org/10.1146%2Fannurev.nucl.52.050102.090645>.
- 3713 [48] G. D. Barr et al. "Three-dimensional calculation of atmospheric neutrinos". In:
3714 *Phys. Rev. D* 70.2 (2004). URL: <https://doi.org/10.1103/physrevd.70.023006>.
- 3715 [49] M. Honda et al. "Calculation of atmospheric neutrino flux using the interaction
3716 model calibrated with atmospheric muon data". In: *Phys. Rev. D* 75.4 (2007). URL:
3717 <https://doi.org/10.1103/physrevd.75.043006>.
- 3718 [50] M. Honda et al. "New calculation of the atmospheric neutrino flux in a
3719 three-dimensional scheme". In: *Phys. Rev. D* 70 (4 2004), p. 043008. URL:
3720 <https://link.aps.org/doi/10.1103/PhysRevD.70.043008>.
- 3721 [51] M. Honda et al. "Improvement of low energy atmospheric neutrino flux
3722 calculation using the JAM nuclear interaction model". In: *Phys. Rev. D* 83 (12
3723 2011), p. 123001. URL:
3724 <https://link.aps.org/doi/10.1103/PhysRevD.83.123001>.
- 3725 [52] A. Fassò et al. *FLUKA: Status and Prospects for Hadronic Applications*. Ed. by
3726 Andreas Kling et al. Berlin, Heidelberg: Springer Berlin Heidelberg, 2001,
3727 pp. 955–960.
- 3728 [53] Y. Ashie et al. "Measurement of atmospheric neutrino oscillation parameters by
3729 Super-Kamiokande I". In: *Phys. Rev. D* 71.11 (2005). URL:
3730 <https://doi.org/10.1103/physrevd.71.112005>.
- 3731 [54] F. Reines et al. "Evidence for high-energy cosmic-ray neutrino interactions". In:
3732 *Phys. Rev. Lett.* 15.9 (Aug. 1965), pp. 429–433.
- 3733 [55] D. Casper et al. "Measurement of atmospheric neutrino composition with the
3734 IMB-3 detector". In: *Phys. Rev. Lett.* 66 (20 1991), pp. 2561–2564. URL:
3735 <https://link.aps.org/doi/10.1103/PhysRevLett.66.2561>.
- 3736 [56] K. S. Hirata et al. "Observation of a small atmospheric ν_μ/ν_e ratio in
3737 Kamiokande". en. In: *Phys. Lett. B* 280.1-2 (Apr. 1992), pp. 146–152.
- 3738 [57] Z. Li et al. "Measurement of the tau neutrino cross section in atmospheric
3739 neutrino oscillations with Super-Kamiokande". In: *Phys. Rev. D* 98.5 (2018). URL:
3740 <https://doi.org/10.1103/physrevd.98.052006>.
- 3741 [58] K. Abe et al. "Atmospheric neutrino oscillation analysis with external constraints
3742 in Super-Kamiokande I-IV". In: *Phys. Rev. D* 97 (7 2018), p. 072001. URL:
3743 <https://link.aps.org/doi/10.1103/PhysRevD.97.072001>.
- 3744 [59] T2K Collaboration. "Constraint on the matter-antimatter symmetry-violating
3745 phase in neutrino oscillations". en. In: *Nature* 580.7803 (Apr. 2020), pp. 339–344.

- 3746 [60] M. A. Acero et al. "First measurement of neutrino oscillation parameters using
3747 neutrinos and antineutrinos by NOvA". en. In: *Phys. Rev. Lett.* 123.15 (Oct. 2019),
3748 p. 151803.
- 3749 [61] M. G. Aartsen et al. "Measurement of atmospheric neutrino oscillations at 6–56
3750 GeV with IceCube DeepCore". In: *Phys. Rev. Lett.* 120.7 (Feb. 2018).
- 3751 [62] P. Adamson et al. "Combined analysis of $\nu\mu$ Disappearance
3752 and $\nu\mu \rightarrow \nu e$ Appearance in MINOS using accelerator and atmospheric neutrinos".
3753 In: *Phys. Rev. Lett.* 112.19 (May 2014).
- 3754 [63] M. Sajjad Athar et al. "Status and perspectives of neutrino physics". In: *Progress*
3755 *in Particle and Nuclear Physics* 124 (2022), p. 103947. URL:
3756 <https://doi.org/10.1016/Fj.pnnp.2022.103947>.
- 3757 [64] S. B. Kim, T. Lasserre, and Y. Wang. "Reactor Neutrinos". In: *Adv. High Energy*
3758 *Phys.* 2013 (2013), pp. 1–34.
- 3759 [65] K Abe et al. "First gadolinium loading to Super-Kamiokande". en. In: *Nucl.*
3760 *Instrum. Methods Phys. Res. A* 1027.166248 (Mar. 2022), p. 166248.
- 3761 [66] F. P. An et al. "Observation of Electron-Antineutrino Disappearance at Daya Bay".
3762 In: *Phys. Rev. Lett.* 108 (17 2012), p. 171803. URL:
3763 <https://link.aps.org/doi/10.1103/PhysRevLett.108.171803>.
- 3764 [67] J. K. Ahn et al. "Observation of Reactor Electron Antineutrinos Disappearance in
3765 the RENO Experiment". In: *Phys. Rev. Lett.* 108 (19 2012), p. 191802. URL:
3766 <https://link.aps.org/doi/10.1103/PhysRevLett.108.191802>.
- 3767 [68] Y. Abe et al. "Indication of Reactor $\bar{\nu}_e$ Disappearance in the Double Chooz
3768 Experiment". In: *Phys. Rev. Lett.* 108 (13 2012), p. 131801. URL:
3769 <https://link.aps.org/doi/10.1103/PhysRevLett.108.131801>.
- 3770 [69] JUNO Collaboration. "TAO Conceptual Design Report: A Precision
3771 Measurement of the Reactor Antineutrino Spectrum with Sub-percent Energy
3772 Resolution". In: *arXiv* (2020). arXiv: 2005.08745 [physics.ins-det].
- 3773 [70] M. P. Decowski. "KamLAND's precision neutrino oscillation measurements". en.
3774 In: *Nucl. Phys. B*. 908 (July 2016), pp. 52–61.
- 3775 [71] A. Gando et al. "Constraints on θ_{13} from a three-flavor oscillation analysis of
3776 reactor antineutrinos at KamLAND". In: *Phys. Rev. D* 83 (5 2011), p. 052002. URL:
3777 <https://link.aps.org/doi/10.1103/PhysRevD.83.052002>.
- 3778 [72] P. Dunne. "Latest Neutrino Oscillation Results from T2K". In: *Neutrino 2020*
3779 (2020). URL: <https://zenodo.org/record/3959557>.
- 3780 [73] Particle Data Group. "Review of particle physics". en. In: *Prog. Theor. Exp. Phys.*
3781 2020.8 (Aug. 2020).
- 3782 [74] R. L. Workman et al. "Review of Particle Physics". In: *PTEP* 2022 (2022),
3783 p. 083C01.
- 3784 [75] K. Abe et al. "Precise Measurement of the Neutrino Mixing Parameter θ_{23} from
3785 Muon Neutrino Disappearance in an Off-Axis Beam". In: *Phys. Rev. Lett.* 112 (18
3786 2014), p. 181801. URL:
3787 <https://link.aps.org/doi/10.1103/PhysRevLett.112.181801>.

- 3788 [76] R. Wendell. "Three Flavor Oscillation Analysis of Atmospheric Neutrinos in
3789 Super-Kamiokande". PhD thesis. University of North Carolina, 2008.
- 3790 [77] A. M. Dziewonski and D. L. Anderson. "Preliminary reference Earth model". en.
3791 In: *Phys. Earth Planet. Inter.* 25.4 (June 1981), pp. 297–356.
- 3792 [78] Y. Fukuda et al. "Evidence for oscillation of atmospheric neutrinos". In: *Phys. Rev.*
3793 *Lett.* 81.8 (Aug. 1998), pp. 1562–1567.
- 3794 [79] K. Abe et al. "Calibration of the Super-Kamiokande detector". In: *Nuclear*
3795 *Instruments and Methods in Physics Research Section A* 737 (2014), pp. 253–272. URL:
3796 <https://doi.org/10.1016/j.nima.2013.11.081>.
- 3797 [80] L. Wan. "Atmospheric Neutrino Super-K". In: *Neutrino 2022* (2022). URL:
3798 <https://zenodo.org/record/6694761>.
- 3799 [81] M. Jiang. "Study of the neutrino mass hierarchy with the atmospheric neutrino
3800 data collected in Super-Kamiokande IV". PhD thesis. Kyoto University, 2019.
- 3801 [82] S. Fukuda et al. "The super-kamiokande detector". en. In: *Nucl. Instrum. Methods*
3802 *Phys. Res. A* 501.2-3 (Apr. 2003), pp. 418–462. eprint:
3803 <http://www.sciencedirect.com/science/article/pii/S016890020300425X>.
- 3804 [83] Y. Itow et al. "The JHF-Kamioka neutrino project". In: *arXiv* (2001).
- 3805 [84] M. Jiang et al. "Atmospheric neutrino oscillation analysis with improved event
3806 reconstruction in Super-Kamiokande IV". en. In: *Prog. Theor. Exp. Phys.* 2019.5
3807 (May 2019).
- 3808 [85] H. Kume et al. "20 inch diameter photomultiplier". In: *Nuclear Instruments and*
3809 *Methods in Physics Research* 205.3 (1983), pp. 443–449. URL:
3810 <https://www.sciencedirect.com/science/article/pii/0167508783900078>.
- 3811 [86] A. Suzuki et al. "Improvement of 20 in. diameter photomultiplier tubes". In:
3812 *Nuclear Instruments and Methods in Physics Research Section A: Accelerators,*
3813 *Spectrometers, Detectors and Associated Equipment* 329.1-2 (May 1993), pp. 299–313.
3814 URL: [https://doi.org/10.1016/0168-9002\(93\)90949-i](https://doi.org/10.1016/0168-9002(93)90949-i).
- 3815 [87] Y. Nakano et al. "Measurement of the radon concentration in purified water in
3816 the Super-Kamiokande IV detector". en. In: *Nucl. Instrum. Methods Phys. Res. A*
3817 977.164297 (Oct. 2020), p. 164297.
- 3818 [88] Hamamatsu. *Hamamatsu Photonics Photomultiplier Tubes Handbook*. URL:
3819 https://www.hamamatsu.com/content/dam/hamamatsu-photonics/sites/documents/99_SALES_LIBRARY/etd/PMT_handbook_v4E.pdf.
- 3820 [89] J. F. Beacom and M. R. Vagins. "Antineutrino Spectroscopy with Large Water
3821 Čerenkov Detectors". In: *Phys. Rev. Lett.* 93 (17 2004), p. 171101. URL:
3822 <https://link.aps.org/doi/10.1103/PhysRevLett.93.171101>.
- 3823 [90] L. Marti et al. "Evaluation of gadolinium's action on water Cherenkov detector
3824 systems with EGADS". en. In: *Nucl. Instrum. Methods Phys. Res. A* 959.163549
3825 (Apr. 2020), p. 163549.
- 3826 [91] M. Vagins. "Solar/DSNB Neutrino SK-Gd". In: *Neutrino 2022* (2022). URL:
3827 <https://zenodo.org/record/6696210>.
- 3828 [92] J. Focht. "Dark Noise Calibration of the Super-Kamiokande Outer Detector".
3829 PhD thesis. Massachusetts Institute of Technology, 2004.

- 3831 [93] T. Tanimori et al. "Design and performance of semi-custom analog IC including
3832 two TACs and two current integrators for 'Super-Kamiokande'". In: *IEEE*
3833 *Transactions on Nuclear Science* 36.1 (1989), pp. 497–501.
- 3834 [94] J. Hosaka et al. "Solar neutrino measurements in Super-Kamiokande-I". In: *Phys.*
3835 *Rev. D* 73 (11 2006), p. 112001.
- 3836 [95] H. Nishino et al. "High-speed charge-to-time converter ASIC for the
3837 Super-Kamiokande detector". en. In: *Nucl. Instrum. Methods Phys. Res. A* 610.3
3838 (Nov. 2009), pp. 710–717.
- 3839 [96] S. Yamada et al. "Commissioning of the New Electronics and Online System for
3840 the Super-Kamiokande Experiment". In: *IEEE Transactions on Nuclear Science* 57.2
3841 (2010), pp. 428–432.
- 3842 [97] S. Yamada et al. "New online system without hardware trigger for the
3843 Super-Kamiokande experiment". In: *2007 IEEE Nuclear Science Symposium*
3844 *Conference Record*. Honolulu, HI, USA: IEEE, Oct. 2007.
- 3845 [98] G. Carminati. "The new wide-band solar neutrino trigger for super-kamiokande".
3846 In: *Phys. Procedia* 61 (2015), pp. 666–672.
- 3847 [99] P. A. Čerenkov. "Visible radiation produced by electrons moving in a medium
3848 with velocities exceeding that of light". In: *Phys. Rev.* 52.4 (Aug. 1937),
3849 pp. 378–379.
- 3850 [100] I. Frank and I. Tamm. "Coherent visible radiation of fast electrons passing
3851 through matter". In: *Selected Papers*. Berlin, Heidelberg: Springer Berlin
3852 Heidelberg, 1991, pp. 29–35.
- 3853 [101] The T2K Collaboration. "Letter of Intent: Neutrino Oscillation Experiment at
3854 JHF". In: *KEK Proposal* (2001). eprint:
3855 <http://neutrino.kek.jp/jhfnu/loi/loi.v2.030528.pdf>.
- 3856 [102] The K2K Collaboration and S. H. Ahn. "Detection of Accelerator-Produced
3857 Neutrinos at a Distance of 250 km". In: (Feb. 2001). arXiv: [hep-ex/0103001](https://arxiv.org/abs/hep-ex/0103001)
3858 [hep-ex].
- 3859 [103] The T2K Collaboration. "Tokai-to-Kamioka (T2K) Long Baseline Neutrino
3860 Oscillation Experiment Proposal". In: *KEK Proposal* (2006). eprint: [http://j-](http://j-parc.jp/researcher/Hadron/en/pac\0606/pdf/p11-Nishikawa.pdf)
3861 [parc.jp/researcher/Hadron/en/pac\0606/pdf/p11-Nishikawa.pdf](http://j-parc.jp/researcher/Hadron/en/pac\0606/pdf/p11-Nishikawa.pdf).
- 3862 [104] C. Bronner. "Accelerator Neutrino I Recent results from T2K". In: *Neutrino 2022*
3863 (2022). URL: <https://zenodo.org/record/6683821>.
- 3864 [105] K. Abe et al. "Observation of Electron Neutrino Appearance in a Muon Neutrino
3865 Beam". In: *Phys. Rev. Lett.* 112 (6 2014), p. 061802. eprint:
3866 <https://link.aps.org/doi/10.1103/PhysRevLett.112.061802>.
- 3867 [106] T. Fukuda et al. "Proposal for precise measurement of neutrino-water
3868 cross-section in NINJA physics run". Proposal for J-PARC and KEK. 2017.
- 3869 [107] T. Ovsiannikova et al. "New experiment WAGASCI to measure cross sections of
3870 neutrino interactions in water and hydrocarbon using J-PARC beam". In: *Physics*
3871 *of Particles and Nuclei* 48.6 (2017), pp. 1014–1017. eprint:
3872 <https://doi.org/10.1134/S1063779617060478>.

- 3873 [108] M. Antonova et al. "Baby MIND: a magnetized segmented neutrino detector for
3874 the WAGASCI experiment". In: *Journal of Instrumentation* 12.07 (2017), p. C07028.
3875 eprint: <http://stacks.iop.org/1748-0221/12/i=07/a=C07028>.
- 3876 [109] K. Abe et al. "First measurement of the charged current $\bar{\nu}_\mu$ double differential
3877 cross section on a water target without pions in the final state". In: *Phys. Rev. D*
3878 102 (1 2020), p. 012007. URL:
3879 <https://link.aps.org/doi/10.1103/PhysRevD.102.012007>.
- 3880 [110] K. Abe et al. "Measurements of $\bar{\nu}_\mu$ and $\bar{\nu}_\mu + \nu_\mu$ charged-current cross-sections
3881 without detected pions or protons on water and hydrocarbon at a mean
3882 anti-neutrino energy of 0.86 GeV". In: *Progress of Theoretical and Experimental*
3883 *Physics* 2021.4 (Mar. 2021). URL: <https://doi.org/10.1093/ptep/ptab014>.
- 3884 [111] K. Matsuoka et al. "Design and performance of the muon monitor for the T2K
3885 neutrino oscillation experiment". In: *Nuclear Instruments and Methods in Physics*
3886 *Research Section A* 624.3 (2010), pp. 591–600. eprint:
3887 <http://www.sciencedirect.com/science/article/pii/S016890021002098X>.
- 3888 [112] K. Abe et al. "Improved constraints on neutrino mixing from the T2K experiment
3889 with 3.13×10^{21} protons on target". en. In: *Phys. Rev. D.* 103.11 (June 2021).
- 3890 [113] T. Vladisavljevic. *Predicting the T2K neutrino flux and measuring oscillation*
3891 *parameters*. 1st ed. Springer theses. Cham, Switzerland: Springer Nature, Sept.
3892 2020.
- 3893 [114] D. Beavis, A. Carroll, and I. Chiang. "Long baseline neutrino oscillation
3894 experiment at the AGS. Physics design report". In: *Office of Scientific and Technical*
3895 *Information (OSTI)* (Apr. 1995).
- 3896 [115] P.-A. Amaudruz et al. "The T2K fine-grained detectors". In: *Nuclear Instruments*
3897 *and Methods in Physics Research Section A: Accelerators, Spectrometers, Detectors and*
3898 *Associated Equipment* 696 (Dec. 2012), pp. 1–31. URL:
3899 <https://doi.org/10.1016/j.nima.2012.08.020>.
- 3900 [116] N. Abgrall et al. "Time projection chambers for the T2K near detectors". In:
3901 *Nuclear Instruments and Methods in Physics Research Section A: Accelerators,*
3902 *Spectrometers, Detectors and Associated Equipment* 637.1 (May 2011), pp. 25–46. URL:
3903 <https://doi.org/10.1016/j.nima.2011.02.036>.
- 3904 [117] S. Assylbekov et al. "The T2K ND280 off-axis pi-zero detector". In: *Nuclear*
3905 *Instruments and Methods in Physics Research Section A: Accelerators, Spectrometers,*
3906 *Detectors and Associated Equipment* 686 (Sept. 2012), pp. 48–63. URL:
3907 <https://doi.org/10.1016/j.nima.2012.05.028>.
- 3908 [118] D. Allan et al. "The electromagnetic calorimeter for the T2K near detector
3909 ND280". In: *Journal of Instrumentation* 8.10 (2013), P10019–P10019. URL:
3910 <https://doi.org/10.1088%2F1748-0221%2F8%2F10%2Fp10019>.
- 3911 [119] CERN Courier. *UA1 magnet sets off for a second new life*. 2008. URL: <https://cerncourier.com/a/ua1-magnet-sets-off-for-a-second-new-life/>.
- 3912 [120] F. Vannucci. "The NOMAD Experiment at CERN". In: *Advances in High Energy*
3913 *Physics* 2014 (2014), pp. 1–20. URL: <https://doi.org/10.1155/2014/129694>.

- 3915 [121] S. Aoki et al. "The T2K Side Muon Range Detector (SMRD)". In: *Nuclear*
3916 *Instruments and Methods in Physics Research Section A: Accelerators, Spectrometers,*
3917 *Detectors and Associated Equipment* 698 (Jan. 2013), pp. 135–146. URL:
3918 <https://doi.org/10.1016/j.nima.2012.10.001>.
- 3919 [122] K. Suzuki et al. "Measurement of the muon beam direction and muon flux for the
3920 T2K neutrino experiment". In: *Progress of Theoretical and Experimental Physics*
3921 2015.5 (2015), pp. 53C01–0. URL: <https://doi.org/10.1093%2Fptep%2Fptv054>.
- 3922 [123] S. Brooks et al. *Handbook of Markov Chain Monte Carlo*. CRC Press, 2011.
- 3923 [124] W. R. Gilks, S. Richardson, and D. J. Spiegelhalter. *Markov Chain Monte Carlo in*
3924 *Practice*. Chapman & Hall/CRC Interdisciplinary Statistics, 1995.
- 3925 [125] C. Wret. "Minimising systematic uncertainties in the T2K experiment using
3926 near-detector and external data". PhD thesis. Imperial College London, 2018.
- 3927 [126] K. E. Duffy. "Measurement of the Neutrino Oscillation Parameters $\sin^2 \theta_{23}$, Δm_{32}^2 ,
3928 $\sin^2 \theta_{13}$, and δ_{CP} in Neutrino and Antineutrino Oscillation at T2K". PhD thesis.
3929 Oriel College, University of Oxford, 2016.
- 3930 [127] C. Bojeckho and A. Kabooth. "Muon neutrino disappearance simultaneous fit of
3931 ND280 and SK with Run 1+2+3 data using Markov Chain Monte Carlo Analysis".
3932 In: *T2K Technical Note* 140 (2013).
- 3933 [128] T. Bayes. "An essay toward solving a problem in the doctrine of chances". In: *Phil.*
3934 *Trans. Roy. Soc. Lond.* 53 (1764), pp. 370–418.
- 3935 [129] A. Sztuc. "Standard and Non-Standard Neutrino-Antineutrino Oscillation
3936 Analyses and Event Reconstruction Studies using Markov Chain Monte Carlo
3937 Methods at T2K". PhD thesis. Imperial College London, 2021.
- 3938 [130] N. Metropolis et al. "Equation of State Calculations by Fast Computing
3939 Machines". In: *Journal of Chemical Physics* 21.6 (1970).
- 3940 [131] W. K. Hastings. "Monte Carlo Sampling Methods Using Markov Chains and
3941 Their Applications". In: *Biometrika* 57.1 (1970).
- 3942 [132] J. Dunkley et al. "Fast and reliable Markov chain Monte Carlo technique for
3943 cosmological parameter estimation". en. In: *Mon. Not. R. Astron. Soc.* 356.3 (Jan.
3944 2005), pp. 925–936.
- 3945 [133] H. Jeffreys. *The Theory of Probability*. Oxford Classic Texts in the Physical Sciences.
3946 1939.
- 3947 [134] R. E. Kass and A. E. Raftery. "Bayes factors". en. In: *J. Am. Stat. Assoc.* 90.430
3948 (June 1995), pp. 773–795.
- 3949 [135] T.T. Böhlen et al. "The FLUKA Code: Developments and Challenges for High
3950 Energy and Medical Applications". In: *Nuclear Data Sheets* 120 (2014), pp. 211
3951 –214. eprint:
3952 <http://www.sciencedirect.com/science/article/pii/S0090375214005018>.
- 3953 [136] R. Brun et al. *GEANT: Detector Description and Simulation Tool; Oct 1994*. CERN
3954 Program Library. Long Writeup W5013. Geneva: CERN, 1993. eprint:
3955 <http://cds.cern.ch/record/1082634>.

- 3956 [137] C. Zeitnitz and T.A. Gabriel. "The GEANT-CALOR interface and benchmark
3957 calculations of ZEUS test calorimeters". In: *Nuclear Instruments and Methods in*
3958 *Physics Research Section A* 349.1 (1994), pp. 106–111. eprint:
3959 <http://www.sciencedirect.com/science/article/pii/0168900294906130>.
- 3960 [138] A. Fiorentini et al. "Flux Prediction and Uncertainty Updates with NA61 2009
3961 Thin Target Data and Negative Focussing Mode Predictions". In: *T2K Technical*
3962 *Note* 217 (2017).
- 3963 [139] N. Abgrall et al. "Measurements of cross sections and charged pion spectra in
3964 proton-carbon interactions at 31 GeV". In: *Phys. Rev. C* 84.3 (2011). URL:
3965 <https://doi.org/10.1103%2Fphysrevc.84.034604>.
- 3966 [140] N. Abgrall et al. "Measurement of production properties of positively charged
3967 kaons in proton-carbon interactions at 31 GeV". In: *Phys. Rev. C* 85.3 (2012). URL:
3968 <https://doi.org/10.1103%2Fphysrevc.85.035210>.
- 3969 [141] N. Abgrall et al. "Pion emission from the T2K replica target: Method, results and
3970 application". In: *Nuclear Instruments and Methods in Physics Research Section A* 701
3971 (2013), pp. 99–114. eprint:
3972 <http://www.sciencedirect.com/science/article/pii/S016890021201234X>.
- 3973 [142] M. Apollonio et al. "Forward production of charged pions with incident protons
3974 on nuclear targets at the CERN Proton Synchrotron". In: *Phys. Rev. C* 80 (3 2009),
3975 p. 035208. eprint: <https://link.aps.org/doi/10.1103/PhysRevC.80.035208>.
- 3976 [143] B. Blau et al. "The superconducting magnet of AMS-02". In: *Nuclear Physics B -*
3977 *Proceedings Supplements* 113.1-3 (Dec. 2002), pp. 125–132. URL:
3978 [https://doi.org/10.1016/s0920-5632\(02\)01831-5](https://doi.org/10.1016/s0920-5632(02)01831-5).
- 3979 [144] S. Haino et al. "Measurements of primary and atmospheric cosmic-ray spectra
3980 with the BESS-TeV spectrometer". In: *Physics Letters B* 594.1-2 (July 2004),
3981 pp. 35–46. URL: <https://doi.org/10.1016/j.physletb.2004.05.019>.
- 3982 [145] NASA. *U.S. Standard Atmosphere, 1976.* 1976. URL: <https://ntrs.nasa.gov/api/citations/19770009539/downloads/19770009539.pdf>.
- 3984 [146] S. Roesler, R. Engel, and J. Ranft. "The Monte Carlo Event Generator
3985 DPMJET-III". In: *Advanced Monte Carlo for Radiation Physics, Particle Transport*
3986 *Simulation and Applications*. Springer Berlin Heidelberg, 2001, pp. 1033–1038. URL:
3987 https://doi.org/10.1007/978-3-642-18211-2_166.
- 3988 [147] K. Niita et al. "PHITS—a particle and heavy ion transport code system". In:
3989 *Radiation Measurements* 41.9-10 (Oct. 2006), pp. 1080–1090. URL:
3990 <https://doi.org/10.1016/j.radmeas.2006.07.013>.
- 3991 [148] T. Sanuki et al. "Measurements of atmospheric muon spectra at mountain
3992 altitude". In: *Physics Letters B* 541.3-4 (2002), pp. 234–242. URL:
3993 <https://doi.org/10.1016%2Fs0370-2693%2802%2902265-7>.
- 3994 [149] P. Achard et al. "Measurement of the atmospheric muon spectrum from 20 to
3995 3000 GeV". In: *Physics Letters B* 598.1-2 (2004), pp. 15–32. URL:
3996 <https://doi.org/10.1016%2Fj.physletb.2004.08.003>.
- 3997 [150] K. Sato. "Atmospheric Neutrino Reviews on neutrino fluxes (low E atm nu)". In:
3998 *Neutrino 2022* (2022). URL: <https://zenodo.org/record/6695711>.

- 3999 [151] Y. Hayato and L. Pickering. "The NEUT neutrino interaction simulation program
4000 library". In: *The European Physical Journal Special Topics* 230.24 (Oct. 2021),
4001 pp. 4469–4481. URL: <https://doi.org/10.1140/epjs/s11734-021-00287-7>.
- 4002 [152] Y. Hayato. "A Neutrino Interaction Simulation Program Library NEUT". In: *Acta
4003 Physica Polonica B* 40.9 (2009).
- 4004 [153] C. H. Llewellyn Smith. "Neutrino reactions at accelerator energies". In: *Physics
4005 Reports* 3.5 (1972), pp. 261 –379. eprint:
4006 <http://www.sciencedirect.com/science/article/pii/0370157372900105>.
- 4007 [154] O. Benhar, A. Fabrocini, and S. Fantoni. "The nucleon spectral function in infinite
4008 nuclear matter". In: *Nuclear Physics A* 497 (June 1989), pp. 423–430. URL:
4009 [https://doi.org/10.1016/0375-9474\(89\)90484-3](https://doi.org/10.1016/0375-9474(89)90484-3).
- 4010 [155] R. Bradford et al. "A New Parameterization of the Nucleon Elastic Form Factors".
4011 In: *Nuclear Physics B - Proceedings Supplements* 159 (2006). Proceedings of the 4th
4012 International Workshop on Neutrino-Nucleus Interactions in the Few-GeV
4013 Region, pp. 127 –132. eprint:
4014 <http://www.sciencedirect.com/science/article/pii/S0920563206005184>.
- 4015 [156] A. A. Aguilar-Arevalo et al. "First measurement of the muon neutrino charged
4016 current quasielastic double differential cross section". In: *Phys. Rev. D* 81.9 (2010).
4017 URL: <https://doi.org/10.1103/2Fphysrevd.81.092005>.
- 4018 [157] R. Gran et al. "Neutrino-nucleus quasi-elastic and 2p2h interactions up to 10
4019 GeV". In: *Phys. Rev. D* 88 (11 2013), p. 113007. eprint:
4020 <https://link.aps.org/doi/10.1103/PhysRevD.88.113007>.
- 4021 [158] C. Berger and L. M. Sehgal. "Lepton mass effects in single pion production by
4022 neutrinos". In: *Phys. Rev. D* 76 (11 2007), p. 113004. URL:
4023 <https://link.aps.org/doi/10.1103/PhysRevD.76.113004>.
- 4024 [159] C. Berger and L. M. Sehgal. "Partially conserved axial vector current and
4025 coherent pion production by low energy neutrinos". In: *Phys. Rev. D* 79 (5 2009),
4026 p. 053003. eprint: <https://link.aps.org/doi/10.1103/PhysRevD.79.053003>.
- 4027 [160] T. Sjöstrand. "High-energy-physics event generation with PYTHIA 5.7 and
4028 JETSET 7.4". In: *Computer Physics Communications* 82.1 (Aug. 1994), pp. 74–89.
4029 URL: [https://doi.org/10.1016/0010-4655\(94\)90132-5](https://doi.org/10.1016/0010-4655(94)90132-5).
- 4030 [161] C. Bronner and M. Hartz. "Tuning of the Charged Hadrons Multiplicities for
4031 Deep Inelastic Interactions in NEUT". In: *Proceedings of the 10th International
4032 Workshop on Neutrino-Nucleus Interactions in Few-GeV Region (NuInt15)*. Journal of
4033 the Physical Society of Japan, Dec. 2016. URL:
4034 <https://doi.org/10.7566/jpscp.12.010041>.
- 4035 [162] M. Glück, E. Reya, and A. Vogt. "Dynamical parton distributions revisited". In:
4036 *The European Physical Journal C* 5.3 (1998), pp. 461–470. URL:
4037 <https://doi.org/10.1007%2Fs100529800978>.
- 4038 [163] A. Bodek and U. Yang. "Axial and Vector Structure Functions for Electron- and
4039 Neutrino- Nucleon Scattering Cross Sections at all Q^2 using Effective Leading
4040 order Parton Distribution Functions". In: *arXiv* (2010). URL:
4041 <https://arxiv.org/abs/1011.6592>.

- 4042 [164] A. Bodek and U. Yang. "Update to the Bodek-Yang Unified Model for Electron-
4043 and Neutrino- Nucleon Scattering Cross Sections". In: *arXiv* (2010). URL:
4044 <https://arxiv.org/abs/1012.0261>.
- 4045 [165] S. Gollapinni. "Neutrino Cross section Future". In: *arXiv* (2016). URL:
4046 <https://arxiv.org/abs/1602.05299>.
- 4047 [166] E. S. Pinzon Guerra et al. "Using world π^\pm -nucleus scattering data to constrain
4048 an intranuclear cascade model". In: *Phys. Rev. D* 99 (5 2019), p. 052007. URL:
4049 <https://link.aps.org/doi/10.1103/PhysRevD.99.052007>.
- 4050 [167] S. Agostinelli et al. "GEANT4: A Simulation toolkit". In: *Nucl. Instrum. Meth.*
4051 A506 (2003), pp. 250–303.
- 4052 [168] R. Brun et al. "GEANT3". In: *Cern Document Server* (Sept. 1987).
- 4053 [169] A. Himmel et al. "Super-Kamiokande events and data quality studies for T2K
4054 Runs 5 and 6". In: *T2K Technical Note* 219 (2015).
- 4055 [170] S. Berkman et al. "fiTQun: A New Reconstruction Algorithm for Super-K". In:
4056 *T2K Technical Note* 146 (2013).
- 4057 [171] R.B. Patterson et al. "The extended-track event reconstruction for MiniBooNE".
4058 In: *Nuclear Instruments and Methods in Physics Research Section A* 608.1 (2009),
4059 pp. 206–224. URL: <https://doi.org/10.1016/j.nima.2009.06.064>.
- 4060 [172] M. Shiozawa. "Reconstruction algorithms in the Super-Kamiokande large water
4061 Cherenkov detector". In: *Nuclear Instruments and Methods in Physics Research
4062 Section A: Accelerators, Spectrometers, Detectors and Associated Equipment* 433.1-2
4063 (Aug. 1999), pp. 240–246. URL:
4064 [https://doi.org/10.1016/s0168-9002\(99\)00359-9](https://doi.org/10.1016/s0168-9002(99)00359-9).
- 4065 [173] K. Abe et al. "Search for CP Violation in Neutrino and Antineutrino Oscillations
4066 by the T2K Experiment with 2.2×10^{21} Protons on Target". In: *Phys. Rev. Lett.*
4067 121.17 (Oct. 2018). URL: <https://doi.org/10.1103/physrevlett.121.171802>.
- 4068 [174] K. Abe et al. "Measurements of neutrino oscillation in appearance and
4069 disappearance channels by the T2K experiment with 6.6×10^{20} protons on
4070 target". In: *Phys. Rev. D* 91.7 (Apr. 2015). URL:
4071 <https://doi.org/10.1103/physrevd.91.072010>.
- 4072 [175] F. James. "MINUIT Function Minimization and Error Analysis". In: *Reference
4073 Manual, Version 94.1, CERN Program Library Long Writeup D506 D.506* (1994).
4074 eprint:
4075 <https://root.cern.ch/sites/d35c7d8c.web.cern.ch/files/minuit.pdf>.
- 4076 [176] X. Li and M. Wilking. "FiTQun Event Selection Optimization". In: *T2K Technical
4077 Note* 319 (2017).
- 4078 [177] S. Tobayama. "An Analysis of the Oscillation of Atmospheric Neutrinos".
4079 PhD thesis. British Columbia U., 2016.
- 4080 [178] D. Barrow et al. "Super-Kamiokande Data Quality, MC, and Systematics in Run
4081 10". In: *T2K Technical Note* 399 (2020).
- 4082 [179] A. Maghrabi, A. Aldosari, and M. Almutairi. "Correlation analyses between solar
4083 activity parameters and cosmic ray muons between 2002 and 2012 at high cutoff
4084 rigidity". In: *Advances in Space Research* 68.7 (Oct. 2021), pp. 2941–2952.

- 4085 [180] J. Beringer et al. "Review of Particle Physics". In: *Phys. Rev. D* 86 (1 2012),
4086 p. 010001. URL: <https://link.aps.org/doi/10.1103/PhysRevD.86.010001>.
- 4087 [181] S. Nakayama K. Iyogi and Y. Obayashi. "T2K data acquisition and FC event
4088 selection at Super-Kamiokande". In: *T2K Technical Note* 027 (2011).
- 4089 [182] L. K. Pik. "Study of the neutrino mass hierarchy with the atmospheric neutrino
4090 data observed in Super-Kamiokande". PhD thesis. Tokyo University, 2012.
- 4091 [183] R. Wendell et al. "Atmospheric neutrino oscillation analysis with subleading
4092 effects in Super-Kamiokande I, II, and III". In: *Phys. Rev. D* 81 (9 2010), p. 092004.
- 4093 [184] J. Hosaka et al. "Three flavor neutrino oscillation analysis of atmospheric
4094 neutrinos in Super-Kamiokande". In: *Phys. Rev. D* 74 (3 2006), p. 032002. URL:
4095 <https://link.aps.org/doi/10.1103/PhysRevD.74.032002>.
- 4096 [185] D. Barrow et al. "Flux and interaction models for the initial T2K-SK atmospheric
4097 joint fit studies". In: *T2K Technical Note* 422 (2022).
- 4098 [186] L. Munteanu et al. "Constraining the Flux and Cross Section Models with Data
4099 from ND280 using FGD1 and FGD2 for the 2020 Oscillation Analysis". In: *T2K*
4100 *Technical Note* 395 (2020).
- 4101 [187] P. Bartet et al. " ν_μ CC event selections in the ND280 tracker using Run 2+3+4
4102 data". In: *T2K Technical Note* 212 (2015).
- 4103 [188] W. Parker. "Constraining Systematic Uncertainties at T2K using Near Detector
4104 Data". PhD thesis. Royal Holloway University of London, 2020.
- 4105 [189] V. Berardi et al. " $\bar{\nu}_\mu$ event selection in the ND280 tracker using Run 5c and Run 6
4106 anti-neutrino beam data". In: *T2K Technical Note* 246 (2015).
- 4107 [190] B. Kirby J. Kim and M. Wilking. "Michel Electron Tagging in FGD1". In: *T2K*
4108 *Technical Note* 104 (2012).
- 4109 [191] J. Missert. "TN-318: Fit to Super-K Atmospheric Neutrino Data for Optimization
4110 of the fiTQun Fiducial Volume Cuts and Estimation of Detector Uncertainties".
4111 In: *T2K Technical Note* 318 (2017).
- 4112 [192] J. Chakrani et al. "NIWG model and uncertainties for 2021 oscillation analysis".
4113 In: *T2K Technical Note* 414 (2022).
- 4114 [193] M. Wascko. "T2K Status, Results, And Plans". In: *Neutrino 2018* (2018). URL:
4115 <https://zenodo.org/record/1286752>.
- 4116 [194] T. Vladislavljevic et al. "Flux Prediction and Uncertainty with NA61/SHINE 2009
4117 Replica-Target Data (TN354 version 3.3)". In: *T2K Technical Note* 354 (2020).
- 4118 [195] G. Ambrosini et al. "K/ π production ratios from 450 GeV/c protons on
4119 beryllium". en. In: *Phys. Lett. B* 420.1-2 (Feb. 1998), pp. 225–232.
- 4120 [196] E. Atkin et al. "NIWG model and uncertainties for 2019-2020 oscillation analysis".
4121 In: *T2K Technical Note* 344 (2019).
- 4122 [197] D. Barrow et al. "SK atmospheric T2K beam joint fit technical note, MaCh3
4123 details". In: *T2K Technical Note* 426 (2022).
- 4124 [198] A. A. Aguilar-Arevalo et al. "Measurement of ν_μ and $\bar{\nu}_\mu$ induced neutral current
4125 single π^0 production cross sections on mineral oil at $E_\nu \sim \mathcal{O} (1 \text{ GeV})$ ". In: *Phys.*
4126 *Rev. D* 81 (1 2010), p. 013005. eprint:
4127 <https://link.aps.org/doi/10.1103/PhysRevD.81.013005>.

- 4128 [199] P. Perio and J. Imber. "Super-K Systematic Uncertainties for RUN1-4 Joint ν_e and
4129 ν_μ Analyses". In: *T2K Technical Note* 186 (2014).
- 4130 [200] P. Perio and J. Imber. "Update of SK ν_e systematic error for 2012a oscillation
4131 analysis". In: *T2K Technical Note* 107 (2012).
- 4132 [201] D. Barrow and C. Vilela. *T2K-SK Detector Matrix Uncertainties - MaCh3 Integration.*
4133 <https://git.t2k.org/t2k-sk/t2ksk-detcovmat/-/tree/feature/MaCh3Integration>. Accessed: 22-06-2022.
- 4135 [202] R. Barlow and C. Beeston. "Fitting using finite Monte Carlo samples". en. In:
4136 *Comput. Phys. Commun.* 77.2 (Oct. 1993), pp. 219–228.
- 4137 [203] J. S. Conway. "Incorporating Nuisance Parameters in Likelihoods for Multisource
4138 Spectra". In: *arXiv* (2011). URL: <https://arxiv.org/abs/1103.0354>.
- 4139 [204] D. Barrow et al. "Oscillation probability calculation for the T2K+SK atmospheric
4140 joint fit". In: *T2K Technical Note* 425 (2022).
- 4141 [205] R. G. Calland, A. C. Kaboth, and D. Payne. "Accelerated event-by-event neutrino
4142 oscillation reweighting with matter effects on a GPU". In: *IOP Journal of
4143 Instrumentation* 9.04 (Apr. 2014), P04016–P04016.
- 4144 [206] R. Wendell. *Prob3++ Oscillation Probability Calculation*. URL:
4145 <http://www.phy.duke.edu/~raw22/public/Prob3++/>.
- 4146 [207] F. Kallenborn et al. "Massively parallel computation of atmospheric neutrino
4147 oscillations on CUDA-enabled accelerators". In: *Computer Physics Communications*
4148 234 (2019), pp. 235–244.
- 4149 [208] L. Warsame. *MaCh3 Analysis Progress*. Implementation of CUDAProb3 in MaCh3
4150 for DUNE. URL: https://indico.fnal.gov/event/50217/contributions/241232/attachments/155318/202209/MaCh3ProgressforDUNELBL_May17%20%282%29.pdf.
- 4153 [209] S. Bourret et al. "Neutrino oscillation tomography of the Earth with
4154 KM3NeT-ORCA". In: *Journal of Physics: Conference Series* 888 (2017), p. 012114.
- 4155 [210] C. Rott, A. Taketa, and D. Bose. "Spectrometry of the Earth using Neutrino
4156 Oscillations". In: *Scientific Reports* 5.1 (Oct. 2015). URL:
4157 <https://doi.org/10.1038/srep15225>.
- 4158 [211] K. Hagiwara, N. Okamura, and K. Senda. "The earth matter effects in neutrino
4159 oscillation experiments from Tokai to Kamioka and Korea". In: *Journal of High
4160 Energy Physics* 2011.9 (Sept. 2011).
- 4161 [212] D. Typinski. *Earth Gravity*.
4162 <http://www.typnet.net/Essays/EarthGravGraphics/EarthGrav.pdf>.
4163 Accessed: 24-06-2022.
- 4164 [213] D. Barrow. *T2K Beam + SK Atmospheric Joint Fit*. Plenary Slides for May 2022 T2K
4165 Collaboration Meeting, 2022. URL:
4166 https://t2k.org/meet/collab/CM_May_2022/Talks/Friday/T2KSKPlenary.
- 4167 [214] E. Atkin et al. "Measuring PMNS parameters in a joint ND280-SK analysis using
4168 MCMC". In: *T2K Technical Note* 393 (2020).

- ⁴¹⁶⁹ [215] K. Abe et al. "Neutron Tagging following Atmospheric Neutrino Events in a
⁴¹⁷⁰ Water Cherenkov Detector". In: *arXiv* (2022). URL:
⁴¹⁷¹ <https://arxiv.org/abs/2209.08609>.